UNIVERSIDAD
NACIONAL
DE COLOMBIA

Analysis of a depropanizer column with internal energy integration of concentric configuration

Javier Alexander Mancera Apolinar

National university of Colombia

Faculty of Engineering, Department of Chemical Engineering

Bogotá, Colombia

2022

Análisis de una columna depropanizadora con integración energética interna de configuración concéntrica

Javier Alexander Mancera Apolinar

Universidad Nacional de Colombia
Facultad de Ingeniería, Departamento de Ingeniería Química y Ambiental
Bogotá, Colombia
2022

Analysis of a depropanizer column with internal energy integration of concentric configuration

Javier Alexander Mancera Apolinar

Thesis presented as a partial requirement to qualify for the title of:

PhD in Chemical Engineering

Advisor:

Ph.D. Carlos Arturo Martínez Riascos

Co-Advisor:

Ph.D. Diego Fernando Mendoza Muñoz

Research area:

Process modeling and simulation

Research Group:

Process System Engineering

Universidad Nacional de Colombia

Faculty of Engineering, Department of Chemical and Environmental Engineering

Bogotá, Colombia

2022

Dedication

To my savior Jesus Christ and to my mother who is in his presence.

Declaration of original work

I declare that:

I have read Agreement 035 of 2003 of the Academic Council of Universidad Nacional. "Regulation on intellectual property" and the National Regulations related to the respect of copyright. This dissertation represents my original work, except where I have acknowledged the ideas, words, or materials of other authors.

When ideas or words from other authors have been presented in this dissertation, I have made their respective recognition by correctly applying the citation and bibliographic reference schemes in the required style.

When it was necessary, I have obtained permission from the author or publisher to include any copyrighted material (e.g., tables, figures, survey instruments, or large portions of text).

Finally, I have submitted this dissertation to the academic integrity tool, defined by the university.

Javier Alexander Mancera Apolinar
10/11/2022

Acknowledgments

To GOD first for giving me the opportunity to study. To Professors Carlos Martinez and Diego Mendoza for their direction and wise advice.

To Professor Ronnie from the University of Chalmers for receiving me in the internship and for his useful collaboration for the development of the thesis.

To my mother, who is with GOD, for all those years she was with me and for supporting me in every project I undertake. To my brothers for the simple fact of being my brothers, I love them.

Abstract

In this study, the performance of a concentric distillation column with internal energy integration (HIDiC) was analyzed, considering the system propylene-propane and based on the second thermodynamic law. Additionally, the hydraulic behavior was studied and the efficiency of some trays in different points of column was estimated by CFD. To achieve that, five specific objectives were established: 1) Select the most suitable type of concentric HIDiC configuration for the separation of the propylene-propane mixture, considering second thermodynamic law, as well as the effect of the configuration on the entropy generation, the energy and exergy required for the separation. 2) Fit a CFD model for predicting the hydraulic behavior and mass transfer efficiency in a tray of the selected HIDiC. 3) Identify effects of column design and operating variables on thermal, hydraulic and mass transfer performance in a HIDiC tray. 4) Analyze the second law efficiency in the selected HIDiC, distinguishing the exergetic losses by phenomena, and 5) Propose a preliminary methodology for the conceptual design of concentric HIDiCs, considering the operational viability and its thermodynamic efficiency.

In the development of the first objective, it was possible to determine that the HIDiC column that presents the best exergetic behavior, for the separation of the studied system, is the Top-HIDiC (Chapter 1). In the second objective, due to the absence of experimental data for the chosen system, we first proceeded to validate the use of CFD for a known binary system with experimental data of its hydrodynamic behavior (Chapter 2), and mass transfer, through tray efficiency (Chapter 3). Once the hydrodynamic and mass transfer components were validated, the CFD was applied to a tray of the HIDiC for the propylene-propane system (Chapter 4), predicting the clear liquid height and the tray efficiency in rectification and stripping sections, obtained results were coherent with the studied phenomenon. For the third objective (Chapter4), three integrated trays – located in different places of the HIDiC: above, in the middle and in the lower– were analyzed to check the influence of initial and boundary conditions on the studied properties (clear liquid height and tray efficiency). For the fourth objective, it was possible to discriminate the exergetic losses for each component of the HIDiC column and they were compared with the losses generated in a Conventional Column and a Vapor Recompression Column, confirming a higher thermodynamic performance for the HIDiC (Chapter 5). Finally, in the development of the last objective, it was possible to establish a preliminary conceptual design through 5 general steps, with the exergetic loss as the main design criteria (Chapter 6).

Resumen

En este estudio se analizó el desempeño termodinámico de una columna de destilación concéntrica, con integración energética interna, para separar la mezcla propileno-propano, mediante el análisis de segunda ley de la columna. Adicional, se estudió el comportamiento hidráulico y se determinó la eficiencia de un plato en diferentes secciones de este tipo de columnas mediante CFD. Para lograr esto, se establecieron cinco objetivos específicos: 1) Seleccionar del tipo de configuración HIDiC concéntrica más adecuado para la separación de la mezcla propileno-propano mediante el análisis de segunda ley de la termodinámica aplicado en la columna completa considerando el efecto de la configuración sobre la entropía generada, la energía y exergía requerida para la separación. 2) Predecir el comportamiento hidráulico y la eficiencia de transferencia de masa en un plato de la HIDiC seleccionada usando CFD. 3) Identificar efectos de las variables de diseño y de operación de la columna sobre el desempeño térmico, hidráulico y de transferencia de masa en un plato de la columna HIDiC. 4) Analizar la eficiencia de segunda ley en la HIDiC seleccionada considerando las pérdidas exergéticas generadas por cada uno de los fenómenos, y 5) Proponer una metodología preliminar para el diseño conceptual de columnas HIDiC concéntricas, considerando la viabilidad operacional y su eficiencia termodinámica.

En el desarrollo del primer objetivo, se logró determinar que la columna HIDiC que presenta mejores resultados exergéticos (segunda ley), para la separación del sistema de estudio, fue la HIDiC de tope (Capítulo 1). En el segundo objetivo, debido a la ausencia de datos experimentales del sistema en este tipo de columnas, se procedió primeramente a validar el uso de CFD para el caso de un sistema binario conocido que contara con datos experimentales tanto en la parte hidrodinámica mediante la propiedad altura del líquido claro (Capítulo 2), como de transferencia de masa mediante la eficiencia de plato (Capítulo 3) obteniéndose resultados muy cercanos a los experimentales; éstas simulaciones se realizaron sobre un plato perforado rectangular. Una vez validado la parte hidrodinámica y de transferencia de masa, se procedió a aplicar el CFD a una sección de plato de la columna HIDiC (Capítulo 4), prediciendo la altura del líquido claro y la eficiencia de plato, en ambas secciones, rectificación y agotamiento, obteniéndose resultados coherentes con los fenómenos estudiados. Para dar cumplimento al objetivo tres, se tomaron tres platos integrados ubicados en diferentes lugares de la columna HIDiC, uno arriba, otro en el medio y otro en la parte de debajo de la columna las cuales contaban con tres condiciones diferentes (Capítulo 4) comprobando la influencia de estas condiciones iniciales y de frontera sobre las propiedades estudiadas (altura del líquido claro y eficiencia de plato). En el cuarto objetivo se logró discriminar las perdidas exergéticas por cada componente de la columna HIDiC y se compararon con las pérdidas generadas con la columna convencional y la de recompresión de vapor obteniéndose mejores resultados en la columna HIDiC (Capítulo 5). Para finalizar, en el desarrollo del último objetivo, se logró establecer un diseño conceptual preliminar mediante 5 pasos generales teniendo como base principal del diseño el principio de pérdida exergética (Capítulo 6).

Keywords: HIDiC, exergy, CFD, distillation sieve tray, clear liquid height, tray efficiency.

Table of Contents

List of Figures

List of Table

Introduction

The use of renewable energies and the development of energy efficient technologies are priority issues to achieve the sustainable development of our society (Hanley et al., 2009; Hepbasli, 2008). Proof of that are the intense studies related to the energy integration of processes (Morar & Agachi, 2010), which have allowed the development of energy use methodologies such as: pinch analysis (Kemp, 2007), exergy analysis (Kotas, 1995) and Analysis of the second law (Bejan, 2013), which seeks to reduce the net energy demand of the processes, identifying conditions and/or designs that reduce irreversibilities. In the analysis of processes, an eye has also been focused on the study of hydrodynamics, due to its role on the behavior and efficiency of equipment, therefore, in recent years, the use of computational fluid dynamics has awakened great interest for both, the academic and industrial sectors, allowing improvement in R&D in terms of equipment, products and processes (Krishna & Van Baten, 2003; Tu et al., 2018).

A process of relevant interest in the search for greater energy efficiency, is distillation, because it is one of the most widely used separation techniques in spite of having high energy consumption and low thermodynamic efficiency (Sun, 2010). One case of great importance in the petrochemical industry is the separation of propylene-propane system by distillation. In this sense, Heat Integrated Columns (HIDiC) have been seen as an interesting alternative in the separation of this type of mixtures, because they have shown advantages in the energy use for separation of mixtures of low relative volatility (Nakaiwa et al., 2003), but due to its complexity, specific studies are required to make its implementation feasible.

In the design of HIDiCs, some barriers have been identified, such as: 1) Lack of systematic methods and mathematical models that allow to simulate, analyze, design and establish control strategies; In addition, more experimental evidence is required to demonstrate the scope and limitations of this technology. 2) Absence of strategies and methodologies for the conceptual design of these systems, including the selection of the type of concentric configuration, based on the analysis of the second law of thermodynamics, which considers thermodynamic efficiency, and 3) In available literature there are no studies on tray hydraulics or efficiency for this type of configuration.

To partially address these inconvenience, two good tools are: 1) The knowledge that has been achieved in the analysis of exergy and conceptual designs for conventional columns and 2.) The studies and advances that have been obtained in the use of CFD techniques in the analysis of trays for conventional columns, the latter used for the purpose of analyzing the fluid-dynamic behavior and the effect of geometry in the design of columns. However, there is still a long way to go and many obstacles to overcome in terms of physical aspects and simulation, in order to move from empirical designs to designs with a greater technical-scientific basis. In the case of HIDiC columns, due to the complexity in their configuration, a great effort is required, in the first instance, in the use of simulations that allow a better understanding of the operation, advantages and limitations of the column. Within these analyzes, CFD tools make it possible to study, in depth, the hydraulic behavior of a column, and with the help of mass transfer models, also to determine the efficiency of the tray, which is key to obtaining designs that meet operational and energy expectations.

In accordance with the aforementioned, this work makes use of these two tools in order to contribute to the knowledge, use and application of HIDiC columns, which can bring benefits to the petrochemical and chemical industry in general, and in an indirect way, to environmental issues. For this reason, the general objective of this study was to "Analyze the thermodynamic performance of a concentric distillation column with internal energy integration to separate the propylene-propane mixture, by second law column analysis, and hydraulic and efficiency of one plate by CFD". To achieve this purpose, five specific objectives were established: 1) Select the most suitable type of concentric HIDiC configuration for the separation of the propylene-propane mixture through the analysis of the second thermodynamic law, considering the effect of the configuration on the entropy generated, the energy and exergy required for the separation. 2) Predict hydraulic behavior and mass transfer efficiency in a selected HIDiC platter using CFD. 3) Identify effects of column design and operating variables on thermal, hydraulic, and mass transfer performance in a HIDiC tray. 4) Analyze the efficiency of the second law in the selected HIDiC considering the exergetic losses generated by each one of the phenomena, and 5) Propose a preliminary methodology for the conceptual design of concentric HIDiC, considering the operational viability and its thermodynamic efficiency. To achieve these objectives, specific methodologies were established. In the development of the first objective, the different types of concentric HIDiC configuration were simulated, together with conventional and vapor recompression columns; the exergy losses were calculated for each one and the results obtained were compared, selecting the most efficient from the exergetic point of view. In the second objective, due to the absence of experimental data for the study case, the methodology starts with a validation of CFD for sieve trays analysis. A binary system with experimental data –both in the hydrodynamic issue, through the clear liquid height property, and mass transfer, through the tray efficiency– was selected for this step. Once the hydrodynamic and mass transfer part had been validated, the CFD was applied, with the models established in the first validation, to a tray section of the HIDiC column, predicting the clear liquid height and the efficiency of the plate, in both sections, rectification and stripping. To fulfill the third objective, three integrated trays were taken, located in different places of the HIDiC column, one on the top, one in the middle and another at the bottom of the column, this strategy allowed to cover the entire range of possible operational conditions. In the fourth objective, the exergy losses for each component of the HIDiC column were calculated and they were compared with the losses generated in a conventional column and a vapor recompression column. Finally, in the development of the last objective, the conceptual design of conventional columns was taken as a basis, adjusting it to HIDiC columns, and adding the exergetic criterion.

References

Bejan, A. (2013). *Entropy generation minimization: the method of thermodynamic optimization of finite-size systems and finite-time processes*. CRC press.

Hanley, N., McGregor, P., Swales, J., & Tuner, K. (2009). Do increases in resource productivity improve environmental quality and sustainability? *Ecological Economics*, *68*(3), 692–709. https://dspace.stir.ac.uk/bitstream/1893/7707/1/Hanley et al Ecological Economics 2009_turner last.pdf

Hepbasli, A. (2008). A key review on exergetic analysis and assessment of renewable energy resources for a sustainable future. *Renewable and Sustainable Energy Reviews*, *12*(3), 593–661. https://doi.org/10.1016/j.rser.2006.10.001

Kemp, I. C. (2007). *Pinch Analysis and Process Integration: A User Guide on Process Integration for the Efficient Use of Energy* (I. C. B. T.-P. A. and P. I. (Second E. Kemp (ed.); Second). Butterworth-Heinemann. https://doi.org/https://doi.org/10.1016/B978-075068260-2.50006-7

Kotas, T. J. (1995). *The exergy method of thermal plant analysis*. Krieger Pub.

Krishna, R., & Van Baten, J. M. (2003). Modelling sieve tray hydraulics using computational fluid dynamics. *Chemical Engineering Research and Design*, *81*(1), 27–38. https://doi.org/10.1205/026387603321158168

Morar, M., & Agachi, P. S. (2010). Review: Important contributions in development and improvement of the heat integration techniques. *Computers and Chemical Engineering*, *34*(8), 1171–1179.

https://doi.org/10.1016/j.compchemeng.2010.02.038

Nakaiwa, M., Huang, K., Endo, A., Ohmori, T., Akiya, T., & Takamatsu, T. (2003). Internally heat-integrated distillation columns: A review. *Chemical Engineering Research and Design*, *81*(1), 162–177. https://doi.org/10.1205/026387603321158320

Sun, A. (2010). *Internal heat exchange in a concentric tray heat integrated distillation column (HIDiC)*. DELF UNIVERSITY OF TECHNOLOGY.

Tu, J., Yeoh, G. H., & Liu, C. (2018). *Computational fluid dynamics: a practical approach* (Third). Butterworth-Heinemann.

Chapter 1

HIDiC configuration selection by exergetic analysis

Highlights

- *Problem:* There is no criteria for the selection of the type of HIDiC configuration
- *Contribution:* A criterion is defined based on exergetic analysis to select the most suitable HIDiC configuration for the separation of the propylene propane mixture
- The study proposes an exergy-based strategy for selecting the appropriate Heat Integrated Distillation Column (HIDiC) for separating the propylene-propane system.
- Different column configurations were analyzed, including a conventional column, vapor recompression column (VRC), and several HIDiC configurations (Top, Bottom, Basic, Optimal, and Total).
- The results show that the Top HIDiC has the best performance, with a 66.4% exergy saving compared to a conventional column, followed by the Total HIDiC with a 43.4% exergy saving.
- The Top HIDiC performs better than VRC, which is currently used in the industry for the separation of the studied system.
- The study concludes that selecting the configuration for energy integration is not a straightforward task and that the proposed strategy can be applied to analyze the separation of other mixtures.

Abstract

The present study shows an exergy-based strategy for defining the type of Heat Integrated Distillation Column HIDiC, most suitable for separating the propylene-propane system. For comparing and validating the results, the analysis was performed on conventional column, vapor recompression column (VRC) and several HIDiC configurations: Top, Bottom, Basic, Optimal and Total. Uniform heat transfer area was used for the heat distribution between the internal and external column sections. As main

result, it was found that Top HIDiC has the best performance among the HIDiC configurations with a 66.4% of exergy saving compared to a conventional column, followed by the Total HIDiC with a 43.4%. In fact, Top HIDiC shows better exergetic behavior than VRC (55.0% of exergy saving), which is currently used in the industry for the separation of the studied system. Additionally, results confirm that the selection of the configuration for energy integration is not an obvious task and that the presented strategy can be applied for the analysis of the separation of other mixtures.

1.1 Introduction

Conventional distillation columns tend to have low second law efficiencies. An important condition that reduces the column efficiency is the way heat load is distributed through the column. In a conventional column heat input and output are located at the hottest (reboiler) and the coldest (condenser) points of the distillation column, demanding higher exergetic quality of the heating input in the reboiler and withdrawing lower exergetic quality heat in the condenser, if compared to diabatic columns that allow heat distribution in the internal stages of the column (Mendoza & Riascos, 2011).

The HIDiC is a non-conventional distillation column developed from the diabatic distillation concept; in a HIDiC (Figure 1-1), heat is transferred from stages located in rectification zone to stages located in the stripping zone. The temperature difference between the rectification and stripping stages is achieved operating each distillation zone at different pressure, while heat transfer is allowed by heat exchangers located in the stages.

The internal heat transfer reduces the heat demand in the condenser and reboiler, in an ideal HIDiC (i-HIDiC) the external heat transfer is not necessary; while in a partial HIDiC (p-HIDiC) only a part of the required heat is internally transferred, therefore the use of the external reboiler and the condenser is still necessary. Detailed descriptions of HIDiC technology and some implementations are presented elsewhere (Kiss & Olujić, 2014). The energy saving, compared to conventional columns, estimated by several authors (Liu & Qian, 2000; Matsuda et al., 2010; Nakaiwa et al., 1997, 2001) are from 52 to 90%, these studies considered systems with relative volatilities from 1.15 (propylene-propane) to 2.40 (benzene-toluene).

Within the concentric type HIDiC there are several configurations (Figure 1-2), which can be grouped in symmetric and asymmetric. In the symmetric HIDiC stripping and rectifying sections are the same size, symmetric configurations are: Basic, Feed Optimum and

Total. The Basic HIDiC has equal number of trays in both columns (annular and internal), the rectification zone is only the internal column, and the stripping zone is only the annular one, allowing tray to tray heat transfer. In the Optimum Feed HIDiC, part of the rectification zone is in the annular column at a lower pressure, i.e., the rectification zone has more trays than the stripping one, both columns (annular and internal) have equal number of trays, thus heat is transferred tray to tray.

On the other hand, in asymmetric HIDiCs, the sizes of the annular and internal columns are different and heat integration is performed into a part of the internal column and the whole annular one. Within this type of columns, the most common are the Top and Bottom HIDiCs. In these configurations, the name refers to the section in which the heat transfer is made (Pulido, 2008). There are many other possibilities for asymmetric HIDiCs (Suphanit, 2010), however, for this study, only we will analyze the Top and Bottom ones.

Propylene is a key component for the petrochemical industry; in a general way, it is obtained in mixture with propane from 40 to 60%, depending on the process, and propylene is commonly purified to three different grades: refinery (> 60%), chemical (> 92%), and polymer grade (> 99.5) (González Plaza et al., 2011). Due to the low relative volatility, this mixture is separated using distillation columns (C3 splitter or PP splitter) with high reflux ratio and large number of theoretical steps (above 100), generating huge capital and energy costs (Mendoza et al., 2013). Thus, by adopting the HIDiC concept, the energy required in a column could be reduced about 50% compared to the recompression column (VRC), which uses one sixth of the energy required in a conventional distillation column (Olujić et al., 2006). In that way, the energy requirement in HIDiC could be close to the theoretical limit.

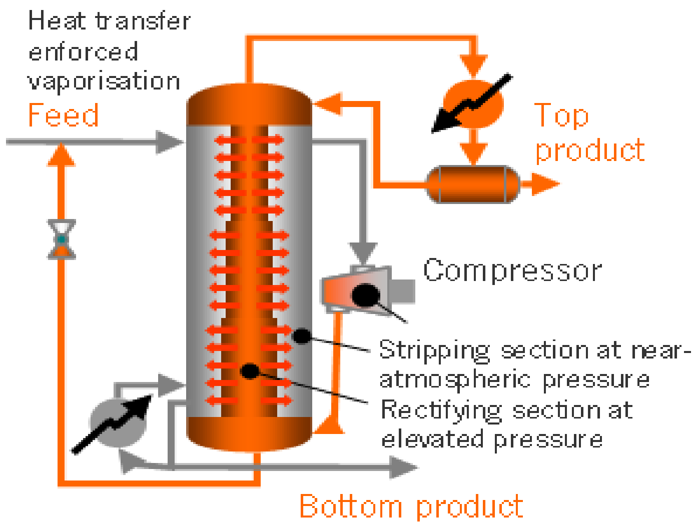

Figure 1-1: Concentric HIDiC scheme. (Source: Process Systems Enterprise).

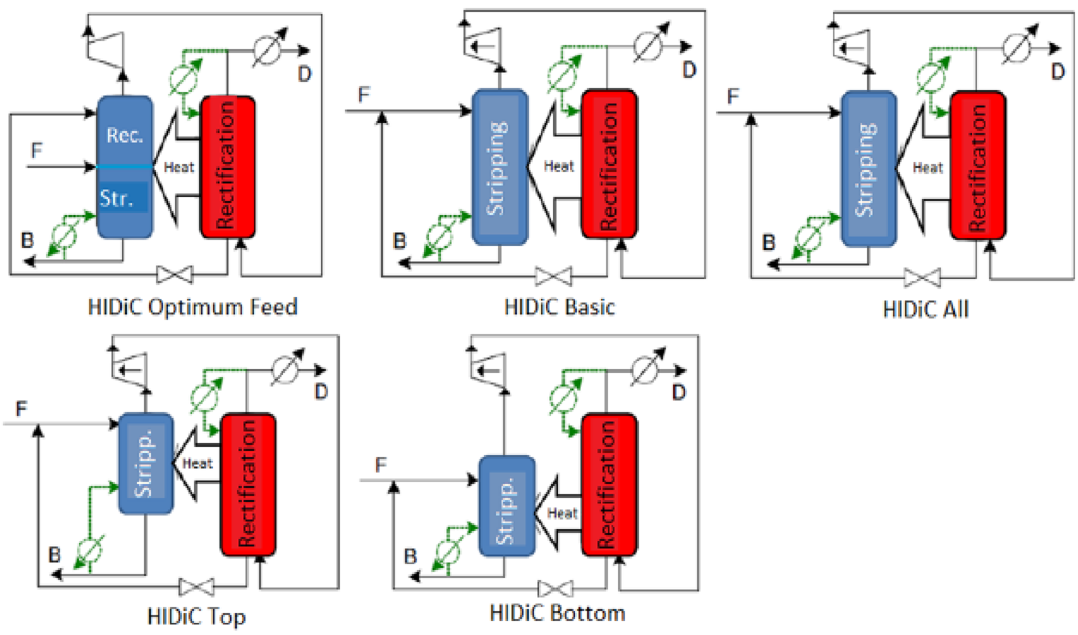

Figure 1-2: Configuration options schematic for concentric HIDiC columns. (Pulido, 2008).

Despite the high number of studies on Basic HIDiCs, currently, there is no detailed information on the energy efficiency of other HIDiC configurations for the separation of propane-propylene. Thus, we perform an exergy analysis for selecting the more suitable type of HIDiC for separation of propane-propylene.

1.2 Methodology

The aim is to perform an exergy analysis for the separation of the propylene propane mixture using not only the basic HIDiC configuration but other configurations, such as:

Total, Optimal Feed, Bottom and Top and compare them with the conventional column and the VRC. It is mentioned that the HIDIC configurations do not have external heat exchangers. This analysis will be carried out globally on each column using the following methodology: 1). A vapour recompression column was taken as base case with data supplied by Olujić et al. (2006). 2) The characteristics of the studied HIDiCs were determined. 3) The heat distribution schemes in the HIDiCs were defined, and 4) the exergy loss in each HIDiC were estimated.

1.2.1 Base case

The operational conditions of the base case (VRC) are shown in Table 1-1.

Table 1-1: VRC operational conditions (Olujić et al., 2006)

Feature	Value
Rectification section pressure (bar)	11.2
Stripping section pressure (bar)	11.2
Number of stages rectification section	165
Number of stages stripping section	66
Feeding stage	165
Rectification section pressure (bar)	11.2
Feed flow (kg/h)	112000
Feed mole fraction (propylene)	0.53
Feed thermal condition feed (q)	0.37
Distillate mole fraction (propylene)	0.996
Bottoms mole fraction (propylene)	0.011

1.2.2 HIDiC designs

In order to make the most appropriate selection of the HIDiC type, the five configurations of this type of column are compared according to the conditions shown in Table 1-2.

Table 1-2: Operational conditions of the different studied HIDiC configurations

Characteristic	Top HIDiC	Bottom HIDiC	Basic HIDiC	Total HIDiC	Opt. Feed HIDiC
Rectification section pressure (bar)	14.6	14.6	14.6	14.6	14.6 – 11.2
Stripping section pressure (bar)	11.2	11.2	11.2	11.2	11.2
Rectification section stages	170	170	115	170	170
Stripping section stages	61	61	115	61	61
Feeding stage	171	171	116	171	171
Trays in the Concentric Column	169	169	115	169	114
Trays in the Annular column	60	60	115	60	114
Feed flow (kg / h)	112000	112000	112000	112000	112000
Feed mole fraction (propylene)	0.57	0.57	0.57	0.57	0.57
Feed thermal condition (q)	0.37	0.37	0.37	0.37	0.37
Distillate mole fraction (propylene)	0.996	0.996	0.996	0.996	0.996
Bottoms mole fraction (propylene)	0.011	0.011	0.011	0.011	0.011

1.2.3 Heat distribution scheme

The scheme selected for the heat distribution between the rectification and the stripping sections was the uniform heat transfer area adapted from the procedure by Suphanit (Suphanit, 2010), which is summarized in the following steps: (1) to define the feed, the pressures, the number of stages and the products specifications; (2) to obtain the total amount of heat rejected from the rectifying section, Q_R, the total amount of heat required in the stripping section, Q_S, and the temperature driving force at any stage location, ΔT_i, along the column without integration; (3) to calculate the heat transferred in each tray, Q_i, by the Equation 1; (4) to perform the simulation with heat integration and input the values of each, Q_i, on the respective stage within each HIDiC and to recalculate Q_R, Q_S and the temperature driving force, ΔT_i.

$$Q_i = \Delta T_i \left[\frac{Q_T}{\sum_{i=1}^{n} \Delta T_i}\right] \tag{1}$$

where Q_T is the smallest value between Q_R and Q_C.

1.2.4 Calculation of the destroyed exergy

The exergy calculation was performed by first making an entropy balance on each column, Equation 2, and then using the relationship between destroyed exergy and entropy generated, Equation 3:

$$FS_F + V_i S_{Vi} + A_i S_{Ai} + S_{gen} = DS_D + V_o S_{Vo} + A_o S_{Ao} + WS_W \tag{2}$$

where F is the feed, S_F is the entropy of the feed, V_i and S_{Vi} are the steam flow and the entropy at the reboiler inlet; A_i and S_{Ai} are the flow of cooling water and entropy at the condenser inlet; S_{gen} is the entropy generated in the column; D and S_D are the distillate flow and its entropy; V_o and S_{Vo} are the steam flow and the entropy at the exit of the reboiler; A_o and S_{Ao} are the flow of cooling water and entropy at the condenser outlet; W and S_W are the flow of bottoms and their entropy respectively.

$$X_{destroyed} = T_o S_{gen} \tag{3}$$

where $X_{destroyed}$ is the exergy destroyed and T_o is the temperature of the environment (298.15 K). The simulation of both the VRC and the HIDiC were carried out using Aspen Plus™. The thermodynamic model used for the system was Peng-Robinson. The exergy analysis of each column was performed through the interaction of ASPEN™ and Excel™.

1.3 Results and analysis

Figures 1-3 and 1-4 show the destroyed exergy and exergy saving for the VRC column and the different HIDiC configurations, related to the conventional column. It is observed the columns with the lowest exergy losses are the VRC and the Top HIDiC. The Top HIDiC has the best performance among the HIDiC configurations with a 66.4% of exergy saving, followed by the Total HIDiC with a 43.4%. In the other way, the VRC, which is currently used in the industry for the separation of the studied system, achieve 55.0% of exergy saving. The other types of HIDiC configuration, from the exergy point of view, seem to be less favorable than the VRC for the study case. It should be noted that the HIDiC configuration that presents the most exergetic loss is the Bottoms one, due to the large flows of steam and cooling water required in the external exchangers.

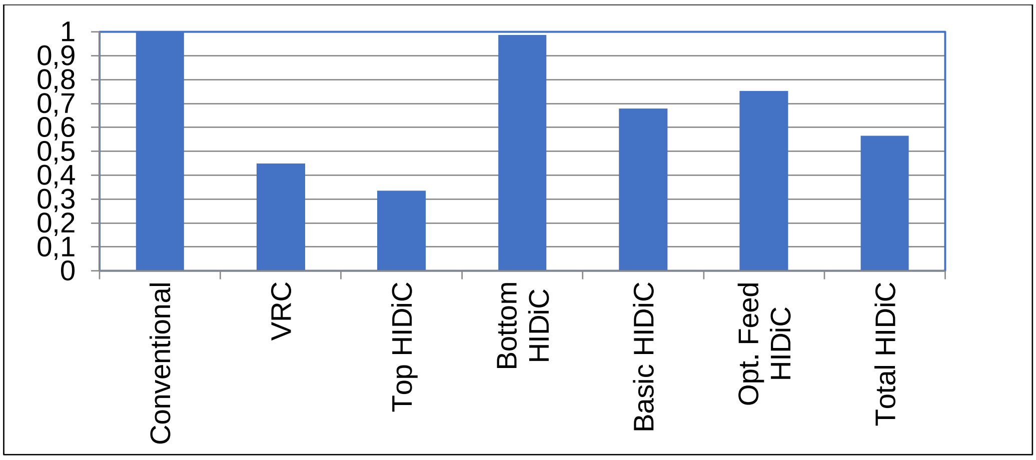

Figure 1-3: Relative exergy destroyed by column type

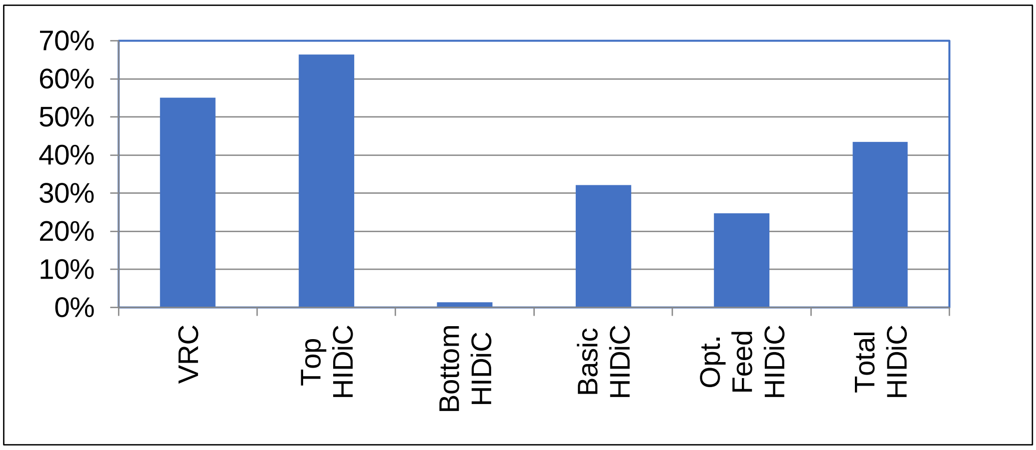

Figure 1-4: Exergy saving regarding to conventional column

Below is a comparison of the temperature profiles by column type, only in the thermally coupled stages, grouped into two groups, the first (Figure 1-5) where the Top, Bottom and Total HIDiC are found, corresponding to the HIDiC where heat transfer is carried out in all 60 trays of the stripping section; the second group (Figure 1-6) corresponds to those configurations where the annular section of the HIDiC column has 115 trays and on these the heat transfer is carried out, which is the case of the Basic HIDiC and Optimal Feeding.

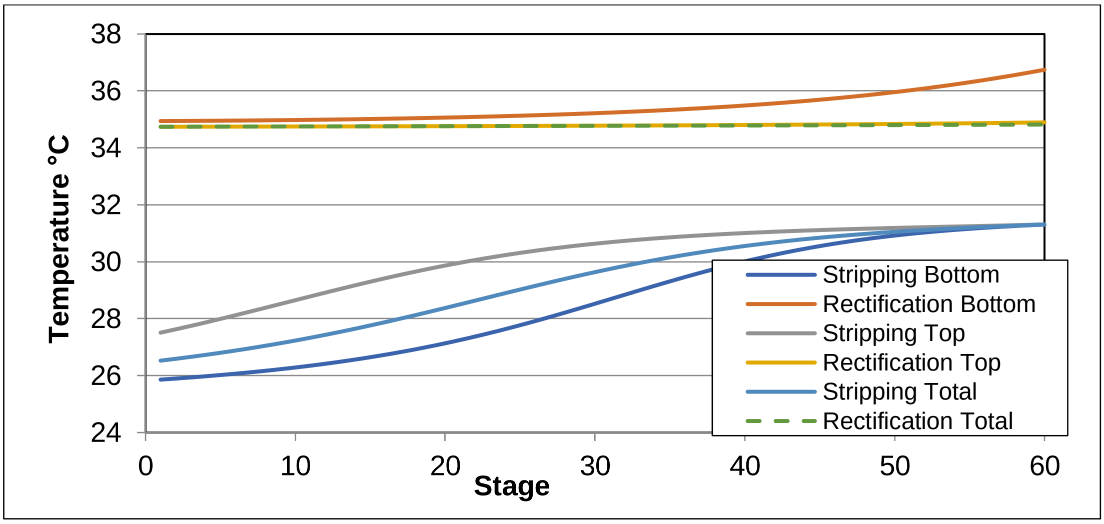

Figure 1-5: Temperature profiles of thermally coupled sections of Top, Bottom and Total HIDiC

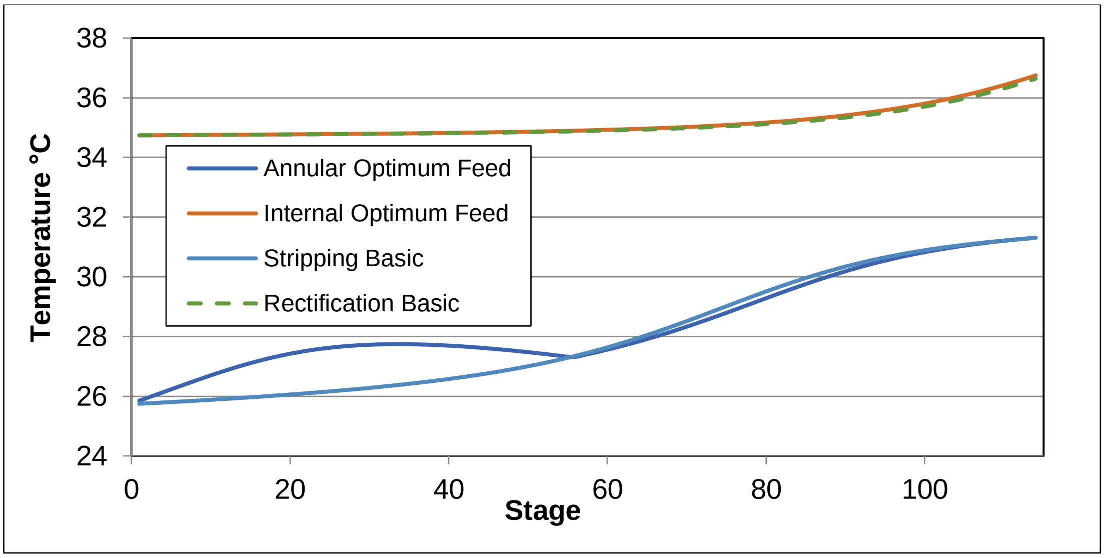

Figure 1-6: Temperature profiles of thermally coupled sections of Opt. Feed and Basic HIDiC

As shown in Figure 1-5, the temperature of the rectification zone is always higher than the temperature of the stripping zone, favoring a consistent design where heat exchange is from rectification to stripping. In Figure 1-6 a similar behavior to the one described above is presented except for the presence of a different trajectory in the first stages of the annular column of the Optimal Feeding HIDiC because this column contents the stripping zone (first 61 trays) and part of the rectification zone (remaining trays of the annular column).

The HIDiC with the highest temperature differences is the Bottom one (between 5.04 and 9.08 °C), Figure 1-7, which favor the heat transfer rate. On the other hand, the configuration with the lowest temperature difference is the Top HIDiC ($\Delta T \sim$ 3.6 °C) being less effective for a heat flow, however, this benefit of the Bottoms column is not reflected in the exergy, since irreversibility associated to heat transfer increases as temperature difference does.

In Figure 1-8 a significant difference in the temperature driving force profile is observed for the Optimum Feed configuration in relation to the other HIDiCs is observed, this because a part of the plates in the rectification section are in the annular column, which operates at a lower pressure (11.2 bar) than the central column (14.6 bar).

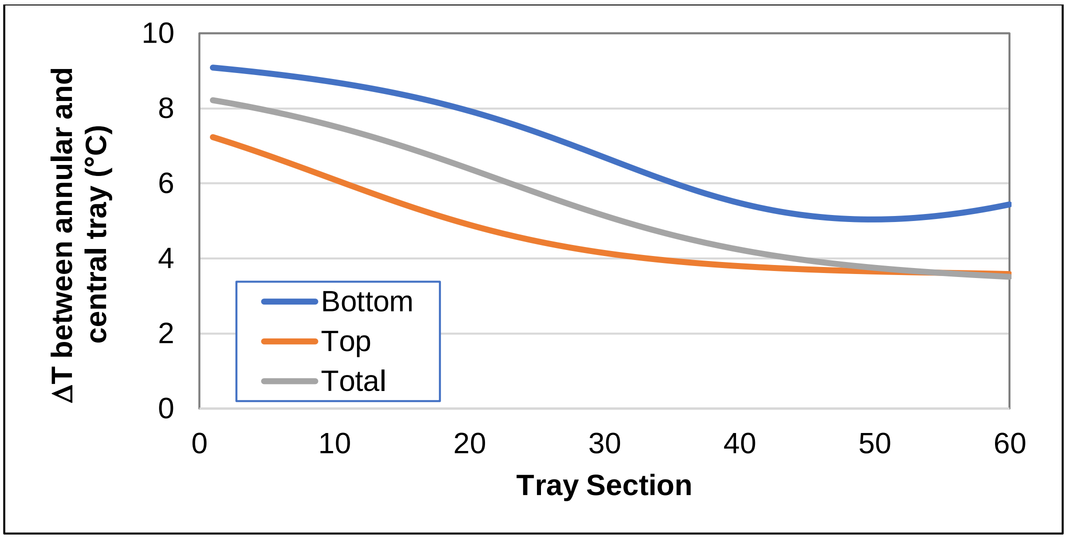

Figure 1-7: Temperature difference profiles for Top, Bottom and Total HIDiC

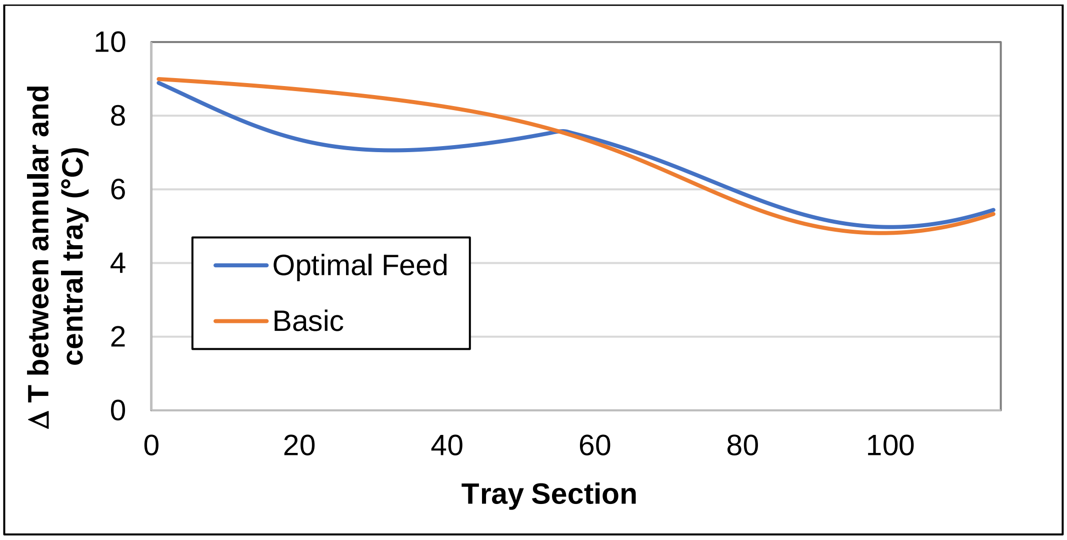

Figure 1-8: Temperature difference profiles for the Optimum Feed and Basic HIDiC

In order to deepen the analysis for the selection of the HIDiC type, the temperature profiles in the stripping zones for each configuration before and after the energy integration were also determined (Figures 1-9 to 1-13), with the purpose to verify if, after the integration, the heat flow from the highest-pressure section to the lowest one will occur.

As shown in Figure 1-9, the energy integration increased the temperature throughout the stripping section corroborating a suitable integration. On the other way, when the integration is made in the bottom HIDiC, in the first 25 stages, cooling occurs implying that the flows at these stages are losing heat and becoming colder, contrary to what is wished in this section (Figure 1-10). This is a consequence of the fact that due to insufficient separation in the rectification section, the upper stages of the stripping section contain relatively much more propylene and consequently have a lower temperature at the same pressure. Due to the above, more heat needs to be transferred between the two sections to reduce the demand on the reboiler. Similar to the bottom HIDiC, the same problem occurs in the Basic and Total ones but in a lesser degree, as shown in Figures 1-11 and 1-12.

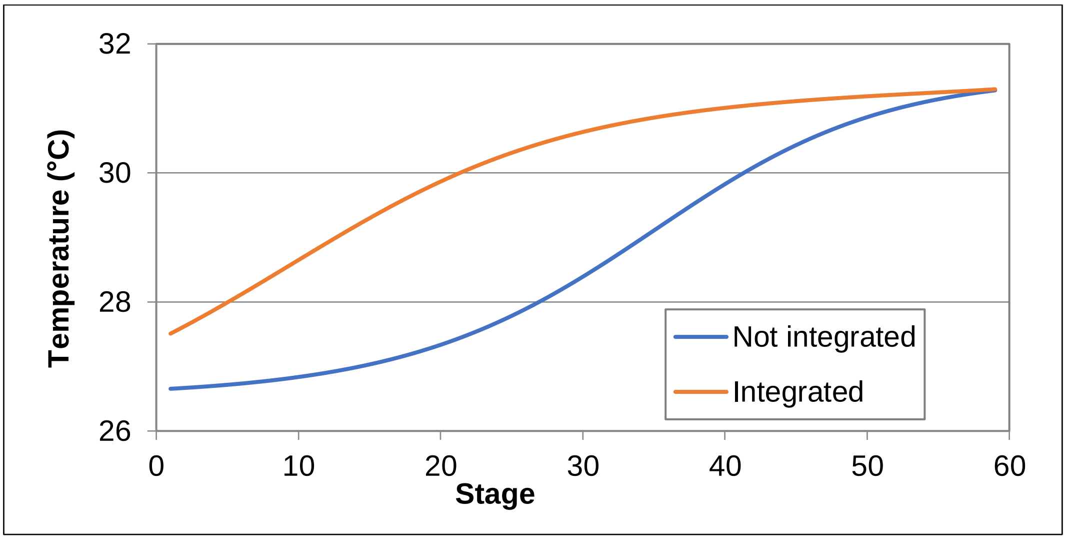

Figure 1-9: Temperature profiles before and after integration in stripping section of the Top HIDiC

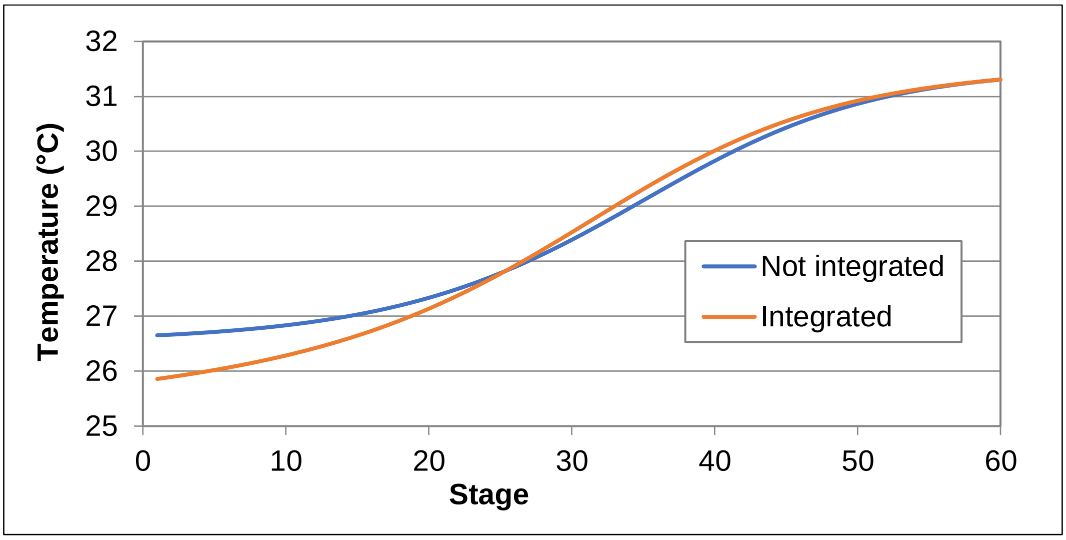

Figure 1-10: Temperature profiles before and after integration in stripping section of the Bottom HIDiC

The Optimal Feed HIDiC (Figure 1-13) does not have the cooling disadvantages of the aforementioned ones, however it is observed that it presents a temperature drop between trays 30 to 55 in the stripping section after the energy integration, different from the normal behavior in columns that, as it descends through the plates, the temperature increases. This is due to the fact that the first 56 trays of this column are located before the feeding plate producing a cooling effect in the upper plates.

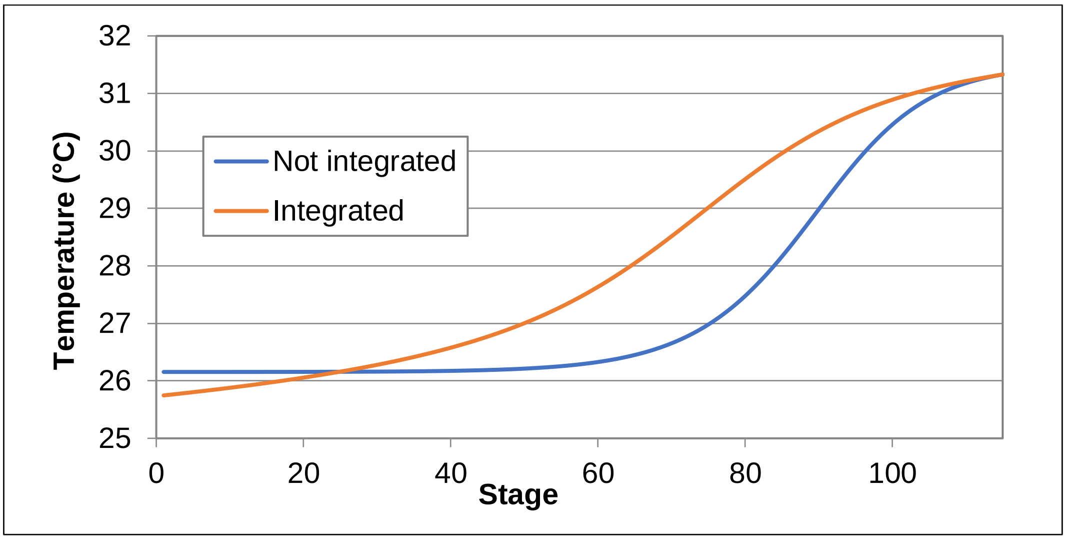

Figure 1-11: Temperature profiles before and after integration in stripping section of the Basic HIDiC

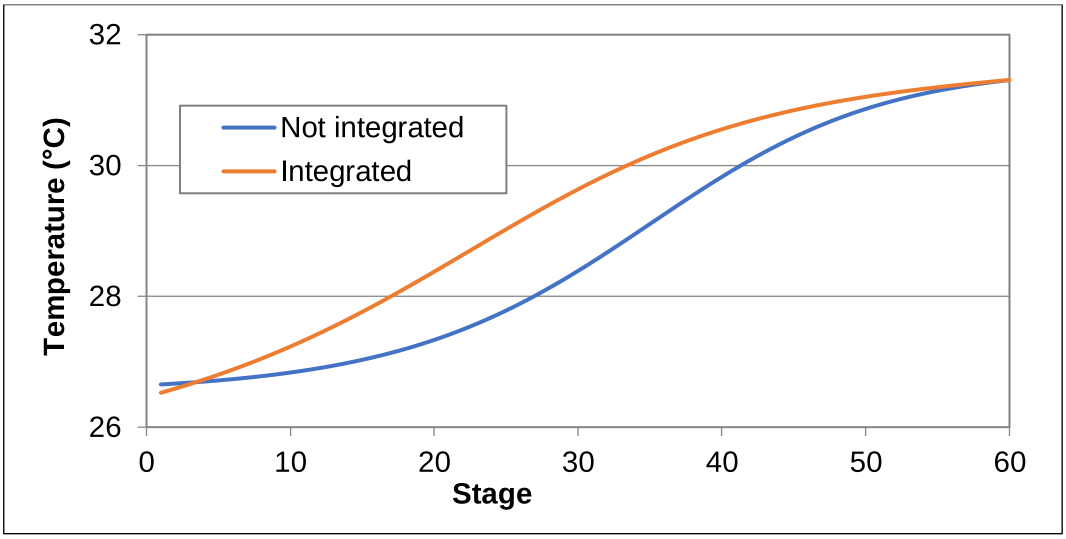

Figure 1-12: Temperature profiles before and after integration in stripping section of the Total HIDiC

Figure 1-14 shows the mole fraction of propylene in the liquid per stage, for the different HIDiC configurations. In Bottom HIDiC it is observed that most of the separation is concentrated in the thermally coupled zone (last 60 stages), the distribution of the separation task is increased in the following order: Total HIDiC, basic HIDiC, Optimum Feed and finally the Top HIDiC where the separation is more efficiently distributed. As mentioned in previously, the Optimum Feed HIDiC presents a behavior different from the others, in this column there is a drop in the propylene fraction between plates 170 to 150, returning again to an increase in the propylene fraction as ascending in the column, it occurs because part of the rectification section is in the annular column, as is characteristic of this type of columns.

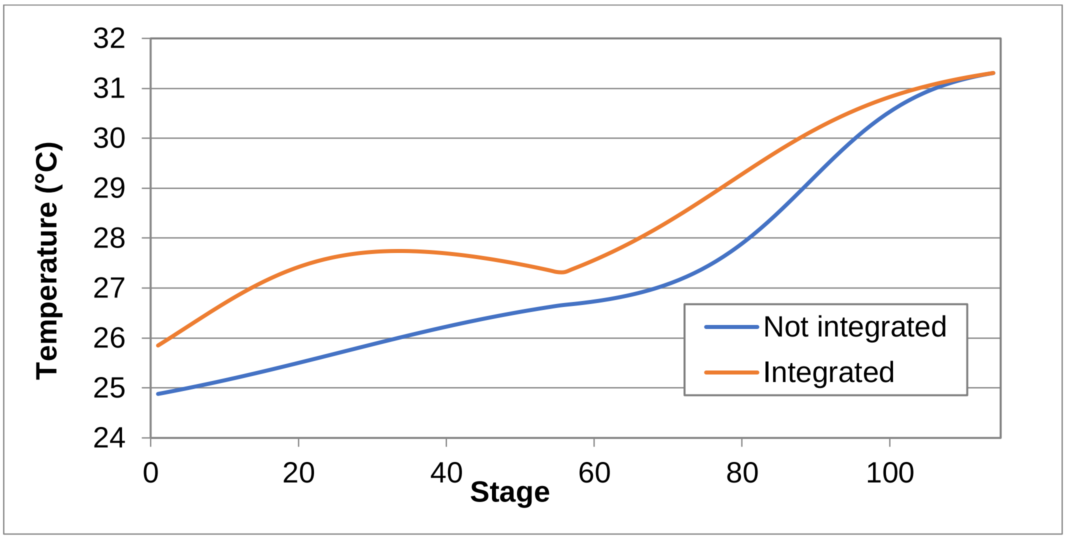

Figure 1-13: Temperature profiles before and after integration in stripping section of the Opt. Feed HIDiC

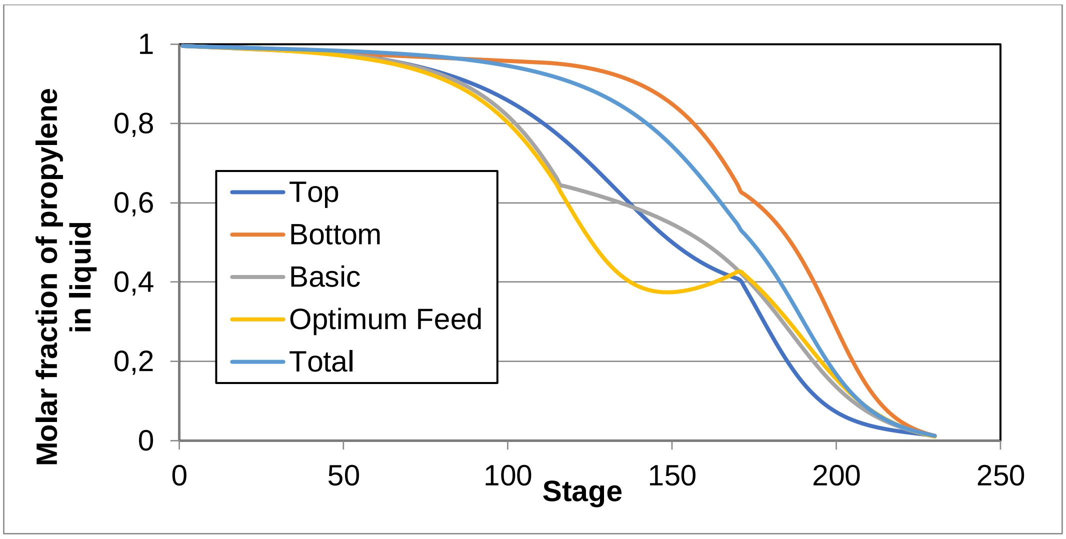

Figure 1-14: Molar fractions of Propylene in liquid per stage for the different HIDiC configurations

1.4 Conclusions

According to the study carried out, the type of HIDiC has a strong effect on the energy efficiency that can be achieved and should be considered in the selection of these systems.

For the case study, it can be concluded that among the various HIDiC studied configurations, the one with the best benefits from the exergy point of view is the Top one. It is also important to mention that this configuration presented better exergetic behavior than the column usually used for the separation of propylene-propane system (vapor recompression column), therefore it can be concluded that the Top HIDiC would be a good option for the separation of the study system improving its energy efficiency.

It is clear that although the other HIDiC configurations did not show good results, they should not be ruled out for other systems, since it is always necessary to carry out previous studies with these configurations like the one performed here and verify if they are efficient or not from the point of energetic and operational view.

The Optimum Feed HIDiC presents a different behavior, it is due to the changes in heat transfer direction along the column: one part of the rectification section receives energy, and the other part gives it.

Acknowledgments

J.A. Mancera-Apolinar is grateful for the financial support of Colciencias, under the 617 grant.

References

González Plaza, M., Ferreira, A., Santos, J., Ribeiro, A., Müller, U., Trukhan, N., Loureiro, J., & Rodrigues, A. (2011). Propane/propylene separation by adsorption using shaped copper trimesate MOF. *Microporous and Mesoporous Materials - MICROPOROUS MESOPOROUS MAT*, *157*. https://doi.org/10.1016/j.micromeso.2011.06.024

Kiss, A. A., & Olujić, Ž. (2014). A review on process intensification in internally heat-integrated distillation columns. *Chemical Engineering and Processing: Process Intensification*, *86*, 125–144. https://doi.org/10.1016/j.cep.2014.10.017

Liu, X. G., & Qian, J. X. (2000). Modeling, Control, and Optimization of Ideal Internal Thermally Coupled Distillation Columns. *Chemical Engineering and Technology*, *23*(3), 235–241. https://doi.org/10.1201/b11330-2

Matsuda, K., Iwakabe, K., Ohmori, T., & Nakaiwa, M. (2010). Dynamic behavior of an internally heat-integrated distillation column (HIDiC). *Chemical Engineering Transactions*, *21*, 127–132. https://doi.org/10.3303/CET1021022

Mendoza, D. F., Palacio, L. M., Graciano, J. E. A., Riascos, C. A. M., Vianna, A. S., & Roux, G. A. C. Le. (2013). Real-Time Optimization of an Industrial-Scale Vapor Recompression Distillation Process . Model Validation and Analysis. *Industrial and Engineering Chemistry Research*, *52*, 5735–5746.

Mendoza, D. F., & Riascos, C. A. M. (2011). Entropy minimization in design of extractive distillation system with internal heat exchangers. *Chemical Engineering Transactions*, *25*, 405–410. https://doi.org/10.3303/CET1125068

Nakaiwa, M., Huang, K., Naito, K., Endo, A., Akiya, T., Nakane, T., & Takamatsu, T. (2001). Parameter analysis and optimization of ideal heat integrated distillation columns. *Computers and Chemical Engineering*, *25*(4–6), 737–744. https://doi.org/10.1016/S0098-1354(01)00649-4

Nakaiwa, M., Huang, K., Owa, M., Akiya, T., Nakane, T., Sato, M., & Takamatsu, T. (1997). Energy savings in heat-integrated columns. *Energy*, *22*(6), 621–625.

Olujić, Ž., Sun, L., de Rijke, A., & Jansens, P. J. (2006). Conceptual design of an internally heat integrated propylene-propane splitter. *Energy*, *31*(15), 3083–3096. https://doi.org/10.1016/j.energy.2006.03.030

Pulido, J. L. (2008). Study of a New Concept of Distillation Column: Heat-Integrated Distillation Column (HIDiC). In *Bachelor Thesis in Chemical Engineering*. Industrial University of Santander.

Suphanit, B. (2010). Design of internally heat-integrated distillation column (HIDiC): Uniform heat transfer area versus uniform heat distribution. *Energy*, *35*(3), 1505–1514. https://doi.org/10.1016/j.energy.2009.12.008

Chapter 2

Predicting clear liquid height in sieve tray using CFD-PBM and bubble-induced turbulence model

Highlights

- *Problem:* There is no availability experimental data for the validation of the hydrodynamic behavior in plates of a HIDiC Column.
- *Contribution:* A CFD-based methodology to predict the hydrodynamic behavior in a sieve tray.
- Implementation and validation of a CFD model to simulate sieve trays hydrodynamics of distillation columns was conducted.
- The proposed adjusted drag coefficient approach generated better results compared with the ones obtained in previous studies.
- Bubble-induced turbulence was added to the CFD simulation of a sieve tray obtaining a good representation of the hydrodynamics of the dynamic system.
- Population balance equation was included for the first time in a CFD model to study the multiphase hydrodynamic behavior in sieve trays.

Abstract

The purpose of the present study was to design a methodology for predicting the clear liquid height (h_{cl}) in sieve trays. Thus, based on computational fluid dynamics (CFD), we created a model that could simulate the hydrodynamic behavior of sieve trays and calibrated it by comparing its results with experimental data. The construction of the model was divided in two general steps: i) we reviewed experimental data on the h_{cl} of air at different superficial gas velocities (Vs) in order to refine the Grace Drag Law (GDL) equation originally proposed by Grace; ii) we evaluated how some changes in several key variables of the model affected h_{cl}. For instance, we explored the effects of variations in geometry type (2D and 3D), weir height (h_w), liquid load, and Vs in simulations carried

out without a population balance model (PBM) (Approach 1). Afterwards, we evaluated the effects of three different bubble-induced turbulence (BIT) models —Sato's, Simonin's, and Troshko-Hassan's— on h_{cl} (Approach 2) — Finally, we used a PBM to simulate bubble size distribution during distillation and evaluated how h_{cl} would be affected by variations in geometry type and h_w in that case (Approach 3). At the time, PBMs had not been used to study the multiphase hydrodynamic behavior of fluids in sieve trays. The results of these simulations were validated with experimental data, which also proved that our model allows for an accurate representation of the phase momentum exchange of fluids. Moreover, the adjusted drag coefficient proposed in the present study is a good alternative to estimate liquid hold-up in CFD models, since it performs better than Bennet's approach, the one that is currently being used in most research on CFD sieve-tray simulations. Indeed, the margin of error in the proposed CFD model (Approach 1) was around 3.42%, compared with the 40% average reported in previous studies. Approach 2, for its part, showed that Simonin's BIT model was slightly better when compared to other BIT models. However, the increase in overall performance was not significant when compared to the results of a simulation ran without a BIT model. Finally, when compared to Approach 1, Approach 3 showed that including a PBM in the simulations does not significantly improve the prediction of the clear liquid height.

Keywords

distillation sieve tray; bubble-induced turbulence; population balance model; bubble-size distribution; clear liquid height

2.1 Introduction

Distillation is a separation process of major importance in the chemical and petroleum industries worldwide. It is also the most studied one due to its relatively high energy consumption. For this reason, both researchers and industry experts have had an interest in improving separation efficiency and developing accurate mathematical models that are able to predict the outcomes of the process.

The quality and type of the internal parts of a distillation column directly determine the performance and efficiency of the distillation process. Sieve trays are one of the most common internals in distillation equipment due to their simple design , low cost, and low manufacture time (Kiss & Olujić, 2014). Due to the widespread use of this kind of tray, some attempts have been made to accurately simulate sieve tray hydrodynamics using computational fluid dynamics (CFD) (Gesit et al., 2003; Krishna, Van Baten, et al., 1999; Li et al., 2014; Roshdi et al., 2013; Zhao et al., 2019). Since clear liquid height (h_{cl}) is the most influential variable for hydraulic behavior, the accuracy of this type of simulations depends heavily on it (Lockett, 1986).

However, the experimental data with which the results of the aforementioned CFD studies were compared shows that they fail to accurately represent h_{cl}. Indeed, these CFD models overestimate h_{cl} by 20% to 30%. This is due to the fact that these researchers rely too heavily on the Bennet correlation in order to model the liquid holdup fraction of the system, which, in turn, affects the coupling of its two-phase equations.

Drag force, on the other hand, is very often considered the predominant force for modeling gas-liquid flows in bubble columns (Chen et al., 2014) since the magnitude of this force can be over 100 times greater than other forces such as the lift, added-mass, and turbulent-dispersion forces (Magolan et al., 2019). However, more accurate approaches for modeling drag in sieve trays, such as those that take into account bubble-induced turbulence (BIT) or bubble size distribution by through a population balance model (PBM), have not been given enough attention in the academic literature.

Hence, the purpose of this research is to fill a gap in this area by developing a CFD model capable of predicting h_{cl} in sieve trays more accurately, on the one hand, and of integrating BIT, on the other hand. Thus, instead of using the Bennet correlation for our model, we worked with a modified drag coefficient which was fine-tuned by observing the effects of different variables —such as geometry type, weir height (h_w), and liquid load per weir length (Q_L/W)— on h_{cl}. Additionally, we evaluated different BIT models (Sato et al., 1981; Simonin & Viollet, 1990; Troshko & Hassan, 2001) by integrating them into the main k-ε turbulence model to see how BIT affects h_{cl}. Finally, we simulated the bubble-size distribution of the gas-liquid flow within a sieve tray by using a CFD-PBM model. All of our final results were compared with experimental data on h_{cl} to measure the accuracy of the proposed models.

This chapter is structured as follows: section 2.2 presents a background of research and advances in modeling of hydrodynamic in bubbling systems, section 2.3 describes que model for each phenomenon considered into the system, section 2.4 introduces a population balance model, section 2.5 presents the methodology employed to assess the models, section 2.6 presents the main simulation remarks that allow to develop the assessment, section 2.7 presents the results and their discussion and; finally, section 8 presents the conclusion.

2.2 Background

Many drag models (Grace et al., 1976; Ishii & Zuber, 1979; Schiller & Naumann, 1935; Tomiyama, 1998) have been used to calculate the drag force in gas-liquid flows (Gupta & Roy, 2013; Laborde-Boutet et al., 2009). For small spherical bubbles, the Schiller-Naumann model is frequently applied (Schiller and Naumann, 1935); while the Grace et al. model is well suited to gas-liquid flows in which the bubbles can have a range of shapes such as spheres, ellipses, and caps (Grace et al., 1976).

It is also important to mention BIT interaction forces between gas and liquid phases and local bubble size distribution are emphasized and highly coupled with each other (Magolan et al., 2019). Bubble-induced turbulence has been less studied and assessed as an alternative for CFD modeling of two-phase systems with bubbles (Rzehak & Krepper, 2013a, 2013b). Turbulence in this type of system has a strong impact on other important phenomena such as turbulent dispersion of bubbles, bubble coalescence, and breakup. The development of a suitable and accurate model for BIT is critical to achieving a complete working model that allows predictive CFD simulations for engineering applications involving bubbly multiphase flows at multiscale.

To model the influence of bubbles on the multiphase turbulence phenomenon, several models are available; among them, the Sato, Simonin, and Troshko-Hassan models are most frequently used in CFD studies. However, a common practice in engineering multiphase flow CFD simulations is to simply add an extra bubble-induced contribution to the effective viscosity (Sato et al., 1981). In the Sato model only the shear-induced turbulent viscosity is calculated from a two-equation model, and the bubble effects are included by an extra bubble-induced contribution to the turbulent viscosity; unlike the Simonin and Troshko-Hassan models that add explicit source terms to the turbulence equations.

In the PBM, bubble coalescence and breakup phenomena are very important for obtaining reasonable predictions for the bubble size distribution. In dispersed gas-liquid flows, the bubble size distribution plays an important role in the phase structure as well as in the interphase forces. The PBM has received much attention in both academic and industrial research because it is an effective method for calculating the size distribution of the dispersed phase in a wide variety of processes. In recent years, much work has been done using the PBM to simulate the bubble size distribution in gas-liquid flows (Bhole et al., 2008; Sun et al., 2005; Wang et al., 2005, 2006; Xing et al., 2013; Yang et al., 2017) These works evidence the great potential of the PBM in such kind of systems;

however, this model, to the best of the authors' knowledge, has not yet been used in the design of sieve trays.

Krishna *et al.* , for instance, developed several CFD models to simulate a 3D, two-phase flow in order to represent the hydrodynamics of distillation in sieve trays (Krishna, Urseanu, et al., 1999; Krishna, Van Baten, et al., 1999; Van Baten et al., 2001). The two-phase equations used in these studies were coupled, on the one hand, through an interphase drag term that was estimated using the drag coefficient correlation proposed by Krishna *et al.* (Krishna, Van Baten, et al., 1999) and, on the other hand, the Bennett correlation for the liquid holdup fraction in the froth (Bennett et al., 1983). Gesit *et al.* (Gesit et al., 2003), for their part, developed a three-dimensional CFD model to predict the flow patterns and hydraulics of commercial-scale sieve trays; the Bennett correlation for the liquid holdup fraction was also used in this case. Roshdi *et al.* (Roshdi et al., 2013) used CFD to describe the hydraulic characteristics of packed sieve trays (PST). Li *et al.* (Li et al., 2014) developed a 3D transient CFD model for describing the hydraulics of flow-guided sieve trays, within the two-phase Eulerian−Eulerian framework. Zhao *et al.* (Zhao et al., 2019) optimized the design process of flow-guiding sieve trays (FGST).

2.3 Mathematical model

The model considers the gas and liquid flows in a Eulerian-Eulerian framework, where each phase is treated as an interpenetrating continuum having separate transport equations. The following assumptions are imposed on the model developed for a distillation sieve tray: A two-phase system is considered, and the gas phase is the dispersed phase. We integrated a two-equation turbulence model based on the Reynolds Averaged Navier Stokes (RANS) into our liquid-phase calculations. Additionally, another set of source terms, both for k and ε, that allow for a more precise description of bubble-induced effects were included. We also evaluated several plausible models in order to test the overall influence of certain variables, such as drag, lift, virtual mass, turbulent dispersion forces and the bubble size distribution in a gas-liquid flow (Wang et al., 2006).

2.3.1 Flow equations

The two-fluid model, proposed in this study, treat both the vapor and liquid phases as continua and is based on two sets of conservation equations, one for each phase; these equations include mass, momentum, and energy balances.

Continuity equation for the liquid phase (Eq. 1):

$$\frac{\partial(\alpha_L\rho_L)}{\partial t}+\nabla\cdot(\alpha_L\rho_L\boldsymbol{u}_L)=0 \tag{1}$$

Continuity equation for the vapor phase (Eqs. 2a and 2b):

$$\frac{\partial(\alpha_G\rho_G)}{\partial t}+\nabla\cdot(\alpha_G\rho_G\boldsymbol{u}_G)=0 \qquad \textit{Without PBM} \tag{2a}$$

$$\frac{\partial(\alpha_G\rho_G f_i)}{\partial t}+\nabla\cdot(\alpha_G\rho_G\boldsymbol{u}_G f_i)=S_i \qquad \textit{With PBM} \tag{2b}$$

In the equations 1, 2a and 2b the first and second terms on the left-hand side are the rate of accumulation of mass and transport by convection, respectively, where ρ_L, ρ_G, $\boldsymbol{u}_L$, and $\boldsymbol{u}_G$ are the liquid and gas phase densities and velocities, in that order. In Eq. 2b, S_i represents the extent to which each of the discrete bubble classes coalesce or break up. We offer a more detailed description of this source term in Section 2.4. Finally, the gas void fraction (α_G) and the scalar fraction (f_i) of each size group are related to the number density of the discrete *i*th bubble class (Eq. 3).

$$\alpha_G f_i = N_i v_i \tag{3}$$

Momentum equations for the liquid and vapor phases (Eqs. 4 and 5):

$$\frac{\partial(\alpha_L\rho_L\boldsymbol{u}_L)}{\partial t}+\nabla\cdot(\alpha_L\rho_L\boldsymbol{u}_L\boldsymbol{u}_L) = -\alpha_L\nabla P+\nabla\cdot[\alpha_L\mu_L^e(\nabla\boldsymbol{u}_L+(\nabla\boldsymbol{u}_L)^T)]+\alpha_L\rho_L g+\boldsymbol{F}_{LG} \tag{4}$$

$$\frac{\partial(\alpha_G\rho_G\boldsymbol{u}_G)}{\partial t}+\nabla\cdot(\alpha_G\rho_G\boldsymbol{u}_G\boldsymbol{u}_G) = -\alpha_G\nabla P+\nabla\cdot[\alpha_G\mu_G^e(\nabla\boldsymbol{u}_G+(\nabla\boldsymbol{u}_G)^T)]+\alpha_G\rho_G g+\boldsymbol{F}_{GL} \tag{5}$$

where p, μ_i^e and g correspond to pressure, effective viscosity ($\mu_L^e=\mu_{lam,L}+\mu_{t,L}$; $\mu_G^e=\mu_{lam,G}+\mu_{t,G}$), and gravity, respectively. The first term on the left side of each equation is the momentum accumulation in the phase, while the second one is the net momentum outlet from the phase.

The equations that we used for calculating momentum exchange at the liquid-vapor interface, $\boldsymbol{F}_{LG}$ or $\boldsymbol{F}_{GL}$, consider drag, lift, virtual mass, and turbulent dispersion forces (Eqs 6-9).

$$\boldsymbol{F}_{LG}=\boldsymbol{F}_{LG}^{drag}+\boldsymbol{F}_{LG}^{lift}+\boldsymbol{F}_{LG}^{VM}+\boldsymbol{F}_{LG}^{TD}=-\boldsymbol{F}_{GL} \tag{6}$$

where

$$\boldsymbol{F}_{LG}^{lift}=C_l\alpha_G\rho_L(\boldsymbol{u}_G-\boldsymbol{u}_L)(\nabla\boldsymbol{u}_L) \qquad \textit{Without PBM} \tag{7a}$$

$$\boldsymbol{F}_{LG}^{lift}=\sum_{i=1}^{M} f_i C_{l,i}\alpha_G\rho_L(\boldsymbol{u}_G-\boldsymbol{u}_L)(\nabla\boldsymbol{u}_L) \qquad \textit{With PBM} \tag{7b}$$

$$\boldsymbol{F}_{LG}^{VM}=C_{VM}\alpha_G\rho_L\frac{D}{Dt}(\boldsymbol{u}_G-\boldsymbol{u}_L) \tag{8}$$

$$\boldsymbol{F}_{LG}^{TD}=-C_{TD}k\frac{\mu_{t,L}}{0.9\rho_L}\left(\frac{\nabla\alpha_G}{\alpha_G}-\frac{\nabla\alpha_L}{\alpha_L}\right) \tag{9}$$

In the above equations, C_l, C_{VM}, and C_{TD}, were set to be 0.5, 0.25, and 0.7, respectively, following the current scientific consensus (ANSYS Release 19, 2018; Lote et al., 2018).

2.3.2 Drag model

In multiphase flows, the correlations of interfacial forces describe and quantify the interaction between different phases. In fact, one of these forces, the drag force, dominates the interactions between the liquid and the gas phase in this type of flows. Solving the momentum equations (Eqs. 10a and 10b) allows for the determination of the drag force (Krishna & Van Baten, 2003; Laborde-Boutet et al., 2009; Liang et al., 2016):

$$\boldsymbol{F}_{LG}^{drag} = f\,\frac{3C_D}{4d_b}\alpha_G\rho_L|\boldsymbol{u}_G-\boldsymbol{u}_L|(\boldsymbol{u}_G-\boldsymbol{u}_L) \qquad \textit{without PBM} \tag{10a}$$

$$\boldsymbol{F}_{LG}^{drag} = \sum_{i=1}^{M}\eta f_i\frac{3C_{Di}}{4d_{bi}}\alpha_G\rho_L|\boldsymbol{u}_G-\boldsymbol{u}_L|(\boldsymbol{u}_G-\boldsymbol{u}_L) \qquad \textit{with PBM} \tag{10b}$$

where C_{Di} and C_D are the drag coefficient, whose values can be obtained from the model developed by Grace *et al.* (Grace et al., 1978). Grace's model is particularly well suited for gas-liquid flows in which the bubbles exhibit a range of shapes, such as a sphere, ellipsoid, and spherical cap. However, when working with bubbles of different shapes, other equations (11-16) are more suited for the task.

$$C_{Di} = \max\left(\min\left(C_{Di,ellipse}, C_{Di,cap}\right), C_{Di,sphere}\right) \tag{11}$$

where

$$C_{Di,sphere} = \begin{cases} 24/Re_{bi} & Re_{bi} < 0.01 \\ 24(1+0.15Re_{bi}^{0.687})/Re_{bi} & Re_{bi} \geq 0.01 \end{cases} \tag{12}$$

$$C_{Di,cap} = \frac{8}{3} \quad (13) \tag{13}$$

$$C_{Di,ellipse} = \frac{4}{3}\frac{gd_{bi}}{U_t^2}\frac{(\rho_L-\rho_G)}{\rho_G} \tag{14}$$

$$Re_{bi} = \frac{\rho_l|\boldsymbol{u}_{G-}\boldsymbol{u}_L|d_{bi}}{\mu_L} \tag{15}$$

$$U_t = \frac{\mu_l}{\rho_L d_{bi}}Mo^{-0.149}(J-0.857) \tag{16}$$

where Re_{bi} represents the Reynolds number as function of bubble size of group i (d_{bi}), which also allows the shape of the bubbles to be considered in the equation. The Morton number (Mo), and the piecewise function (J) used in previous equations are calculated as follows:

$$Mo = \frac{\mu_L^4 g(\rho_L-\rho_G)}{\rho_L^2\sigma^3} \tag{17}$$

$$J = \begin{cases} 0.94H^{0.757} & 2 < H < 59.3 \\ 3.42H^{0.441} & H > 59.3 \end{cases} \tag{18}$$

$$H = \frac{4}{3} Eo Mo^{-0.149} \left(\frac{\mu_L}{\mu_{ref}}\right)^{-0.14} \tag{19}$$

where $\mu_{ref} = 0.0009\, kg/(m\, s)$ and Eo is the Eötvös number, defined as:

$$Eo = \frac{g(\rho_L - \rho_G) d_{bi}^2}{\sigma} \tag{20}$$

When calculating the drag coefficient for the model without PBM, we used the same equations (11-20). However, we omitted the subscript i, which corresponds to the bubble group.

2.3.3 Customized drag model

The Grace model for sieve-tray simulations is based on a balance of forces acting on a single bubble moving freely under gravity within a liquid (Grace et al., 1976). Since the present study aims to model bubble swarms, we modified Grace's drag coefficient as follows:

$$C_{D,modified} = F_{corr} C_D \tag{21}$$

where C_D is the drag coefficient calculated through the Grace model (Eq. 11) and F_{corr} is a *correction factor*. This factor was formulated as a function of superficial velocity of the fluid, following the work of Liang *et al.*, (Liang et al., 2016) and it was further adjusted with the aid of experimental data on clear liquid height and superficial gas velocity (Krishna, Van Baten, et al., 1999). This modified drag coefficient is used in all three approaches described later in the methodology.

2.3.4 Induced Turbulence

Turbulence is integrated in the present study through the two-time-constants model proposed by (Lopez de Bertodano M, Lahey RT, 1994), in which the total turbulent-energy dissipation rate is determined through two forces: one shear-induced and another bubble-induced. Additionally, we derived and reduced a previously available balance equations for the liquid turbulent kinetic energy and turbulent dissipation (C, 1995; Kataoka & Serizawa, 1989). As usual, the terms describing the coupling between phases need to be modeled. Eqs. 22 and 23 were the final k-ε equations that we obtained.

$$\begin{aligned} \frac{\partial(\alpha_L \rho_L k_L)}{\partial t} &+ \nabla \cdot (\alpha_L \rho_L \boldsymbol{u}_L k_L) \\ &= \nabla \cdot \left[\alpha_L \left(\mu_L + \frac{\mu_{t,L}}{\sigma_k}\right) \nabla k_L\right] + \alpha_L \left(G_{k,L} - \rho_L \varepsilon_L\right) + \alpha_L \rho_L S_{k,L} \end{aligned} \tag{22}$$

$$\frac{\partial(\alpha_L \rho_L \varepsilon_L)}{\partial t} + \nabla \cdot (\alpha_L \rho_L \boldsymbol{u}_L \varepsilon_L) = \nabla \cdot \left[\alpha_L \left(\mu_L + \frac{\mu_{t,L}}{\sigma_\varepsilon}\right) \nabla \varepsilon_L\right] + \alpha_L \frac{\varepsilon_L}{k_L}\left(C_{1\varepsilon} G_{k,L} - C_{2\varepsilon} \rho_L \varepsilon_L\right) + \alpha_L \rho_L S_{\varepsilon,L} \tag{23}$$

where $S_{k,L}$, $S_{\varepsilon,L}$ are source terms describing the effects of the dispersed phase on the continuous phase, i.e., bubble-induced turbulence. The values of these terms depend on the model used. Table 2-1 shows two of the three BIT models used in this work.

Table 2-1: Source terms for bubble-induced turbulence in this study

Model	$S_{k,L}$	$S_{\varepsilon,L}$
Simonin et al.	$C_s \alpha_L K_{GL} (\boldsymbol{u}_G - \boldsymbol{u}_L) \cdot \boldsymbol{v}_{dr}$	$C_{3\varepsilon} \frac{\varepsilon_k}{k_L} S_{k,L}$
Troshko-Hassan	$C_{ke} \alpha_L K_{GL} \lvert \boldsymbol{u}_G - \boldsymbol{u}_L \rvert^2$	$C_{td} \frac{1}{\tau_p} S_{k,L}$

Unlike the Simonin and Troshko-Hassan models, the remaining BIT model relevant for our study does not add explicit source terms to the turbulence equations. Instead, in an attempt to incorporate the effect of the random primary-phase motion induced by the dispersed phase in bubbly flow, Sato et al. (1981) proposed to modify μ_L as follows:

$$\frac{\mu_L}{\rho_L} = C_\mu \frac{k^2}{\varepsilon} + C_{\mu,G} \alpha_G d_b \lvert \boldsymbol{u}_G - \boldsymbol{u}_L \rvert \tag{24}$$

where $C_{\mu,G} = 0.6$ and k, ε are the liquid-phase turbulence intensity and eddy dissipation rate, respectively (Eqs. 23 and 24 with a $S_{k,L}$ and a $S_{\varepsilon,L}$ values of 0).

2.4 CFD-PBM coupled model

In order to couple a PBM with the two-fluid model to be used in Approach 3 (see *Methodology*), we expressed the population balance of the fluid in terms of f_i, i.e., the volume fraction of bubble group *i* in the gas holdup α_G (see Table 10).

$$\frac{\partial}{dt}(\alpha_G f_i) + \nabla \cdot (\alpha_G \boldsymbol{u}_b f_i) = \sum_{\substack{j.k \\ x_i \le (x_j + x_k) \le x_{i+j}}}^{j \ge k} \left(1 - \frac{1}{2}\delta_{j,k}\right) \eta_{i,jk} c_{j,k} \alpha_G f_j \alpha_G f_k \, v_i / v_j / v_k - \alpha_G f_i \sum_{k=1}^{M} c_{i,j} \alpha_G f_k v_i / v_k + \sum_{k=1}^{M} \zeta_{i,k} b_k \alpha_G f_k v_i / v_k - b_i \alpha_G f_i \tag{25}$$

$$\eta_{i,jk} = \begin{cases} (x_{i+1} - v)/(x_{i+1} - x_i) & x_i < v \le x_{i+1} \\ (v - x_{i-1})/(x_i - x_{i-1}) & x_{i-1} < v \le x_i \end{cases} \qquad v = v_j + v_k \tag{26}$$

$$\zeta_{i,k} = \int_{x_i}^{x_{i+1}} \frac{x_{i+1} - v}{x_{i+1} - x_i} \beta(v, x_k) dv + \int_{x_{i-1}}^{x_i} \frac{v - x_{i-1}}{x_i - x_{i-1}} \beta(v, x_k) dv \tag{27}$$

The first term on the left side of Eq. 25 is the time variation, the second term is convection. On the right side, the first term is the source ascribed to coalescence, the second is the sink ascribed to coalescence, the third is the source ascribed to break up and the fourth is the sink ascribed to breakup. Here, $c_{i,j}$ (or $c(d_i, d_j)$) is the bubble coalescence rate, b_k (or $b(d)$) is the bubble breakup rate, and $\beta(v, x_k)$ (or $\beta(f_v, d)$) is the unknown daughter bubble-size distribution.

Table 2-2: Breakup and coalescence models for PBM (Population Balance Model) implementation

	Mechanism	Equations
Bubble breakup due to turbulent eddies	Breakup rate	$b(d) = \int_0^{0.5} b(f_v \vert d) df_v$
	Daughter bubble size distribution	$\beta(f_v, d) = 2b(f_v \vert d) \left(\int_0^1 b(f_v \vert d) df_v \right)^{-1}$
	Complement equations	$b(f_v \vert d) = 0.923(1 - \alpha_d) n \varepsilon^{\frac{1}{3}} * \int_{\lambda_{min}}^{d_b} P_b(f_v \vert d.\lambda)(\lambda + d)^2 \lambda^{-11/3} d\lambda$ $P_b(f_v \vert d, \lambda) = \int_0^{\infty} P_b(f_v \vert d, e(\lambda), \lambda) P_e(e(\lambda)) de(\lambda)$ $P_e(e(\lambda)) = \left(\frac{1}{\bar{e}(\lambda)}\right) \exp\left(-\frac{e(\lambda)}{\bar{e}(\lambda)}\right)$ $\bar{e}(\lambda) = 1/12 \pi \lambda^3 \rho_l \bar{u}_\lambda^2$ $c_{f,max} = min\left(\left(2^{1/3} - 1\right), e(\lambda)/(d^2 \sigma \pi)\right)$ $f_{v.min} = (\lambda^3 \sigma \pi / (6 e(\lambda) d))^3$ $P_b(f_v \vert d, e(\lambda), \lambda) = \begin{cases} (f_{v.max} - f_{v.min})^{-1} & f_{v.max} - f_{v.min} \ge 0.01 . f_{v.min} < f_v < f_{v.max} \\ 0 & \text{else} \end{cases}$
Coalescence rate due to turbulent	Collision frequency	$\varpi_t(d_i, d_j) = \frac{1}{4} \pi \alpha_{G,max} (\alpha_{G,max} - \alpha_G)^{-1} * \zeta_{ij} \sqrt{2} \varepsilon^{1/3} (d_i + d_j)^2 (d_i^{2/3} + d_j^{2/3})^{1/2}$

	Mechanism	Equations
eddies: $c(d_i, d_j)=\varpi_t P_t$		$\zeta_{ij} = exp\left[-\left(\frac{l_{bt,ij}}{h_{b,ij}}\right)^{6.0}\right]; \quad l_{bt,ij} = \sqrt{l_{bt,i}^2 + l_{bt,j}^2}$ $l_{bt} = 0.89 d_b; \quad h_{b,ij} = \left(N_i + N_j\right)^{1/3}$
	Coalescence efficiency	$P_t\left(d_i, d_j\right)$ $= exp\left\{-\frac{\left[0.75\left(1+\xi_{ij}^2\right)\left(1+\xi_{ij}^3\right)\right]^{1/2}}{\left(\rho_G/\rho_L + C_{VM}\right)\left(1+\xi_{ij}\right)^3} We_{ij}^{1/2}\right\}$ $\xi_{ij} = d_i/d_j$

The total coalescence rate is calculated as the sum of the coalescences produced by turbulent eddies, different bubble rise velocities, and bubble wake entrainment. The total bubble breakup rate is calculated as the sum of the breakups produced by eddy collision and instability of large bubbles. In this work, we focused only on the mechanisms inherent to turbulent eddies for bubble coalescence and breakup. This simplification is reasonable at low-to-medium superficial gas velocities since coalescence due to turbulent eddies is the main mechanism in such conditions (Wang & Wang, 2007). The models for bubble coalescence and breakup to be used in Approach 3 are listed in Table 2-2. For details of the CFD–PBM coupled model we considered (Wang et al., 2006).

2.5 Methodology

The CFD model used in the present study for sieve-tray-hydrodynamics simulations is based on the water-air experiments published by Krishna *et al.* (1999). Figure 1-1 presents an overview of the methodology used in this work. A more detailed description of the set-up of each CFD simulation is given later in this section.

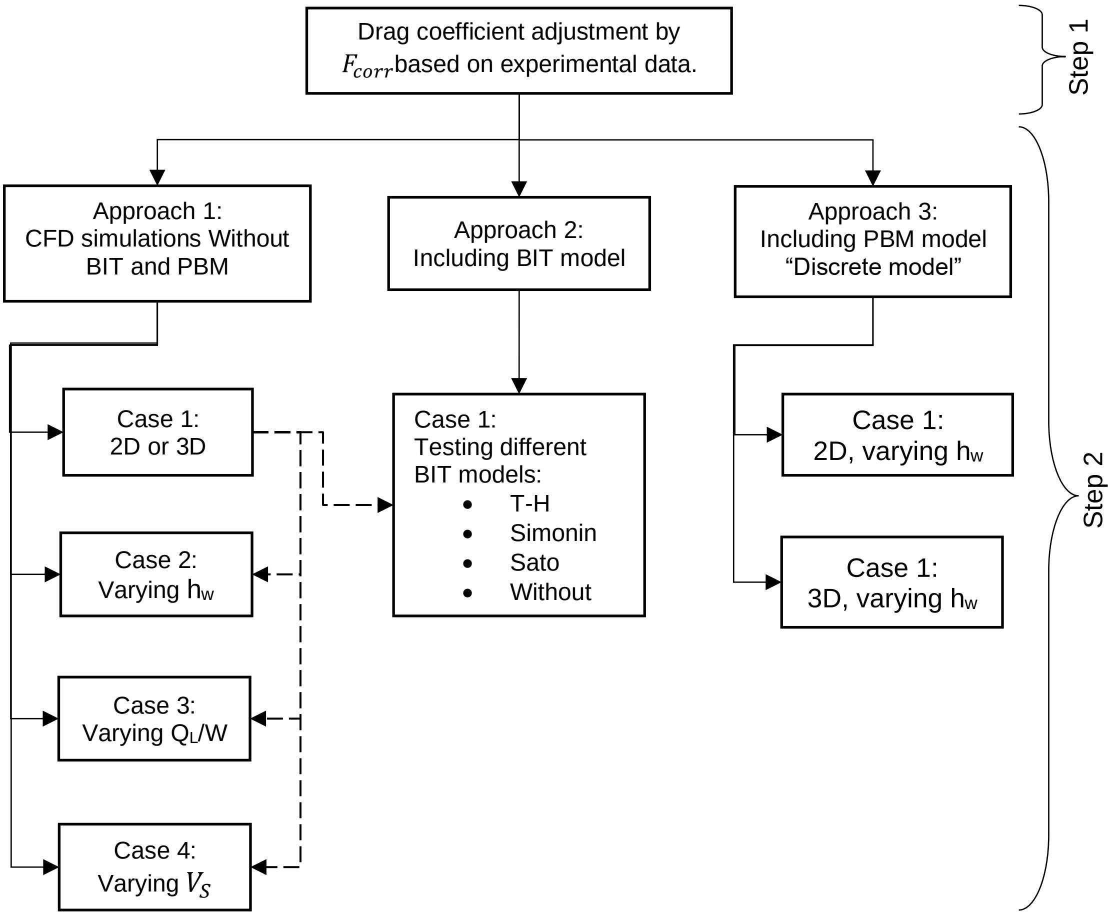

Figure 2-1: Flow diagram of the methodology used in this work.

The type and characteristics of boundary conditions for all the simulations in both steps are shown in Table 2-3. The details of each CFD simulation set-up are described later in this section.

Table 2-3: Type and characteristics of the boundary conditions used for the set-up of the CFD modeling for all simulations.

Boundary Conditions	Type of boundary condition	Gas-phase volume fraction
Liquid inlet	Uniform profile $u_{L,in} = \frac{Q_L}{h_{DC} L_w}$	0
Gas inlet	Uniform profile $V_{hole} = \frac{V_S A_a}{N_h A_h}$	1
Liquid outlet	Pressure outlet	0
Gas outlet	Pressure outlet	1
Wall	No-slip wall	Grad=0

2.5.1 Step 1: Drag-coefficient adjustment by F_{corr}

The first step of our CFD entailed modifying the drag coefficient with the aid of the correction factor (F_{corr}) presented above (Eq. 21). Thus, the drag coefficient was adjusted to the available experimental data, i.e., the h_{cl} of the gas at three different surface velocities (0.5, 0.7 and 0.9 m/s), at a Q_L/W of 8.25x10^{-4} m^3/s.m, and with a h_w of 80mm. The purpose of these adjustments was to guarantee that the simulated values would not exceed a 3% deviation compared to the experimental data. Finally, we used the least-squares method to express F_{corr} as a function of the surface velocity of the gas. This equation was then used for the simulation set-ups of the next step.

2.5.2 Step 2: CFD Simulation

Once the drag coefficient correction factor was established, three types of simulations were carried out.

- Approach 1: Simulations with the modified drag coefficient, but without PBM, and BIT.
- Approach 2: Simulations with modified drag coefficient and BIT, but without PBM.
- Approach 3: Simulations with modified drag coefficient and PBM, but without BIT.

Thus, we evaluated the effect of varying the operating conditions of sieve-tray distillations on h_{cl}. We chose to focus primarily on h_{cl}, since this property is used in most sieve-tray studies to validate the hydrodynamics of the system (Krishna, Van Baten, et al., 1999; Rahimi et al., 2012; Sadripour et al., 2012).

2.5.2.1 Approach 1

In Approach 1, four cases were studied. First, for Case 1, we studied the effect of varying the type of sieve tray geometry on h_{cl} in order to determine whether there are significant differences between working with a 2D geometry and working with a 3D one. Additionally, we compared these results with the experimental data for h_{cl} at different weir heights (60, 80, 90 and 100 mm). Thus, the four evaluated weir heights were simulated with both types of geometry. Then, for Case 2, we used 2D geometry in all simulations and varied h_w in order to determine the effects of this parameter on h_{cl}. Additionally, we compared the results of our simulations with the experimental data reported by Krishna et al., (1999), and adjusted the Bennet correlation for h_{cl}. For Case 3, on the other hand, we varied the liquid load per length unit of the weir (Q_L/W). The results of these variations on h_{cl} were then noted and compared with the experimental data. Finally, for Case 4, we varied the superficial gas velocity of the system in order to test the influence of this factor on h_{cl}. These results were also compared with the Krishna simulation, on the one hand, and the Bennett and Colwell correlations, on the other hand. Table 2-4 summarizes the methodology followed in this approach.

Table 2-4: Overview of the four simulated cases in Approach 1.

Case	Fixed variable	Evaluated variable	Number of simulations
1	V_S = 0.7 m/s Q_L/W = 8.25 x 10^{-4} $m^3/s.m$ h_w: 60, 80, 90, 100 mm	Geometry: • 2D • 3D	8
2	V_S = 0.7 m/s Q_L/W = 8.25 x 10^{-4} $m^3/s.m$	h_w (mm): • 60 • 80 • 90 • 100	4
3	V_S = 0.7 m/s h_w: 80 mm	Q_L/W (10^{-4} $m^3/s.m$): • 4 • 8.25 • 12	3
4	Q_L/W = 8.25 x 10^{-4} $m^3/s.m$ h_w: 80 mm	V_S (m/s): • 0.5 • 0.7 • 0.9	3

2.5.2.2 Approach 2

This approach includes an evaluation of the effect of BIT on h_{cl}. For this purpose, we used three different models: Troshko-Hassan, Simonin, and Sato. The results of these simulations were compared with the experimental data and the results simulations that did not include a BIT model. Table 2-5 summarizes the methodology followed for this approach.

Table 2-5: Overview of the simulated case in Approach 2.

Case	Fixed variable	Evaluated variable	Number of simulations
1	V_S = 0.7 m/s Q_L/W = 8.25 x 10^{-4} $m^3/s.m$ hw: 80 mm	BIT models: • T-H • Simonin • Sato • Without model	4

2.5.2.3 Approach 3

In this approach, a PBM was included in the simulations in order to determine whether h_{cl} could be more accurately determined thus. Two cases were evaluated in this approach. For both cases h_w was varied in order to determine the effects of this variable on h_{cl}. All results were compared with experimental data. However, Case 1 was based on a 2D geometry and Case 2 was based on a 3D geometry. Table 2-6 summarizes the methodology followed in this approach.

Table 2-6: Overview of the simulated case in Approach 3.

Case	Fixed variable	Evaluated variable	Number of simulations
1	V_S = 0.7 m/s Q_L/W = 8.25 x 10^{-4} $m^3/s.m$ Geometry: 2D	hw (mm): • 60 • 80 • 90 • 100	4
2	V_S = 0.7 m/s Q_L/W = 8.25 x 10^{-4} $m^3/s.m$ Geometry: 3D	hw (mm): • 60 • 80 • 90 • 100	4

The boundary conditions for the three approaches were similar. Additionally, uniform inlet boundaries for both the gas and the liquid phases were implemented in all simulations. Table 2-7 summarizes the different modeling set-ups for all the evaluated cases of this research.

Table 2-7: Set-up of the CFD simulations carried out in each evaluation approach.

	Approach 1	Approach 2	Approach 3
System	Air-water	Air-water	Air-water
Geometry	2D and 3D	2D or 3D depending of Approach 1/Case 1	2D and 3D
Multiphase Models	Eulerian two phases	Eulerian two phases	Eulerian two phases
Phase interactions	Virtual Mass Drag (Grace model) Lift (Tomiyama Model) Wall Lubrication (Antal) Turbulence Interaction: none	Virtual mass Drag (Grace model) Lift (Tomiyama Model) Wall Lubrication (Antal) Turbulence Interaction: Troshko-Hassan, Sato and Simonin	Virtual mass Drag (Grace model) Lift (Tomiyama Model) Wall Lubrication (Antal) Turbulence Interaction: none
Surface Tension	Constant: 0.072 N/m	Constant: 0.072 N/m	Constant: 0.072 N/m
Viscous Model	Standard *k-ε*	Standard *k-ε*	Standard *k-ε*
Population Balance Model	None	None	Discrete method with a kv of 0.5236. Aggregation: Kernel Luo Model. Breakage: Kernel Luo Model.

2.6 Simulation remarks

Simulations were performed with ANSYS-Fluent® V18.0 on a Dell Intel Xeon W3530 2.8GHz. The Design Modeler® and ANSYS meshing® tools were used for geometry and mesh development.

Tray geometry was defined based on the work carried out by Krishna et al., (1999). The Air-Water system was simulated within a two-phase Eulerian framework with a standard *k-ε* model and was compared with the experimental data on h_{cl} reported by the same researchers. Both the 2D and 3D simulations were transient and SIMPLE was used as the solution scheme for their pressure-velocity coupling. Additionally the spatial and temporal discretization of the model was carried out through the first-order upwind method. The geometry and mesh used in the simulations are shown in Figure 2-2.

a)

b)

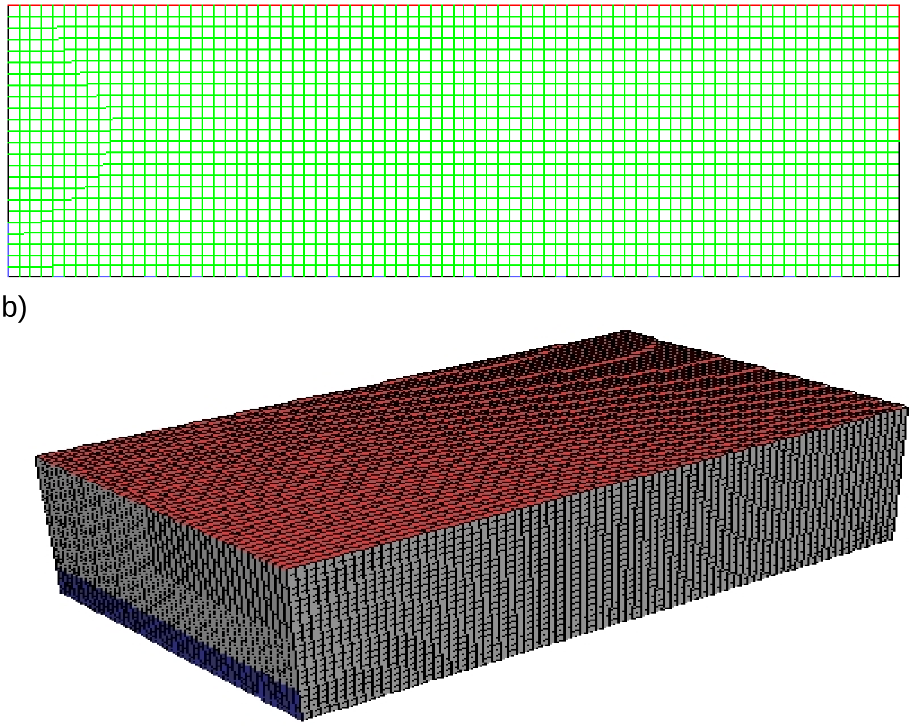

Figure 2-2: Mesh and flow geometry. a) 2D b) 3D system domains

Additionally, we used a hexahedral mesh in order to maximize mesh quality and minimize convergence errors due to the mesh configuration. Figure 2-3 offers a more a detailed account of the boundary conditions of the system in the CFD simulation.

a)

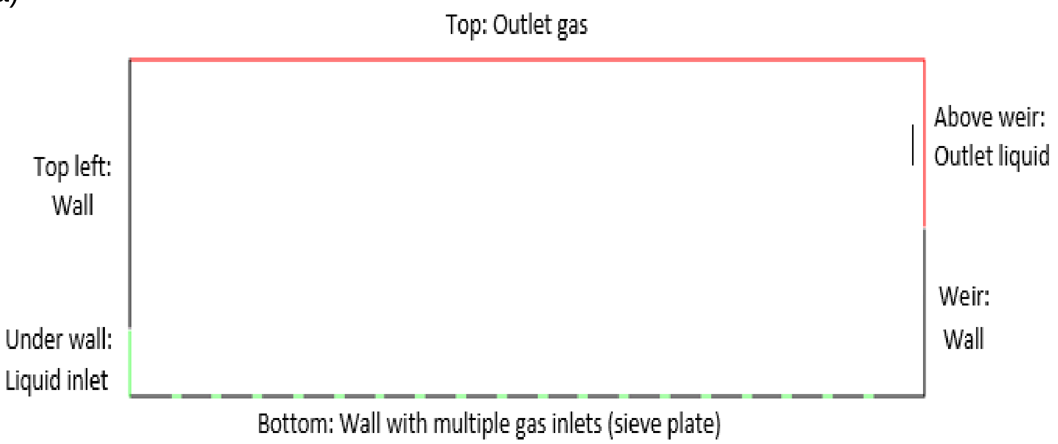

b)

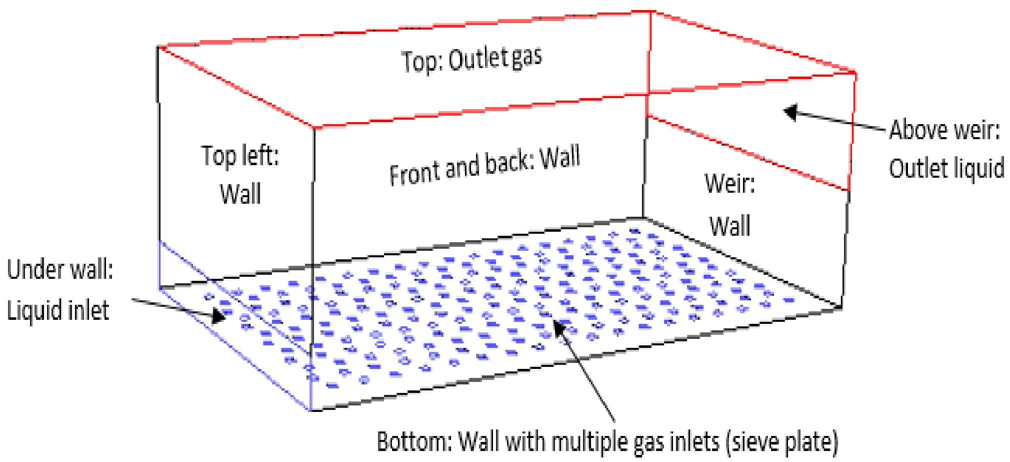

Figure 2-3: Boundary-condition locations for the 2D-geometry (a) and 3D-geometry (b) simulated sieve tray.

The inlet linear gas and liquid velocities used in our model were obtained from the superficial gas velocity and liquid load, respectively. Additionally, the sieve tray was assumed to be full of air at the beginning of the simulation. Table 2-8 presents the type and number of cells used in the model according to the different geometries and weir heights that were evaluated. The dimensions of the computational domain for the 2D and 3D simulations are summarized in Table 2-9.

Table 2-8: Geometry and meshes characteristics used for the CFD study

		Number of cells			
Type of geometry	Type of cell	Weir 60mm	Weir 80mm	Weir 90mm	Weir 100mm
2D	Quadrilateral (5mm x 5mm)	2808	3871	4212	4680
3D	Hexahedron (5mm x 5mm x 5mm)	123552	164736	185328	205920

Table 2-9: Geometry dimensions of the sieve tray for 2D and 3D simulations

Weir	2D simulation (length x height)	3D simulation (length x depth x height)
60	0.39x0.18m	0.39x0.22x0.18m
80	0.39x0.24m	0.39x0.22x 0.24m
90	0.39x0.27m	0.39x0.22x 0.27m
100	0.39x0.3m	0.39x0.22x 0.3m

With regard to PBM, the bubble size was divided into 7 groups (Table 2-10) using the geometric-ratio method with a r =2 factor. Thus, the smallest bubble volume was of $1.25 \times 10^{-3} m$, while the largest was of $20 \times 10^{-3} m$. The aforementioned method for determining this range of diameters was based on the works of (Hofer, 1983; Kaltenbacher, 1984; Lockett et al., 1979; Wang et al., 2006).

Table 2-10: Diameter of each discrete bubble class used in the PBM

Group #	Central group diameter d_i (mm)
1	1.25
2	1.98
3	3.15
4	5.00
5	7.94
6	12.59
7	20.00

Furthermore, the transport equations for additional scalars are assumed to have the form of the general scalar convective-diffusion equation. The convergence criterion for the simulations was set at $1x10^{-3}$ for most variables besides the volume fraction, which was set at $1x10^{-4}$. Additionally, the implicit first-order backward time differencing of the simulation was carried out every $1x10^{-3}$seconds. The values of the under-relaxation factor of the simulation always remained under 0.8. Finally, the 2D and 3D simulations took two and seven days, respectively, to reach a steady-state. This state is achieved when no more changes in the total liquid hold-up of the system are observed for a period long enough to obtain a time average.

2.7 Results and discussion

2.7.1 Step 1

Table 2-11 presents the F_{corr} values obtained, thorough adjustments based on experimental data on h_{cl}, for the three superficial velocities evaluated in the model.

Table 2-11: Results $\boldsymbol{F_{corr}}$ as a function of $\boldsymbol{V_s}$

V_s (m/s)	F_{corr}	h_{cl} calculated with the F_{corr}	h_{cl} experimental	% deviation
0.5	0.07	0.042	0.0418	0.48%
0.7	0.04	0.0398	0.0387	2.84%
0.9	0.03	0.034	0.0343	0.87%

The equation found through the least squares method for calculating the correction factor is:

$$F_{corr} = 0.25\boldsymbol{V}_s^2 - 0.45\boldsymbol{V}_s + 0.2325 \qquad 0.5 \leq \boldsymbol{V}_s \leq 0.9 \tag{28}$$

However, Eq. 28 can only be applied if the following condition is:

$$\frac{\boldsymbol{V}_s A_a}{N_h A_h} > \frac{0.0229\sigma}{\mu_G}\left(\frac{\mu_G^2}{\sigma\rho_G d_h}\frac{\rho_L}{\rho_G}\right)^{0.379}\left(\frac{l}{d_h}\right)^{0.293}\left(\frac{2A_a d_h}{\sqrt{3}p'^3}\right)^{2.8}\Big/\left(z/d_h\right)^{0.724} \tag{29}$$

This prerequisite is put in place in order to avoid weeping on the tray (Treybal, 1981).

2.7.2 Step 2

2.7.2.1 Approach 1

Case 1: As Figure 2-4 shows, there are no significant differences between 2D and 3D simulations within Approach 1. Thus, since 2D models demand less computational resources and have shorter calculation periods, it was decided to work with the 2D system. Additionally, working with fewer dimensions makes 2D simulations much more stable from a numerical point of view.

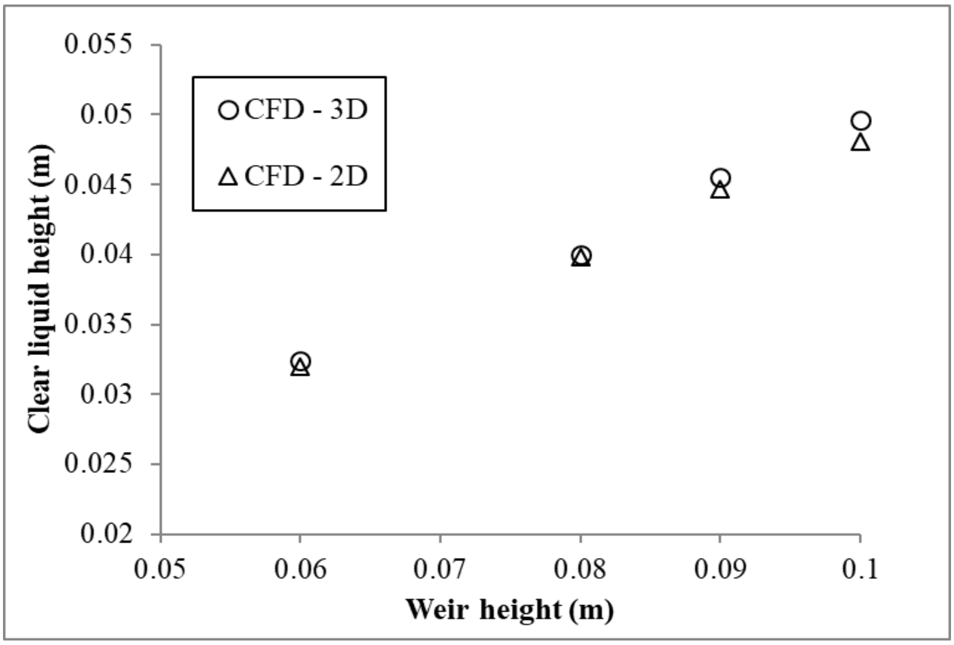

Figure 2-4: Clear liquid height from 3D and 2D CFD simulations for approach 1. V_s = 0.7 m/s. $Q_L/W = 8.25 \times 10^{-4}$ m^3/s m

Case 2: Figure 2-5 compares the results of the 2D simulation carried out for Case 1 with experimental data on weir height and clear liquid height, on the one hand, and with the results of Krishna's simulation and the Bennet correlation, on the other hand. The higher accuracy of the present model is due to the adjustment made to the drag coefficient through the drag correction factor (Krishna, Van Baten, et al., 1999).

The performance of Krishna's model is similar to Bennet's because it adjusts the drag coefficient through the Bennet correlation, while the simulations carried out in the present work are independent of said correlation. It worth noting that the average time that it took for Krishna's simulation to stabilize was of six seconds, while the simulations performed took approximately 40 seconds to reach that point, possibly due to the adjustment of the drag coefficient.

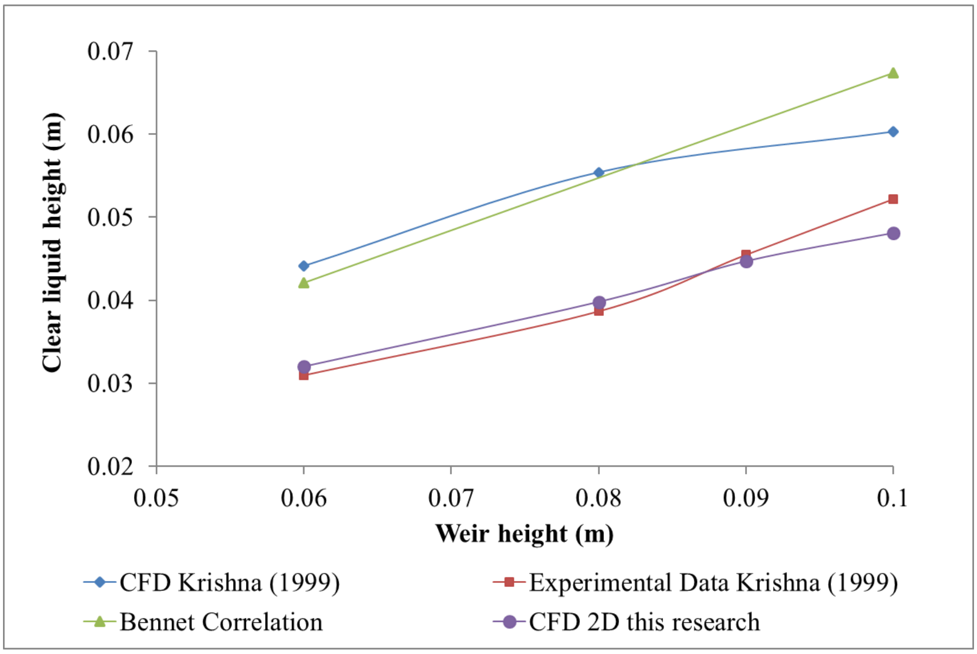

Figure 2-5: Relationship between the clear liquid height and weir height from the 2D CFD model approach 1. V_S = 0.7 m/s; $Q_L/W=8.2\times10^{-4}$ m^3/s m, experimental data, bennet correlation, and simulation results reported in the literature

Table 2-12 presents the individual and averaged margins of error of the aforementioned models. These values were calculated by comparing the results of each model, at the same operational conditions, against the experimental data. The results confirm that model proposed in the present work has the lowest margin of error.

Table 2-12: Margin of error of the different simulations and correlation against the experimental data for V_S = 0.7 m/s; $Q_L/W=8.2\times10^{-4}$ m^3/m s

Weir height (m)	Krishna	Bennet	This work
0.06	42.3%	35.8%	3.2%
0.08	43.2%	41.6%	2.84%
0.09	N/A	34.3%	1.8%
0.1	15.5%	29.1%	7.9%
Average	**33.6%**	**35.2%**	**3.93%**

Case 3: Figure 2-6 shows the results of comparing the h_{cl} results obtained by each model —the Colwell correlation was also considered in this case— when the liquid load per unit weir length is the evaluated variable. Once again, our model was the one that resembled the experimental data to the greatest extent, which shows the effectiveness of our drag-coefficient adjustments. Additionally, the similarities between Krishna's simulation and the Bennet correlation can be appreciated again.

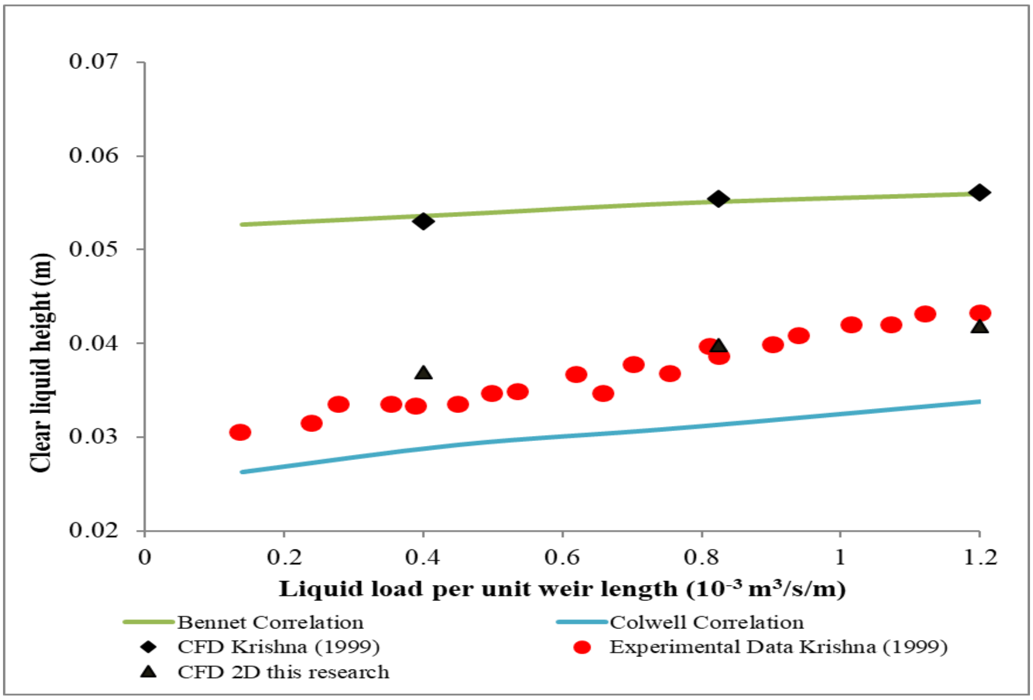

Figure 2-6: Relationship between the clear liquid height and weir load from the 2D CFD model approach 1 h_w=80mm; $\boldsymbol{V_S}$= 0.7m/s, experimental data, Bennet correlation, Colwell correlation, and simulation results reported in the literature.

Table 2-13 presents the individual and averaged margins of error of the aforementioned models. The fact that the margin of error of our model is lower than the others is a consequence of the fact that initialization and convergence values that we used were not forced to meet the estimations that result from the Bennet correlation.

Table 2-13: Margin of error of the different simulations and correlations against the experimental data for h_w = 80mm; V_S = 0.7 m/s.

Liquid weir load ($10^{-3}m^3$/m s)	Krishna	Bennet	Colwell	This work
0.4	55.88%	58.82%	14.71%	8.53%
0.825	43.15%	42.12%	19.90%	2.84%
1.2	29.56%	29.33%	21.48%	3.46%
Average	**42.87%**	**43.42%**	**18.69%**	**4.94%**

Case 4: Figure 2-7 shows the results of comparing the h_{cl} results obtained by each model when the superficial gas velocity was the variable being evaluated. Once again, adjusting the drag coefficient in our proposed model resulted in a higher accuracy.

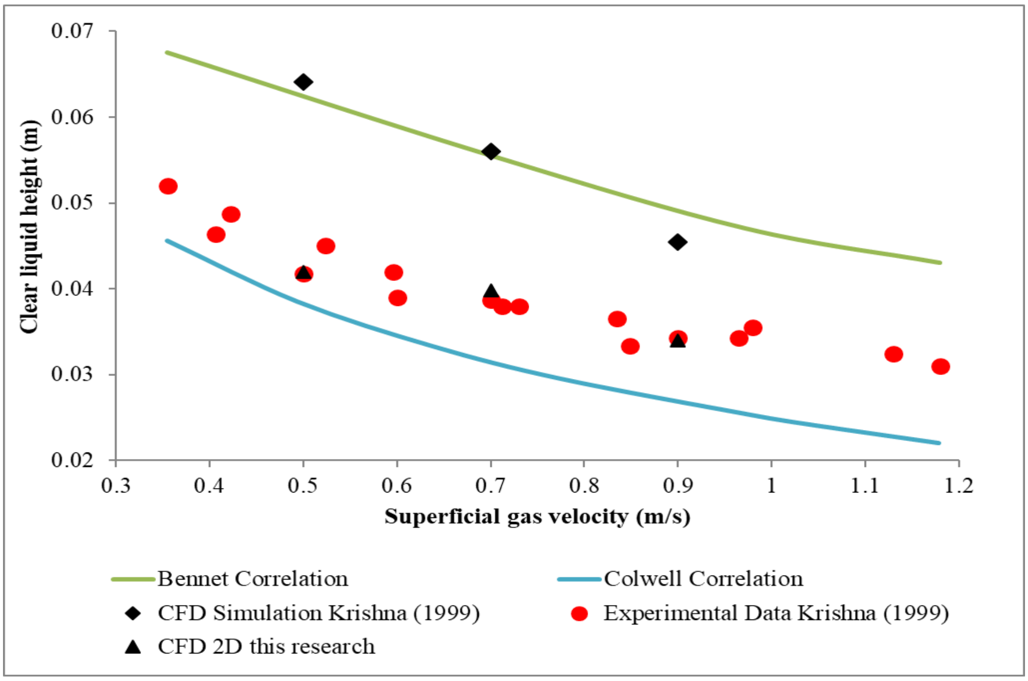

Figure 2-7: Relationship between the clear liquid height and superficial gas velocity from the 2D CFD model h_w=80mm, Q_L/W=8.2x10^{-4}m^3/s m, experimental data, Bennet correlation, Colwell correlation, and simulation results reported in the literature.

Table 2-14 presents the individual and averaged margins of error of all the aforementioned models. As it had happened when liquid load was the variable being evaluated, the fact that the margin of error of our model is lower than the others in this case is a consequence of the fact that initialization and convergence values that we used were not forced to meet the estimations that result from the Bennet correlation.

Table 2-14: Margin of error for the different simulations and correlations against the experimental data for h_w= 80mm; Q_L/W=8.2x10^{-4} m^3/m s.

Superficial gas velocity (m/s)	Krishna	Bennet	Colwell	This work
0.5	53.35%	50.0%	8.13%	0.48%
0.7	44.7%	43.67%	18.86%	2.84%
0.9	32.65%	43.15%	21.87%	0.87%
Average	**43.57%**	**45.61%**	**16.29%**	**1.40%**

Table 2-15 summarizes the margin of error of the different simulations proposed in the present study and those of Krishna's model.

Table 2-15: Average error for this work and Krishna's simulations

Case	This work	Krishna
2	3.93%	33.6%
3	4.94%	42.87%
4	1.40%	43.57%
Average	**3.42%**	**40.0%**

2.7.2.2 Approach 2

With the purpose of creating a more realistic simulation, we integrated the BIT phenomenon in our two-phase CFD model. In order to find the most suitable BIT model, three different proposals were compared: (Sato et al., 1981; Simonin & Viollet, 1990; Troshko & Hassan, 2001). Figure 2-8 shows the results of clear liquid height when BIT models were applied.

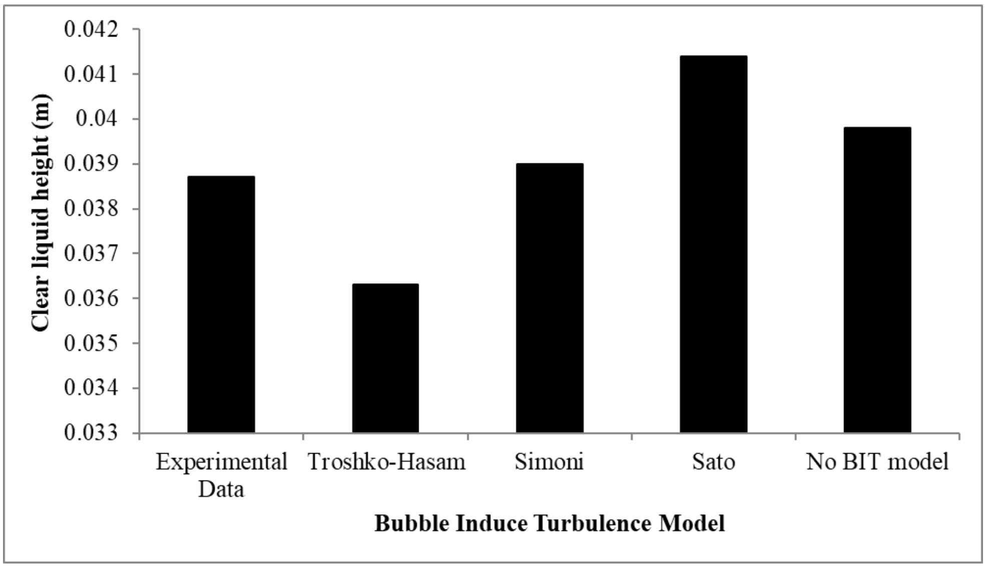

Figure 2-8: Comparisons of the clear liquid height experimental value and the results using different bubble-induced turbulence models: Troshko-Hasam, Simoni, Sato, and No BIT model. Data shown correspond to conditions: V_S= 0.7 m/s, Q_L/W = 8.25 x 10^{-4} m^3/s m, weir 80mm.

Simonin's model is able to simulate BIT by including additional source terms in the turbulence-transport equations and is only usable in dispersed and per-phase turbulence models. The T-H model, on the other hand, is an alternative that accounts for the turbulence of the dispersed phase in the *k*-epsilon equations (ANSYS, 2021; ANSYS Release 19, 2018). Sato's model had the highest margin of error (9%), probably due to the effects of including certain bubble-induced effects within a more general term of the equation instead of considering them on their own. The margin of error of the T-H model was similar to that of the Sato model (see Table 2-16), possibly because of the quadratic term of the equations used for the former. Indeed, this term does not allow for a negative value to affect the turbulent kinetic energy. In other words, given that $|u_G - u_L|^2$ (see Table 2-1), when the liquid velocity is superior to the gas velocity this value will increase kinetic energy instead of decreasing it, which, in turn, decreases h_{cl} when it should increase. Simonin's model, on the other hand, can simulate systems where the liquid velocity is greater than the gas velocity.

However, despite their shortcomings, all three models are close enough to the experimental data to be acceptable. Table 2-16 summarizes the margins of error of the different models.

Table 2-16: Margin of error of the bubble-induced turbulence (BIT) models.

BIT model	% Deviation of experimental data
Troshko-Hassan	6.20%
Simonin	1.29%
Sato	7.0%
No BIT model	2.84%

Simonin's model is, thus, the most accurate of the evaluated BIT models. However, integrating Simonin's model reduces the margin of error by less than 2%, when compared with a 2D non-BIT model. Therefore, at least for initial studies, working without BIT models does not entail a significant sacrifice of accuracy.

2.7.2.3 Approach 3

In another attempt at creating more realistic simulations, we integrated a PBM in our 2D and 3D models. Additionally, since other models —such as those use to study bubble columns— also use it, we chose to work with the discretization method for our PBM models (Bhole et al., 2008; Wang et al., 2006). This approach has the advantage of directly computing particle size distribution. Indeed, as shown in Figure 2-9, small bubbles prevail over larger ones, which favors mass transfer. However, if the PBM skews too far towards small-size bubbles, the amount of transferred mass can be overestimated. Indeed, the main difficulty in two-fluid modelling is the accurate representation of the interphase forces, on the one hand, and turbulence, on the other hand.

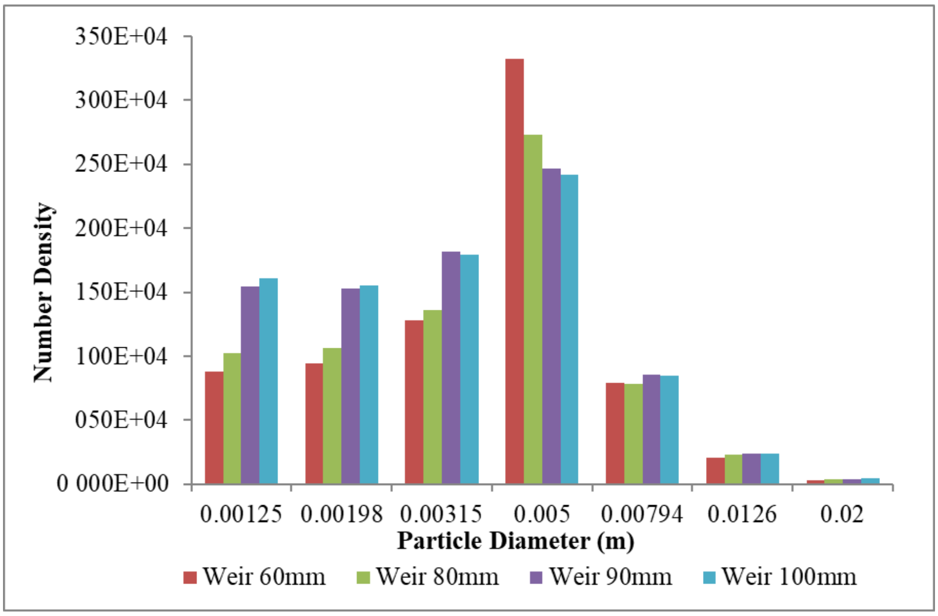

Figure 2-9: Number density bubbles for 60, 80, 90, 100mm weir with V_S=0.7m/s. $Q_L/W = 8.25\times10^{-4} m^3/s$ m in 2D

Figure 2-10 shows the results of 2D and 3D simulations with PBM and compares them with the available experimental data. However, as was the case with Approach 1, using a 3D model only increases accuracy slightly. This might be due to de fact that most of the bubble movement takes place in the *x* and *y* axes and only a negligible amount of bubble movement flows along the *z* axis.

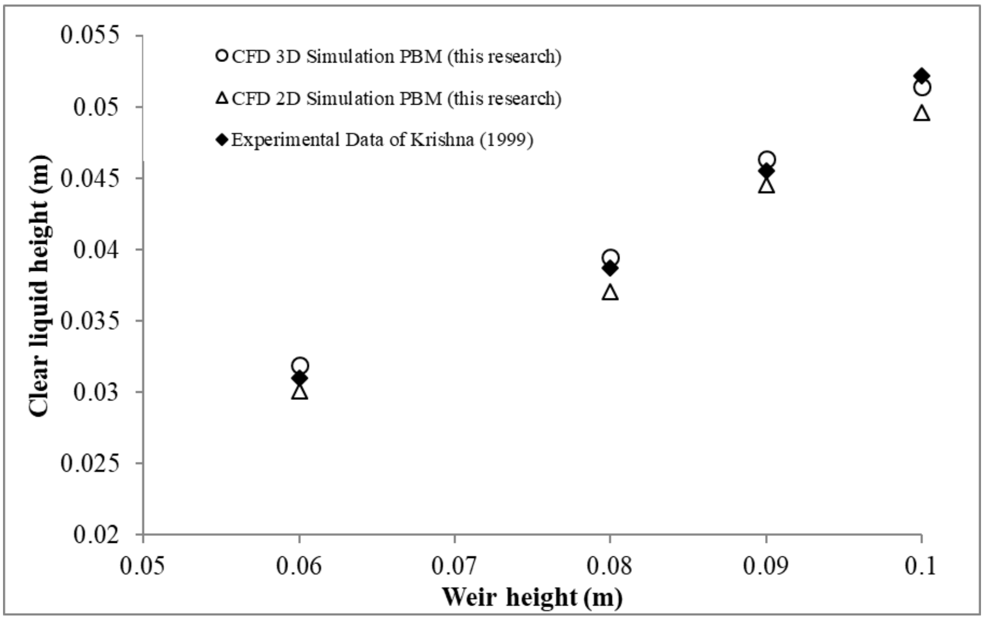

Figure 2-10: Comparisons of clear liquid height in 3D and 2D simulation with PBM. V_S = 0.7 m/s, $Q_L/W = 8.25 \times 10^{-4} m^3/s$ m

Table 2-17 shows how the 2D and 3D models without PBM compare with those with PBM. Indeed, implementing PBM in the simulations leads to a small difference in the results for the two types of geometry. However, the average margin of error for

Approaches 1 and 3 is not significant by any means: the difference between the largest margin of error (3.9%; 2D, no PBM) and the smallest margin of error (2.1%; 3D, with PBM) is only 1.8%. Thus, a 2D simulation without PBM and BIT remains a viable alternative that, furthermore, requires less processing time and computational power than slightly more precise models.

Table 2-17: Margin of error of 2D from approach 1, and 2D and 3D from approach 3 against the experimental data, for $\boldsymbol{V_S}$ = 0.7 m/s; Q_L/W = 8.2x10^{-4} m^3/s m.

Weir height (m)	Approach 1 (no PBM)	Approach 3 (with PBM)	
	2D	2D	3D
0.06	3.2%	3.0%	2.8%
0.08	2.8%	2.5%	2.1%
0.09	1.8%	2.1%	1.9%
0.1	7.9%	4.9%	1.5%
Average	**3.9%**	**3.1%**	**2.1%**

Contour plots and velocity vectors for the gas volume fraction for Approach 1 (2D model) and Approach 3 (3D model) are shown in Figures 2-11 and 2-12, respectively. As can be seen, the 2D model without PBM is less turbulent than the 3D model with PBM, possibly due to the fact that only one bubble size is being considered.

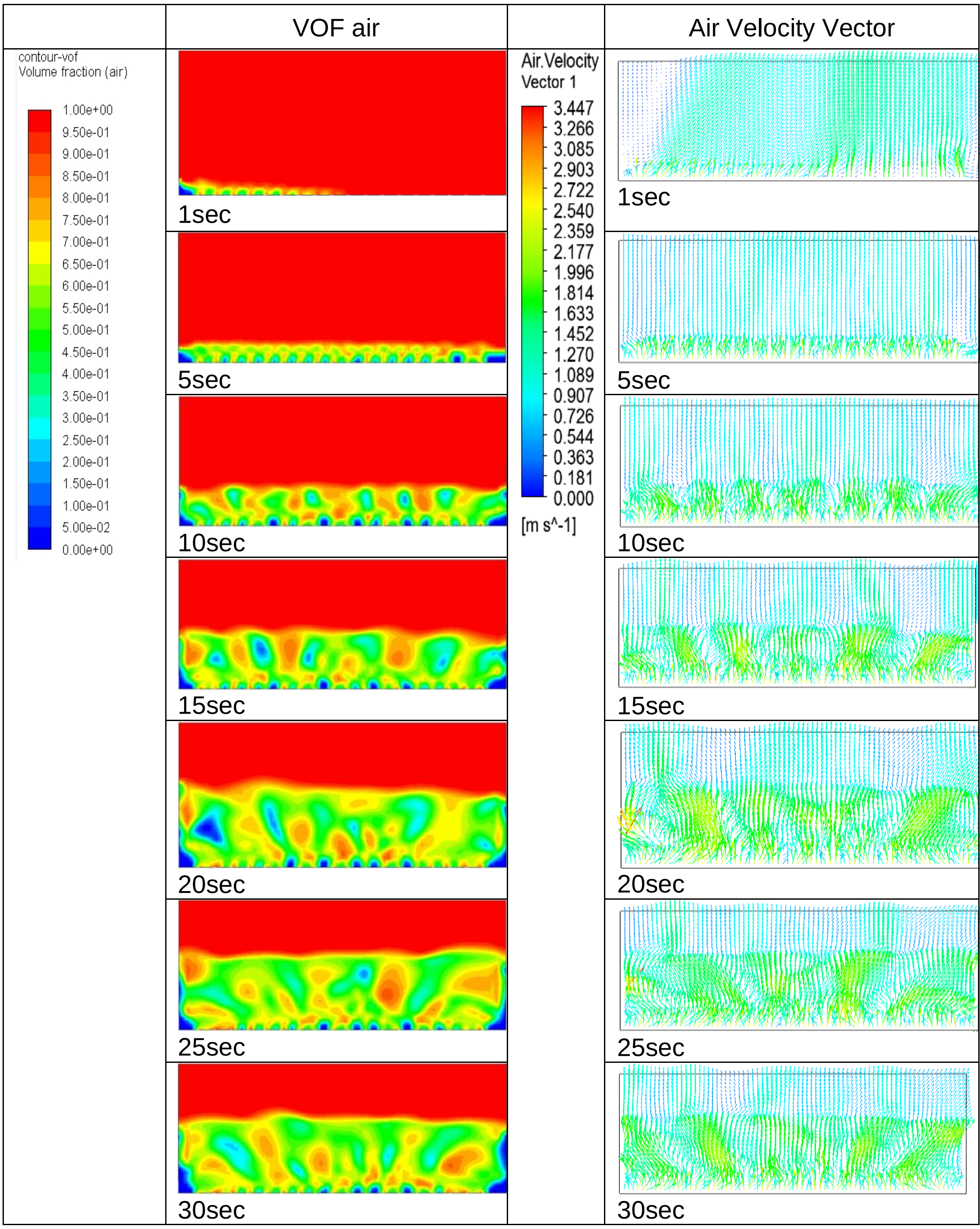

Figure 2-11: Evolution of instant gas hold-up distribution and vector gas velocity for weir 100mm. $\boldsymbol{V_S}$=0.7m/s. Q_L/W=8.25x10^{-4}m^3/s m, in 2D without PBM and BIT.

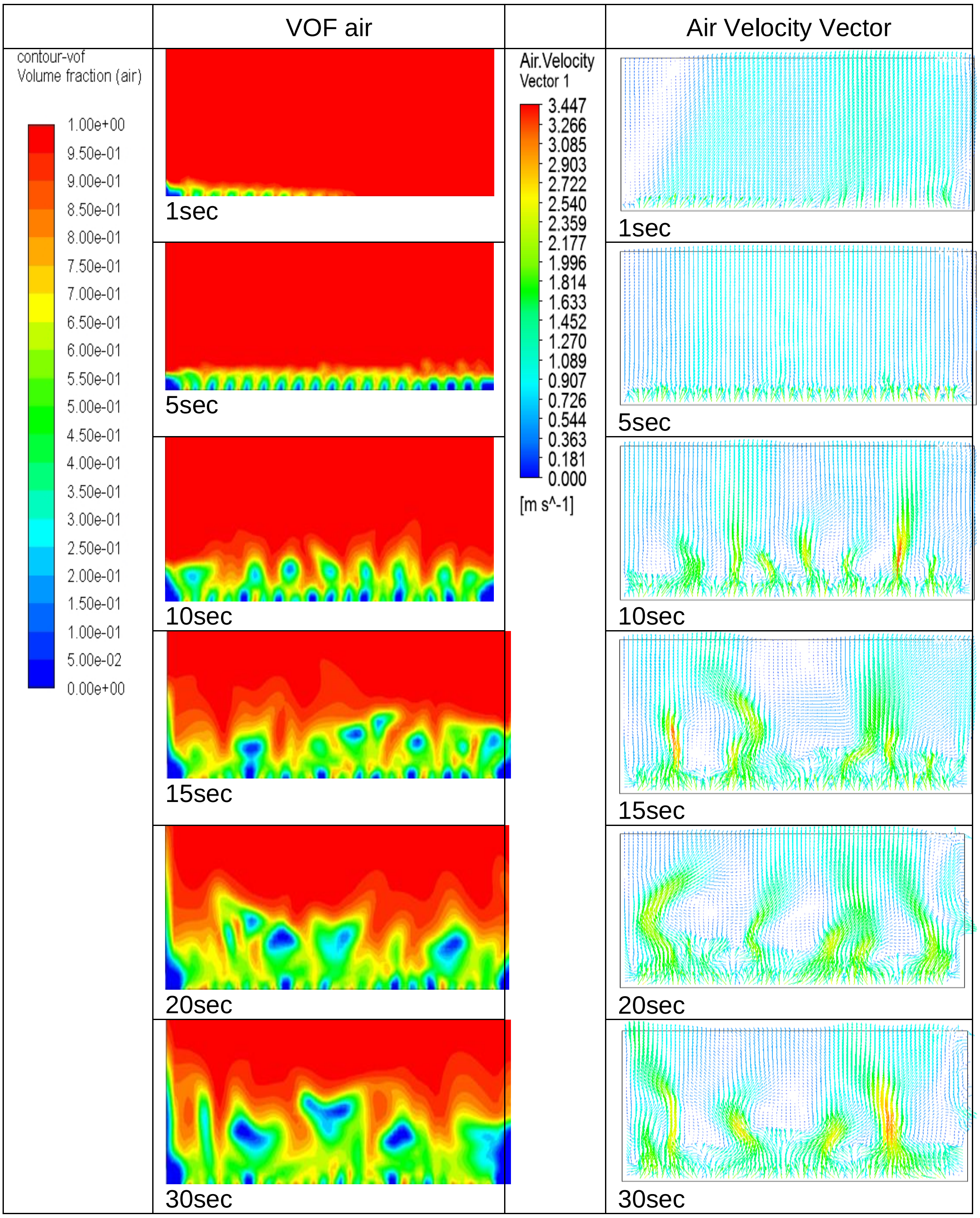

Figure 2-12: The evolution of instant gas hold up distribution and vector gas velocity for weir = 100mm, $\boldsymbol{V_S}$=0.7m/s. $Q_L/W = 8.25 \times 10^{-4} m^3/s$ m, in 3D incorporating PBM.

2.8 Conclusions

With the CFD models developed in the present research, we were able to successfully simulate distillation in sieve trays. Additionally, for the first time in a study of this kind, we tested the effects of integrating PBM and BIT into a CFD model on its h_{cl} simulation accuracy. The performance of these models was also evaluated by changing their geometry (2D and 3D). Moreover, ANSYS Fluent® proved to be a suitable tool to simulate this type of complex fluid system, since the various meshes and geometries used throughout the simulations did not lead to any issues during the processing stage and the numerical performance was stable in all cases.

The accuracy of models was confirmed by comparing their results against experimental data. Thus, the average h_{cl} margin of error of these models was: 3.42% for Approach one (Table 2-15), 1.29% for Approach 2 (using the Simonin model) (Table 2-16), and 2.1% for Approach 3 (using 3D geometry) (Table 2-17).

When compared to those of Krishna's simulations (40.0%), the error margins of our models seem much better. The same might be said when compared to Bennet's and Cowell's.

The obtained results led us to conclude that for this type of two-phase system with turbulence, a 2D model is accurate enough. Despite being slightly more accurate, the other models that we developed for this study are not as resource-effective as the 2D model.

The same might be said about including BIT models in the CFD model. The Simonin BIT model was the most accurate in representing h_{cl}, but even so, when compared to that of a plain model, the margin of error of the BIT model does not improve significantly: 1.29% vs. 2.84%.

Finally, including PBM in our model also improved h_{cl} precision, compared to the Krishna simulations and the Bennet correlation (Tables 2-11, 2-12, and 2-13), but they only improved marginally when compared to our plain CFD model (Table 2-17). Thus, at least for preliminary studies, including a PBM in the CFD model is not strictly necessary. However, PBM might be more crucial when working with the mass transfer phenomena. Thus, more studies are needed to determine whether it is worth it to include PBM in other circumstances.

Acknowledgements

The authors acknowledge the financial support of the Universidad Nacional de Colombia and Colciencias (agreement 617).

Javier Mancera thanks Professor Ronnie Andersson for offering him an internship at Chalmers Technology University.

The authors would like to thank the company S&S S.A.S for its technical support and contributions to this research.

Notation

a_{if}	Interfacial area concentration, m^{-1}
A_a	Active area on sieve tray, m^2
A_b	Area bubble Sauter diameter, πD_s^2, m^2
A_h	Hole area on sieve tray, m^2
$b(f_v\|d)$	Breakup kernel function
$b(v), b_i, b(d)$	bubble breakup rate, s^{-1}
b^*	Model parameter, 100 s^{-1}
C_p	specific heat, J/kg K
C_D	drag coefficient
C_l	lift force coefficient
C_{VM}	virtual mass force coefficient
C_{TD}	turbulent dispersion coefficient
$C_{1\varepsilon}$	Model constant, 1.44
$C_{2\varepsilon}$	Model constant, 1.9
C_s	User modifiable model, by default 1
$C_{3\varepsilon}$	Model constant, 1.2
C_{ke}	User modifiable model, by default 0.75
C_{td}	User modifiable model, by default 0.45
$c_{j,k}$	abbreviation of $c(d_j, d_k)$, m^3/s
$c(d_j, d_k)$	bubble coalescence kernel function, m^3/s
D_l	diffusion coefficient, $m^2\ s^{-1}$
D_s	bubble Sauter diameter, $D_s = 1/\sum_i f_i/d_i$, m
d	diameter of the mother bubble, m
d_h	Hole diameter of a sieve tray, m
d_c	critical size of bubbles having wake effect for bubble coalescence, m
d_{c2}	critical size of bubbles with breakup resulting from instability, m
$e(\lambda)$	kinetic energy of an eddy of size λ, J
$\bar{e}(\lambda)$	Mean kinetic energy of an eddy of size λ, J
f_i	scalar fraction of each bubble size group
F	total interfacial force, N
F^{drag}	drag force, N
F^{lift}	lift force, N
F^{VM}	Virtual mass force, N
F^{TD}	turbulent dispersion force, N
$f_{b,large}$	fraction of large bubbles
f_v	breakup fraction defined by v_1/v
$G_{k,L}$	turbulence production term in the liquid phase, J/m^3s
g	gravitational acceleration, m/s^2
H	enthalpy, J/kg
h	inter-phase heat transfer coefficient
h_{DC}	Downcomer Clearance, m
I	model parameter
$k_{b,large}$	model parameter accounting for bubble wake effect
k	kinetic energy turbulent, m^2/s^2

K_{GL}	Covariance of the velocities of liquid and gas
L_w	Weir length, m
l	Plate thickness, m
M	number of bubble groups
m	Model parameter, 6.0
n	Number of bubbles per unit dispersion volume, m^{-3}
N_h	Number of holes in the sieve tray
N_i	number of the bubbles with volume between (v_i, v_{i+1}), m^{-3}
$P_b(f_v\|d,\lambda)$	breakup probability for a bubble of size d breaking with breakup fraction f_v when hit by an eddy of size λ
$P_b(f_v\|d,e(\lambda),\lambda)$	breakup probability for a bubble of size d breaking with breakup fraction f_v when hit by an eddy of size λ and kinetic energy $e(\lambda)$
$P_e(e(\lambda))$	Energy distribution density function for eddy of size λ, J^{-1}
P	Pressure, Pa
p'	pitch of perforations, m
Q	Volumetric flow, m^3/s
s	fractional rate of surface element replacement
S_i	Source term due to coalescence and breakup, Kg/m^3 s
$S_{k,L}$	source terms describing the effects of the dispersed phase on the continuous phase
$S_{\varepsilon,L}$	source terms describing the effects of the dispersed phase on the continuous phase
T	temperature, K
t	Thermo-fluid time scale, s
T_{sat}	saturation temperature, K
t_e	exposure time in the penetration model, s
u_{slip}	bubble slip velocity, m/s
u_b	bubble velocity, m/s
u	velocity, m/s
$\bar{u}_\lambda$	Mean velocity for eddy of size λ
v_{dr}	Drift velocity
v	volume of the mother bubble, m^3
v_1	volume of the smaller daughter bubble, m^3
V_b	volume bubble Sauter diameter, $\pi D_s^3/6$, m^3
V_s	Superficial gas velocity, m/s
x_i	pivot bubble size of the bubble interval (v_i, v_{i+1}), m^3
Z	length of travel on a tray, m

Greek letters

α	Void fraction
ρ	Density, kg/m3
Γ	mass transfer rate duo to phase change, kg/m^3 s
μ^e	effective viscosity, kg/m s
μ	Viscosity, kg/m s
λ^e	effective thermal conductivity, W/m K
σ	Surface tension,N/m
σ_k	Model constant, 1
ε	dissipation rate of the kinetic energy, m^2/s^3
τ_p	Characteristic time of induce turbulence
δ	model parameter

$\beta(v, v')$, $\beta(v, x_k)$	daughter bubble size distribution function
λ	eddy size, m
ν_l	kinematic viscosity of liquid, m^2s^{-1}
Υ	Model constant

Subscripts

G	Vapor
L	Liquid
GL	transfer of quantities from liquid phase to vapor
LG	transfer of quantities from vapor phase to liquid
t	turbulence

References

ANSYS. (2021). *ANSYS Engineering Analysis System User's Manual*.

ANSYS Release 19. (2018). *ANSYS Fluent Theory Guide*.

Bennett, D. L., Agrawal, R., & Cook, P. J. (1983). New pressure drop correlation for sieve tray distillation columns. *AIChE Journal*, *29*(3), 434–442. https://doi.org/10.1002/aic.690290313

Bhole, M. R., Joshi, J. B., & Ramkrishna, D. (2008). CFD simulation of bubble columns incorporating population balance modeling. *Chemical Engineering Science*, *63*(8), 2267–2282. https://doi.org/10.1016/j.ces.2008.01.013

C, M. (1995). An order of magnitude analysis of the two-phase k–e model. *International Fluid Mechanics*. https://doi.org/10.1615/InterJFluidMechRes.v22.i3-4.30

Chen, G., Xiong, Q., Morris, P. J., Paterson, E. G., Sergeev, A., & Wang, Y.-C. (2014). OpenFOAM for Computational Fluid Dynamics. *Notices of the American Mathematical Society*, *61*(4), 354. https://doi.org/10.1090/noti1095

Gesit, G., Nandakumar, K., & Chuang, K. T. (2003). CFD modeling of flow patterns and hydraulics of commercial-scale sieve trays. *AIChE Journal*, *49*(4), 910–924. https://doi.org/10.1002/aic.690490410

Grace, J. R., Wairegi, T., & Brophy, J. (1978). Break-up of drops and bubbles in stagnant media. *The Canadian Journal of Chemical Engineering*, *56*(1). https://doi.org/10.1002/cjce.5450560101

Grace, J. R., Wairegi, T., & Nguyen, T. H. (1976). Shapes and velocities of single drops and bubbles moving freely through immiscible liquids. In *Trans Inst Chem Eng* (Vol. 54, Issue 3). Universidad Industrial de Santander.

Gupta, A., & Roy, S. (2013). Euler-Euler simulation of bubbly flow in a rectangular bubble column: Experimental validation with Radioactive Particle Tracking. *Chemical Engineering Journal*, *225*. https://doi.org/10.1016/j.cej.2012.11.012

Hofer, H. (1983). Influence of gas-phase dispersion on plate column efficiency. *German Chemical Engineering*, *6*(2).

Ishii, M., & Zuber, N. (1979). Drag coefficient and relative velocity in bubbly, droplet or particulate flows. *AIChE Journal*, *25*(5), 843–855. https://doi.org/10.1002/aic.690250513

Kaltenbacher, E. (1984). On the Effect of the Bubble Size Distribution and the Gas-Phase Diffusion on the Selectivity of Sieve Trays. *Chemical Engineering Fundamentals*, *1*(47).

Kataoka, I., & Serizawa, A. (1989). Basic equations of turbulence in gas-liquid two-phase flow. *International Journal of Multiphase Flow*, *15*(5). https://doi.org/10.1016/0301-9322(89)90045-1

Kiss, A. A., & Olujić, Ž. (2014). A review on process intensification in internally heat-integrated distillation columns. *Chemical Engineering and Processing: Process Intensification*, *86*, 125–144. https://doi.org/10.1016/j.cep.2014.10.017

Krishna, R., Urseanu, M. I., Van Baten, J. M., & Ellenberger, J. (1999). Rise velocity of a swarm of large gas bubbles in liquids. *Chemical Engineering Science*, *54*(2), 171–183. https://doi.org/10.1016/S0009-2509(98)00245-0

Krishna, R., & Van Baten, J. M. (2003). Modelling sieve tray hydraulics using computational fluid dynamics. *Chemical Engineering Research and Design*, *81*(1), 27–38. https://doi.org/10.1205/026387603321158168

Krishna, R., Van Baten, J. M., Ellenberger, J., Higler, A. P., & Taylor, R. (1999). CFD simulations of sieve tray hydrodynamics. *Chemical Engineering Research and Design*, *77*(7), 639–646. https://doi.org/10.1205/026387699526575

Laborde-Boutet, C., Larachi, F., Dromard, N., Delsart, O., & Schweich, D. (2009). CFD simulation of bubble column flows: Investigations on turbulence models in RANS approach. *Chemical Engineering Science*, *64*(21). https://doi.org/10.1016/j.ces.2009.07.009

Li, X., Yang, N., Sun, Y., Zhang, L., Li, X., & Jiang, B. (2014). Computational fluid dynamics modeling of hydrodynamics of a new type of fixed valve tray. *Industrial and Engineering Chemistry Research*, *53*(1), 379–389. https://doi.org/10.1021/ie400408u

Liang, X. F., Pan, H., Su, Y. H., & Luo, Z. H. (2016). CFD-PBM approach with modified drag model for the gas–liquid flow in a bubble column. *Chemical Engineering Research and Design*, *112*, 88–102. https://doi.org/10.1016/j.cherd.2016.06.014

Lockett, M. J. (1986). *Distillation tray fundamentals*. Cambridge University Press.
Lockett, M. J., Kirkpatrick, R. D., & Uddin, M. S. (1979). Froth regime point efficiency for gas-film controlled mass transfer on a two-dimensional sieve tray. *Trans Inst Chem Eng*, *57*(1).
Lopez de Bertodano M, Lahey RT, J. O. (1994). Development of a k-e model for bubbly two-phase flow. *Journal of Fluids Engineering*, *116*. https://doi.org/https://doi.org/10.1115/1.2910220
Lote, D. A., Vinod, V., & Patwardhan, A. W. (2018). Comparison of models for drag and non-drag forces for gas-liquid two-phase bubbly flow. *Multiphase Science and Technology*, *30*(1), 31–76. https://doi.org/10.1615/MultScienTechn.2018025983
Magolan, B., Lubchenko, N., & Baglietto, E. (2019). A quantitative and generalized assessment of bubble-induced turbulence models for gas-liquid systems. *Chemical Engineering Science: X*, *2*, 100009. https://doi.org/10.1016/j.cesx.2019.100009
Rahimi, R., Mazarei Sotoodeh, M., & Bahramifar, E. (2012). The effect of tray geometry on the sieve tray efficiency. *Chemical Engineering Science*, *76*, 90–98. https://doi.org/10.1016/j.ces.2012.01.006
Roshdi, S., Kasiri, N., Hashemabadi, S. H., & Ivakpour, J. (2013). Computational fluid dynamics simulation of multiphase flow in packed sieve tray of distillation column. *Korean Journal of Chemical Engineering*, *30*(3), 563–573. https://doi.org/10.1007/s11814-012-0166-1
Rzehak, R., & Krepper, E. (2013a). Bubble-induced turbulence: Comparison of CFD models. *Nuclear Engineering and Design*, *258*, 57–65. https://doi.org/10.1016/j.nucengdes.2013.02.008
Rzehak, R., & Krepper, E. (2013b). CFD modeling of bubble-induced turbulence. *International Journal of Multiphase Flow*, *55*, 138–155. https://doi.org/10.1016/j.ijmultiphaseflow.2013.04.007
Sadripour, M., Rahimi, A., & Hatamipour, M. S. (2012). Experimental Study and CFD Modeling of Wall Deposition in a Spray Dryer. *Drying Technology*, *30*(6), 574–582. https://doi.org/10.1080/07373937.2011.653613
Sato, Y., Sadatomi, M., & Sekoguchi, K. (1981). Momentum and heat transfer in two-phase bubble flow-I. Theory. *International Journal of Multiphase Flow*, *7*(2). https://doi.org/10.1016/0301-9322(81)90003-3
Schiller, L., & Naumann, Z. (1935). A drag coefficient correlation. In *Z.Ver.Deutsch.Ing* (Vol. 77, Issues 13–14). https://doi.org/10.1016/j.ijheatmasstransfer.2009.02.006
Simonin, O., & Viollet, P. L. (1990). Prediction of an oxygen droplet pulverization in a compressible subsonic coflowing hydrogen flow. *American Society of Mechanical Engineers, Fluids Engineering Division (Publication) FED*, *91*.

Sun, Z. M., Liu, B., Yuan, X. G., Liu, C. J., & Yu, K. T. (2005). New turbulent model for computational mass transfer and its application to a commercial-scale distillation column. *Industrial and Engineering Chemistry Research*, *44*(12), 4427–4434. https://doi.org/10.1021/ie049382y

Tomiyama, A. (1998). Struggle with computational bubble dynamics. Multiphase Sci Technol. *Multiphase Science Technology*, *10*.

Treybal, R. E. (1981). Mass Transfer Operations 3th edition. In *McGraw-Hill*.

Troshko, A. A., & Hassan, Y. A. (2001). A two-equation turbulence model of turbulent bubbly flows. *International Journal of Multiphase Flow*, *27*(11). https://doi.org/10.1016/S0301-9322(01)00043-X

Van Baten, J. M., Ellenberger, J., & Krishna, R. (2001). Hydrodynamics of reactive distillation tray column with catalyst containing envelopes: Experiments vs. CFD simulations. *Catalysis Today*, *66*(2–4), 233–240. https://doi.org/10.1016/S0920-5861(00)00625-8

Wang, T., & Wang, J. (2007). Numerical simulations of gas-liquid mass transfer in bubble columns with a CFD-PBM coupled model. *Chemical Engineering Science*, *62*(24), 7107–7118. https://doi.org/10.1016/j.ces.2007.08.033

Wang, T., Wang, J., & Jin, Y. (2005). Population balance model for gas - Liquid flows: Influence of bubble coalescence and breakup models. *Industrial and Engineering Chemistry Research*, *44*(19), 7540–7549. https://doi.org/10.1021/ie0489002

Wang, T., Wang, J., & Jin, Y. (2006). A CFD-PBM coupled model for gas-liquid flows. *AIChE Journal*, *52*(1), 125–140. https://doi.org/10.1002/aic.10611

Xing, C., Wang, T., & Wang, J. (2013). Experimental study and numerical simulation with a coupled CFD-PBM model of the effect of liquid viscosity in a bubble column. *Chemical Engineering Science*, *95*, 313–322. https://doi.org/10.1016/j.ces.2013.03.022

Yang, G., Guo, K., & Wang, T. (2017). Numerical simulation of the bubble column at elevated pressure with a CFD-PBM coupled model. *Chemical Engineering Science*, *170*, 251–262. https://doi.org/10.1016/j.ces.2017.01.013

Zhao, H., Li, Q., Yu, G., Dai, C., & Lei, Z. (2019). Performance analysis and quantitative design of a flow-guiding sieve tray by computational fluid dynamics. *AIChE Journal*, *65*(5), 1–13. https://doi.org/10.1002/aic.16563

Chapter 3

CFD modeling study of the mass transfer and hydrodynamics of a sieve tray distillation column

Highlights

- *Problem:* There is no availability experimental data for the validation of the mass transfer in plates of a HIDiC Column.
- *Contribution:* A CFD-based methodology to predict mass transfer in a sieve tray.
- Implementation and validation of a CFD model to simulate the separation of methanol/propanol system representing the hydrodynamics and mass transfer in a sieve tray.
- Equilibrium and non-equilibrium approaches were used and evaluated for the modeling of the distillation process with CFD.
- A CFD solid model is proposed for the representation of hydrodynamics and mass transfer in distillation detailed studies.
- An important improvement in the reproduction of the phenomena linked to distillation is achieved in comparison to previous studies.

Abstract

Computational fluid dynamics (CFD) is used to represent transport phenomena in fluid systems, in this case, interest is focused on hydrodynamics and mass transfer in a sieve tray of a distillation column. The tray geometry characteristics are based on a large rectangular tray. The methanol/propanol system was simulated using thermodynamic equilibrium and non-equilibrium approaches. The obtained results were compared with the experimental data and Aspen Plus® results. Different modeling alternatives were investigated addressing resistance in gas and liquid phases, and the equilibrium ratio at

the interphase. The modeling data were used to calculate the Murphree efficiency as an indicator of the mass transfer capacity, and the clear liquid height as an indicator of hydrodynamic behavior of the system. The proposed model considers the two-dimensional, two-phase flow of vapor and liquid in which each phase is treated as an interpenetrating continuum, with independent transport equations (Eulerian-Eulerian framework). Interaction between the two phases occurs via interphase momentum and species mass transfer. The final results regarding the clear liquid height and Murphree tray efficiencies were used for the analysis and validation of the modeling approach proposed in this research. The validation was carried out by the comparison of the simulation results against experimental data, average percentages of difference between experimental data and obtained CFD results were: 3.38% for the Murphree efficiency (a significant improvement in comparison to previous studies that report a 16.52% of difference) and 1.56% for the clear liquid height. Additionally, validation of some hydrodynamic variables, phase fraction and vapor velocity field, was performed.

Keywords

Distillation CFD model; Murphree efficiency; clear liquid height; non-equilibrium; process simulation; sieve tray.

3.1 Introduction

Distillation is the separation process of major importance in chemical and petroleum industries worldwide. Increasing separation efficiency, as well as improving its prediction, has been a major task in the design and operation of distillation columns (Kockmann, 2014; Olujić et al., 2009; Yanagi & Sakata, 1982). Efforts to maximize the efficiency of distillation columns are still justified on economic grounds and environmental impact due to the large energy consumption of these units (Dejanović et al., 2010).

In the operation and design of distillation columns, one of the most used internals is the sieve tray, because of its design simplicity and low cost. Despite the widespread use of this kind of tray, few attempts have been made to model its hydrodynamics (Gesit et al., 2003; Krishna, Van Baten, et al., 1999; Li et al., 2014; Malvin et al., 2014; Van Baten & Krishna, 2000). In this way, some CFD studies of mass transfer in sieve trays has been developed before (Abbasnia et al., 2019; Noriler et al., 2010; M. R. Rahimi et al., 2006; R. Rahimi et al., 2012; Sun et al., 2007; Wang et al., 2004). Some important approaches have been to developed CFD models to simulate a three-dimensional two-phase flow to represent the hydrodynamics on a distillation sieve tray (Gesit et al., 2003; Krishna, Van Baten, et al., 1999; Van Baten & Krishna, 2000), and to couple the two-phase equations through an interphase drag term, estimated using the drag coefficient correlation of Krishna (Krishna, Van Baten, et al., 1999) and the Bennet correlation (Bennett et al., 1983) for the liquid holdup fraction in the froth.

Other studies developed a three-dimensional transient CFD model for describing the hydraulics of flow-guided sieve tray, within the two-phase Eulerian−Eulerian framework (Li et al., 2014). However, these CFD simulations showed that the interphase momentum exchange (the drag), estimated using Bennett correlation, fails to give fitted results, compared with the experimental data for clear liquid height.

In the other way, some works have applied the method of the Droplet Size Distribution (DSD) and the CFD flow pattern for sieve trays (Malvin et al., 2014). In these studies, a biphasic and tridimensional model based on the volume of fluid (VOF) and large eddy simulation (LES) approaches for simulating the complex phenomena of flow in sieve trays were used. Considering the clear liquid height, the reported results complied with experimental data.

Regarding the mass transfer phenomenon, one of the first works (Wang et al., 2004) presents a single-phase tridimensional CFD model capable of representing the liquid phase flow and its composition profile on a sieve tray. They calculated the velocity distribution and composition profile for a 1.2 m diameter tray and compared it with experimental results. Other complementary works focused on simulating a tridimensional and biphasic model for predicting hydrodynamic, heat transfer, and mass transfer of sieve trays (Noriler et al., 2010; R. Rahimi et al., 2006; Sun et al., 2007). In their work, Rahimi and co-workers developed a 3D two-fluid CFD model to predict the fluid flow patterns, hydraulics, and mass transfer; the results of the simulation were compared with experimental data. Whereas Sun (2007) offered the semi-one-fluid tridimensional model for predicting penetration of turbulent mass transfer, In this study, the tridimensional profiles for velocity, composition, and, additionally, the separation efficiency were predicted. In another interesting approach, (Noriler et al., 2009, 2010) presented a biphasic tridimensional model following Eulerian–Eulerian approach for hydraulic simulation of mass and heat transfer on distillation sieve trays; a combination of encoding and simulating software was employed to calculate the auxiliary equations and the concurring changes of composition along with the changes of pressure and velocity on the tray were showed. In their simulations, they used the Ranz-Marshall equation to calculate the heat transfer coefficient (Ranz & Marshall, 1952).

In more recent research, (R. Rahimi et al., 2012), used the permanent and tridimensional CFD model for simulating a rectangular sieve tray. They simulated two rectangular trays which differed only in the diameter of the holes and showed that the tray with smaller holes diameters would give more uniform liquid phase mixture, lower back mixing and higher efficiency.

There are few studies about other kind of tray, Abbasnia and coworkes (2019) studied the mass transfer and efficiency of sieve trays and Nye trays. Their simulations were based on a 3D domain. Results showed that the liquid composition profile on the Nye tray corresponds to a more efficient separation, and, consequently, Murphree efficiency in Nye tray is about ten percent higher than in sieve trays.

Due to the interaction of transport phenomena, mass transfer in real operational sieve trays is linked to hydrodynamics and heat transfer. The hydrodynamics, mass, and heat transfer are mainly expressed for each phase in terms of the time and spatial distribution fields of velocity, temperature, pressure, volume fraction, and compositions. From the concentration fields, efficiencies (in a given point and in the whole tray) can be calculated. These efficiencies are used to quantify the efficiency of mass transfer and separation and, during the column and tray design, to translate the theoretical number of trays into a real number of trays.

An impasse that has hindered the further improvement of sieve trays is the fact that little is known about the flow phenomena prevailing inside a tray as functions of the geometry and operating conditions. The main reason for this is the poor knowledge of the complex behavior of the phases inside the tray. How are hydrodynamics, heat, and mass transfer for a given geometry, and operating conditions? which is a major problem facing the current practice of tray design and analysis. As a result, the current design and analysis of sieve trays are based on experience and empirical correlations rather than on specific data or models. The spatial behavior of the multiphase flow field is lacking, and the designer relies heavily on gross oversimplifications. These practices do not consider the actual hydrodynamics, and heat and mass transfer processes inside the tray. Therefore, better models and methods for modeling and predicting sieve tray hydrodynamics, and heat and mass transfer are needed.

Once a method or methods have been fitted to solve the above problems, it will be possible to design trays having specific flow patterns that give rise to the best performance. Over the past years, only experimental methods could be thought of in solving such a problem. Although experimental methods are generally expected to give reliable data, the chaotic, three-dimensional, and multiphase flow behavior inside a distillation tray severely limit the use of experimental methods and the amount of data they can generate.

Advances in numerical methods and improvements in multiphase flow models allow to address complex flow problems, also this is supported on the current computational power available. CFD combines and uses these two characteristics, it is an approach with important predictive and design capabilities for flow analysis in processing units. Compared to experimental methods, it gives complete information (time and spatial distributions of variables) and has a relatively low cost. A major advantage of CFD over experimental methods is its flexibility as it typically enables changing flow geometry and system conditions without incurring in high cost (M. Guevara & Belalcazar, 2017).

The present research aims to verify the use of the CFD to represent the separation in sieve trays, considering the system methanol/propanol as a case study. To propose a suitable setup for this modeling goal two thermodynamic conditions were considered: equilibrium and non-equilibrium. This study also shows the importance of including the resistance in the vapor phase for the system in non-equilibrium and the equilibrium ratio in the interface as a function of the concentration, unlike Rahimi's work (Rahimi *et al.*, 2006), which took into account only resistance in the liquid phase and equilibrium ratio constant.

The developed model is capable of reproducing the hydrodynamics and mass transfer of a sieve tray, and as a consequence, it allows to accurately predict tray efficiency and clear liquid height. This is supported by a comparison of the obtained results against experimental data.

This chapter is ordered as follows, the mathematical model of the two-phase flow is given in Section 3.2, the case study is described in Section 3.3, the methodology in section 3.4, the simulation results are shown in section 3.5 and the main conclusions are given in section 3.6.

3.2 Mathematical model

Concerning turbulence in bubbly flows, it suffices to consider a continuous liquid phase based on the small density and small spatial scales of the dispersed gas. We adopt a two-equation turbulence RANS (Reynolds Averaged Navier Stokes) model for the liquid and vapor phases (Bird et al., 1958; Kataoka & Serizawa, 1989; Morel, 1995), the energy equation and the momentum equation. Momentum exchange is modeled considering drag, lift, and virtual mass.

3.2.1 Flow equations

The two-fluid model considers vapor and liquid phases as continua, and it solves two sets of conservation equations for mass, momentum, and energy, which are written for each phase by Equations 1 to 4.

Continuity equation of liquid phase (Eq. 1).

$$\frac{\partial(\alpha_L \rho_L)}{\partial t} + \nabla \cdot (\alpha_L \rho_L \boldsymbol{u}_L) = S_{LG} \tag{1}$$

Continuity equation of vapor phase (Eq. 2).

$$\frac{\partial(\alpha_G \rho_G)}{\partial t} + \nabla \cdot (\alpha_G \rho_G \boldsymbol{u}_G) = -S_{LG} \tag{2}$$

The momentum equation of liquid (Eq. 3) and vapor (Eq. 4) phase correspond to

$$\begin{aligned} \frac{\partial(\alpha_L \rho_L \boldsymbol{u}_L)}{\partial t} &+ \nabla \cdot (\alpha_L \rho_L \boldsymbol{u}_L \boldsymbol{u}_L) \\ &= -\alpha_L \nabla P + \nabla \cdot [\alpha_L \mu_L^e (\nabla \boldsymbol{u}_L + (\nabla \boldsymbol{u}_L)^T)] + \alpha_L \rho_L g + \boldsymbol{F}_{LG} \\ &+ (S_{LG} \boldsymbol{u}_G - S_{GL} \boldsymbol{u}_L) \end{aligned} \tag{3}$$

$$\begin{aligned} \frac{\partial(\alpha_G \rho_G \boldsymbol{u}_G)}{\partial t} &+ \nabla \cdot (\alpha_G \rho_G \boldsymbol{u}_G \boldsymbol{u}_G) \\ &= -\alpha_G \nabla P + \nabla \cdot [\alpha_G \mu_G^e (\nabla \boldsymbol{u}_G + (\nabla \boldsymbol{u}_G)^T)] + \alpha_G \rho_G g + \boldsymbol{F}_{GL} \\ &+ (S_{GL} \boldsymbol{u}_L - S_{LG} \boldsymbol{u}_G) \end{aligned} \tag{4}$$

The terms at the left-hand side correspond to the momentum accumulation in the phase and the net momentum outlet from the phase, respectively. For the momentum exchange at the liquid-vapor interface, $\boldsymbol{F}_{LG}$, drag, lift, and virtual mass are considered:

$$\boldsymbol{F}_{LG} = \boldsymbol{F}_{LG}^{drag} + \boldsymbol{F}_{LG}^{lift} + \boldsymbol{F}_{LG}^{VM} = -\boldsymbol{F}_{GL} \tag{5}$$

where

$$\boldsymbol{F}_{LG}^{lift} = C_l \alpha_G \rho_L (\boldsymbol{u}_G - \boldsymbol{u}_L)(\nabla \boldsymbol{u}_L) \tag{6}$$

$$\boldsymbol{F}_{LG}^{VM} = C_{VM} \alpha_G \rho_L \frac{D}{Dt} (\boldsymbol{u}_G - \boldsymbol{u}_L) \tag{7}$$

3.2.2 Drag Model

In multiphase flows, the correlations for interfacial forces are developed to study the interaction between different phases (Ishii & Zuber, 1979; Schiller & Naumann, 1935).

The interaction between liquid and gas phases is dominated by the drag force and it is determined by solving the momentum equation (Eqs. 3 and 4). The drag force is calculated using the Eq. 8.

$$\boldsymbol{F}_{LG}^{drag} = \frac{3C_D}{4d_b}\alpha_G\rho_L|\boldsymbol{u}_G - \boldsymbol{u}_L|(\boldsymbol{u}_G - \boldsymbol{u}_L) \quad (8)$$

where C_{Di} is the drag coefficient, which can be obtained from the Grace model (Grace et al., 1978). This model is well suited for gas-liquid flows in which the bubbles exhibit a range of shapes, such as the sphere, ellipsoid, and spherical cap. The drag coefficients for different shapes of bubbles are calculated by:

$$C_D = \max\left(\min\left(C_{D_{ellipse}}, C_{D_{cap}}\right), C_{D_{sphere}}\right) \quad (9)$$

where

$$C_{D,sphere} = \begin{cases} 24/Re_b & Re_b < 0.01 \\ 24\left(1 + 0.15Re_b^{0.687}\right)/Re_b & Re_b \geq 0.01 \end{cases} \quad (10)$$

$$C_{D,cap} = \frac{8}{3} \quad (11)$$

$$C_{D,ellipse} = \frac{4}{3}\frac{gd_b}{U_t^2}\frac{\left(\rho_l - \rho_g\right)}{\rho_l} \quad (12)$$

and

$$Re_b = \frac{\rho_l\left|\boldsymbol{u}_{g-}\boldsymbol{u}_l\right|d_b}{\mu_l} \quad (13)$$

$$U_t = \frac{\mu_l}{\rho_l d_b}Mo^{-0.149}(J - 0.857) \quad (14)$$

where Mo is the Morton number and J is given by a piecewise function, defined by:

$$Mo = \frac{\mu_l^4 g\left(\rho_l - \rho_g\right)}{\rho_l^2\sigma^3} \quad (15)$$

$$J = \begin{cases} 0.94H^{0.757} & 2 < H < 59.3 \\ 3.42H^{0.441} & H > 59.3 \end{cases} \quad (16)$$

In Equation (16) H is defined by:

$$H = \frac{4}{3}EoMo^{-0.149}\left(\frac{\mu_l}{\mu_{ref}}\right)^{-0.14} \quad (17)$$

where $\mu_{ref} = 0.0009\, kg/(m.s)$ and Eo is the Eötvös number:

$$Eo = \frac{g\left(\rho_l - \rho_g\right)d_b^2}{\sigma} \quad (18)$$

3.2.3 Modified drag model

In this research, we use a modified drag coefficient ($C_{D,corr}$), based in the Grace model and developed in the chapter 2. This correction on drag coefficient is supported on the idea that Grace model considers the balance forces acting on a single bubble moving into the liquid, instead of a multi-bubble system where each bubble interact with the liquid and with other bubbles. The equation used is:

$$C_{D,corr} = F_{corr} C_D \tag{19}$$

here, C_D is the drag coefficient calculated with Grace's model (Eq. 9), and F_{corr} is the correction factor. The value of the correction factor was estimated using experimental data of clear liquid height as function of the specific superficial gas velocity.

3.2.4 Species Mass Transfer

To model interphase mass transfer, phase species transport equations are solved along with the mass, momentum, and energy equations. The transport equations for the mass fraction of the light component (LK), are the Equations 20 and 21 (similar equations are considered for the heavy component):

Vapor phase:

$$\frac{\partial(\alpha_G \rho_G Y_{LK})}{\partial t} + \nabla \cdot (\alpha_G \rho_G \boldsymbol{u}_G Y_{LK}) = \nabla \cdot \left[\alpha_G \rho_G D_{LK,G} \nabla Y_{LK}\right] - S_{LG,LK} \tag{20}$$

Liquid phase:

$$\frac{\partial(\alpha_L \rho_L X_{LK})}{\partial t} + \nabla \cdot (\alpha_L \rho_L \boldsymbol{u}_L X_{LK}) = \nabla \cdot \left[\alpha_L \rho_L D_{LK,L} \nabla X_{LK}\right] + S_{LG,LK} \tag{21}$$

The interphase species mass transfer term $S_{LG,LK}$ is the interphase mass transfer rate of the light component per unit volume (Eq. 22), where relationship of Eq. 23 is used to calculate k_{LG}.

$$S_{LG,LK} = k_{LG} A (K \rho_L^{LK} - \rho_G^{LK}) \tag{22}$$

$$\frac{1}{k_{LG}} = \frac{1}{k_G} + \frac{K}{k_L} \tag{23}$$

where A is the interfacial area per unit volume, K is the mole fraction equilibrium ratio as in $y_e = K * x$, ρ_p^{LK} is the mass concentration of the light component in the phase p, k_G and k_L are the volumetric individual film mass transfer coefficients of gas and liquid, respectively.

3.2.5 Mass Transfer model

Interphase mass transfer was modeled using the two-resistance model in ANSYS Fluent (ANSYS Release 19, 2018). There are many theories available in the literature for the calculation of the mass transfer coefficient k_G and k_L (Lamont & Scott, 1970), however the most used are those mentioned next (Eqs 24 – 27):

Penetration theory (Higbie, 1935):

$$k_L = \frac{2}{\sqrt{\pi}}\sqrt{\frac{D_{L,LK}}{t_L}} \tag{24}$$

$$k_G = \frac{2}{\sqrt{\pi}}\sqrt{\frac{D_{G,LK}}{t_G}} \tag{25}$$

where t_e is the exposure time, calculated as:

$$t_L = \frac{d_b}{\boldsymbol{u}_{rise}} \tag{26}$$

$$t_G = \frac{d_b}{\boldsymbol{u}_H} \tag{27}$$

where d_b is the bubble diameter, $\boldsymbol{u}_{rise}$ is the bubble slip velocity and $\boldsymbol{u}_H$ is the vapor velocity through the tray holes. Therefore, the expressions for the local mass transfer coefficient are:

$$k_L = 2\Upsilon\sqrt{\frac{D_{L,LK}\boldsymbol{u}_{rise}}{\pi d_b}} \tag{28}$$

$$k_G = 2\Upsilon\sqrt{\frac{D_{G,LK}\boldsymbol{u}_H}{\pi d_b}} \tag{29}$$

where Υ is a model constant.

Ranz-Marshall model (Ranz & Marshall, 1952) uses an analogous approach to that for the Ranz-Marshall heat transfer coefficient model based on the Sherwood number (Treybal, 1981):

$$Sh_q = \frac{k_q L_q}{D_q} = 2 + 0.6Re_q^{1/2}Sc_q^{1/3} \tag{30}$$

where k_q is the mass transfer coefficient in the q^{th} phase, D_q is the diffusivity in the q^{th} phase, L_q is a characteristic length (such as the bubble diameter), Sc_q is the Schmidt number of the phase and Re_q is the relative Reynolds number.

3.3 Simulations setup

Sieve tray geometry was selected due to the availability of experimental results (Dribika and Biddulph, 1986) for the system Methanol-Propanol at ten different experimental composition profiles and simulated within the two-phase Eulerian framework and the standard k-epsilon model. In that way, results were compared against experimental data of Murphree efficiency, liquid composition profiles and clear liquid height reported by (Biddulph & Dribika, 1986; Dribika & Biddulph, 1986). The simulations were two-dimensional transient, and the tray dimensions are in Table 3-1. In the simulations, the solution scheme for Pressure-Velocity Coupling was SIMPLE algorithm and for spatial discretization and transient formulation was first-order upwind (Versteeg & Malalasekera, 1995).

Table 3-1: Sieve tray technical specifications used in this study.

Characteristics	**Experimental**	**Simulation**
Weir length	83 mm	85 mm
Liquid flow path	991 mm	985 mm
Tray spacing	154 mm	155 mm
Hole diameter	1.8 mm	5 mm
Percentage of free area	8%	8%
Outlet weir height	25 mm	25 mm
Inlet weir height	4.8 mm	5 mm

Simulations were done with ANSYS-Fluent® V18.0 on a Dell Intel Xeon W3530 2.8GHz. The transport equations for additional scalars were assumed to have the form of the general scalar convective-diffusion equation. The convergence absolute criteria for the simulations were $1x10^{-3}$ for most variables except for the volume fraction which was $1x10^{-4}$ (ANSYS Release 19, 2018).

For the time-dependent term, implicit first-order backward time differencing was used with a fixed time step of $1x10^{-3}$s. The simulations were run with a small underrelaxation factor generally less than 0.8. The values from the simulation were obtained after averaging over a sufficiently long-time-interval once quasi-steady-state conditions were established. The time for each simulation took around seven days.

The geometry and mesh used in the simulations are shown in Figure 3-1. Geometry was developed using Design Modeler® and the mesh was made with the software ANSYS meshing®. The number of cells and type of mesh is shown in Table 3-2, this type of mesh guarantees the maximum mesh quality and minimizes the convergence errors due to mesh configuration. Locations of the boundaries of the system in the CFD simulation are shown in Figure 3-2.

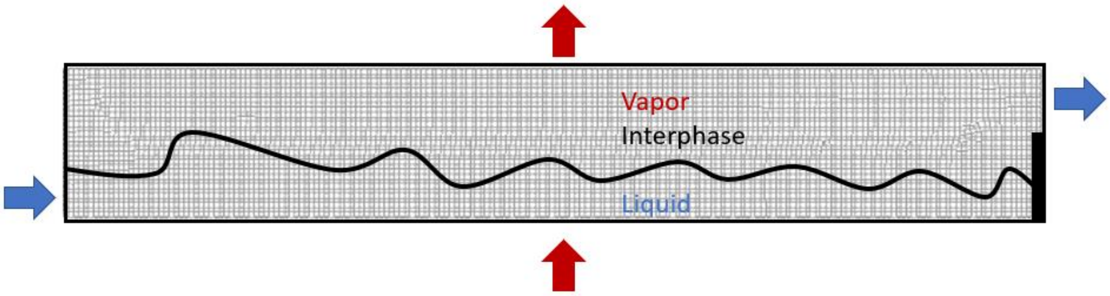

Figure 3-1: Mesh and Flow geometry system 2D domain for the development of the CFD simulations.

Table 3-2: Mesh data: type of geometry, type of element, and the number of cells, used in the development of the CFD model applied in this study.

Type of geometry	Type of cell	Number of cells
2D	Quadrilateral (5mm x 5mm)	6107

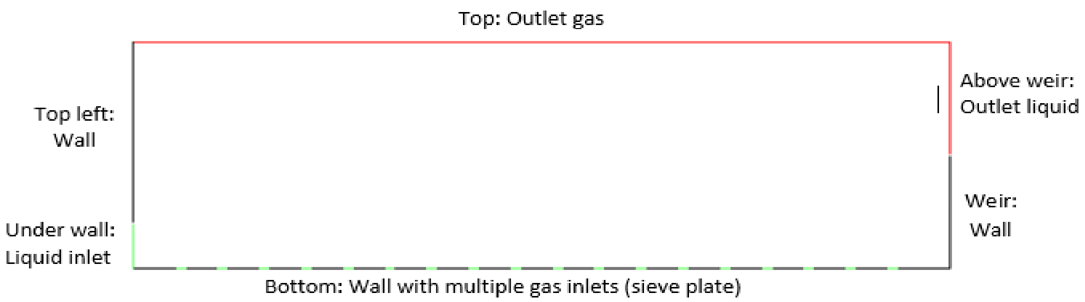

Figure 3-2: Boundary conditions locations used for the setup of the CFD model: Inlets, outlets, and walls of the geometry 2D.

3.4 Methodology

For the development of the work, two steps were employed:

In the First step, simulations were performed in thermodynamic equilibrium using Aspen Plus® and Ansys Fluent®. The objective of this step was to verify the use of the CFD model to describe a tray that attains thermodynamic equilibrium. Results from CFD were compared with results of the same system simulated with Aspen Plus®.

In the second step simulations in Ansys Fluent® consider non-equilibrium conditions. Results regarding the Murphree efficiency and the clear liquid heigh were obtained and they were validated by comparison with experimental data.

Additionally, a verification of the hydrodynamics representation by the resulting model was performed to give a robust and wide consideration of the different phenomena involved in the separation of the mixture occurring in the modeled tray.

3.4.1 Step 1 Thermodynamic Equilibrium model

These simulations were performed based on the next procedure:

1. Ten (10) simulations in Aspen Plus® considering a distillation column under thermodynamic equilibrium conditions. Each of these 10 simulations was formulated to match the inlet and operation conditions of the trays for which the experimental data is available. The velocity and average concentration were obtained as results of these simulations. In all simulations, the value of the F factor of the experimental part was maintained; this value was 0.4.

2. The liquid and vapor inlet velocity, concentrations, temperatures, and equilibrium ratio were taken as initial and boundary conditions for the CFD simulations. Table 3-3 describes the general characteristics of the boundary conditions and Table 3-4 their respective used values. The general setup used in each simulation is shown in Table 3-5. After, the CFD results (average liquid concentration of methanol, in equilibrium) were compared with results from simulations with Aspen Plus®.

Table 3-3: Boundary conditions description for the CFD modeling.

Boundary Conditions	Property	Gas-phase volume fraction
Liquid inlet	Uniform profile $U_{L,in} = \frac{Q_L}{h_{DC}L_w}$	0
Gas inlet	$V_{hole} = \frac{V_S A_B}{N_H A_{hole}}$	1
Liquid outlet	Pressure outlet	1
Gas outlet	Pressure outlet	1
Wall	No-slip wall	Grad=0

Table 3-4: Boundary conditions used for each simulation under equilibrium conditions.

Run	Inlet liquid composition (Molar fraction)	Inlet vapor composition (Molar fraction)	Inlet velocity liquid (m/s)	Inlet velocity vapor (m/s)	Inlet temperature liquid (K)	Inlet temperature vapor (K)	Molar fraction Equilibrium ratio
1	0.911	0.7887	0.001578	0.1081	339.25	349.24	0.8282
2	0.88	0.7114	0.001614	0.1075	340.05	352.3	0.7663

Run	Inlet liquid composition (Molar fraction)	Inlet vapor composition (Molar fraction)	Inlet velocity liquid (m/s)	Inlet velocity vapor (m/s)	Inlet temperature liquid (K)	Inlet temperature vapor (K)	Molar fraction Equilibrium ratio
3	0.862	0.6807	0.001677	0.1103	340.41	353.42	0.7418
4	0.794	0.5793	0.001743	0.1098	341.88	356.76	0.6623
5	0.759	0.5354	0.001778	0.1097	342.67	358.09	0.6285
6	0.714	0.4847	0.001825	0.1098	343.72	359.53	0.5902
7	0.622	0.3976	0.001926	0.1103	346.01	361.83	0.5263
8	0.569	0.3543	0.001955	0.1090	347.43	362.89	0.4959
9	0.483	0.2922	0.002039	0.1089	347.43	362.89	0.4541
10	0.320	0.1896	0.002225	0.1097	355.32	366.61	0.3916

Table 3-5: Set up of the CFD model used to simulate the tray with equilibrium conditions.

Characteristic	Set up
System	Methanol-Propanol
Geometry	2D
Multiphase Models	Eulerian two phases
Phase interactions	Virtual Mass Drag (grace model) with modification Mass: two mass transfer mechanisms → model options: equilibrium ratio
Surface Tension	Constant: 0.00224 N/m
Viscous Model	Standard k-epsilon

3.4.2 Step 2 Non-equilibrium thermodynamic

This step was performed to evaluate the system under non-equilibrium conditions. Results were validated by comparing with available experimental data. This step considers: 1) Determination of Murphree efficiency and 2) Determination of the clear liquid height.

3.4.2.1. Determination of Murphree efficiency

To determine the Murphree efficiency results regarding the concentrations of the components within the system are necessary. To represent the interphase mass transfer phenomenon the double resistance model was used. To validate these results they are compared with experimental data. The Higbie theory model was used to calculate the mass transfer coefficient in the liquid phase, and to implement Higbie's model a UDF was developed (see appendix). This analysis was developed according to the following substeps:

1. A baseline initial case “Run 1” was designed, the conditions used to set up this run are shown in the first row of Table 3-4. There is an important effect of three variables on the Murphree efficiency: resistance in the liquid phase, resistance in the vapor phase, and thermodynamic model in the interfacial equilibrium ratio. Based on the effects of these variables, four simulation configurations were formulated. This allows to choose the best simulation configuration to represent the conditions of Run 1:

   Simulation 1: Resistance in the liquid phase using Higbie model by UDF, constant value for equilibrium ratio in the interface, and zero resistance in the vapor phase.

   Simulation 2: Resistance in the liquid phase using the Higbie model by UDF, equilibrium ratio in the interface adjusted using a UDF based on Wilson's activity coefficient model (M. A. Guevara et al., 2018), which was the same used by Dribika and Biddulph (1986), and zero resistance in the vapor phase.

   Simulation 3: Resistance in the liquid phase, using the Higbie model by UDF, resistance in the vapor phase using the Ranz-Marshall model and constant value for equilibrium ratio in the interface.

   Simulation 4: Resistance in the liquid phase, using the Higbie model by UDF, resistance in the vapor phase using the Ranz-Marshall model and equilibrium ratio in the interface adjusted using a UDF (see appendix) based on Wilson's thermodynamic equilibrium model.

The objective of these four simulations was to reproduce the conditions of Run 1. Obtained results for each simulation were compared with experimental data to select the most accurate strategy to represent the system. After that, best strategy will be used for the simulation of the other nine (9) runs.

2. The next nine runs were performed using the simulation configuration identified as the best in substep 1 above, in each of the runs the corresponding conditions in Table 3-4 were used.

3.4.2.2. Determination of the clear liquid height

To determine the height of clear liquid, the modified approach to estimate the drag coefficient was used, this drag correction factor was taken based on the formulation in section 3.2.3. In this case, the ten runs were simulated according to the initial and boundary conditions shown in Table 3-4; then, the results regarding the height of clear liquid were compared with the experimental data.

3.5 Results and discussion

3.5.1 Step 1 Thermodynamic Equilibrium model

Table 3-6 shows the CFD modeling results under equilibrium conditions according to step 1 described in the methodology. The equilibrium fraction of methanol in the liquid phase on the tray has a good agreement between the Aspen Plus and the CFD results; similarly, equilibrium vapor composition achieves a good agreement between both datasets (Aspen Plus and CFD).

Figure 3-3 shows the comparison for methanol fraction in the liquid phase: equilibrium composition and inlet mean composition. Both series of data have a good correspondence. The plotted curves show that the relationship is not linear between these two variables.

According to the results of step 1, the CFD results are in agreement with the ones from thermodynamic equilibrium process modeling obtained from Aspen plus®. CFD results have the advantage that it takes into account the geometry of the plate in the development of its transport equations unlike Aspen Plus®, which performs the calculations only from the thermodynamic point of view and its hydrodynamic calculations are carried out using empirical correlations.

Table 3-6: CFD modeling results under thermodynamic equilibrium conditions (step 1)

Run	Inlet liquid composition	Equilibrium methanol fraction for liquid phase in the tray		Equilibrium methanol fraction for vapor phase in the tray	
		Aspen Plus	CFD	Aspen plus	CFD
1	0.911	0.7665	0.7661	0.9254	0.9255
2	0.880	0.6811	0.6817	0.8887	0.8885
3	0.862	0.647	0.6483	0.8723	0.8724
4	0.794	0.5357	0.5411	0.8088	0.8089
5	0.759	0.4882	0.4912	0.7764	0.7766
6	0.714	0.4334	0.4401	0.7336	0.7340
7	0.622	0.342	0.3450	0.6459	0.6462
8	0.569	0.2959	0.2971	0.5968	0.5971
9	0.483	0.2328	0.2331	0.5130	0.5131
10	0.320	0.1381	0.1402	0.3523	0.3524

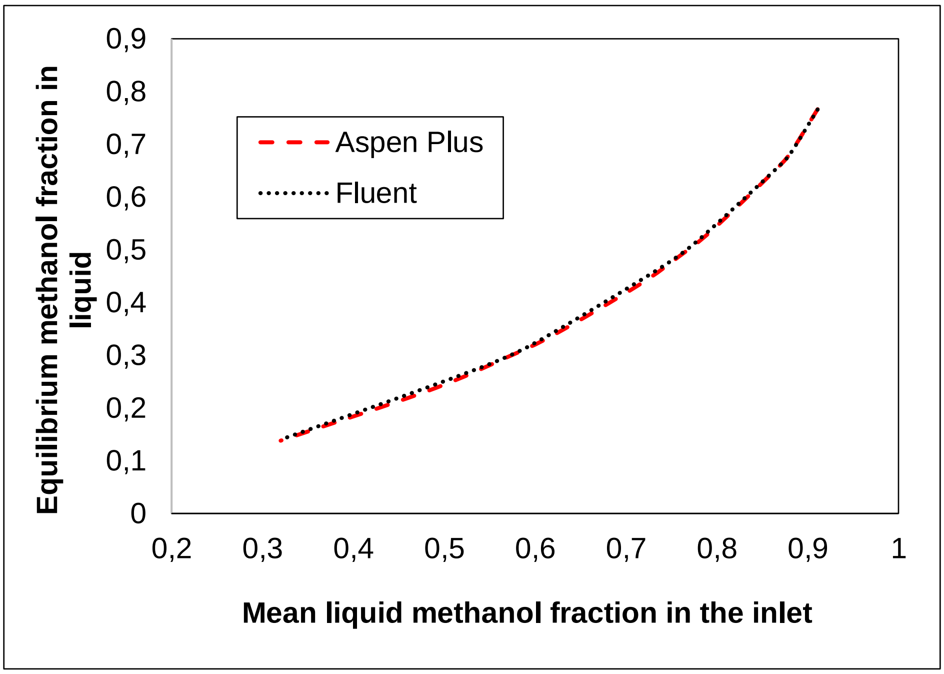

Figure 3-3: Comparison of results for equilibrium simulations.

3.5.2 Step 2 non-equilibrium thermodynamics

3.5.2.1 Murphree tray efficiency

The Murphree tray efficiency for the vapor phase considers the comparison of a real tray with an ideal one (Treybal, 1981). In this study, Murphree tray efficiency is calculated by:

$$E_{MV} = \frac{y_n - y_{n-1}}{y_n^* - y_{n-1}} \tag{31}$$

where: y_n is the actual vapor fraction in tray n, y_{n-1} is the actual vapor fraction in tray n-1, y_n^* is the vapor fraction under equilibrium conditions in the tray n, y_n^* is determined by Wilson's thermodynamics equilibrium model.

Results for Run 1 of step 2 of the methodology proposed are shown in Table 3-7, this table shows the Murphree efficiency calculated with four simulation configurations evaluated with the base case conditions established as Run 1 (Table 3-4). Since the goal of this step is to define the best configuration to be used for the analysis of the mass transfer within the tray, the estimated Murphree efficiency of each simulation configuration (i.e. Simulation 1, Simulation 2, Simulation 3, and Simulation 4) was compared with the corresponding experimental efficiency value. Based on this assessment, we found the simulation configuration that better represents the efficiency is Simulation 4. This is explained by the consideration of the effect of resistance in the vapor phase (i.e. Higbie model) coupled with the use of the equilibrium ratio in the interface as a function of the phase concentration rather than constant. Therefore, the remaining nine runs were performed using the configuration corresponding to Simulation 4.

Table 3-7: Murphree efficiency base on step 2, substep 1.

Dataset	Experimental	Configuration of Simulation 1	Configuration of Simulation 2	Configuration of Simulation 3	Configuration of Simulation 4
Murphree Efficiency	92.16	110.4	90.1	89.8	92.83
% of difference*	-	19.8%	-2.2%	-2.6%	*<u>0.7%</u>*

**% of the difference is calculated as:* $\frac{E_{MV,s} - E_{MV,Experimental}}{E_{MV,Experimental}} * 100$, *where s is the corresponding simulation.*
*** underlined italic text corresponds to the lowest % of difference found.*

Table 3-8 shows the results of step 2 substep 2, it includes the results for the ten simulation conditions (boundaries) in Table 3-4, using the configuration of Simulation 4, which was found to be the best in terms of Murphree efficiency (Table 3-7).

The showed experimental data corresponds to the Murphree efficiency estimated in the literature, additionally, results found in a previous study with the same geometry and conditions (R. Rahimi et al., 2012) are reported. These two datasets (experimental and literature modeling results) were compared with the CFD results of this study. The percentual deviation was used for a quantitative comparison between the datasets.

The Rahimi study only reports 5 configurations, which gave results well above the experimental ones, with a mean deviation of 16.52% compared with 3.38% obtained in this work, what is a significant improvement. Large deviations of the results reported in Rahimi study are explained by the use of the standard drag model (see section 3.2.3) rather than the modification proposed in this study. Additionally, neglection of the effect of the resistance in the gas phase and representation of the equilibrium conditions as a constant equilibrium ratio in the interface may be linked to less accurate results.

Table 3-8: Murphree efficiency calculated base on step 2 of substep 2 for different conditions of inlet liquid composition of methanol in a sieve tray.

Conditions			Murphree Efficiency			deviation from experimental data**	
Run	Inlet liquid methanol composition	Mean liquid methanol composition	Experimental	CFD (Higbie theory)	simulation Rahimi*	CFD (Higbie theory)	Simulation Rahimi*
1	0.911	0.80176	92.16	92.83	-	0.73%	-
2	0.880	0.77303	92.68	89.76	107.70	3.15%	16.21%
3	0.862	0.72167	92.31	90.05	-	2.45%	-
4	0.794	0.63251	92.98	90.61	108.80	2.55%	17.01%
5	0.759	0.56148	93.12	89.28	110.70	4.12%	18.88%
6	0.714	0.51614	93.10	89.19	-	4.20%	-
7	0.622	0.41038	98.21	97.09	113.50	1.15%	15.57%
8	0.569	0.281	109.1	97.81	125.40	10.35%	14.94%
9	0.483	0.26525	114.67	112.29	-	2.08%	-
10	0.320	0.16094	134.88	139.03	-	3.08%	-
					Average	**3.38%**	**16.52%**

**Corresponds to literature reported data for previous simulations* ((R. Rahimi et al., 2012)

*** it is calculated as:* $\frac{|E_{MV,R} - E_{MV,Experimental}|}{E_{MV,Experimental}} * 100$ *where R defines the run conditions from Table 3-4.*

3.5.2.2 Clear liquid height

Table 3-9 shows the CFD results and the experimental data regarding the clear liquid heigh for the conditions established (Table 3-4). The average percentage of deviation is 1.56%, what is a relatively low value and several cases present zero deviation. This is evidence of the good performance of the proposed CFD model.

Table 3-9: Clear liquid height estimated based on the results of stage 2.

Run	Inlet liquid methanol fraction	Mean liquid methanol fraction	Clear liquid height		deviation from experimental data*
			Experimental	CFD	
1	0.911	0.80176	27	28	3.70%
2	0.880	0.77303	27	27	0.00%
3	0.862	0.72167	26	26	0.00%
4	0.794	0.63251	26	26	0.00%
5	0.759	0.56148	25	25	0.00%
6	0.714	0.51614	26	24	7.69%

Run	Inlet liquid methanol fraction	Mean liquid methanol fraction	Clear liquid height		deviation from experimental data*
			Experimental	CFD	
7	0.622	0.41038	25	25	0.00%
8	0.569	0.281	25	25	0.00%
9	0.483	0.26525	24	25	4.17%
10	0.320	0.16094	23.5	23.5	0.00%
				Average	**1.56%**

* *it is calculated as:* $\frac{|E_{MV,R} - E_{MV,Experimental}|}{E_{MV,Experimental}} * 100$ *where R defnes the run conditions from Table 4.*

Figure 3-4 shows the clear liquid heigh variation as a function of the mean liquid composition of methanol. Good agreement is evidenced and both curves have similar trend. These simulation results are highly consistent since their comparison with experimental data leads to low percentual deviation, nulls in most of the cases (Table 3-9). This is evidence of the validity of the adjustment for the friction coefficient proposed in this work.

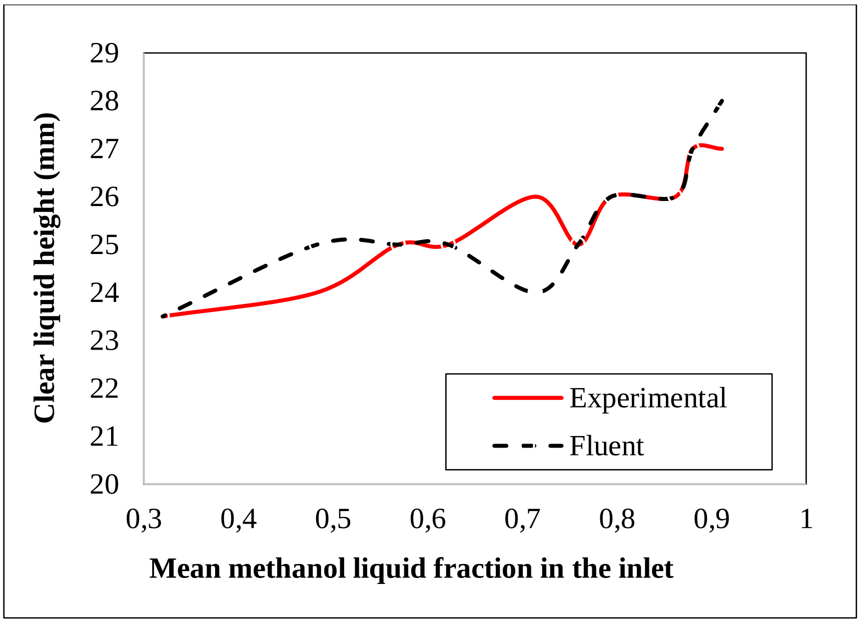

Figure 3-4: Clear liquid height for each of the ten boundary conditions studied.

3.5.3 Hydrodynamics analysis

Complementary to the mass transfer modeling described in the sections above, a qualitative analysis of the hydrodynamic was performed. This analysis considers the phases and velocity field within the modeled sieve tray. Figure 3-5 shows the time evolution of the phases distributions through the vapor phase fraction (left), and the velocity field of the vapor phase (right) in the tray along time. Based on these qualitative results, a coherent and clear prediction of the phase hydrodynamics is evidenced with the proposed CFD model.

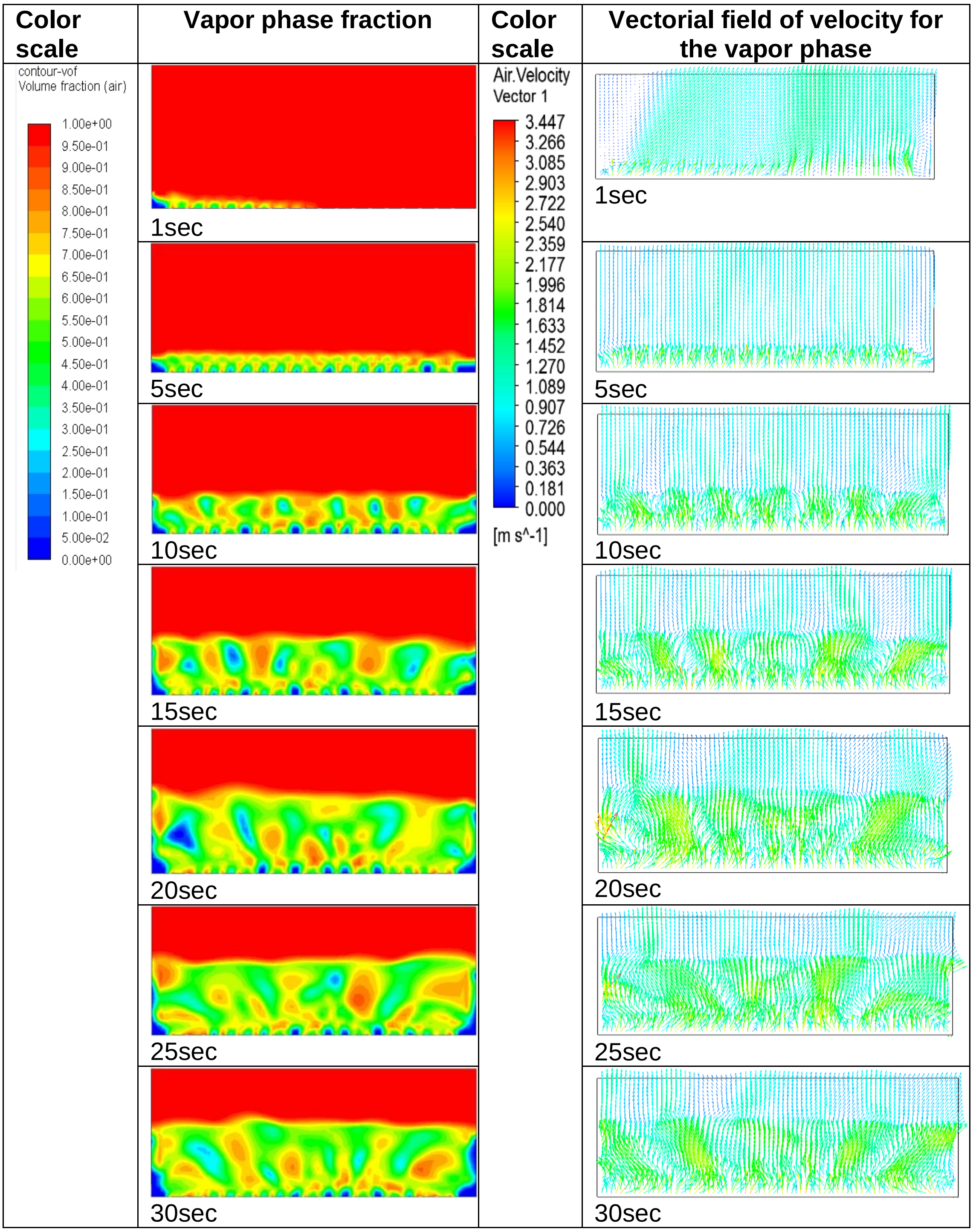

Figure 3-5: Evolution of instant gas hold-up distribution and vector gas velocity for the proposed CFD model.

Table 3-10 shows the comparison of the predicted weir height by the CFD model and the experimental data (Krishna, Urseanu, et al., 1999; Krishna, Van Baten, et al., 1999), this comparison allows to estimate an average difference of 3.1%, which is a satisfactory result for the prediction of the weir height as a benchmark for the hydrodynamics within the tray.

Table 3-10: Hydrodynamic results of the proposed CFD model in terms of the weir height of the sieve tray.

Experimental Weir height (m)	CFD Weir Height (m)	difference*
0.06	0.058	3.00%
0.08	0.078	2.50%
0.09	0.088	2.10%
0.1	0.095	4.90%
Average		**3.10%**

$$* \ it\ is\ calculated\ as: \frac{|weir_{CFD} - weir_{Experimental}|}{weir_{Experimental}} * 100$$

3.6 Conclusions

A CFD model was developed for the representation and prediction of hydrodynamics and mass transfer for methanol/propanol system on a sieve tray. The proposed model was evaluated and validated with experimental data to demonstrate its capabilities. The analyses were performed based on qualitative and quantitative results from the developed CFD simulations.

Several possible setup options were evaluated aiming to consider mass transfer properly, for this, the models: Higbie's penetration theory and Ranz-Marshall model were evaluated.

Results were validated by comparing the Murphree efficiency and the clear liquid height against experimental data. The obtained results lead to propose a CFD model based on: Higbie's approach for the resistance in the liquid phase, the Ranz-Marshall model for the resistance in the vapor phase, and Wilson's thermodynamic equilibrium model for the equilibrium ratio in the interface rather than constant. Based on these results, This CFD modeling strategy is proposed for the representation of hydrodynamics and mass transfer in sieve tray simulations for distillation, and as a part of models for more compex systems -i.e. columns for intensificated processes- which will be considered in a future work.

The proposed model allows the representation of the system considered as a case study with an average deviation of 3.38% and 1.56% in terms of the Murphree efficiency and the clear liquid height, respectively. A significant improvement in comparison to previous studies based on classical approaches for the modeling of the same system.

An additional analysis of the proposed CFD model capability to reproduce the hydrodynamics was performed showing that the model can represent accurately the phase development in terms of the phase fraction and velocity fields. A quantitative comparison between the weir height represented by the CFD model and the experimental data reported in the literature shows that differences of less than 3.1% can be expected.

Acknowledgments

The authors acknowledge the financial support of Universidad Nacional de Colombia and Colciencias, and the collaboration and advice of Professor Ronnie Andersson. The authors would like to thanks the company S&S S.A.S for its technical support and contributions to this research.

Notation

A	Interfacial area per unit volume, m^{-1}
A_B	Bubbling area, m^2
A_{hole}	Hole area on sieve tray, m^2
C_D	drag coefficient
C_l	lift force coefficient
C_{VM}	virtual mass force coefficient
D	diffusion coefficient, m^2/s
d_b	diameter of the bubble, m
d_h	Hole diameter of a sieve tray, m
E_{MV}	Murphree Efficiency, --
F	total interfacial force, N
F^{drag}	Interfacial drag force, N
F^{lift}	lift force, N
F^{VM}	Virtual mass force, N
g	gravitational acceleration, m/s^2
H	enthalpy, J/kg
h_{cl}	Clear liquid height, mm
h_{DC}	Hight downcomer, m
L_w	Length weir, m
k	kinetic energy turbulent, m^2/s
K_{GL}	Covariance of the velocities of liquid and gas
K_l	gas–liquid mass transfer coefficient, m/s
N_H	Number of holes in the sieve tray
P	Pressure, Pa
$S_{k,L}$	source terms describing the effects of the dispersed phase on the continuous phase
T	temperature, K
t	Thermo-fluid time scale, s
t_e	exposure time in the penetration model, s
u_{slip}	bubble slip velocity, m/s
u_b	bubble velocity, m/s
u	velocity, m/s
V_s	Superficial gas velocity, m/s
X_{LK}	Mass fraction of the light component in liquid phase
Y_{LK}	Mass fraction of the light component in vapor phase
Z	length of travel on a tray, m

Greek letters

α	Void fraction
ρ	Density, kg/m^3
μ^e	effective viscosity, kg/m s
μ	Viscosity, kg/m s
σ	Surface tension,N/m

Subscripts

G	Vapour
L	Liquid
GL	transfer of quantities from liquid phase to vapor

LG transfer of quantities from vapor phase to

LK liquid

Light component

References

Abbasnia, S., Nasri, Z., & Najafi, M. (2019). Comparison of the mass transfer and efficiency of Nye tray and sieve tray by computational fluid dynamics. *Separation and Purification Technology*, *215*. https://doi.org/10.1016/j.seppur.2019.01.010

ANSYS Release 19. (2018). *ANSYS Fluent Theory Guide*.

Bennett, D. L., Agrawal, R., & Cook, P. J. (1983). New pressure drop correlation for sieve tray distillation columns. *AIChE Journal*, *29*(3), 434–442. https://doi.org/10.1002/aic.690290313

Biddulph, M. W., & Dribika, M. M. (1986). Distillation efficiencies on a large sieve plate with small-diameter holes. *AIChE Journal*, *32*(8), 1383–1388. https://doi.org/10.1002/aic.690320817

Bird, R., Stewart, W., & Lightfoot, E. (1958). *Transport Phenomena* (2nd ed.).

Morel, C. (1995). An order of magnitude analysis of the two-phase k–e model. *International Fluid Mechanics*. https://doi.org/10.1615/InterJFluidMechRes.v22.i3-4.30

Dejanović, I., Matijašević, L., & Olujić, Ž. (2010). Dividing wall column-A breakthrough towards sustainable distilling. *Chemical Engineering and Processing: Process Intensification*, *49*(6), 559–580. https://doi.org/10.1016/j.cep.2010.04.001

Dribika, M. M., & Biddulph, M. W. (1986). Scaling-up distillation efficiencies. *AIChE Journal*, *32*(11), 1864–1875. https://doi.org/10.1002/aic.690321112

Gesit, G., Nandakumar, K., & Chuang, K. T. (2003). CFD modeling of flow patterns and hydraulics of commercial-scale sieve trays. *AIChE Journal*, *49*(4), 910–924. https://doi.org/10.1002/aic.690490410

Grace, J. R., Wairegi, T., & Brophy, J. (1978). Break-up of drops and bubbles in stagnant media. *The Canadian Journal of Chemical Engineering*, *56*(1). https://doi.org/10.1002/cjce.5450560101

Guevara, M. A., Guevara, F. A., & Belalcazar, L. C. (2018). Experimental Data and New Binary Interaction Parameters for Ethanol- Water VLE at Low Pressures Using NRTL and UNIQUAC. *TECCIENCIA*, *8*(24), 17–26. https://doi.org/http://dx.doi.org/10.18180/tecciencia.2018.24.3.

Guevara, M., & Belalcazar, L. (2017). NGL supersonic separator: modeling, improvement, and validation and adjustment of k-epsilon RNG modified for swirl flow turbulence model. *Revista Facultad de Ingeniería*, *82*, 82–93. https://doi.org/10.17533/udea.redin.n82a11

Higbie, R. (1935). The rate of absorption of a pure gas into a still liquid during short periods of exposure. *Transactions of the American Institute of Chemical Engineers*, *35*, 365–389.

Ishii, M., & Zuber, N. (1979). Drag coefficient and relative velocity in bubbly, droplet or particulate flows. *AIChE Journal*, *25*(5), 843–855. https://doi.org/10.1002/aic.690250513

Kataoka, I., & Serizawa, A. (1989). Basic equations of turbulence in gas-liquid two-phase flow. *International Journal of Multiphase Flow*, *15*(5). https://doi.org/10.1016/0301-9322(89)90045-1

Kockmann, N. (2014). 200 Years in Innovation of Continuous Distillation. *ChemBioEng Reviews*, *1*(1), 40–49. https://doi.org/10.1002/cben.201300003

Krishna, R., Urseanu, M. I., Van Baten, J. M., & Ellenberger, J. (1999). Rise velocity of a swarm of large gas bubbles in liquids. *Chemical Engineering Science*, *54*(2), 171–183. https://doi.org/10.1016/S0009-2509(98)00245-0

Krishna, R., Van Baten, J. M., Ellenberger, J., Higler, A. P., & Taylor, R. (1999). CFD simulations of sieve tray hydrodynamics. *Chemical Engineering Research and Design*, *77*(7), 639–646. https://doi.org/10.1205/026387699526575

Lamont, J. C., & Scott, D. S. (1970). An eddy cell model of mass transfer into the surface of a turbulent liquid. *AIChE Journal*, *16*(4). https://doi.org/10.1002/aic.690160403

Li, X., Yang, N., Sun, Y., Zhang, L., Li, X., & Jiang, B. (2014). Computational fluid dynamics modeling of hydrodynamics of a new type of fixed valve tray. *Industrial and Engineering Chemistry Research*, *53*(1), 379–389. https://doi.org/10.1021/ie400408u

Yanagi, T., & Sakata, M. (1982). Performence of a comercial scale 14% hole area sieve tray. *Industrial & Engineering Chemistry Process Design and Development*, *21*(4), 712–717. https://doi.org/https://doi.org/10.1021/i200019a029

Malvin, A., Chan, A., & Lau, P. L. (2014). CFD study of distillation sieve tray flow regimes using the droplet size distribution technique. *Journal of the Taiwan Institute of Chemical Engineers*, *45*(4), 1354–1368. https://doi.org/10.1016/j.jtice.2014.01.002

Noriler, D., Barros, A. A. C., Wolf Maciel, M. R., & Meier, H. F. (2010). Simultaneous momentum, mass, and energy transfer analysis of a distillation sieve tray using CFD techniques: Prediction of efficiencies. *Industrial and Engineering Chemistry Research*, *49*(14), 6599–6611. https://doi.org/10.1021/ie9013925

Noriler, D., Meier, H. F., Barros, A. A. C., & Wolf Macel, M. R. (2009). Prediction of efficiencies through simultaneous momentum, mass and energy transfer analyses in a distillation sieve tray by CFD techniques. In *Computer Aided Chemical Engineering* (Vol. 27, Issue C). Elsevier Inc. https://doi.org/10.1016/S1570-7946(09)70415-8

Olujić, Ž., Jödecke, M., Shilkin, A., Schuch, G., & Kaibel, B. (2009). Equipment improvement trends in distillation. *Chemical Engineering and Processing: Process Intensification*, *48*(6), 1089–1104. https://doi.org/10.1016/j.cep.2009.03.004

Rahimi, M. R., Rahimi, R., Shahraki, F., & Zivdar, M. (2006). Prediction of temperature and concentration distributions of distillation sieve trays by CFD. *Tamkang Journal of Science and Engineering*, *9*(3), 265–278.

Rahimi, R., Mazarei Sotoodeh, M., & Bahramifar, E. (2012). The effect of tray geometry on the sieve tray efficiency. *Chemical Engineering Science*, *76*, 90–98. https://doi.org/10.1016/j.ces.2012.01.006

Rahimi, R., Rahimi, M., Shahraki, F., & Zivdar, M. (2006). *Prediction of Temperature and Concentration*. *152*, 220–229.

Ranz, W. E., & Marshall, W. R. (1952). Evaporation from drops. Parts I & II. *Chem. Eng. Progr*, *48*(22).

Schiller, L., & Naumann, Z. (1935). A drag coefficient correlation. In *Z.Ver.Deutsch.Ing* (Vol. 77, Issues 13–14). https://doi.org/10.1016/j.ijheatmasstransfer.2009.02.006

Sun, Z. M., Yu, K. T., Yuan, X. G., & Liu, C. J. (2007). A modified model of computational mass transfer for distillation column. *Chemical Engineering Science*, *62*(7), 1839–1850. https://doi.org/10.1016/j.ces.2006.12.021

Treybal, R. E. (1981). Mass Transfer Operations 3th edition. In *McGraw-Hill*.

Van Baten, J. M., & Krishna, R. (2000). Modelling sieve tray hydraulics using computational fluid dynamics. *Chemical Engineering Journal*, *77*(3), 143–151. https://doi.org/10.1016/S1385-8947(99)00164-3

Versteeg, H. K., & Malalasekera, W. (1995). An Introduction to Computational Fluid Dynamics The Finite Volume Method. In *Fluid flow handbook. McGraw-Hill …*. Longman Scitific & Technical. https://doi.org/10.2514/1.22547

Wang, T., Wang, J., & Jin, J. (2004). An efficient numerical algorithm for "A novel theoretical breakup kernel function of bubble/droplet in a turbulent flow." *Chemical Engineering Science*, *59*(12), 2593–2595. https://doi.org/10.1016/j.ces.2004.03.011

Appendix A. Employed User-Defined Functions

UDF of Higbie theory model

```
#include "udf.h"
#define SCT 0.7 /* turbulent Schmidt number */
#define DMP 1.46e-9 /* m2/s estimation of MetOH molecular diffusion coefficient at 20°C*/
#define pi 3.14159
#define PMM 32 /* molecular weight methanol */
#define PMP 60 /* molecular weight propanol */

DEFINE_MASS_TRANSFER (Higbie, cell, thread, from_index, from_species_index, to_index,
to_species_index)
{
	real kl, Sh, Sc, Re,diam;
	real NV_VEC(V), vel,a;
	Thread *gas, *liq;
	liq = THREAD_SUB_THREAD(thread, from_index);
	gas = THREAD_SUB_THREAD(thread, to_index);
	diam=C_PHASE_DIAMETER(cell,gas);

	/*Calculation of relative velocity for Reynolds number calculation*/
	NV_DD(V,=,C_U(cell,gas),C_V(cell,gas),C_W(cell,gas),
		-,C_U(cell,liq),C_V(cell,liq),C_W(cell,liq));

	vel=NV_MAG(V);
	Re=RE_NUMBER(C_R(cell,liq),vel,diam,C_MU_L(cell,liq));
	Sc= C_MU_L(cell,liq)/(C_R(cell,liq)*DMP);

	Sh=1.13* pow(Re,0.5)*pow(Sc,0.5); /*Higbie correlation based on Sherwood number*/

	kl=Sh*DMP/diam; /* Higbie correlation providing mass transfer coefficient*/

	a=(6*C_VOF(cell,gas)*C_VOF(cell,liq)/diam); /* calculation of interfacial area */

	return (kl*a);
}

DEFINE_MASS_TRANSFER (Higbie2, cell, thread, from_index, from_species_index, to_index,
to_species_index)
{
	real kl, Sh, Sc, Re, diam;
	real NV_VEC(V), vel, a;
	Thread* gas, * liq;
	gas = THREAD_SUB_THREAD(thread, from_index);
	liq = THREAD_SUB_THREAD(thread, to_index);
	diam = C_PHASE_DIAMETER(cell, gas);

	/*Calculation of relative velocity for Reynolds number calculation*/
	NV_DD(V, =, C_U(cell, gas), C_V(cell, gas), C_W(cell, gas),
		-, C_U(cell, liq), C_V(cell, liq), C_W(cell, liq));

	vel = NV_MAG(V);
	Re = RE_NUMBER(C_R(cell, liq), vel, diam, C_MU_L(cell, liq));
	Sc = C_MU_L(cell, liq) / (C_R(cell, liq) * DMP);

	Sh = 1.13 * pow(Re, 0.5) * pow(Sc, 0.5); /*Higbie correlation based on Sherwood number*/

	kl = Sh * DMP / diam; /* Higbie correlation providing mass transfer coefficient*/
```

```
	a = (6 * C_VOF(cell, gas) * C_VOF(cell, liq) / diam); /* calculation of interfacial area */

	return (kl * a);
}
```

UDF of equilibrium ratio model

```
DEFINE_MASS_TRANSFER (equi_ratiometoh, cell, thread, from_index, from_species_index, to_index,
to_species_index)
{
	real keq, x_frac, y_frac;
	Thread* gas, * liq;
	liq = THREAD_SUB_THREAD(thread, from_index);
	gas = THREAD_SUB_THREAD(thread, to_index);

	x_frac = (C_YI(cell, liq, 0) / PMM) / ((C_YI(cell, liq, 0) / PMM) + ((1-C_YI(cell, liq, 0))/PMP));
	y_frac = (5.5528 * pow(x_frac, 3)) - (2.0615 * pow(x_frac, 4)) - (5.8529 * pow(x_frac, 2)) + (3.35
* x_frac) + 0.0053;

	keq = x_frac / y_frac; /*fraccion de equilibrio metOH*/

	return keq;
}

DEFINE_MASS_TRANSFER (equi_ratioproh, cell, thread, from_index, from_species_index, to_index,
to_species_index)
{
	real keq, x_frac, y_frac, x_fracproh, y_fracproh;
	Thread* gas, * liq;
	gas = THREAD_SUB_THREAD(thread, from_index);
	liq = THREAD_SUB_THREAD(thread, to_index);

	x_frac = (C_YI(cell, liq, 0) / PMM) / ((C_YI(cell, liq, 0) / PMM) + ((1-C_YI(cell, liq, 0))/PMP));
	y_frac = (5.5528 * pow(x_frac, 3)) - (2.0615 * pow(x_frac, 4)) - (5.8529 * pow(x_frac, 2)) + (3.35
* x_frac) + 0.0053;

	x_fracproh = 1 - x_frac;
	y_fracproh = 1 - y_frac;

	keq = y_fracproh / x_fracproh;

	return keq;
}
```

Chapter 4

Heat and mass transfer study of the Top-Heat-Integrated distillation column (T-HIDiC) using CFD.

Highlights

- *Problem:* There is no availability experimental data for the validation of the hydrodynamics, heat and mass transfer of a sieve tray of a HIDiC Column in different operating and design conditions.
- *Contribution:* A CFD-based methodology to predict the hydrodynamic, heat and mass transfer behavior in a sieve tray of a HIDiC column in different operating and design conditions.
- This study developed a CFD model to analyze momentum, heat, and mass transfer in the separation of a propylene/propane system in a Top HIDiC.
- The CFD model was based on data from Aspen plus process simulations and used Ranz-Marshall approaches to represent heat transfer between phases and resistance in the gas phase.
- The model also employed Higbie's model to calculate the mass transfer coefficient and the Peng-Robinson thermodynamic equilibrium model to estimate the equilibrium ratio at the interface.
- The developed CFD model was used to evaluate three pairs of rectification stage and stripping stage, which are thermally integrated.
- Results of the model included phases distribution, temperature, vapor phase Murphree efficiency, concentration, and clear liquid height, demonstrating the potential of CFD models to analyze new and structurally complex units.

Abstract

Distillation is one of the most widely used separation techniques in chemical processes, this type of separation accounts for a large share of energy consumption worldwide. Process intensification strategies have led to alternative technologies such as Heat Integrated Distillation Columns (HIDiC), these units can reduce energy consumption in a significant fraction. The goal of this study is to develop a CFD model to analyze momentum, heat and mass transfer in the separation of propylene/propane system in a Top HIDiC. The initial and boundary conditions are based on data from Aspen plus process simulations. Ranz-Marshall approaches are used for the representation of the heat transfer between phases and resistance in the gas phase. The mass transfer coefficient was calculated with Higbie's model. The Peng-Robinson thermodynamic equilibrium model was implemented to estimate equilibrium ratio at the interface. The developed CFD model was used to evaluate three pairs of internal rectification stage plus external stripping stage, that are thermally integrated. These stages were selected as characteristic ones of the column. Phases distribution, temperature, vapor phase Murphree efficiency, concentration, and clear liquid height were obtained as results, showing the potentiality of CFD models to analyze new and structurally complex units.

Keywords: CFD; HIDiC; heat transfer modeling; mass transfer modeling; heat Integration.

4.1. Introduction

Distillation is one of the most widely used separation techniques in the chemical industry. Distillation units account for a large share of energy consumption worldwide; in that way, reduction of energy consumption is an important aspect since it is related to operating costs and carbon footprint of refined products. An alternative strategy to reduce energy losses and costs of chemical processes is based on the concept of energy integration. This approach, considered as a process intensification option for distillation units, employs heat and mass integration to reduce the number of equipment, and utilities associated with the operation (e.g. cooling or heating flow streams).

To improve thermodynamic efficiency, and based on the process intensification principles, a new concept of column distillation, HIDiC (Heat-Integrated Distillation Column) has been proposed (M. A. Gadalla, 2009; M. Nakaiwa et al., 2003). This column has a configuration that allows taking advantage of process heat integration. A HIDiC achieves diabatic operation by recompressing vapor with a low compression ratio, offering a high energy-saving potential. This configuration has become an attractive alternative for the separation of close boiling point mixtures (Olujic *et al.*, 2003), e.g., propylene-propane system (Rijke *et al.*, 2006).

In our previous work (Mancera *et al.*, 2008), based on exergetic analysis, a Top HIDiC (T-HIDiC) was selected as the better option for this system. This configuration considers fewer stages in stripping section which are heat integrated, one by one, with the upper stages of the rectification section, because of that there are some adiabatic stages at the rectification. Other studies present an analysis and optimization parameters for an ideal T-HIDiC column through comparative approaches with the conventional column scheme aiming to explore the potential energy savings of T-HIDiC units (Masaru Nakaiwa et al., 2001). In addition, studies developed at the University of Delft (Olujic *et al.*, 2003) showed a new concept for this setting, considering the internal heat integration as the key to reduce energy consumption in distillation columns. Later, a study regarding the reduction of CO_2 emissions and energy consumption by using columns with internal heat integration was performed (Gadalla *et al.*, 2006).

More recently, some works focused on design of HIDiC have been developed (Claumann *et al.*, 2015; Gadalla, 2009; Harvindran & Foo, 2021; Pulido, 2008; Shenvi *et al.*, 2011; Suphanit, 2010). These studies have been performed using traditional flow-sheet simulators such as Aspen Plus® and Aspen Hysys® to predict the performance of these columns, and they do not bring detailed information about the phenomena taking place within the equipment, because of hydraulics, heat and mass transfer, and the related effects of the geometry in the performance were not considered.

Computational fluid dynamic (CFD) approach has been implemented to research the fluid dynamic behavior (Ashrafizadeh *et al.*, 2013; Gesit *et al.*, 2003; Krishna *et al.*, 1999; Li *et al.*, 2014; Malvin *et al.*, 2014; Van Baten & Krishna, 2000), as well as heat and mass transfer in a detailed quantitative way (Abbasnia *et al.*, 2019; Noriler *et al.*, 2010; Rahimi *et al.*, 2006; Sadripour *et al.*, 2012; Sun *et al.*, 2007; Wang *et al.*, 2004). However, only basic HIDiC configuration has been studied using CFD, it considered heat transfer in the solid structure of an only stage, leaving aside the interphase heat and mass transfer (Pulido *et al.*, 2010).

The present study aims to develop a CFD model for HIDiC units and to use it for analyzing the separation of propylene/propane. The specific column configuration is a

Top HIDiC (T-HIDiC) as is suggested in a previous study (Mancera *et al.*, 2018). Results obtained with this model will lead to detailed information on the integrated column operation. Initially, a conventional process simulation was performed, this allows to obtain temperature and concentration profiles, and vapor and liquid flow to estimate boundaries and initial conditions for the CFD analysis of the column. As final results, phases distribution, temperatures, Murphree efficiency, concentrations and clear liquid height were obtained for three characteristic stages of the column.

4.2. T-HIDiC columns

T-HIDiC columns have the typical elements of a conventional distillation column: rectification zone, stripping zone, condenser (C), and reboiler (R); The main difference lies in its geometrical configuration and the use of a compressor (CP) and an expansion valve (V) to achieve internal heat integration. The compressor and valve are used to generate pressure and temperature gradients required for the operation. Figure 4-1 shows the process scheme of the T-HIDiC unit.

The equipment configuration is based on a two concentric columns arrangement, in which the rectifying section is placed in the inner column, and the stripping one in the outer space, this characteristic allows the reduction of heat load in reboiler and condenser. The feed stream (F) enters the column through the top of the stripping zone. The special operational characteristic of HIDiC is the stream leaving the stripping zone (VD) is compressed to raise its temperature before entering the rectification section at its bottom; while, the liquid exiting the bottom of the column (LR) expands before entering the stripping zone.

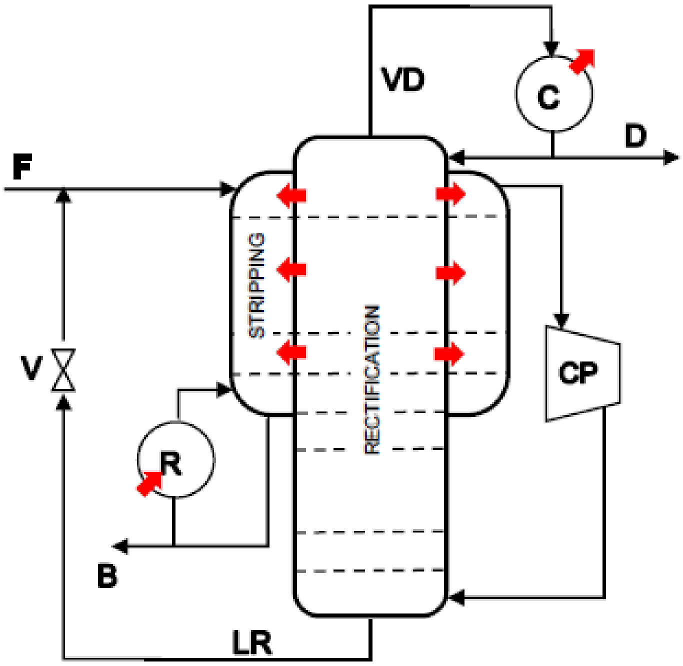

Figure 4-1: T-HIDiC (Top-Heat-Integrated Distillation Column) scheme of process operation.

4.3. CFD and mass transfer model

The approach of continuous liquid phase based on the small density and small spatial scales of the dispersed gas was used for the multiphase behavior. The two-equation turbulence RANS (Reynolds Averaged Navier Stokes) model for the liquid and vapor phase was used (Morel, 1995; Kataoka & Serizawa, 1989; Versteeg & Malalasekera, 1995). The momentum exchange is modeled to consider drag, lift, and virtual mass.

4.3.1. Flow equations

The implemented two-fluid approach considers both, vapor and liquid phases as continuous and their models are based on two sets of conservation equations which estimate mass, momentum, and energy. These equations are written for each phase as (Guevara, 2015; Heng & Tu, 2010; Versteeg & Malalasekera, 1995):

Continuity equation for liquid phase:

$$\frac{\partial(\alpha_L \rho_L)}{\partial t} + \nabla \cdot (\alpha_L \rho_L \boldsymbol{u}_L) = S_{LG} \tag{1}$$

Continuity equation for vapor phase:

$$\frac{\partial(\alpha_G \rho_G)}{\partial t} + \nabla \cdot (\alpha_G \rho_G \boldsymbol{u}_G) = -S_{LG} \tag{2}$$

Volume conservation equation:

$$\alpha_G + \alpha_L = 1 \tag{3}$$

Momentum equation for liquid phase:

$$\begin{aligned}\frac{\partial(\alpha_L \rho_L \boldsymbol{u}_L)}{\partial t} &+ \nabla \cdot (\alpha_L \rho_L \boldsymbol{u}_L \boldsymbol{u}_L) \\ &= -\alpha_L \nabla P + \nabla \cdot [\alpha_L \mu_L^e (\nabla \boldsymbol{u}_L + (\nabla \boldsymbol{u}_L)^T)] + \alpha_L \rho_L g + \boldsymbol{F}_{LG} \\ &+ (S_{LG} \boldsymbol{u}_G - S_{GL} \boldsymbol{u}_L)\end{aligned} \tag{4}$$

Momentum equation for vapor phase:

$$\begin{aligned}\frac{\partial(\alpha_G \rho_G \boldsymbol{u}_G)}{\partial t} &+ \nabla \cdot (\alpha_G \rho_G \boldsymbol{u}_G \boldsymbol{u}_G) \\ &= -\alpha_G \nabla P + \nabla \cdot [\alpha_G \mu_G^e (\nabla \boldsymbol{u}_G + (\nabla \boldsymbol{u}_G)^T)] + \alpha_G \rho_G g + \boldsymbol{F}_{GL} \\ &+ (S_{GL} \boldsymbol{u}_L - S_{LG} \boldsymbol{u}_G)\end{aligned} \tag{5}$$

The two terms at the left-side of Eq. 4 and 5 correspond to the momentum accumulation in the phase and the net momentum outlet from the phase. For the momentum exchange at the liquid-vapor interface, $\boldsymbol{F}_{LG}$, drag, lift, and virtual mass are considered:

$$\boldsymbol{F}_{LG} = \boldsymbol{F}_{LG}^{drag} + \boldsymbol{F}_{LG}^{lift} + \boldsymbol{F}_{LG}^{VM} = -\boldsymbol{F}_{GL} \tag{6}$$

where.

$$\boldsymbol{F}_{LG}^{lift} = C_l \alpha_G \rho_L (\boldsymbol{u}_G - \boldsymbol{u}_L)(\nabla \boldsymbol{u}_L) \tag{7}$$

$$\boldsymbol{F}_{LG}^{VM} = C_{VM} \alpha_G \rho_L \frac{D}{Dt}(\boldsymbol{u}_G - \boldsymbol{u}_L) \tag{8}$$

Energy equation for liquid phase:

$$\frac{\partial(\alpha_L \rho_L H_L)}{\partial t} + \nabla \cdot (\alpha_L \rho_L \boldsymbol{u}_L H_L) = -\nabla \cdot q - Q_{LG} - S_{LG}(H_L - H_G) \tag{9}$$

Energy equation for vapor phase:

$$\frac{\partial(\alpha_G \rho_G H_G)}{\partial t} + \nabla \cdot (\alpha_G \rho_G \boldsymbol{u}_G H_G) = -\nabla \cdot q + Q_{LG} + S_{LG}(H_L - H_G) \tag{10}$$

The first and second term on the left-hand side of the Eq. 9 and 10 are accumulation and convection energy respectively. The first term on the right-hand side is the conductive energy, the second is the rate of energy transfer between phases and the third is the energy transfer associated with the mass transfer between phases.

4.3.2. Drag Model

To model multiphase flows within the T-HIDiC unit, a set of correlations for interfacial forces were implemented to represent the interaction between the phases (Ishii & Zuber, 1979; Schiller & Naumann, 1935). The drag force, which is included in the momentum balances (Eqs. 4 and 5) as a component of the momentum exchange could be calculated using Eq. 11 (Krishna *et al.*, 1999).

$$\boldsymbol{F}_{LG}^{drag} = \frac{3C_D}{4d_b}\alpha_G\rho_L|\boldsymbol{u}_G - \boldsymbol{u}_L|(\boldsymbol{u}_G - \boldsymbol{u}_L) \tag{11}$$

where C_D is the drag coefficient suggested by Grace and coworkers (1976). The Grace model is well suited for gas-liquid flows in which the bubbles exhibit a range of shapes, such as the sphere, ellipsoid, and spherical cap (Grace *et al.*, 1976, 1978). The drag coefficients for different shapes of bubbles are calculated as:

$$C_D = \max\left(\min\left(\mathrm{C}_{\mathrm{D_{ellipse}}}, \mathrm{C}_{\mathrm{D_{cap}}}\right), \mathrm{C}_{\mathrm{D_{sphere}}}\right) \tag{12}$$

where

$$C_{D,sphere} = \begin{cases} 24/Re & Re < 0.01 \\ 24(1 + 0.15Re^{0.687})/Re & Re \geq 0.01 \end{cases} \tag{13}$$

$$C_{D,cap} = \frac{8}{3} \tag{14}$$

$$C_{D,ellipse} = \frac{4}{3}\frac{gd_b}{U_t^2}\frac{(\rho_L - \rho_G)}{\rho_L} \tag{15}$$

The Reynolds number for the bubbles, Re_b, and the U_t, are:

$$Re_b = \frac{\rho_L|\boldsymbol{u}_{G} - \boldsymbol{u}_L|d_b}{\mu_L} \tag{16}$$

$$U_t = \frac{\mu_L}{\rho_L d_b}Mo^{-0.149}(J - 0.857) \tag{17}$$

where Mo is the Morton number and J is given by a piecewise function, defined by:

$$Mo = \frac{\mu_L^4 g(\rho_L - \rho_G)}{\rho_L^2\sigma^3} \tag{18}$$

$$J = \begin{cases} 0.94Ha^{0.757} & 2 < Ha < 59.3 \\ 3.42Ha^{0.441} & Ha > 59.3 \end{cases} \tag{19}$$

Ha is defined by:

$$Ha = \frac{4}{3} Eo Mo^{-0.149} \left(\frac{\mu_L}{\mu_{ref}}\right)^{-0.14} \tag{20}$$

where $\mu_{ref} = 0.0009\, kg/(m.s)$ and Eo is the Eötvös number, defined by:

$$Eo = \frac{g(\rho_L - \rho_G) d_b^2}{\sigma} \tag{21}$$

4.3.3. Customized drag model

As presented in Grace *et al.* (1976), the model for the drag coefficient considers an unique bubble into the liquid phase and do not considers the multi-bubble interaction effect, because of that a correction of this coefficient must be included (this correction was analyzed in chapter 2). The value of the correction factor was estimated using experimental data of clear liquid height as function of the specific superficial gas velocity, and generates a corrected drag coefficient that replaces the one of equation 11:

$$C_{D,corr} = F_{corr} C_D \tag{22}$$

4.3.4. Heat exchange coefficient

The rate of energy transfer between phases, Q_{LG}, is a function of the temperature difference and the interfacial area, A:

$$Q_{LG} = \hat{h} A (T_G - T_L) \tag{23}$$

where $\hat{h}$, represent the heat transfer coefficient between phases and is determined by Ranz-Marshall's correlation (Ranz, 1952; Ranz & Marshall, 1952), based on Nusselt number, Nu:

$$Nu = \frac{\hat{h} L_G}{k_G} = 2 + 0.6 Re_G^{1/2} Pr^{1/3} \tag{24}$$

here k_G is the thermal conductivity of the gas phase, L_G is a characteristic length (such as the bubble diameter), Pr and Re_G are the Prandtl number and Reynolds number of the gas phase.

4.3.5. Species Mass Transfer

To model species mass transfer at the interphase, transport equations for each specie at each phase must be solved along with the mass, momentum, and energy equations.

The transport equations for the mass fraction for light component (LK), are (similar equations are developed for the heavy component):

Vapor phase:

$$\frac{\partial(\alpha_G \rho_G Y_{LK})}{\partial t} + \nabla \cdot (\alpha_G \rho_G \boldsymbol{u}_G Y_{LK}) = \nabla \cdot [\alpha_G \rho_G D_{LK,G} \nabla Y_{LK}] - S_{LG,LK} \tag{25}$$

Liquid phase:

$$\frac{\partial(\alpha_L \rho_L X_{LK})}{\partial t} + \nabla \cdot (\alpha_L \rho_L \boldsymbol{u}_L X_{LK}) = \nabla \cdot [\alpha_L \rho_L D_{LK,L} \nabla X_{LK}] + S_{LG,LK} \tag{26}$$

The interphase mass transfer term $S_{LG,LK}$ is the interphase mass transfer rate of the light component per unit volume. It is given by:

$$S_{LG,LK} = k_{LG} A (K \rho_L^{LK} - \rho_G^{LK}) \tag{27}$$

where

$$\frac{1}{k_{LG}} = \frac{1}{k_G} + \frac{K}{k_L} \tag{28}$$

A is the interfacial area per unit volume, K is the mole fraction equilibrium ratio ($y_e = K/x$), ρ_p^{LK} is the mass/volume concentration of the light component in the phase p (this is the nomenclature used in Fluent, and $\rho_p^{LK} = \rho_L * x_{LK}$), k_G and k_L are the volumetric individual film mass transfer coefficients of gas and liquid, respectively.

4.3.6. Mass Transfer model

Interphase species mass transfer is modeled using the two-resistance model from Ansys Fluent®. There are many theories available in the literature for the calculation of the mass transfer coefficient k_G and k_L (Lamont & Scott, 1970), however the most used are:

Penetration theory (Higbie, 1935):

$$k_L = \frac{2}{\sqrt{\pi}} \sqrt{\frac{D_{L,LK}}{t_{e,L}}} \qquad k_G = \frac{2}{\sqrt{\pi}} \sqrt{\frac{D_{G,LK}}{t_{e,G}}} \tag{29}$$

where $t_{e,L}$ and $t_{e,G}$ are the exposure time in each phase, calculated as:

$$t_{e,L} = \frac{d_b}{\boldsymbol{u}_{rise}} \qquad t_{e,G} = \frac{d_b}{\boldsymbol{u}_H} \tag{30}$$

where d_b is the bubble diameter, $\boldsymbol{u}_{rise}$ is the bubble slip velocity and $\boldsymbol{u}_H$ is the vapor velocity through the tray holes. Therefore, the expression for the local mass transfer coefficient is:

$$k_L = 2\Upsilon\sqrt{\frac{D_{L,LK}\boldsymbol{u}_{rise}}{\pi d_b}} \qquad k_G = 2\Upsilon\sqrt{\frac{D_{G,LK}\boldsymbol{u}_H}{\pi d_b}} \tag{31}$$

where Υ is a constant.

Ranz-Marshall Model (Ranz & Marshall, 1952):

The Ranz-Marshall model uses an analogous approach to that for the Ranz-Marshall heat transfer coefficient model, and it is based on the Sherwood number:

$$Sh = \frac{k_m L_G}{D_G} = 2 + 0.6 Re_G^{1/2} Sc_G^{1/3} \tag{32}$$

where k_m is the mass transfer coefficient in the gas phase, D_G is the diffusivity of the gas phase, L_G is a characteristic length (such as a bubble diameter), Sc_G and Re_G are the Schmidt and Reynolds number of the gas phase.

4.4. Simulation details

Two types of simulation were performed in this study to quantitatively analyze the operation of the T-HIDiC unit:

I. Conventional or classic process simulation (Aspen Plus®)
II. CFD Simulations (Ansys Fluent®)

4.4.1. Simulation in Aspen Plus

Conditions used for this setup of the process simulation are based on our previous work (Mancera *et al.*, 2018). The T-HIDiC unit was simulated using Aspen Plus 8.1. The Propylene-Propane system properties including vapor-liquid equilibrium data were estimated with Peng-Robinson's model. The simulations were performed in steady-state, using isentropic efficiency in the compressor, and avoiding heat flow between system and surroundings. To facilitate simulation in CFD, presented in the next section, a pilot plant scale column was considered (Mancera et al., 2018). Feed and product characteristics, as well as the main parameter for the T-HIDiC are shown in Table 4-1.

Table 4-1: Set up parameters for the process simulation of the T-HIDiC unit in equilibrium conditions.

Parameter	Value
Rectification section Pressure (bar)	14.6
Stripping section pressure (bar)	11.2
Stages rectification section	170
Stages stripping section	61
Feeding stage	171
Trays in the Concentric Column	169
Trays in the Annular column	60
Feed flow (kg/h)	112
Feed fraction mol (propylene)	0.57
Thermal condition food (q)	0.37
Distillate fraction mol (propylene)	0.996
Bottom product fraction mol (propylene)	0.011
Isentropic efficiency	0.72

The scheme selected for the heat distribution between rectification section and stripping section was the uniform heat transfer area using the procedure suggested by (Suphanit, 2010) which is summarized in Figure 4-2. Heat transfer was simulated through the thermal interconnected streams, tray by tray. After specifying the components and thermodynamic model, the column configuration was simulated as shown in Figure 4-3. To properly represent the heat and mass flows, the simulation is performed using two distillation columns, one for stripping column and another for rectifying column. However, the mechanical details of tray internal configuration in the T-HIDiC column cannot be properly specified, as a consequence, the that simulate the T-HIDiC, can represent different geometrical configurations, for instance: a concentric configuration with the rectifying column placed inside the stripping shell or a system with adjacent-two columns (Pulido *et al.*, 2011). The concentric arrangement and tray internal configuration for the analyzed T-HIDiC column are presented in the next section using CFD, which allows a full description and assessment of the phenomena within the unit.

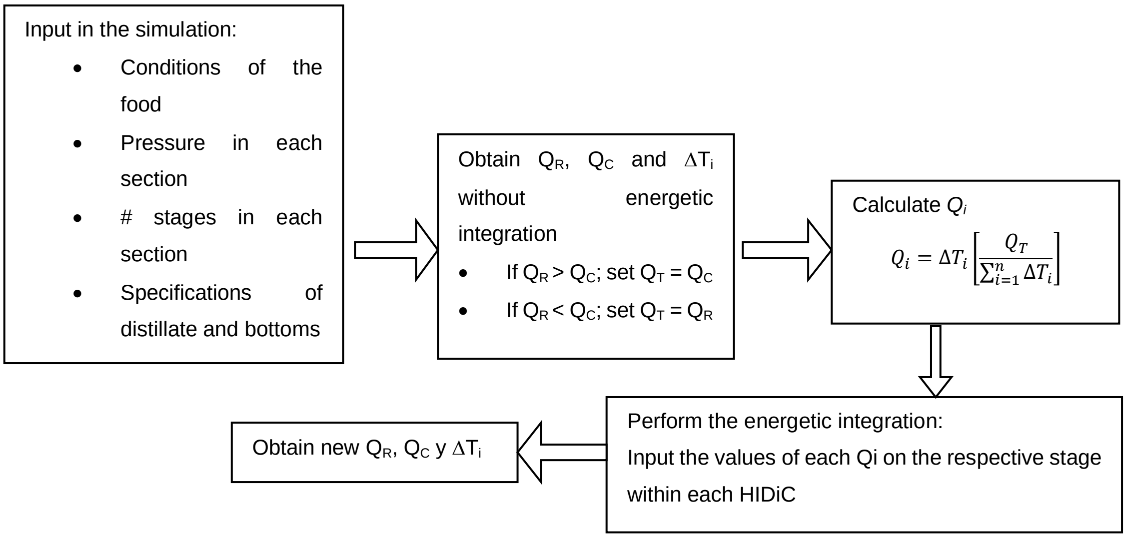

Figure 4-2: Procedure for estimation of heat flow distribution between rectification and stripping sections in the T-HIDiC.

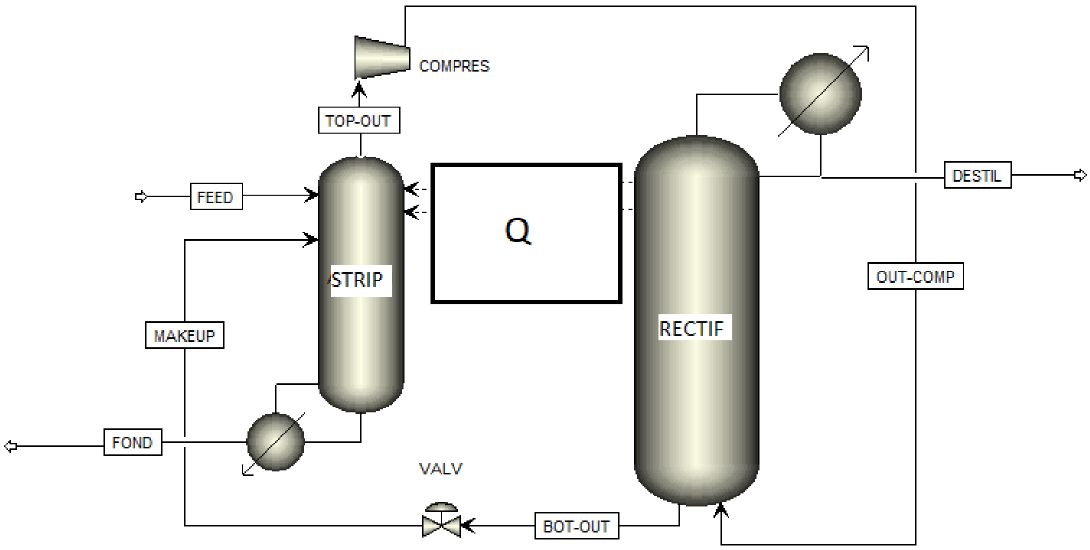

Figure 4-3: Simulation flowsheet for the T-HIDiC in Aspen Plus®

As mentioned above, the design of a T-HIDiC column is usually performed through flowsheet simulators. In this work, this approach is used to calculate initial values for vapor and liquid flows, temperature profiles, and the compressor, condenser, and reboiler duties. Part of these results were used to set the CFD model to study the heat and mass transfer in the concentric doble-tray of the T-HIDiC column.

4.4.2. CFD Simulation

For the geometrical configuration of the tray, concepts of distillation column design and data available in the literature for calculating the diameter of holes and landfills were used (Bernal et al., 2011; Kister, 1992; Lockett, 1986; Winkle, 1967). The mains details of the sieve tray used are reported in Table 4-2.

Table 4-2: Geometrical parameters of the T-HIDiC simulated trays.

Geometry	Stripping section	Rectification section
	Dimension	Dimension
Outside tray diameter	0.32 m	0.2 m
Inside Diameter tray	0.22 m	--
Tray spacing	0.2 m	0.2 m
Hole diameter	0.005 m	0.005 m
Weir height	10mm	10mm
% Bubbling area	82.46 %	82.46 %
% hole area	8.33 %	8.48 %
Solid material	Steel	Steel

Heat transfer between sections is considered using the heat content in the rectifying section to determine the heat transferred to the annular column that operates as a stripping section. This study does not consider exchangers or panels that would increase the heat transfer to the stripping section. The heat transfer at the tray body level is calculated by solving the heat transfer equation in the solid domain and the momentum equation in the fluid domain. The calculation of the heat transfer between phases was developed taking into account the Ranz-Marshall model to determine the heat coefficient (Ranz & Marshall, 1952).

Boundary conditions such as fluid flow rates, concentrations, pressure, and inlet temperatures were obtained based on the column process simulation described in the past section. The main advantage of using CFD simulation is the rigorous numerical analysis, allowing a detailed evaluation of gas and liquid flow inside the column and the mass transfer. An important challenge is the complexity of the internal configuration, which requires a detailed geometry and mesh development able to reproduce accurately the phenomena. These high mesh quality requirements increase computation effort.

The column section considered for the CFD simulation is shown in Figure 4-4. The internal volume is the rectifying section and the external one is the stripping one. This work is simulated within the two-phase Eulerian framework, with a standard k-epsilon model and three-dimensional transient (Khosravi Nikou & Ehsani, 2008; Riaño *et al.*, 2017; Versteeg & Malalasekera, 1995). The solution scheme for the pressure-velocity coupling scheme used is the SIMPLE algorithm, and for spatial discretization and the transient formulation, the first-order upwind approach was used (Khosravi Nikou & Ehsani, 2008).

a) b)

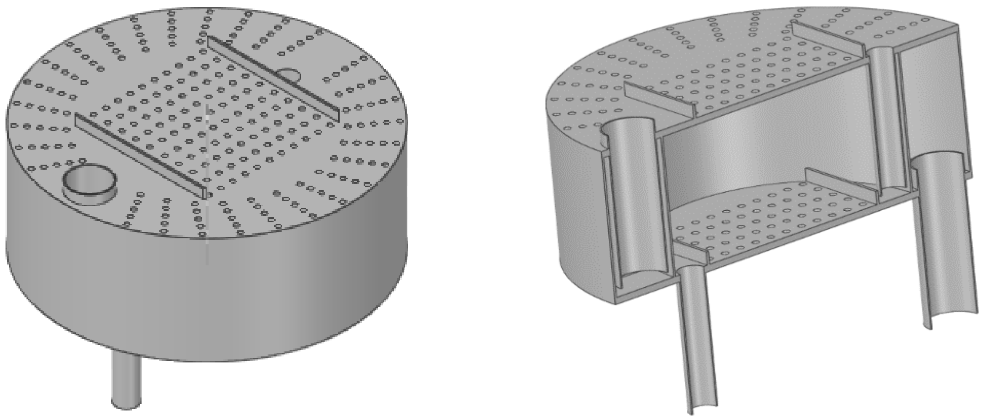

Figure 4-4: Geometry of the tray used for the CDF simulation of the T-HIDiC: a) Isometric view of the stage, b) Transversal section of the stage.

For the calculation of the temperature and concentration profiles of the liquid within the simulation domain, 7 equidistant points were established along a central line in each plate (annular and concentric) at a height of y = 4 mm (Figure 4-5), where the flow direction is from 1 to 7.

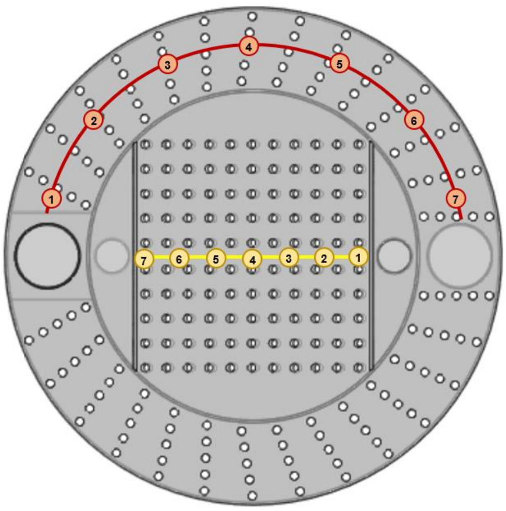

Figure 4-5: Sampling points to determine temperature and concentration profiles of liquid. Yellow points (rectification), red points (stripping).

Ansys Fluent 18.0® software was used for the CFD modeling, which allows three-dimensional analysis by specifying the configuration design of plate and column size scale and performing the calculations using finite volumes (ANSYS, 2021; ANSYS Release 19, 2018). This strategy provided comprehensive modeling to calculate velocity, pressure field, concentration, and temperature profiles.

The transport equations for additional scalars are assumed to have the form of the general scalar convective-diffusion equation. The absolute convergence criteria for the simulations was $1x10^{-3}$ for most variables except for volume fraction and concentrations which was $1x10^{-6}$.

For the time-dependent term, implicit first-order backward time differencing was used with a fixed time step of $3x10^{-4}$s. Simulations were run with an underrelaxation factor of 0.8. Values from these CFD simulations were obtained after averaging over a sufficiently long-time interval once quasi-steady-state conditions were established. The time for each simulation takes around 25 days, on a Dell Intel Xeon W3530 2.8GHz, being a highly expensive simulation.

The mesh and sub mesh used for the CFD simulations is shown in Figure 4-6. The number of cells and type of element are shown in Table 4-3 for the total mesh and the sub meshes. For this case of study, the type of element used guarantees the maximum mesh quality and minimizes the convergence errors due to mesh configuration. Detailed boundary conditions location Figure 4-7, and the main characteristics of the boundaries considered for the CFD model are shown in Figure 4-8.

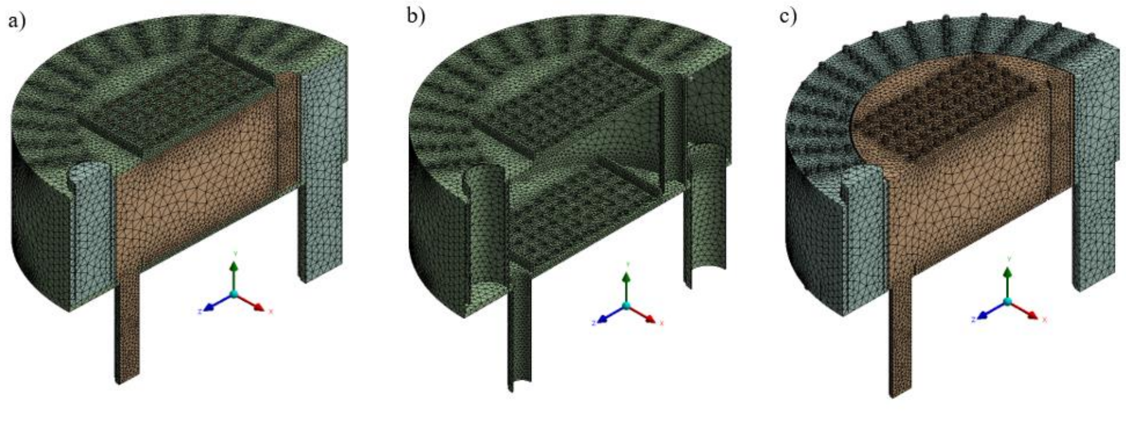

Figure 4-6: Tetrahedral mesh developed for the CFD analysis of the T-HIDiC trays, several meshes with contact faces were used: a) whole domain, b) solid and c) fluid.

Table 4-3: Mesh and submesh characteristics.

Type of geometry	Type of cell	Number of cells
3D	Unstructured Tetralateral Min ($1x10^{-4}$m) Max ($1x10^{-2}$m)	570000
Solid submesh		120000
Fluid Submesh		450000

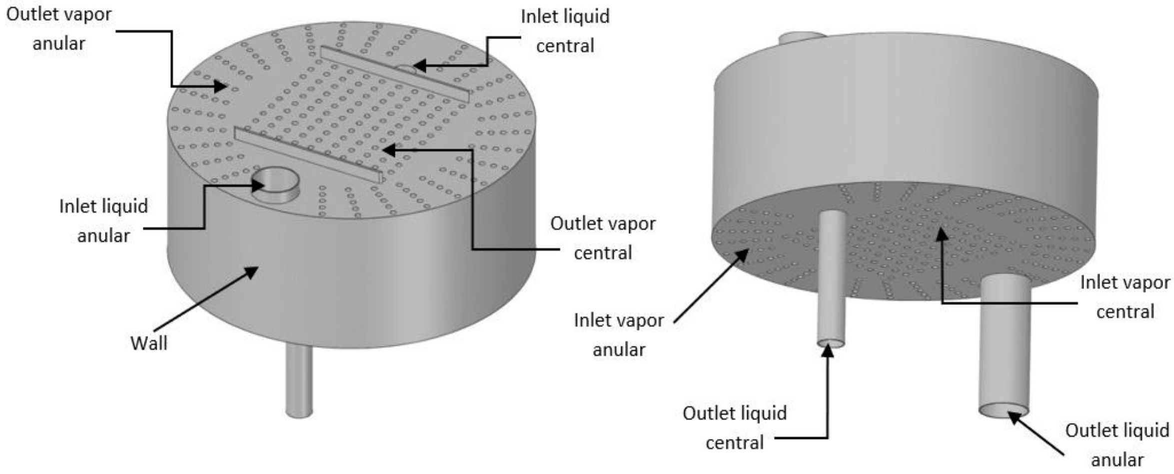

Figure 4-7: Location of the boundaries of the HIDiC stage considered for the CFD model in the system geometry.

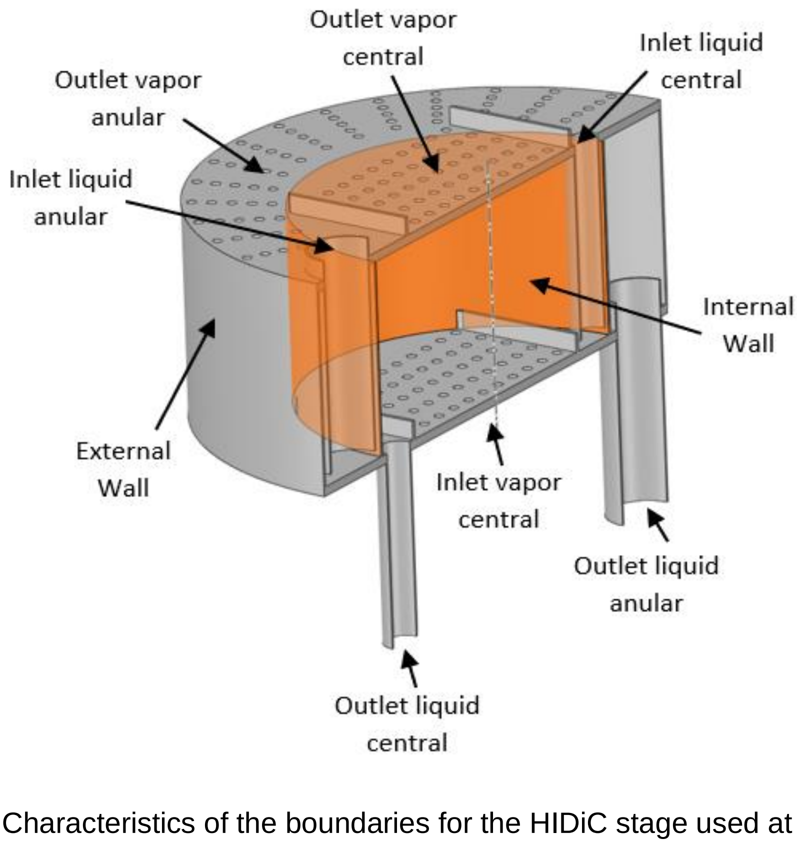

Figure 4-8: Characteristics of the boundaries for the HIDiC stage used at CFD model.

4.5. Methodology

In this research, for CFD simulations a two steps methodology was established:

1. Classical process simulation of the T-HIDiC unit under thermodynamic equilibrium conditions. The objective of this stage is to obtain the macroscopic conditions for each tray (flows, temperature, concentrations, equilibrium ratio), these will be used to set up the boundary and initial conditions in CFD simulations.

2. CFD simulation of the T-HIDiC unit under non-equilibrium conditions. The objective of this second step is to obtain the conditions for three characteristic trays of the HIDiC column considering non-equilibrium conditions, these results are used to estimate two types of data: thermodynamic results (concentration profile, temperature profile, and Murphree Efficiency), and hydrodynamical results (height of clear liquid).

4.5.1. Process simulation of the T-HIDiC unit under thermodynamic equilibrium conditions

The T-HIDiC is initially simulated using the equilibrium conditions with the classical process simulation approach on Aspen Plus®. This process simulation was implemented aiming to get the input values for the CFD model (Table 4-1). The results of this stage were also used for the estimation of the heat transfer rate from the rectification zone to the stripping zone (Figure 4-3). The results at stages 2, 30, and 59 in the stripping section and their respective rectifying stages (stages 3, 31, and 60) are used for the setting up of the boundary and initial conditions of the CFD simulations described in the following section (Table 4-4).

4.5.2. Evaluation under non-equilibrium conditions: CFD modeling

From Aspen Plus simulation, liquid and vapor inlet conditions corresponding to velocities, concentrations, and temperatures were taken at the above mentioned trays (2, 30, and 59 for stripping section and 3, 31, and 60 for rectification section), as well as the equilibrium ratio, and used as initial and boundary conditions for the simulation in CFD.

Using the results, the liquid and vapor inlet operation parameters required for the set-up of the CFD model were established.

These trays were selected for the CFD modeling since they represent the operation of the upper, middle, and bottom region of the stripping column (the shortest section) leading to a general overview of the whole column. Table 4-4 describes the general characteristics of the boundary conditions, and Table 4-6 summarizes the setup used for the CFD simulations of the HIDiC, for the general analysis of this unit under non-equilibrium conditions. With CFD results, Murphree efficiency and height of the clear liquid were determined. Additionally, the results regarding concentration, temperature, and velocity profiles were compared with those obtained from the classic process simulation.

Table 4-4: Boundary conditions used for the CFD simulation.

Boundary Conditions	Property	Gas-phase volume fraction
Liquid inlet	Uniform profile $U_{L,in} = \frac{Q_L}{h_{DC}L_w}$	0
Gas inlet	$V_{hole} = \frac{V_S A_B}{N_H A_{hole}}$	1
Liquid outlet	Pressure outlet	1
Gas outlet	Pressure outlet	1
Wall	No-slip wall	Grad=0

Table 4-5: Set up for the CFD simulations of the HIDiC stages.

Characteristic	Set up
System	Propylene-Propane
Geometry	3D
Multiphase Models	Eulerian two phases
Phase interactions	Virtual Mass Modified Drag (grace model) Mass: two mass transfer mechanisms → model options: equilibrium ratio Liquid Mass transfer coefficient model: Higbie (UDF) Gas Mass transfer coefficient model: Ranz-Marshall
Surface Tension	Constant: 0.007 N/m
Viscous Model	Standard k-epsilon

4.6. Results and discussion

4.6.1. Classic process simulation

From the first approach under equilibrium conditions, the results obtained regarding temperature and concentration profiles, vapor and liquid flow, and the compressor, condenser, and reboiler duties were obtained. The predicted temperature and concentration profiles for the T-HIDiC unit under equilibrium conditions are presented in figures 4-9 and 4-10. Similarly, the estimated vapor and liquid flows are plotted in Figure 4-11.

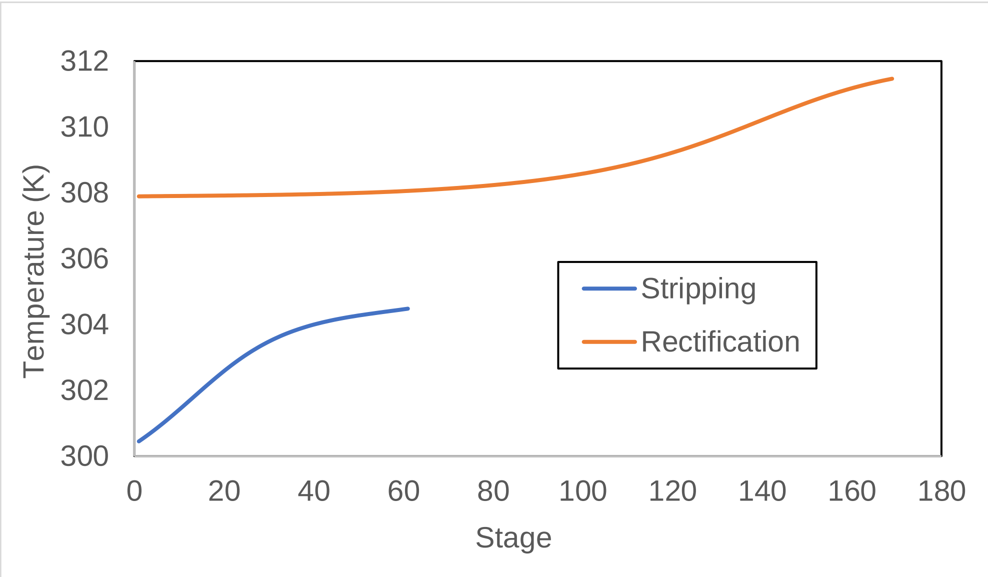

Figure 4-9: Temperature profiles of thermally coupled sections of T-HIDiC obtained from process simulation under equilibrium conditions for the two main sections of the unit: stripping and rectification.

Temperature difference between the rectifying and stripping sections represents the driving force for heat exchange. From these profiles, we observe that the potential of heat transfer between the two sections is greater at the top of the column. This temperature difference is mainly generated by the pressure difference between the two sections. The T-HIDiC column contains 61 stages for stripping section and 160 stages for rectification one; this configuration allows to obtain the purities for propylene and propane, 99.63% and 98.9% in molar base, respectively (Table 4-7).

The target molar fraction for the products (distillate and bottoms) were reached (Figure 4-10 and Table 4-7), however, an asymptotic behavior is observed in the upper 40 stages of the rectification column, this is because to reach the desired distillate composition, ($x_{propylene} = 0.996$), in a system with very low relative volatility, as our case study, a column with a very high stage number is necessary and the composition change from a stage to the next one must be very small, specially at the column ends

.

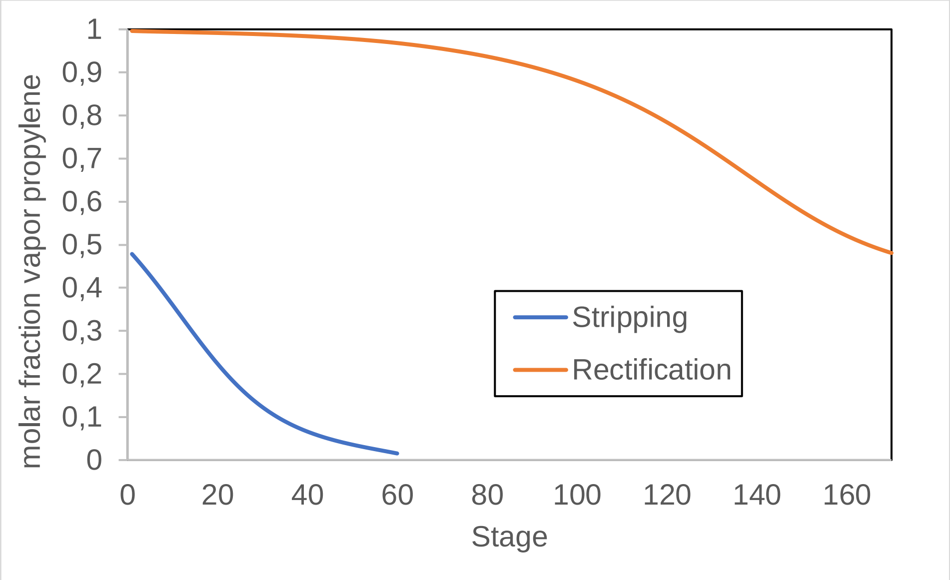

Figure 4-10: Concentration profiles for stripping and rectification sections of T-HIDiC obtained from process simulation under equilibrium conditions.

As an effect of the heat transfer from rectification trays to stripping ones, it can be seen in figure 4-11a that vapor flow decreases as it goes up in the rectification section; in the other way, in the stripping section vapor increases as it goes up. From stage 61 to 170, in the rectification section, the flow remains almost constant since in this portion heat exchange is not considered. Regarding the liquid flow, figure 4-11b shows a behavior similar to that of the vapor flow with an almost constant flow from stage 61 to 170 in the rectification zone. This behavior is consistent with the effect of the internal heat transfer.

a)

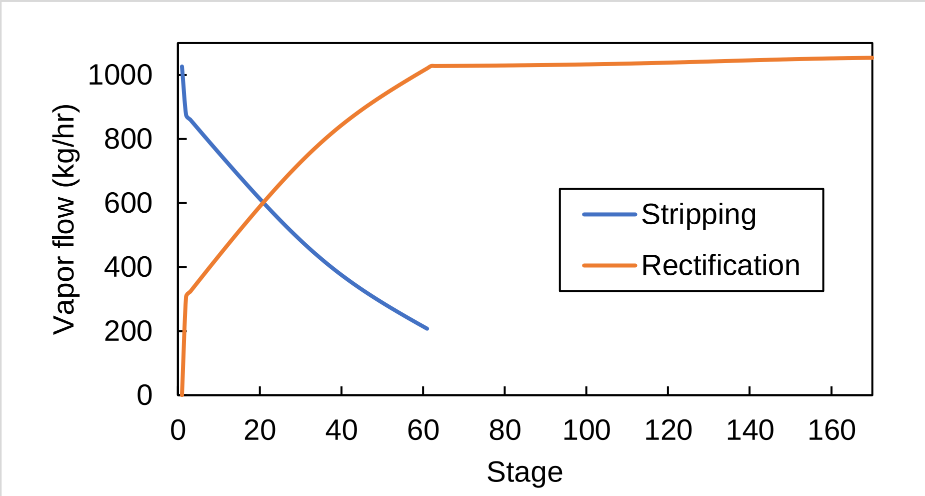

b)

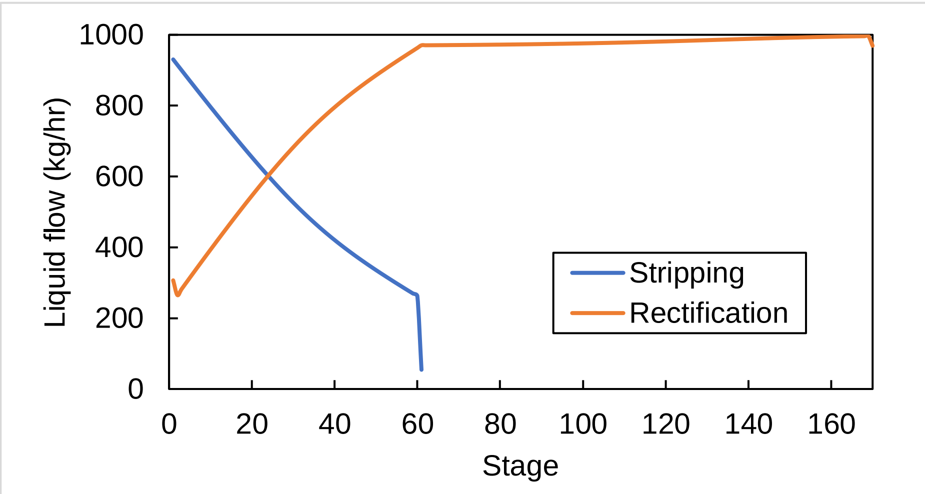

Figure 4-11: Flows estimated with the process simulation for the T-HIDiC under equilibrium conditions: a) Liquid flow profile, b) Vapor flow profile.

The desired distillate and bottom compositions were obtained with the energy requirements supplied in the compressor and reboiler and the energy withdrawal of the condenser (Table 4-6), it is noteworthy that the amount of energy supplied in the reboiler is about 8.2kW lower than that withdrawn in the condenser due to the effect of energy interaction on the entire stripping column and the first 60 trays of the rectification column.

Table 4-6: Condenser and reboiler duties, and product composition obtained from process simulation under equilibrium conditions

Operation condition	**Value**
Reboiler duty (kW)	18.8085
Condenser duty (kW)	26.9966
Compressor power (kW)	4.8756
Compressor efficiency	0.72

Operation condition	Value
Boilup ratio	3.82
Reflux ratio	4.31
Heat transfer (kW) Rectif. → Stripp.	63.29
Composition distillate (propylene)	0.996
Composition bottom (propane)	0.989

Results obtained from Aspen plus to be used in the CFD simulation are shown in Table 4-7 for trays 3, 31, 60 of the rectification column and trays 2, 30, and 59 of the stripping column. Equilibrium ratios are close to unity, resulting in very low relative volatility (α= [1.1 – 1.2]), which is a sign of the difficulty in separating this system.

Table 4-7: Values of boundary conditions for CFD simulation at selected HIDiC stages.

Area	Section	Stage	Inlet liquid composition (C3= molar fraction)	Inlet vapor composition (C3= molar fraction)	Inlet velocity liquid (m/s)	Inlet velocity vapor (m/s)	Inlet liquid temperature (K)	Inlet vapor temperature (K)	Molar equilibrium ratio Vapor/Liquid	
									Propylene (C3=)	Propane (C3)
upper	Rectification	3	0,9956	0.9954	0.4781	1.3961	307.8913	307.8944	1.0003	0.9168
	Stripping	2	0,4406	0.4544	0.4602	3.6125	300.4481	300.6408	1.0887	0.9335
middle	Rectification	31	0,9878	0.9881	1.2071	3.0453	307.9298	307.9338	1.0011	0.9166
	Stripping	30	0,1118	0.1156	0.2716	1.960	303.4091	303.5473	1.1734	0.9796
bottom	Rectification	60	0,9666	0.9671	1.7241	4.1949	308.0373	308.0499	1.0030	0.9164
	Stripping	59	0,0161	0.0154	0.1403	0.8896	304.4227	304.4599	1.2022	0.9970

4.6.2. CFD simulation

The formulated CFD model for the simulations under non-equilibrium conditions of the HIDiC unit was used for a detailed analysis of the heat integration in near-real conditions of three representative trays of the column.

4.6.2.1. Phase volume Fraction

Vapor phase volume fraction is shown in Figure 4-12, it can be seen that the larger volume inside the trays is take up by the vapor phase.

At the top of the tray, the liquid volume fraction is close to zero and increases going down, this operation pattern is observed for all three simulated stages. Comparing the behavior of the tree trays it can be seen a higher phases differentiation and less turbulence as the vapor flow decreases (from bottom to upper). This observation must be related with a higher drag tendency (more liquid in the space over the wire) in the bottom of the rectification, which supports the importance of CFD analysis for design of non-conventional columns.

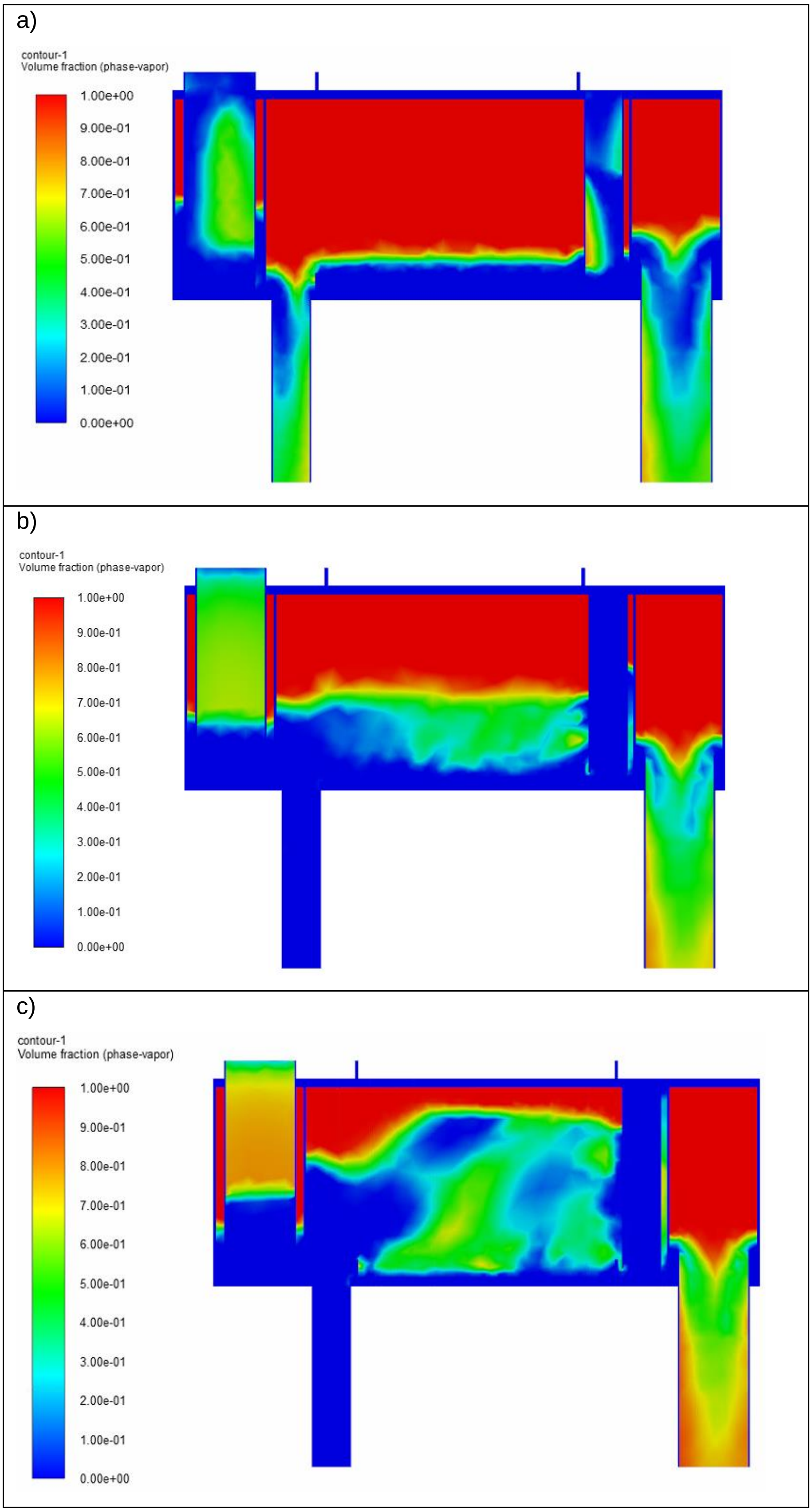

Figure 4-12: Phase volume fraction obtained from the CFD simulations at the three sections of HIDiC: a) upper section, b) middle section and c) bottom section

4.6.2.2. Temperature

Using the CFD results, temperature contours for solid structure and liquid phase in the three simulated trays under non-equilibrium conditions could be analyzed.

Temperature of the tray's structure

The temperature contours of the tray surface are shown in figures 4-13, 4-14, and 4-15. Figure 4-13 shows the temperature contours for the tray at the upper section, including both rectification and stripping sides of the unit respectively. The temperature distribution in the rectification section decreases from 307.89 K at the gas inlet to 306 K at the gas outlet. In the case of the stripping section, where the heat is obtained from the rectification section, it can be seen an increase of the temperature from 300 K in the liquid inlet to 304 K at the internal wall without direct contact with liquid.

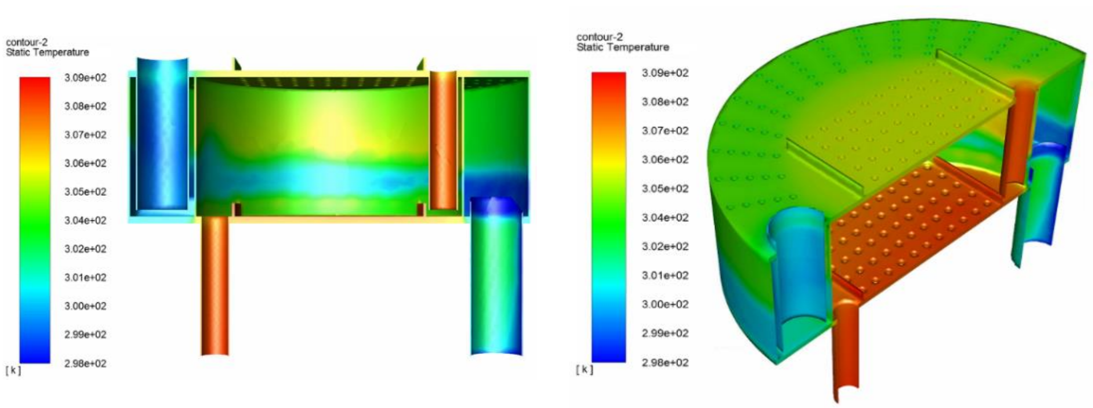

Figure 4-13: Temperature contours for the tray at the upper section, including both rectification and stripping sides of the HIDiC

Figure 4-14 shows temperature contours for the tray at the middle section, and Figure 4-15 for the bottom section. The rectifying section transfers heat to the stripping section, this exchange of heat is main driven by convection heat transfer of the fluid phases flowing. In Figure 4-14 the temperature in the rectification section decreases from 307.93 K at the gas inlet to 305 K at the outlet gas. In the case of the stripping section, the behavior described in the plate above (upper zone), is also observed, where the temperature increases from 303 K in the liquid inlet to 306 K at the internal wall.

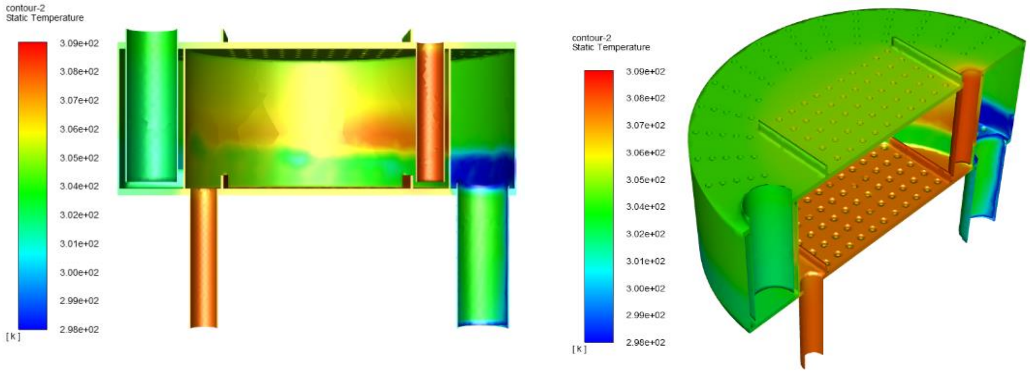

Figure 4-14: Temperature contours for the tray of the middle section, including both rectification and stripping sides of the HIDiC.

In Figure 4-15 the temperature distribution in the rectification section decreases from 308.04 K at the gas inlet to 306 K at the outlet gas. In the case of the stripping section, the temperature increases from 304 K at the liquid inlet to around 305 K at the internal wall.

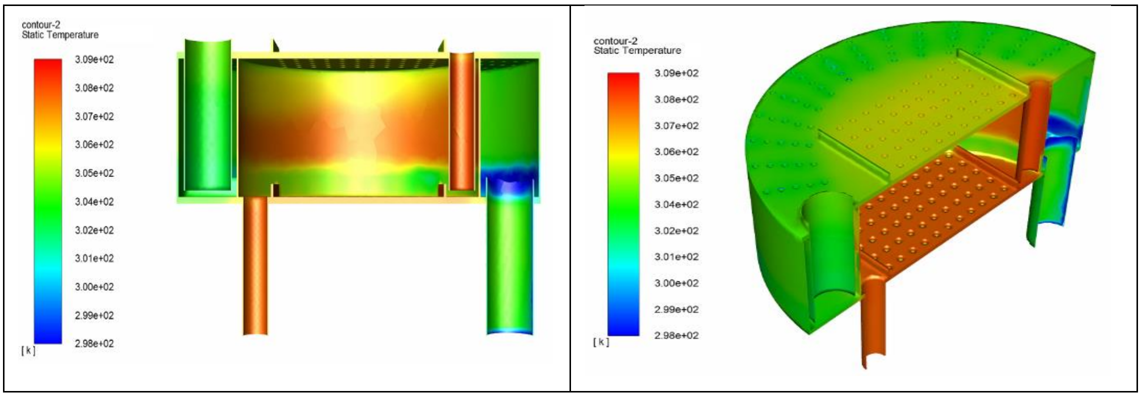

Figure 4-15: Temperature contours for the tray at the bottom section, including both rectification and stripping sides of the HIDiC

A low-temperature difference between rectifying and stripping section was observed, it is found in T-HIDiC column according to the literature (Sun *et al.*, 2003). This leads to a large heat transfer area requirement for the stage, and the T-HIDiC design should allow for large heat transfer area inside the column. Therefore, future studies must be focused on the development of internals panels in the stripping section that allow a more efficient heat distribution inside of the concentric column configuration.

Temperature of the liquid on the plate

According to the sampling points defined in the methodology (Figure 4-5), the temperature profile for liquid at a height of 4mm (y = 4mm) is presented in Figure 4-16.

a)

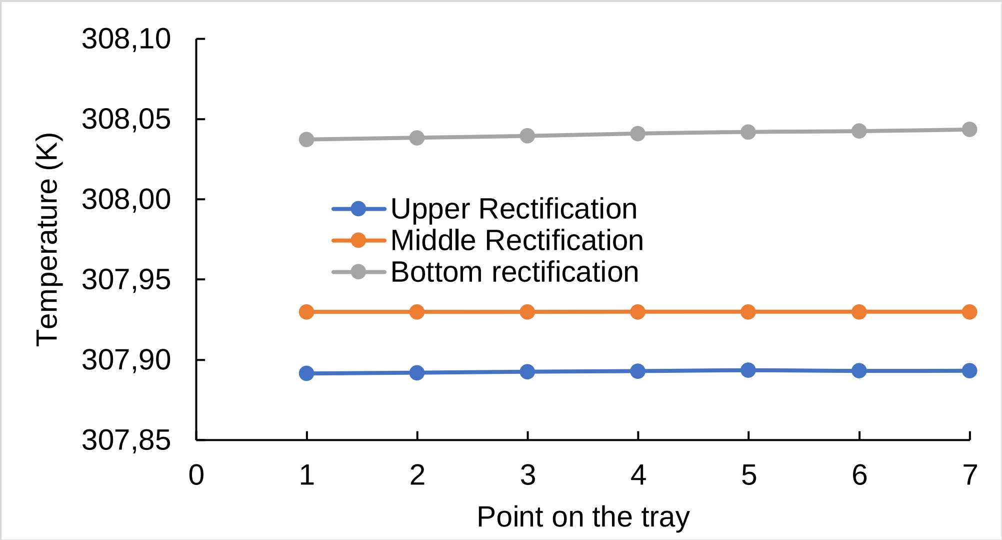

b)

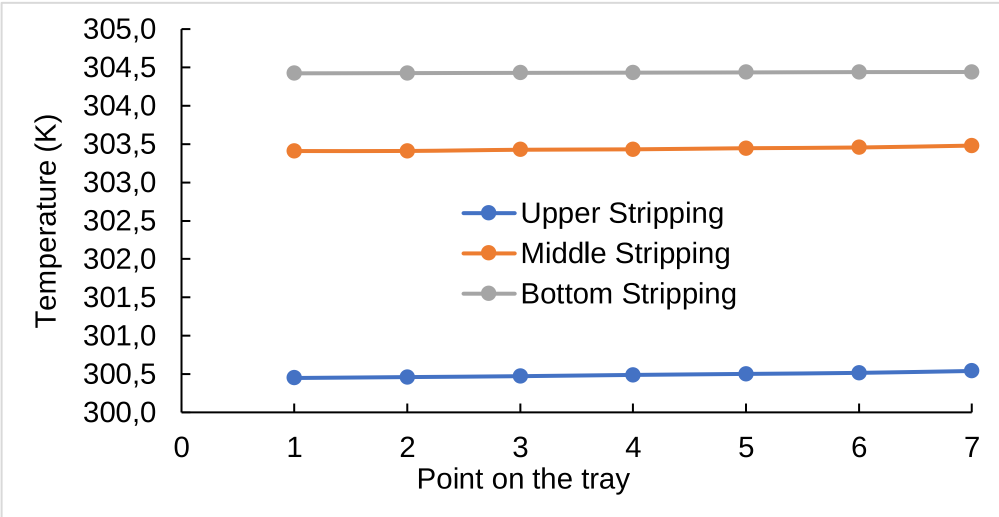

Figure 4-16: Temperature profiles of the liquid at 4mm on the trays (y=4mm). a) rectification trays, b) stripping trays

In Figure 4-16, for both zones (rectification and stripping), there is no a steep slope along with each plate, mainly because the difference between the inlet temperatures of the liquid and vapor are almost negligible (see Table 4-5) and therefore the outlet temperature obtained is between these values, the change becoming almost imperceptible, for example, for the tray in the middle zone of the rectification column, the inlet liquid and vapor temperatures are 307.9298 and 307.9338 K respectively, and their outlet temperature is 307.93 K. Additionally, it can be seen that the temperature difference among points of the same tray (slope of each profile) and the difference among the trays (separation of the profiles) becomes smaller from top to bottom in the stripping zone and from bottom to top in the rectification one, which is consistent with the profiles in Figure 4-9.

4.6.2.3. Murphree tray efficiency

The Murphree tray efficiency is defined by comparing a real tray with an ideal tray, this is the most used definition for tray efficiency. In this work Murphree tray efficiency is calculated by the following equation (Treybal, 1981):

$$E_{MV} = \frac{y_n - y_{n-1}}{y_n^* - y_{n-1}} \tag{33}$$

where y_n^* is the equilibrium vapor concentration, estimated by Peng-Robinson's thermodynamics equilibrium model, and y_n is the real vapor concentration in stage n and y_{n-1} is the concentration of vapor feeding the tray. To compare the efficiency results given by the CFD model, a simulation of the T-HIDiC in non-equilibrium was also carried out in Aspen Plus® using the Rate-Based module with the conditions defined in Table 4-1. Results of this simulation and its comparison with CFD results are shown in Table 4-8 and Figure 4-17.

Table 4-8: Murphree efficiency results, comparison between CFD results and Rate-based model with process simulation

	Section	Stage	Murphree efficiency CFD model (%)	Murphree efficiency Rate-Based model (%)
upper	Rectification	3	41.76	82.45
	Stripping	2	42.66	72.80
middle	Rectification	31	57.65	78.23
	Stripping	30	55.27	72.23
bottom	Rectification	60	37.48	76.51
	Stripping	59	40.77	69.31

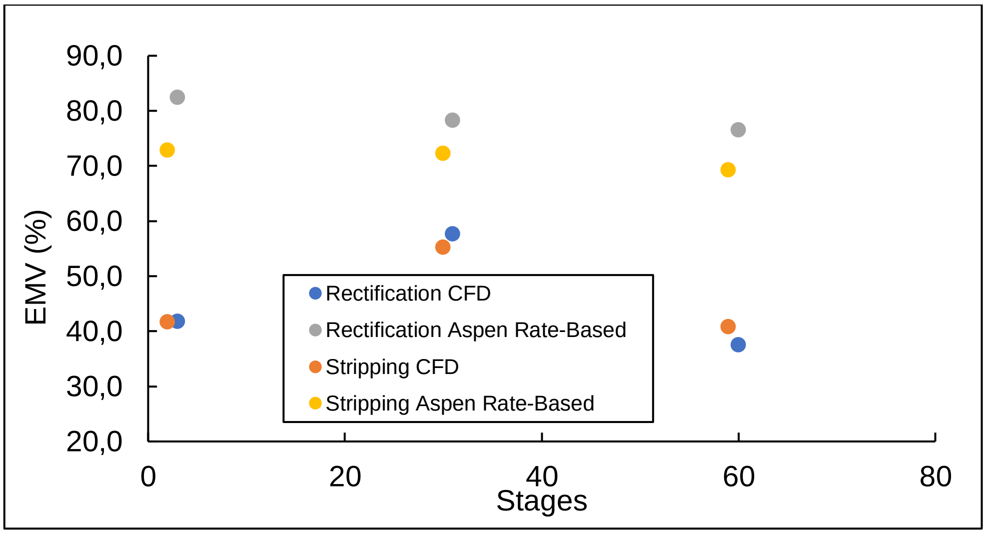

Figure 4-17: Murphree efficiency at analyzed trays for the upper, middle and bottom points obtained from CFD and base-rate model.

The average efficiency per stage using CFD is around 46% compared to 75% for the average value obtained from Rate-Base model (Figure 4-17). This difference is due to different factors: 1) Aspen plus uses different correlations on which the Rate-Base model is based for estimating efficiency, that makes the obtained results approximate what the real values would be, unlike of the CFD, which takes into account the transport phenomena making use of the generalized equations in addition to including the effect of the geometry of the plate; and 2) As mentioned above, due to the fact that thermodynamic equilibrium ratios are close to the unit, which causes small changes in output concentrations comparing with input ones, because of that, values change only in the third and fourth decimal places of the molar fractions. This generates issues in the calculation of the efficiency due to the orders of magnitude handled, for example, in the bottom rectification tray (Tray 60), the mole fraction in the inlet gas is 0.9671 (Table 4-7), and the calculated value with Fluent for the outlet vapor is 0.9677, verifying the existence of effective mass transfer. However, the difference is observed only in the fourth decimal leading to an important percentual difference but in practical terms these differences will be almost imperceptible. According to the above, it is proposed for future studies to verify the results experimentally and to validate the methodology for calculating the efficiency carried out in CFD with a system that has a high thermodynamic equilibrium ratio in order to avoid problems in the orders of magnitude.

4.6.2.4. Concentration of liquid phase

Figure 4-18 shows liquid concentration profiles along the points established previously in Figure 4-5. An important change in the concentration is not visually appreciated across the tray, mainly due to the small changes that were obtained in concentration from a tray to ne next one.

a)

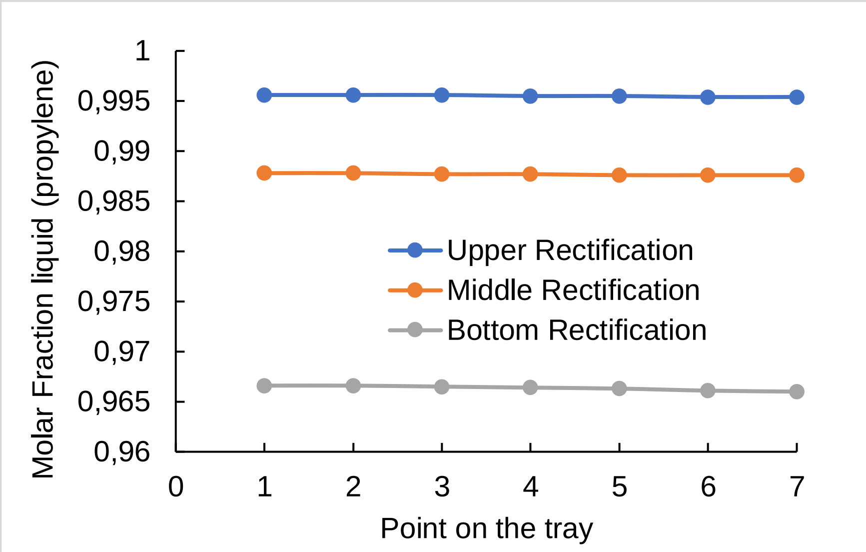

b)

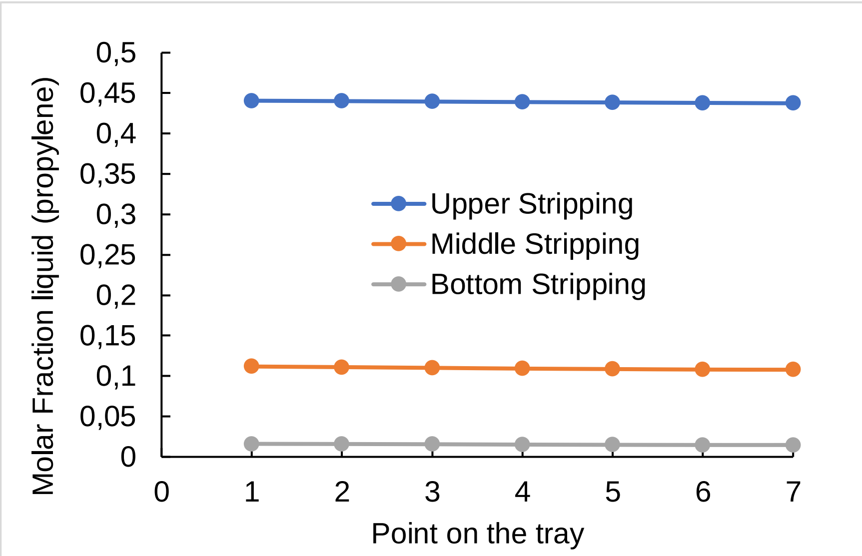

Figure 4-18: Composition profiles of liquid on the trays. a) rectification trays, b) stripping trays

4.6.2.5. Clear liquid height

In Figure 4-19, CFD prediction of clear liquid height is presented and compared against the Bennet correlation prediction for the fluid system in the selected trays (upper, middle, bottom). The Bennett correlation used is (Bennett *et al.*, 1983):

$$h_{CL} = \phi\left[h_w + 15.33 C_B \left(\frac{q_L}{\phi}\right)^{2/3}\right] \tag{34}$$

where h_w is the weir height, q_L is volumetric flow per length of weir, and

$$\phi = exp\left[-12.55\left(V_s\sqrt{\frac{\rho_G}{\rho_L - \rho_G}}\right)^{0.91}\right] \tag{35}$$

$$C_B = 0.0327 + 0.0286exp(-137.7h_w) \tag{36}$$

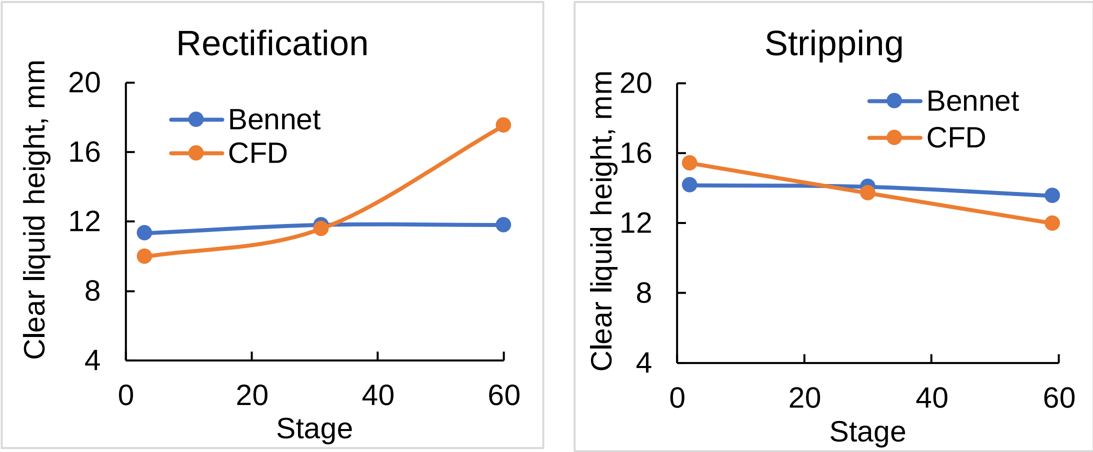

Figure 4-19: Clear liquid height calculated based on the results of the CFD model.

In Figure 4-19 it can be seen that for both models, clear liquid height increases with the vapor inlet velocity (1.396, 3.045 and 4.195 m/s for the rectification trays and 3.613, 1.960 and 0.890 m/s for the stripping ones, see Table 4-7) but CFD give more drastic changes (steeper slopes) than the Bennet correlation. An important observation is that for trays with inlet vapor flow no higher than 3.6 m/s the difference in the predictions from both models is moderate but for the 60th tray in rectification (with velocity of 4.195 m/s) CFD predicts a very higher clear liquid height, this is consistent with the behavior of the phase volume fraction shown in Figure 4-12. These results suggest that with a vapor inlet flow greater than 3.6 m/s the system is dangerously close to the drag condition.

4.7. Conclusions

The search for reduction on energy consumption generates the necessity of develop and implement non classical separation processes, and as a consequence the necessity of suitable modeling approach, which must be capable of giving accurate information about the new processes. Additionally, the growing computational capacity and its availability had increased the importance of simulation, specifically for design purposes. In this way, CFD analysis of HIDiC became an interesting strategy to assess this distillation configuration.

In this work, we propose a modeling approach to study a T-HIDiC unit. This modeling approach considers two main steps: process simulation under equilibrium conditions, and CFD and rate base model under non-equilibrium conditions. To analyze the involved approaches, the separation of the system propylene/propane was used as case study.

Process simulation under equilibrium conditions led to results regarding the vapor and liquid flow, temperature profiles, and the compressor, condenser, and reboiler duties in both distillation sections. These results were used to set up the boundary and initial conditions for the designed CFD model. The proposed CFD model was used for the analysis of three trays in the main sections of the T-HIDiC unit (upper, middle, and bottom).

Results of this first process simulation, under equilibrium conditions, shown that the necessary driving force for internal heat integration (heat transfer from rectification trays to stripping ones) is achieved with the proposed pressures. Due to the thermodynamical behavior of the system, the temperature difference is bigger at the bottom of the column. This could allow to identify stages with minimum temperature differences, which become limiting stages for heat integration and may define a key bottleneck for the configuration.

The compressor power requirement, reboiler, and condenser duties are 4.87, 18.81, and 26.99 kW, respectively, for a total energy requirement of 50.67, which is an important energy saving compared to the conventional column that requires 4,35 times more energy..

Important differences were obtained between both simulation approaches under non-equilibrium conditions (CFD and rate-based). The Murphree efficiencies predicted by the CFD model (between 38 and 58%) are lower than the predicted by a conventional process simulator (between 69 and 83%). i.e. the efficiencies predicted by CFD were, approximately, the half of the efficiencies obtained with the Rate based model from Aspen Plus®.

Based on the performed simulations, the most suitable approach to analyze energy integration in distillation columns, such as T-HIDIC units, is CFD. In this study, the developed CFD model allowed to predict temperatures, phase distribution, concentrations, and pressure and velocity fields coherently with the characteristics of the propylene/propane system, since this separation operation is especially difficult due to its low average relative volatility.

According to the results, the T-HIDiC achieves the proposed separation for Propylene and Propane with molar purities of 99.6% and 98.9%, respectively. The vapor flow presents a high increasing from the top to the bottom of the rectifying section and from the bottom to the top of the stripping one, which must to be considered to avoid hydraulic problems.

The results indicated that CFD is a tool capable of predicting reliably effects of column internals geometry on the multiphase flow field and can be considered as a useful aid for the design and evaluation of the performance of the T-HIDiC column with or without internals.

A significant improvement in the capacity of heat transfer could be achieved by the implementation of internals in the concentric configuration to obtain a sufficiently large surface area for heat transfer. Certainly, further heat transfer improvements are possible and could optimize the plate column design for better contact between the rectifying and stripping sections that will decrease energy consumption.

Acknowledgments

The authors acknowledge the financial support of Universidad Nacional de Colombia and Colciencias, and the collaboration and advice of Professor Ronnie Andersson. The authors would like to thanks the company S&S S.A.S for its technical support and contributions to this research.

Nomenclature

$\boldsymbol{A}$	Interfacial area per unit volume, m−1	***Greek Symbols***	
$\boldsymbol{A_B}$	Bubbling area, m2	α	Void fraction
$\boldsymbol{A_{hole}}$	Hole area on sieve tray, m2	ρ	Density, kg/m3
$\boldsymbol{C_D}$	drag coefficient	μ^e	effective viscosity, kg/m s
$\boldsymbol{C_l}$	lift force coefficient	μ	Viscosity, kg/m s
$\boldsymbol{C_{VM}}$	virtual mass force coefficient	σ	Surface tension,N/m
$\boldsymbol{D}$	diffusion coefficient, m2 s−1	ϕ	Average liquid holdup fraction in froth
$\boldsymbol{d_b}$	diameter of the bubble, m		
$\boldsymbol{d_h}$	Hole diameter of a sieve tray, m	*Subscrips*	
$\boldsymbol{Eo}$	Eötvös number	b	bubble
$\boldsymbol{F}$	total interfacial force, N	cap	Spherical-cap shape bubbles
$\boldsymbol{F^{drag}}$	drag force, N	ellipse	Ellipsoid shape bubbles

F^{lift}	lift force, N
F^{VM}	Virtual mass force, N
F_{corr}	Correction factor of C_D
g	gravitational acceleration, m/s2
H	enthalpy, J/kg
$\hat{h}$	Heat transfer coefficient between phases, W/m^{2}K
h_{DC}	Hight downcomer, m
h_{CL}	Clear liquid height, m
h_w	Hight weir, m
k	kinetic energy turbulent, m2/s 2
K	mole fraction equilibrium ratio
k_{LG}	gas–liquid mass transfer coefficient, m/s
k_G	Gas phase mass transfer coefficient, m/s
k_L	Liquid phase mass transfer coefficient, m/s
k_q	thermal conductivity, W/mK
L_w	Length weir, m
Mo	Morton Number
N_H	Number of holes in the sieve tray
Nu	Nusselt number
P	Pressure, Pa
Pr	Prandtl number
q	Diffusion heat flux, J/m^{2}s
Q	Energy transfer between phases, W/m^3
Q_S	Heat required in the stripping section, W
Q_R	Heat rejected from rectifying section, W
Re	Reynold number
S_{LG}	Rate of interphase mass transfer, kg/m^{3}s
T	temperature, K
t	Thermo-fluid time scale, s
t_e	exposure time in the penetration model, s
u_{rise}	bubble slip velocity, m/s
u_b	bubble velocity, m/s
u_H	Vapor velocity through the tray holes, m/s
u	velocity, m/s
V_s	Superficial gas velocity, m/s
x_n	Mole fraction of light component in the liquid phase on tray n
X_{LK}	Mass fraction of the light component in liquid phase

G	Vapour
L	Liquid
GL	transfer of quantities from liquid phase to vapour
LG	transfer of quantities from vapour phase to liquid
LK	Light component
sphere	Sphere shape bubbles

Superscripts

e	Effective property
T	Transpose of vector

Y_{LK}	Mass fraction of the light component in vapor phase
y_n	Mole fraction of light component in the vapor phase on tray n
y_n^*	Mole fractionof light component in the vapor phase in equilibrium with the liquid phase in tray n
Z	length of travel on a tray, m

References

Abbasnia, S., Nasri, Z., & Najafi, M. (2019). Comparison of the mass transfer and efficiency of Nye tray and sieve tray by computational fluid dynamics. *Separation and Purification Technology*, *215*. https://doi.org/10.1016/j.seppur.2019.01.010

ANSYS. (2021). *ANSYS Engineering Analysis System User's Manual*.

ANSYS Release 19. (2018). *ANSYS Fluent Theory Guide*.

Ashrafizadeh, S. A., Amidpour, M., & Abolmashadi, M. (2013). Exergy analysis of distillation column using concept of driving forces. *Journal of Chemical Engineering of Japan*, *46*(7), 434–443. https://doi.org/10.1252/jcej.11we038

Bennett, D. L., Agrawal, R., & Cook, P. J. (1983). New pressure drop correlation for sieve tray distillation columns. *AIChE Journal*, *29*(3), 434–442. https://doi.org/10.1002/aic.690290313

Bernal, D., Castellanos, O., Bejarano, P., & Rodriguez, G. (2011). *Analisis y diseño de platos y columnas de platos*. Universidad Nacional de Colombia.

Claumann, C. A., Peruzzo, T., Felice, V. De, Marangoni, C., & Machado, R. A. F. (2015). Modeling and process optimization: an approach using aspen plus and matlab in the energy integration study of distillation columns. *VIII Congreso Argentino de Ingeniería Química y 3 JASP*, *1*.

Gadalla, M. A. (2009). Internal heat integrated distillation columns (iHIDiCs)-New systematic design methodology. *Chemical Engineering Research and Design*, *87*(12), 1658–1666. https://doi.org/10.1016/j.cherd.2009.06.005

Gadalla, M., Olujić, Ž., de Rijke, A., & Jansens, P. J. (2006). Reducing CO2 emissions of internally heat-integrated distillation columns for separation of close boiling mixtures. *Energy*, *31*(13), 2409–2417. https://doi.org/10.1016/j.energy.2005.10.029

Gesit, G., Nandakumar, K., & Chuang, K. T. (2003). CFD modeling of flow patterns and hydraulics of commercial-scale sieve trays. *AIChE Journal*, *49*(4), 910–924. https://doi.org/10.1002/aic.690490410

Grace, J. R., Wairegi, T., & Brophy, J. (1978). Break-up of drops and bubbles in stagnant media. *The Canadian Journal of Chemical Engineering*, *56*(1).

https://doi.org/10.1002/cjce.5450560101

Grace, J. R., Wairegi, T., & Nguyen, T. H. (1976). Shapes and velocities of single drops and bubbles moving freely through immiscible liquids. In *Trans Inst Chem Eng* (Vol. 54, Issue 3). Universidad Industrial de Santander.

Guevara Luna, M. A., Guevara, M., & Guevara-Luna, M. A. (2015). Diseño de un equipo de recuperación de líquidos de gas natural empleando CFD. In *Revista Virtual Pro*. Universidad Nacional de Colombia.

Harvindran, V., & Foo, D. C. Y. (2021). Design of Internally Heat-Integrated Distillation Column (HIDiC). *Process Intensification and Integration for Sustainable Design*, 117–129. https://doi.org/10.1002/9783527818730.ch6

Heng Yeoh, G., & Tu, J. (2010). *Computational Techniques for Multi-Phase Flows*. ELSEVIER.

Higbie, R. (1935). The rate of absorption of a pure gas into a still liquid during short periods of exposure. *Transactions of the American Institute of Chemical Engineers*, *35*, 365–389.

Ishii, M., & Zuber, N. (1979). Drag coefficient and relative velocity in bubbly, droplet or particulate flows. *AIChE Journal*, *25*(5), 843–855. https://doi.org/10.1002/aic.690250513

Kataoka, I., & Serizawa, A. (1989). Basic equations of turbulence in gas-liquid two-phase flow. *International Journal of Multiphase Flow*, *15*(5). https://doi.org/10.1016/0301-9322(89)90045-1

Khosravi Nikou, M. R., & Ehsani, M. R. (2008). Turbulence models application on CFD simulation of hydrodynamics, heat and mass transfer in a structured packing. *International Communications in Heat and Mass Transfer*, *35*(9), 1211–1219. https://doi.org/10.1016/j.icheatmasstransfer.2008.05.017

Kister, H. Z. (1992). Tray Design and Operation. *McGraw-Hill Professional*, *1*, 9–11.

Krishna, R., Urseanu, M. I., Van Baten, J. M., & Ellenberger, J. (1999). Rise velocity of a swarm of large gas bubbles in liquids. *Chemical Engineering Science*, *54*(2), 171–183. https://doi.org/10.1016/S0009-2509(98)00245-0

Lamont, J. C., & Scott, D. S. (1970). An eddy cell model of mass transfer into the surface of a turbulent liquid. *AIChE Journal*, *16*(4). https://doi.org/10.1002/aic.690160403

Li, X., Yang, N., Sun, Y., Zhang, L., Li, X., & Jiang, B. (2014). Computational fluid dynamics modeling of hydrodynamics of a new type of fixed valve tray. *Industrial and Engineering Chemistry Research*, *53*(1), 379–389. https://doi.org/10.1021/ie400408u

Lockett, M. . (1986). *Distillation tray fundamentals*. Cambridge University Press.

Malvin, A., Chan, A., & Lau, P. L. (2014). CFD study of distillation sieve tray flow regimes using the droplet size distribution technique. *Journal of the Taiwan Institute of Chemical Engineers*, *45*(4), 1354–1368. https://doi.org/10.1016/j.jtice.2014.01.002

Mancera, J. A., Mendoza, D. F., & Riascos, C. A. M. (2018). HIDiC configuration selection based on exergetic analysis. *Chemical Engineering Transactions*, *69*. https://doi.org/10.3303/CET1869151

Morel, C. (1995). An order of magnitude analysis of the two-phase k–e model. *International Fluid Mechanics*. https://doi.org/10.1615/InterJFluidMechRes.v22.i3-4.30

Nakaiwa, M., Huang, K., Endo, A., Ohmori, T., Akiya, T., & Takamatsu, T. (2003). Internally heat-integrated distillation columns: A review. *Chemical Engineering Research and Design*, *81*(1), 162–177. https://doi.org/10.1205/026387603321158320

Nakaiwa, Masaru, Huang, K., Naito, K., Endo, A., Akiya, T., Nakane, T., & Takamatsu, T. (2001). Parameter analysis and optimization of ideal heat integrated distillation columns. *Computers and Chemical Engineering*, *25*(4–6), 737–744. https://doi.org/10.1016/S0098-1354(01)00649-4

Noriler, D., Barros, A. A. C., Wolf Maciel, M. R., & Meier, H. F. (2010). Simultaneous momentum, mass, and energy transfer analysis of a distillation sieve tray using CFD techniques: Prediction of efficiencies. *Industrial and Engineering Chemistry Research*, *49*(14), 6599–6611. https://doi.org/10.1021/ie9013925

Olujic, Z., Fakhri, F., De Rijke, A., De Graauw, J., & Jansens, P. J. (2003). Internal heat integration - The key to an energy-conserving distillation column. *Journal of Chemical Technology and Biotechnology*, *78*(2–3), 241–248. https://doi.org/10.1002/jctb.761

Pulido, J. L. (2008). Study of a New Concept of Distillation Column: Heat-Integrated Distillation Column (HIDiC). In *Bachelor Thesis in Chemical Engineering*. Industrial University of Santander.

Pulido, Jeffrey L, Martinez, E. L., Bineli, A. R. R., Wolf, M. R., & Filho, R. M. (2010). Heat Transfer Study in a Concentric Stage of an Internally Heat-Integrated Distillation Column (HIDiC) Using CFD Simulation. *Lecture Notes in Engineering and Computer Science*, *2187*(1), 742–747.

Pulido, Jeffrey León, Martínez, E. L., Wolf, M. R., & Filho, R. M. I. (2011). Heat transfer study of heat-integrated distillation column (HIDiC) using simulation techniques. *AIP Conference Proceedings*, *1373*, 242–254. https://doi.org/10.1063/1.3627209

Rahimi, R., Rahimi, M. R., Shahraki, F., & Zivdar, M. (2006). Efficiencies of sieve tray distillation columns by CFD simulation. *Chemical Engineering and Technology*, *29*(3), 326–335. https://doi.org/10.1002/ceat.200500285

RANZ, W. (1952). Evaporation from drops 1. *Chem. Eng. Prog*, *48*(3).

Ranz, W. E., & Marshall, W. R. (1952). Evaporation from drops. Parts I & II. *Chem. Eng. Progr*, *48*(22).

Riaño, S., Guevara, M. A., & Belalcázar, L. C. (2017). CFD Modeling and Evaluation of a Bi-Stable Micro-Diverter Valve. *Ciencia, Tecnologia y Futuro*, *8*(1), 77–84. https://doi.org/10.29047/01225383.94

Rijke, a De, Tesselaar, W., Gadalla, M. a, Olujic, Z., & Jansens, P. J. (2006). *Heat and Mass Transfer Characteristics of an Annular Sieve Tray*. *152*, 181–189.

Sadripour, M., Rahimi, A., & Hatamipour, M. S. (2012). Experimental Study and CFD Modeling of Wall Deposition in a Spray Dryer. *Drying Technology*, *30*(6), 574–582. https://doi.org/10.1080/07373937.2011.653613

Schiller, L., & Naumann, Z. (1935). A drag coefficient correlation. In *Z.Ver.Deutsch.Ing* (Vol. 77, Issues 13–14). https://doi.org/10.1016/j.ijheatmasstransfer.2009.02.006

Shenvi, A. A., Herron, D. M., & Agrawal, R. (2011). Energy efficiency limitations of the conventional heat integrated distillation column (HIDiC) configuration for binary distillation. *Industrial and Engineering Chemistry Research*, *50*(1), 119–130. https://doi.org/10.1021/ie101698f

Sun, L., De Rijke, A., Olujic, Z., & Jansens, P. (2003). *Process innovation and intensification*.

Sun, Z. M., Yu, K. T., Yuan, X. G., & Liu, C. J. (2007). A modified model of computational mass transfer for distillation column. *Chemical Engineering Science*, *62*(7), 1839–1850. https://doi.org/10.1016/j.ces.2006.12.021

Suphanit, B. (2010). Design of internally heat-integrated distillation column (HIDiC): Uniform heat transfer area versus uniform heat distribution. *Energy*, *35*(3), 1505–1514. https://doi.org/10.1016/j.energy.2009.12.008

Treybal, R. E. (1981). Mass Transfer Operations 3th edition. In *McGraw-Hill*.

Van Baten, J. M., & Krishna, R. (2000). Modelling sieve tray hydraulics using computational fluid dynamics. *Chemical Engineering Journal*, *77*(3), 143–151. https://doi.org/10.1016/S1385-8947(99)00164-3

Versteeg, H. K., & Malalasekera, W. (1995). An Introduction to Computational Fluid Dynamics The Finite Volume Method. In *Fluid flow handbook. McGraw-Hill …*. Longman Scitific & Technical. https://doi.org/10.2514/1.22547

Wang, T., Wang, J., & Jin, J. (2004). An efficient numerical algorithm for “A novel theoretical breakup kernel function of bubble/droplet in a turbulent flow.” *Chemical Engineering Science*, *59*(12), 2593–2595. https://doi.org/10.1016/j.ces.2004.03.011

Winkle, M. V. (1967). *Distillation*. McGraw-Hill.

Chapter 5

Exergy analysis of a Top Heat-Integrated Distillation Columns (T-HIDiC) for Propylene-Propane system

Highlights

- *Problem:* Lack of knowledge of the contribution to exergetic losses of the different components of a HIDiC column.
- *Contribution:* Detailed identification and quantification of exergetic fluxes in T-HIDiC columns (Grassmann diagram).
- The purpose of the chapter was to compare the exergy losses of three types of distillation columns: top heat-integrated distillation columns (T-HIDiC), vapor recompression columns (VRC), and conventional columns (CC).
- Mathematical simulations were carried out for each system and results were plotted in Grassmann diagrams.
- Three hypothetical operational conditions of T-HIDiCs were compared: T-HIDiC with equilibrium stage, T-HIDiC integrating tray efficiency, and T-HIDiC without integrating heat transmission.
- Analysis showed that T-HIDiCs have high potential for reducing exergy losses compared to conventional columns and VRC in equilibrium conditions (reduction in exergy losses were 61.2% and 14.5%, respectively).
- Integrating tray efficiency and heat transmission in T-HIDiCs had a significant effect on exergy losses, with the former increasing them almost sixfold and the latter reducing them by around 3.5 times (when compared to T-HIDiC simulations in equilibrium).

Abstract

The purpose of this paper is to compare the exergy losses of three different types of distillation columns in a propylene-propane system: 1) top heat-integrated distillation columns (T-HIDiC), 2) vapor recompression columns (VRC), and 3) conventional columns. In order to do this, we carried out mathematical simulations of each system and plotted the results in Grassmann diagrams. Additionally, for the particular case of T-HIDiCs, three different hypothetical operational conditions are compared, namely: 1) T-HIDiC with equilibrium stage, 2) T-HIDiC integrating tray efficiency, and 3) T-HIDiC without integrating heat transmission. The analysis showed that T-HIDiCs have a high potential for reducing exergy loss when compared with conventional columns and VRC in equilibrium conditions (reduction in exergy losses were 61.2% and 14.5%, respectively). We could also establish the enormous effect of integrating tray efficiency and heat transmission in the model, since, on the one hand, the former increases exergy losses almost sixfold, while the latter makes them around 3.5 times lower (when compared to the T-HIDiC simulations in equilibrium)

Keywords: T-HIDiC; Exergy analysis; Grassmann Diagram; Heat integration; Propylene, Propane.

5.1. Introduction

Distillation columns are major energy consumers in chemical and petrochemical industries (Gorak & Sorensen, 2014). Indeed, due to the way heat load is distributed in conventional distillation columns, their second-law efficiency is very low. The heat input and output of this type of columns are located at their hottest (reboiler) and coldest (condenser) points, which demands the use of an input of higher exergetic quality in the reboiler and results in an output of lower exergetic quality from the condenser. Thus, in order to reduce energy consumption and exergetic inefficiency, several studies have been carried out and many alternatives to conventional distillation columns have been proposed.

For instance, Mendoza & Riascos (2011) proposed reducing exergetic inefficiency with diabatic columns that allow heat distribution in the internal stages of the column. Hence, it was confirmed that columns with sequential heat exchanger (SHE) reduced exergetic loss, even if they do not have an important impact in total energy loads. Vapor-recompression columns (VRC) offer another interesting alternative. Indeed, they take advantage of the vapor produced at the top of the column to provide energy for the vaporization of the bottom stream. Moreover, VRC is appropriate for close-boiling separations, because of the small compressor duty that it needs to allow energy recycle through the combined reboiler-condenser (Jogwar and Daoutidis, 2009).

Heat-Integrated Distillation Columns (HIDiC) are non-conventional distillation columns developed based on the diabatic distillation concept (Nakaiwa *et al.*, 2003; Nakaiwa *et al.*, 1997). A HIDiC (Figure 5-1) is constructed in such a way that its rectifying and stripping sections are separated from each other. However, they are part of a single system in which fluids can flow from one section to the other by passing through a compressor and a throttling valve. Additionally, in order to promote heat transfer from the rectifying section to the stripping section, the former must be operated at a higher pressure than the latter. This internal heat transfer reduces the overall heat demand in the condenser and the reboiler. The energy savings of HIDiCs, compared to conventional columns, are estimated to be between 52 and 90% in systems with relative volatilities between 1.15 (propylene-propane) to 2.40 (benzene-toluene) (Liu & Qian, 2000; Matsuda *et al.*, 2010; Nakaiwa *et al.*, 1997; Nakaiwa *et al.*, 2001).

In an ideal HIDiC (i-HIDiC), external heat transfer is not necessary. However, in a partial HIDiC (p-HIDiC) only a part of the required heat is transferred internally, which makes external reboilers and condensers a necessity for its operation. Kiss & Olujić (2014) offer more detailed descriptions of HIDiC technologies and their implementations.

There are several possible HIDiC configurations, see Fig. 5-2; however, the one that presented the best results for the Propylene-propane system,, based in loss exergy, is the Top-HIDiC (T-HIDiC) (Mancera *et al.*, 2018). For this reason, we carried out an exergy analysis through a Grassmann diagram of precisely this HIDiC configuration. This was then used to compare it with conventional distillation columns and VRCs. In order to increase the amount of detail of the T-HIDiC simulation, we included plate efficiency in the model, as well as ideal stages working at equilibrium conditions and without heat integration.

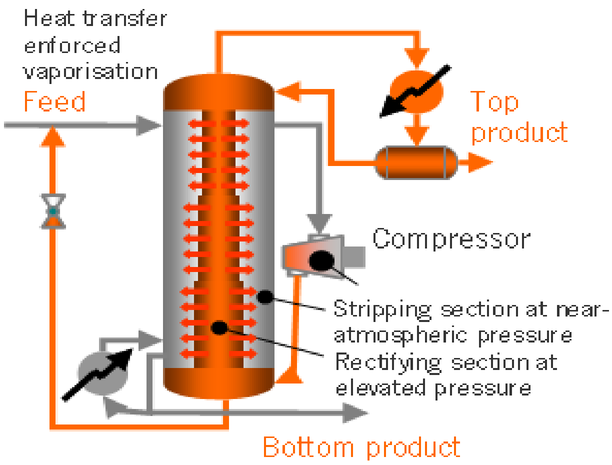

Figure 5-1: Concentric HIDiC scheme. (Source: Process Systems Enterprise)

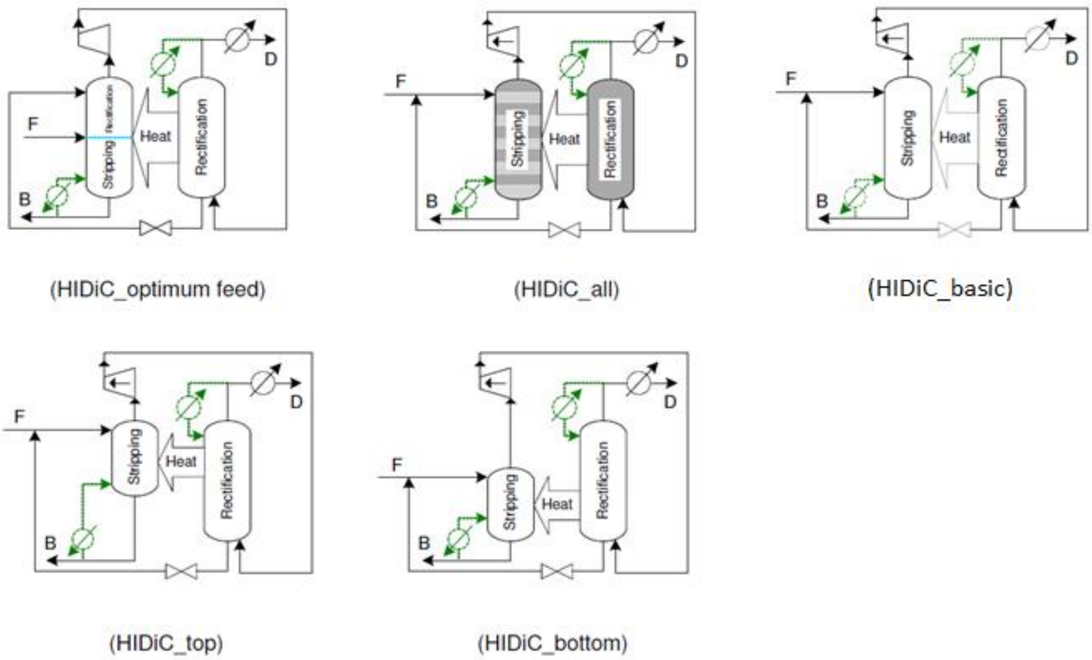

Figure 5-2: Configuration for concentric HIDiC columns (Pulido, 2008)

5.2. Exergy

Exergy can be defined as the useful potential work of a system and it is measured by comparing the state being evaluated to the state of its environment (Boles & Cengel, 2014; Kotas, 1995). The exergy of a stream can generally be divided into two parts: thermo-mechanical exergy and chemical exergy (See Table 5-1). The former, also known as the physical part of exergy, is comprised of a multitude of classifications including temperature, pressure, kinetic, and potential exergies. The latter may be divided in mixing and separation exergies.

Table 5-1: Types of exergies

Exergy				
Thermo-Mechanical			Chemical	
General Physical	Heat	Work and Electricity	Mixing / Separation	Reaction

Source: (Delmar, 2019)

The present work is limited to the study to thermo-mechanical exergy, particularly to the exergy transfer by mass, heat, and work. Thus, it disregards any chemical exergy that may be present in the system.

5.2.1. Physical exergy (exergy transfer by mass)

Physical exergy is a function of the enthalpy and entropy differences measured between an initial and a final state (Delmar, 2019):

$$Ex = H(T,P) - H_0(T_0,P_0) - T_0[S(T,P) - S_0(T_0,P_0)] \tag{1}$$

where Ex is the exergy flow, H, S, P, T are enthalpy, entropy, pressure and temperature for the considered state, while H_0, S_0, P_0, T_0 are the same variables at the environmental or reference state.

5.2.2. Exergy transfer by heat

Heat is a form of disorganized energy, which entails that only a portion of it can be converted to work, which is a form of organized energy. We can only produce work from heat when the latter is at a temperature above ambient temperature by transferring it to a heat engine that returns waste heat to the environment and takes advantage of useful heat. Therefore, heat transfer (Q) in a system at thermodynamic temperature (T) is always accompanied by an exergy transfer (Boles & Cengel, 2014):

$$Ex_{heat} = Q\left(1 - \frac{T_0}{T}\right) \tag{2}$$

5.2.3. Exergy transfer by work

Since exergy is defined as the maximum potential work of a system, the exergy in a process is the same as the available work from that process:

$$Ex_{work} = W \tag{3}$$

5.2.4. Exergy loss

Irreversible processes such as friction, mixing, turbulence, pressure drop, chemical reactions, heat and mass transfer, unrestrained expansion, non-quasiequilibrium compression or expansion always generate entropy, and anything that generates entropy destroys exergy. The exergy destroyed is proportional to the entropy generated and they are related to each other by the Gouy-Stodola theorem (de Koeijer & Rivero, 2003):

$$Ex^{loss} = T_0 \frac{dS^{irr}}{dT} \tag{4}$$

By dividing the exergy loss by the reference temperature ($T_0 = 298{,}15\ K$), the corresponding entropy production rate of the exergy benchmark is obtained. A more general calculation of the exergy loss, in a steady-state system, can be carried out by using the exergy balance thus:

$$Ex^{loss} = Ex_{in} - Ex_{out} \tag{5}$$

where Ex_{in} and Ex_{out} are the entering and leaving total rates of exergy respectively, transferred by heat, work, and mass.

5.2.5. Grassmann diagram

This type of diagram is a graphical representation, similar to the well-known Sankey diagram employed in the energy analysis of processes, where the width of the depicted bands is associated to the exergy rate or exergy flow rate (Grassmann, 1959; Oliveira, 2013). The advantage Grassman diagrams lies in their simple display of the energy inflows and outflows, in addition to including the exergy losses that take place in each piece equipment of the studied process. Indeed, this visual display facilitates understanding and interpretation, which makes it very useful for analyzing systems (de Koeijer & Rivero, 2003).

5.3. Methodology

To perform the exergy analysis, two types of simulations were carried out:

1) Simulations that consider column configuration. This type of analysis allowed us to estimate advantages of T-HIDiC against other configurations. Three different simulations of different types of distillation columns were carried out for this purpose:
   - Conventional Column.

- Vapor Recompression Column (VRC).
- Top Heat-Integrated Distillation Column (T-HIDiC).

2) Simulations of T-HIDiC in different thermodynamic conditions. The purpose of this type of analysis is to quantify the effect of plate efficiency and heat integration on exergy loss. Thus, the following simulations were carried out:
   - T-HIDiC in equilibrium.
   - T-HIDiC with plate efficiency.
   - T-HIDiC without heat integration in equilibrium.

The initial conditions used for the simulations were taken from a previous study (Mancera *et al.*, 2018). Moreover, the distillation columns were simulated in Aspen Plus 8.1 using the Peng-Robinson model to calculate thermodynamic properties and the vapor-liquid equilibrium. Additionally, the simulations were carried out in steady state using isentropic efficiency in the compressor (for VRC and T-HIDiC) and considering that heat flow does not occur between the system and its surroundings. The initial conditions for the simulations are shown in Table 5-2.

Table 5-2: Specifications for Aspen plus simulation

Characteristic	Conventional	VRC	T-HIDiC equilibrium	T-HIDiC efficiency	T-HIDiC without heat integrated
Rectification section Pressure(bar)	11,2	11,2	14,6	14,6	14,6
Stripping section pressure (bar)	11,2	11,2	11,2	11,2	11,2
Stages rectification section	164	164	170	170	170
Stages stripping section	66	66	61	61	61
Feeding stage	165	165	171	171	171
Trays in the Concentric Column	---	--	169	169	169
Trays in the Annular column	---	--	60	60	60
Feed flow (kg/h)	112000	112000	112000	112000	112000
Feed fraction mol (propylene)	0,57	0,57	0,57	0,57	0,57
Feed thermal condition (q)	0,37	0,37	0,37	0,37	0,37
Murphree efficiency stripping	---	---	---	47,02% *	---
Murphree efficiency rectification	---	---	---	49,5% *	---
Fraction mol distillate (propylene)	0,996	0,996	0,996	0,996	0,996
Fraction mol funds (propylene)	0,011	0,011	0,011	0,011	0,011
Compressor (isentropic) efficiency	---	0,72	0,72	0,72	0,72

* Taken from chapter 4 results by CFD simulation.

For the T-HIDiC simulations, we adapted the procedure suggested by Suphanit (2010) for modeling heat distribution between the rectification section and the stripping section (Fig. 5-3). In summary, this proposal requires:

- To calculate the energy demands in the condenser and reboiler, without energy integration.
- To choose the lower energy demand and calculate the flow of energy per tray.
- To include the heat flow of each tray and then re-calculate the resulting column.

The heat transfer of the system was modelled through thermal interconnected streams, tray by tray. After specifying the components and thermodynamic model, the column configuration was simulated as shown in Fig. 5-4.

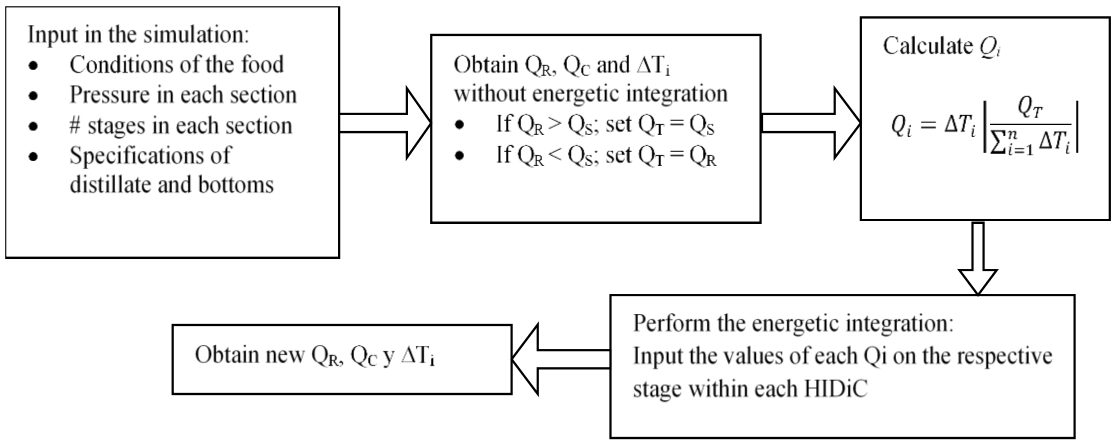

Figure 5-3: Procedure for estimation of heat distribution in HIDiC.

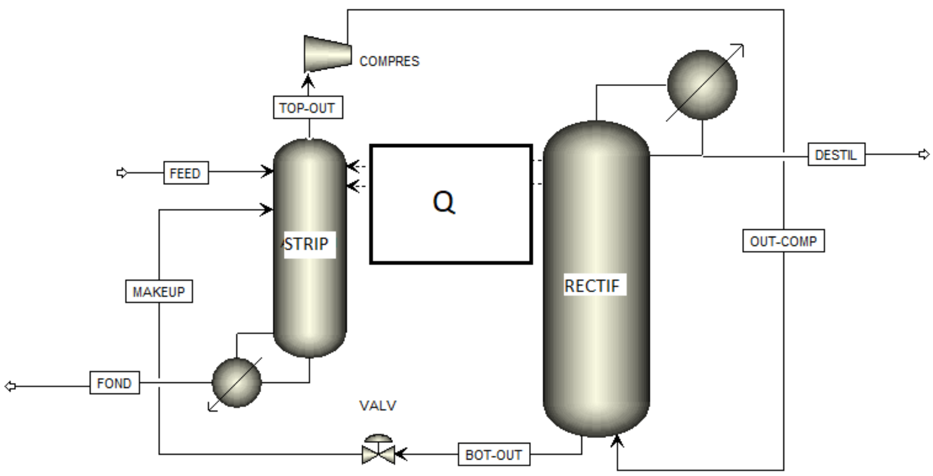

Figure 5-4: Schematic of HIDiC column simulation in ASPEN PLUS.

The exergy calculation was performed for each stream in the distillation process through Eqs. 1, 2 and 3. The reference conditions or dead state were 298,15K and 1 atm. For the calculations of the exergy loss in each equipment, we used version of Eq. 5 adapted to the type of column being modelled.

5.3.1. Exergy loss in conventional columns

The equations used to calculate the exergy losses in each equipment of the conventional distillation systems (reboiler, column, condenser) are described below (see Fig. 5-5):

$$Ex_{Reb}^{loss,C1} = A_{steam}^{C1}\left(Ex_{steam,in}^{C1} - Ex_{steam,out}^{C1}\right) + L_{210}^{C1}Ex_{L210}^{C1} - V_{211}^{C1}Ex_{V211}^{C1} - B^{C1}Ex_{B} \quad (6)$$

$$Ex_{Col}^{loss,C1} = F_{Feed}^{C1}Ex_{feed}^{C1} + R^{C1}Ex_{Reflux}^{C1} + V_{211}^{C1}Ex_{V211}^{C1} - V_{2}^{C1}Ex_{V2}^{C1} - L_{210}^{C1}Ex_{L210}^{C1} \quad (7)$$

$$Ex_{cond}^{loss,C1} = A_{watercool}^{C1}\left(Ex_{watercool,in}^{C1} - Ex_{watercool,out}^{C1}\right) + V_{2}^{C1}Ex_{V2}^{C1} - L_{1}^{C1}Ex_{L1}^{C1} \quad (8)$$

where,

$$L_1^{C1} = R^{C1} + Dist^{C1} \quad (9)$$

The superscript $C1$ in Eqs. 6 – 9 stands for “conventional column”.

5.3.2. Exergy loss in vapor recompression columns

Equations used to calculate the exergy losses in each equipment of the vapor-recompression distillation systems (reboiler, column, compressor, valve, condenser) are described below (see Fig. 5-6):

$$Ex_{Reb}^{loss,C2} = V_{comp}^{C2}Ex_{Vcomp}^{C2} + L_{210}^{C2}Ex_{L210}^{C2} - V_{211}^{C2}Ex_{V211}^{C2} - L_{val,in}^{C2}Ex_{Lval,in}^{C2} - B^{C2}Ex_{B}^{C2} \quad (10)$$

$$Ex_{Col}^{loss,C2} = F_{Feed}^{C2}Ex_{feed}^{C2} + R^{C2}Ex_{Reflux}^{C2} + V_{211}^{C2}Ex_{V211}^{C2} - V_{2}^{C2}Ex_{V2}^{C2} - L_{210}^{C2}Ex_{L210}^{C2} \quad (11)$$

$$Ex_{Comp}^{loss,C2} = V_{2}^{C2}Ex_{V2}^{C2} + W_{comp}^{C2} - V_{comp}^{C2}Ex_{Vcomp}^{C2} \quad (12)$$

$$Ex_{Valv}^{loss,C2} = L_{val,in}^{C2}Ex_{Lval,in}^{C2} + L_{val,out}^{C2}Ex_{Lval,out}^{C2} \quad (13)$$

$$Ex_{cond}^{loss,C2} = A_{watercool}^{C2}\left(Ex_{watercool,in}^{C2} - Ex_{watercool,out}^{C2}\right) + L_{val,out}^{C2}Ex_{Lval,out}^{C2} - L_{1}^{C2}Ex_{L1}^{C2} \quad (14)$$

where

$$L_1^{C2} = R^{C2} + Dist^{C2} \quad (15)$$

5.3.3. Exergy loss calculations for T-HIDiC

Equations used to calculate the exergy losses in each equipment (reboiler, stripping column, compressor, rectification column, valve) of the T-HIDiC distillation system are described below (see Fig. 5-7):

$$Ex_{Reb}^{loss,C3} = A_{steam}^{C3}\left(Ex_{steam,in}^{C3} - Ex_{steam,out}^{C3}\right) + L_{60,S}^{C3}Ex_{L60,S}^{C3} - V_{61,S}^{C3}Ex_{V61,S}^{C3} - B^{C3}Ex_{B}^{C3} \quad (16)$$

$$Ex_{Strip}^{loss,C3} = F_{Feed}^{C3} Ex_{feed}^{C3} + L_{val,out}^{C3} Ex_{Lval,out}^{C3} + Ex_{QStrip} + V_{61,S}^{C3} Ex_{V61,S}^{C3} - V_{1,S}^{C3} Ex_{V1,S}^{C3} - L_{60,S}^{C3} Ex_{L60,S}^{C3} \tag{17}$$

$$Ex_{Comp}^{loss,C3} = V_{1,S}^{C3} Ex_{V1,S}^{C3} + W_{comp}^{C3} - V_{170,R}^{C3} Ex_{V170,R}^{C3} \tag{18}$$

$$Ex_{Rect}^{loss,C3} = R^{C3} Ex_{Reflux}^{C3} + V_{170,R}^{C3} Ex_{V170,R}^{C3} - Ex_{QRect} - V_{2,R}^{C3} Ex_{V2,R}^{C3} - L_{val,in}^{C3} Ex_{Lval,in}^{C3} \tag{19}$$

$$Ex_{Valv}^{loss,C3} = L_{val,in}^{C3} Ex_{Lval,in}^{C3} + L_{val,out}^{C3} Ex_{Lval,out}^{C3} \tag{20}$$

$$Ex_{cond}^{loss,C3} = A_{watercool}^{C3}\left(Ex_{watercool,in}^{C3} - Ex_{watercool,out}^{C3}\right) + V_{2,R}^{C3} Ex_{V2,R}^{C3} - L_{1,R}^{C3} Ex_{L1,R}^{C3} \tag{21}$$

where Ex_{QStrip} is the exergy due to the energy integration effect produced by heat transfer from the rectification column to the stripping column, and Ex_{QRect} is the exergy due to the energy integration effect produced by heat transfer from the rectification column to the stripping column.

$$Ex_{QStrip} = \sum_{n=1}^{60} Q_n \left(1 - \frac{T_0}{T_n^S}\right) \tag{22}$$

$$Ex_{QRect} = \sum_{n=2}^{61} Q_n \left(1 - \frac{T_0}{T_n^R}\right) \tag{23}$$

where

$$L_{1,R}^{C3} = R^{C3} + Dist^{C3} \tag{24}$$

For the case of T-HIDiC without heat integration, Eqs. 22 and 23 are equal to zero.

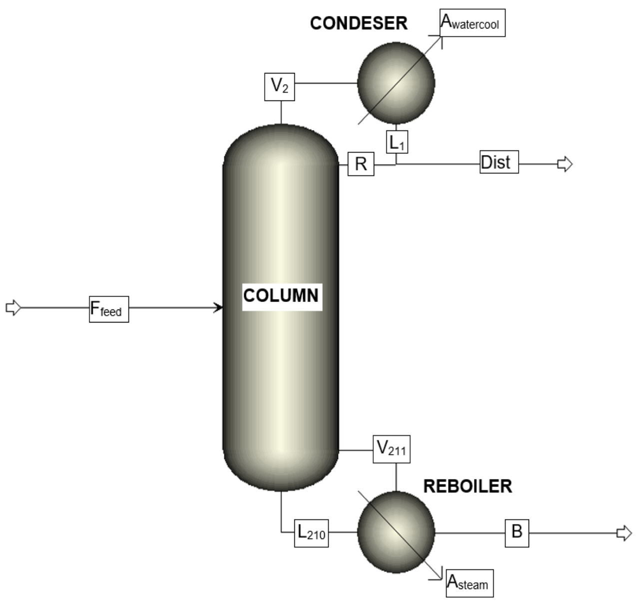

Figure 5-5: Flow diagram of conventional column

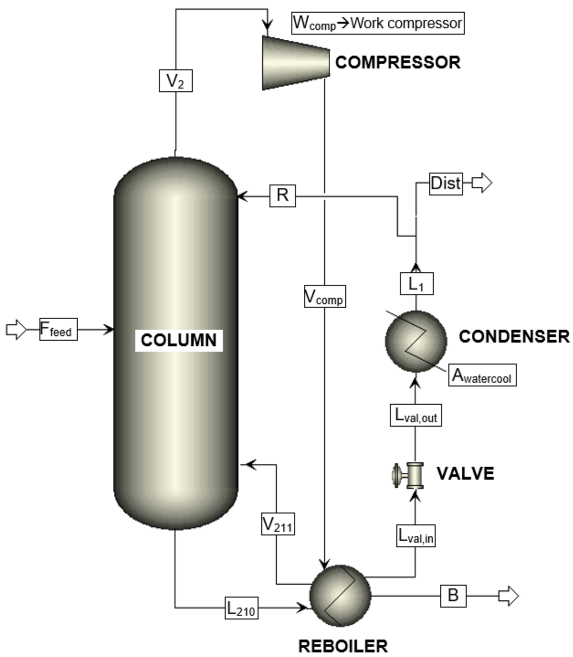

Figure 5-6: Flow diagram of VCR

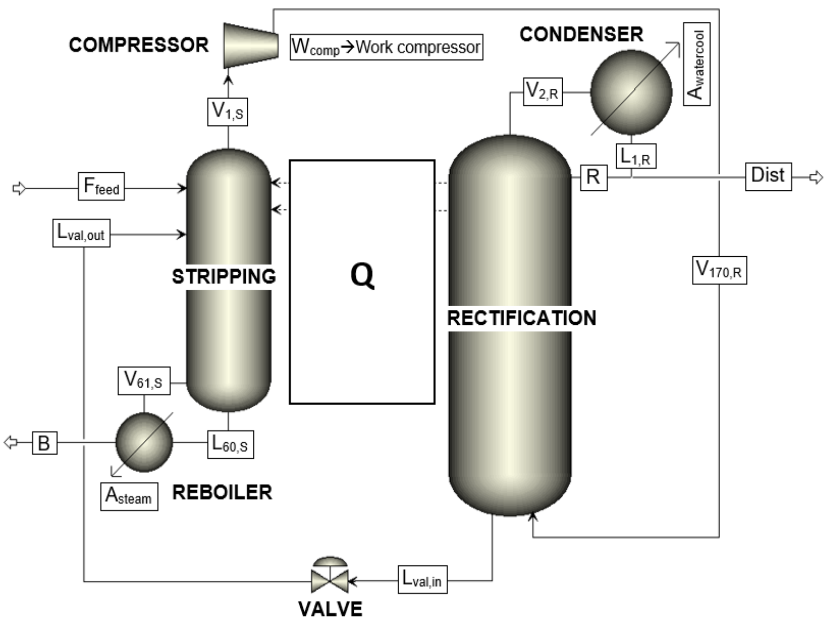

Figure 5-7: Flow diagram of T-HIDiC

Once the exergy values were obtained, the Sankey flow-show (www.sankeyflowshow.com) software was used to make Grassmann diagrams.

5.4 Results and discussion

Retaking what was raised as the objective of this chapter and the cases that were studied; then, the results obtained in the development of the work are presented.

5.4.1 Effects of column type on exergy loss

Fig. 5-8 (a,b and c), presents the exergy flows of each of the column types evaluated in this study. The blue blocks of the diagram represent the different processing equipment of the system, while the green arrows represent the input, output and exergy losses that take place at each point of the process. Each arrow shows the amount, in GJ/hr; of its respective exergy flow.

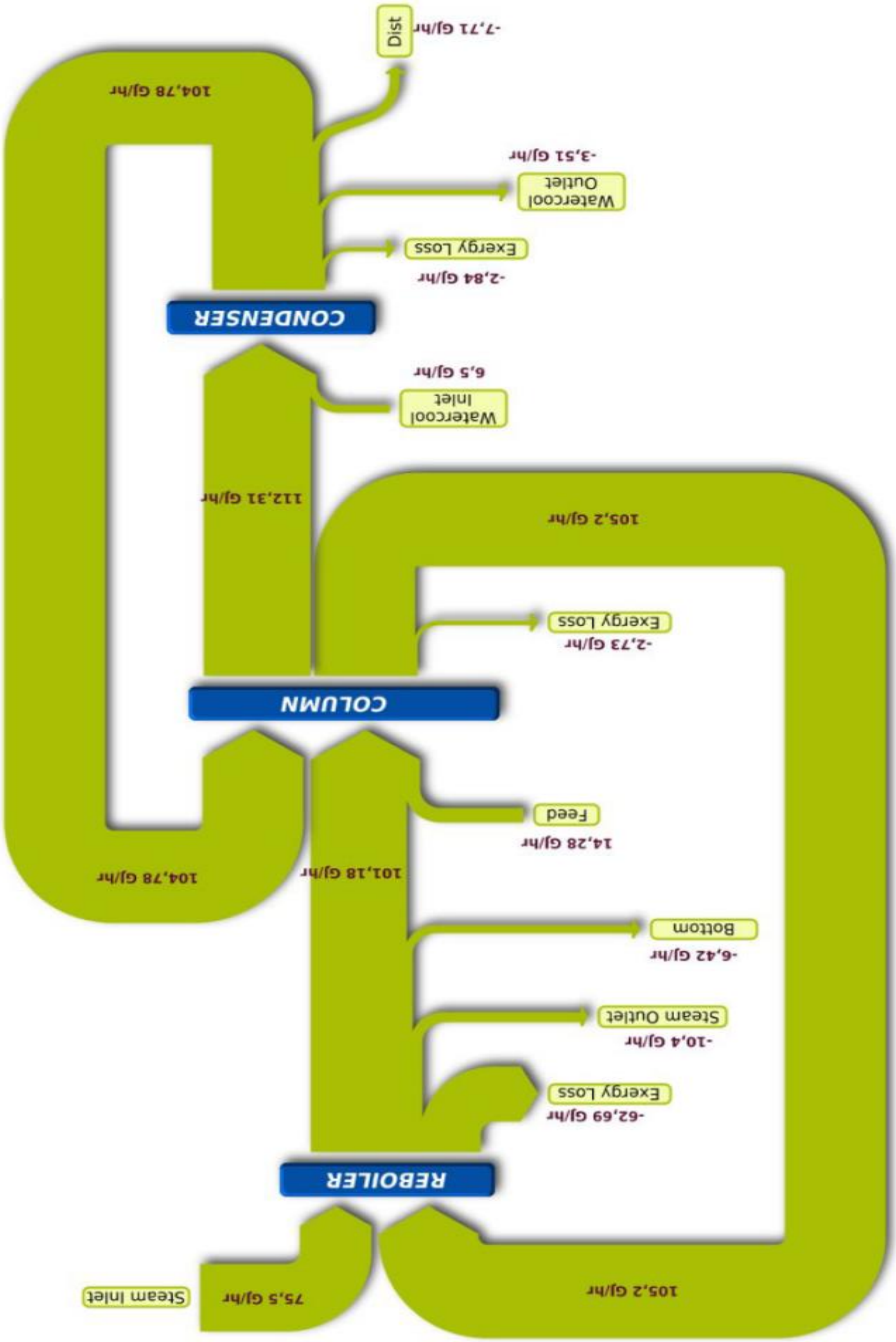

Figure 5-8a: Grassmann Diagram of Conventional column.

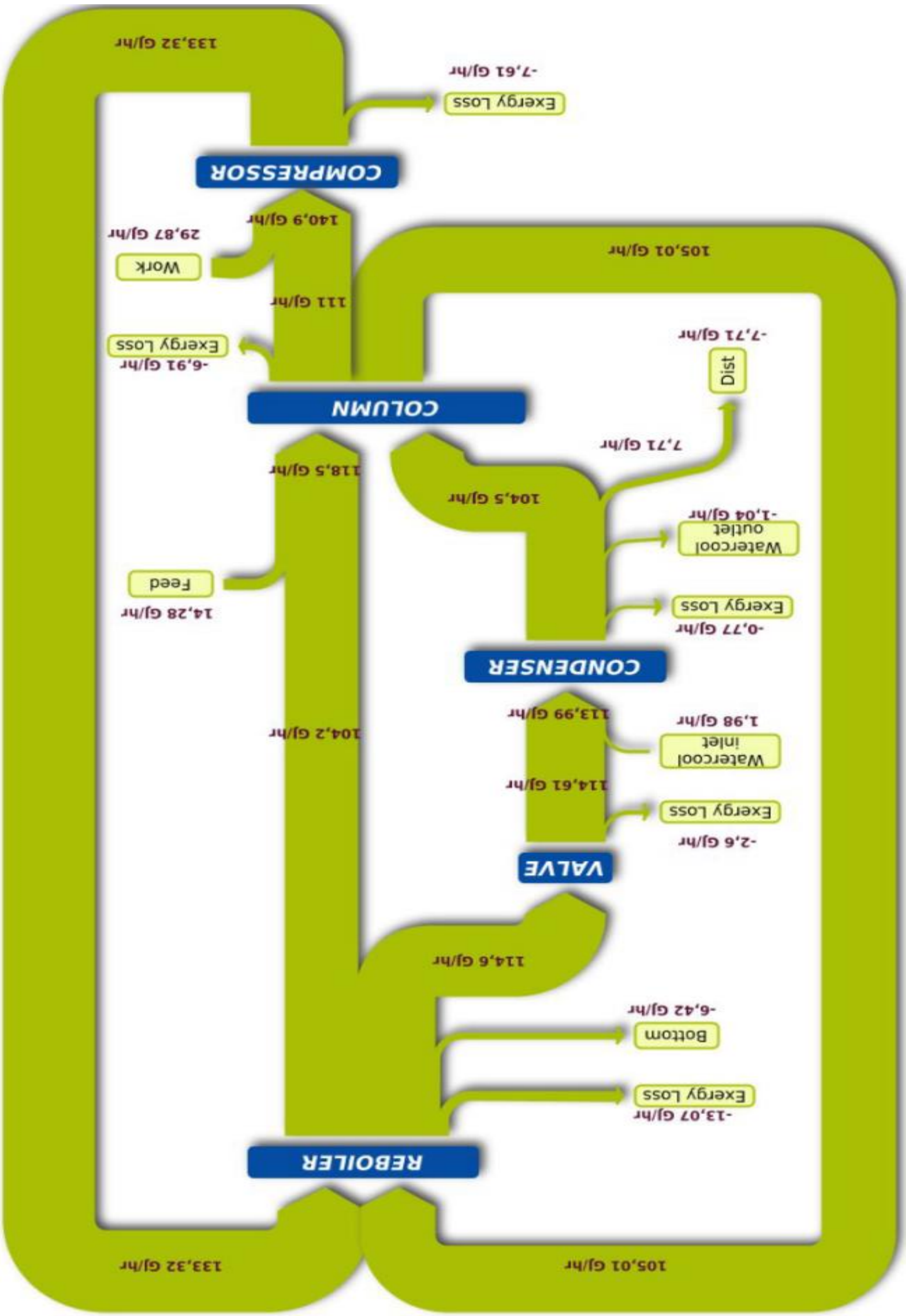

Figure 5-8b: Grassmann Diagram of VRC.

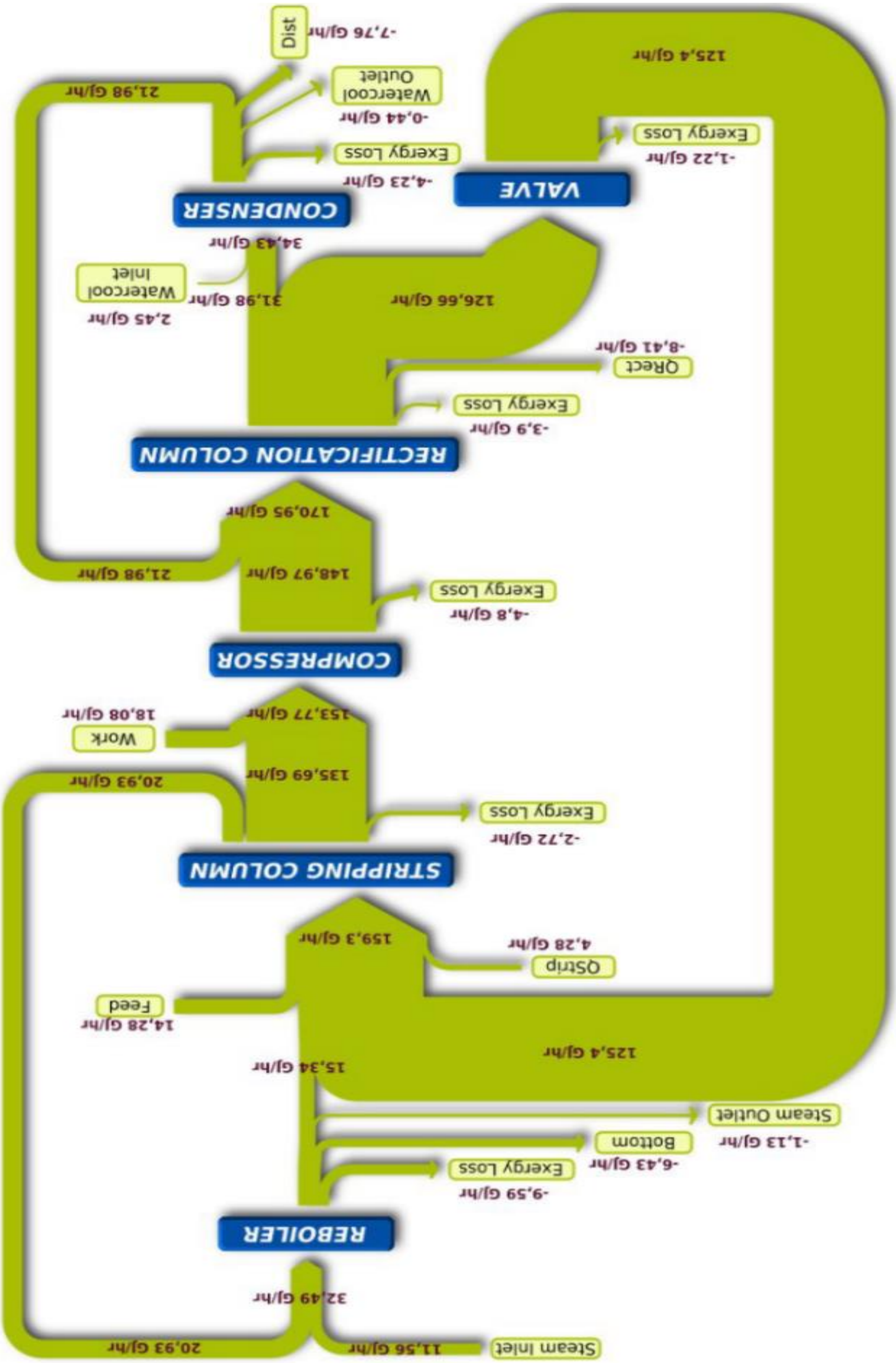

Figure 5-8c: Grassmann Diagram of T-HIDiC

Table 5-3 shows the exergy loss in the different types of distillation columns, these results show that, in general, exergy loss is significatively reduced when conventional columns are compared to VRCs and even further reduced when compared to HIDiCs, which confirms that the latter is the most efficient configuration from the point of view of the second thermodynamic law.

Table 5-3: Comparison of exergy loss in different types of distillation columns

	Conventional column	**VRC**	**T-HIDiC equil.**
Total exergy loss (GJ/h)	68,27	30,96	26,47
Exergy loss by equipment (%)			
Reboiler	91,8	42,2	36,2
Condenser	4,2	2,5	16,0
Column	4,0	22,3	---
Compressor	---	24,6	18,1
Valve	---	8,4	4,6
Rectification column	---	---	14,8
Stripping column	---	---	10,3
Reduction in exergy loss (%)			
vs Conventional column	--	54,65	61,22
vs VRC	--	--	14,49

When the role of each equipment in exergy loss is evaluated, it is clear that the reboiler is the main cause of exergy loss, regardless of the type of column being used. However, its contribution towards exergy losses decreases from 91,8% to 42,2% and 36,2% as more efficient columns are used. This shows the positive impact of implementing heat-recycling technologies in distillation columns. However, the increase in efficiency brought about by heat recycling does not depend exclusively on the quality of the reboiler. Indeed, the compressor plays a key role in this process, become of high importance in energy consumption and its efficiency, what place the operational conditions of this equipment as key variables in heat integrated distillation systems.

It is worth noting that, in general terms, for the three column configurations, the internal exergy flows within the system are much greater than the input and output exergy flows, regardless of the type of column being used. For instance, in the conventional column evaluated in this study, reflux exergy is 104,78 GJ/h, while the input exergy flow at the feed stream is 14,28 GJ/h and the output exergy flow of the distillate is of 7,71 GJ/h. This is due to the low relative volatility of propylene-propane mixtures, which cannot be separated unless the distillation system has a high reflux ratio.

From a visual analysis on the diagrams, it is observed that with the VRC the main improving in energy usage is due to replacing of steam inlet by energy from the condenser, what reduces exergy loss from 62.69 to 13.07 GJ/h, but including the compressor with and exergy loss of 7.61 GJ/h.

In the other way, analyzing VRC vs HIDIC, it could be observed that the exergy fluxes that are not related with mass fluxes have great magnitude reduction for the HIDIC, another exergy flux with an important reduction is the one associated with the mas flow that return form the condenser to the column, which is a consequence of internal heat integration. The advantage in internal integration is evinced in the small exergy loss generated as consequence of the internal heat transfer: 8,41 GJ/h of exergy go out from the rectifying section, associated with the QRect, and 4,28 GJ/h of exergy enters to the stripping one, associated with the QStrip, the difference is a loss of exergy in this integration.

5.4.2 Effect of thermodynamic condition on T-HIDiC exergy loss.

The results of simulating systems with tray efficiency and heat transfer, on the one hand, and without tray efficiency and heat transfer, on the other hand are presented in Figures 5-9a and 5-9b. When compared to the T-HIDiC in equilibrium (Figure 5-8c), i.e., a system that considers heat transfer but does not consider tray efficiency. These results show clearly that the consideration of tray efficiency is a key factor for a consistent analysis in distillation systems, because of total exergy losses increase from 26,47 to 157,77 GJ/h (+496%) when efficiency was included. For this reason, tray performance ought to be studied further in order to improve its efficiency.

Moreover, since the overall performance of real distillation columns always depends on tray efficiency, as opposed to theoretical ones, this parameter should be crucial for column design. In this analysis, simulation-based, in order to guarantee that the system reaches the separation task the reflux rate was increased from 2.83 to 24.64, which drastically increased internal fluxes and the exergy associated to them (see Figures 5.8c and 5.9). It is important to expose that for a real implementation, the reflux rate increasing will be partially reduced with a increasing in the number of stages in both section which requires additional analysis, out of the scope of the present work.

On the other hand, comparing the T-HIDiC in equilibrium with the simulation that did not integrate heat transmission allowed us to analyze the effects of internal thermal interactions between rectification and stripping trays on energetic efficiency. Thus, we were able to determine that including heat transfer in the model reduces the overall heat load and the exergy destruction that takes place in the reboiler and the condenser. An interesting result is that the exergy loss in the T-HIDiC model without heat integration (93,4 GJ/h) minus the exergy loss in its compressor and valve (4,2 and 1,07 GJ/h) is significatively higher than the exergy loss in the conventional column, what is due to higher exergy losses generated in the condenser (17.67 GJ/h) compared with the condenser of the conventional column (2.84 GJ/h), while reboilers' exergy losses are similar (63.6 vs 62.7 GJ/h), this is a consequence of higher pressure and temperature operation in condenser for the HIDiC.

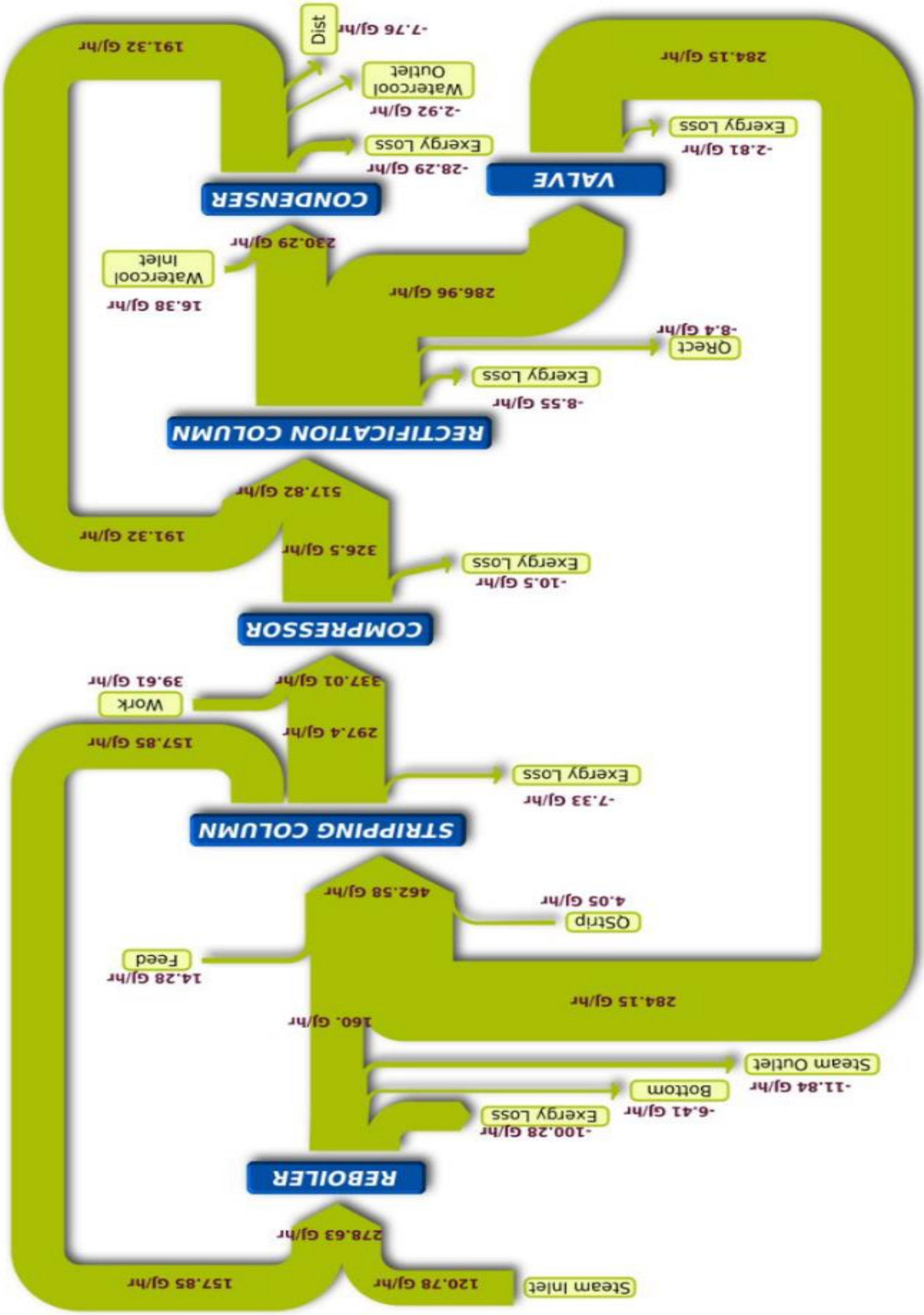

Figure 5-9a: Grassmann Diagram of a T-HIDiC modelled with tray efficiency and heat transfer.

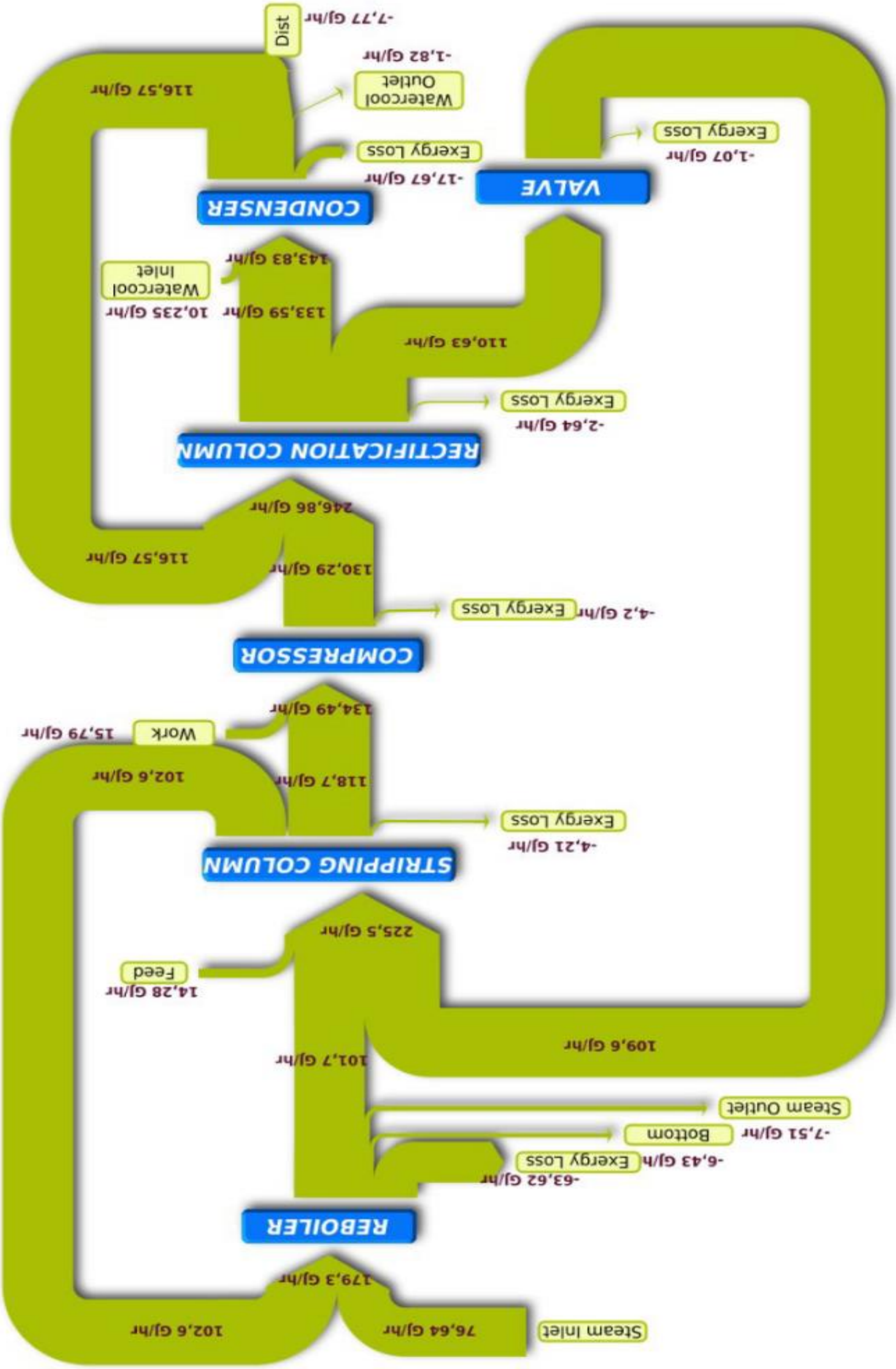

Figure 5-9b: Grassmann Diagram of a T-HIDiC modelled without tray efficiency and heat transfer.

Table 5-4 presents the contribution to exergy loss of each equipment type for the different T-HIDiC configurations evaluated in this study. Thus, the reboiler was the equipment with the largest contribution to exergy loss in all analysis.

Table 5-4: Comparison of exergy losses in T-HIDiC at different thermodynamic conditions.

	T-HIDiC equil.	**T-HIDiC with effic.**	**T-HIDiC equil. without HI**
Total exergy loss (GJ/h)	26,47	157,77	93,4
Exergy loss by equipment (%)			
Reboiler	36,2	63,6	68,1
Condenser	16,0	17,9	18,9
Compressor	18,1	6,7	4,5
Valve	4,6	1,8	1,2
Rectification column	14,8	5,4	2,8
Stripping column	10,3	4,6	4,5
Increasing in exergy loss vs T-HIDiC with HI and equilibrium trays (%)			
	--	+ 496	+ 253

In Table 5-5, the total exergy losses of each of the three evaluated T-HIDiC configurations are compared. As previously stated, the inclusion of tray efficiency in the model increases exergy losses. However, this value is almost 6 times greater than that of the T-HIDiC in equilibrium, which shows that the effect of tray efficiency on the exergy losses is not linear but an exponential behavior.

Table 5-5: Exergy loss and percentage of exergy reduction per column for the T-HIDiC at different thermodynamical conditions.

Column	**Exergy loss (GJ/hr)**	**% reduction in exergy loss compared to T-HIDiC with efficiency**	**% reduction in exergy loss compared to T-HIDiC without integration**
T-HIDiC efficiency	157,77	---	----
T-HIDiC without integration	93,4	40,79	----
T-HIDiC equil.	26,47	83,22	71,66

On the other hand, when the T-HIDiC is modelled without integrating heat transfer, its exergy losses become around 3,5 times higher than the HIDiC in equilibrium, which shows, once again, the importance of including this variable in the simulations.

It worth noting that, in a strict sense, only the T-HIDiC modelled in equilibrium can be compared with the conventional-column and VRC simulations previously presented. In order to measure the results for HIDiC with the different thermodynamical considerations against conventional columns and VRCs, further simulations that integrated tray efficiency and heat transfer would have to be carried out.

5.5 Conclusions

The exergy losses for three configuration of distillation column were analyzed. The analysis –based on simulation of the systems for a fixed separation task, very close design parameters and ideal performance in the trays– showed reductions in exergy losses for the T-HIDiC when compared with a conventional column and a VRC, 54,65% and 14,49% respectively. For VRC, the improving in thermodynamical efficiency, against the conventional column, is generated, mainly, by the reduction of the high exergy heat flux entering to the system and allocated to the reboiler. In the other way, for the HIDiC the additional increase in thermodynamical efficiency is due to the distribution of the heat transfer: in VRC, as well as in CC, the energy for the stripping section enters totally in the reboiler, instead of the distribution that is achieved in all this section for the HIDiC.

Effect of tray efficiency was also analyzed, this consideration in the T-HIDiC simulations (47% for the rectification section and 49% for the stripping section) increases exergy losses sixfold, which technically makes it less effective than conventional columns and VRCs with equilibrium consideration. However, it is necessary to include efficiency in VRC and CC simulations for the final analysis of the three types of distillation columns. These results confirm that efficiency analysis is key for column design, especially in non-conventional systems which hydraulic performance is a challenging issue.

Analysis of a HIDiC without internal heat transfer shows that this interaction between both column section is the key for its higher thermodynamic efficiency; additionally, it was confirmed that near-environment condenser temperature –what is a design recommendation for conventional columns– is so advisable for efficient energy use in conventional columns, the most employed configuration.

Notation

A	Water flow (kg/hr)	Subscripts	
B	Bottom flow (kg/hr)	0	Reference conditions
$Dist$	Distillation flow (kg/hr)	$1, 2, 60, 61, 170, 210, 211.$	Stage 1, 2, 60, 61, 170, 210, 211.
Ex	Exergy (GJ/kg)	Col	Column
F	Feed flow (kg/hr)	$Comp$	Compressor
H	Enthalpy (GJ/kg)	$Cond$	Condenser
L	Liquid flow (kg/hr)	in	In
P	Pression (Pa)	n	Tray or plate Number
Q	Heat (GJ/hr)	out	Out
R	Reflux (kg/hr)	$Qstrip$	Heat input to stripping column
S	Entropy (GJ/K-kg	$Qrect$	Heat input to rectification column
T	Temperature (K)	R	Rectification
V	Vapor flow (kg/hr)	Reb	Reboiler
W	Work (GJ/hr)	$Rect$	Rectification column
		S	Stripping
Superscripts		$steam$	Heating steam
$C1$	Conventional Column	$Strip$	Stripping column
$C2$	VRC	Val	Valve
$C3$	T-HIDiC	$watercool$	Cooling Water
irr	Irreversible		
$loss$	Exergy loss		
R	Rectification section		
S	Stripping section		

Acknowledgements

The authors thank to the Universidad Nacional de Colombia and Colciencias for supporting this research.

References

Boles, M. A., & Cengel, Yunus A. (2014). *Thermodynamics: An Engineering Approach*. McGraw-Hill Education. https://books.google.com.co/books?id=Ao95ngEACAAJ

de Koeijer, G., & Rivero, R. (2003). Entropy production and exergy loss in experimental distillation columns. *Chemical Engineering Science*, *58*(8), 1587–1597. https://doi.org/10.1016/S0009-2509(02)00627-9

Delmar, T. (2019). *An introduction to exergy and its evaluation using Aspen Plus*. University of Utah.

Gorak, A., & Sorensen, E. (2014). *Distillation: Fundamentals and Principles*. Academic Press.

Grassmann, P. (1959). The exergy and the flow diagram of the technically available power. *Allg Warmetech*, *9*, 79–86.

Jogwar, Sujit S. & Daoutidis, Prodromos (2009). Vapor Recompression Distillation: Multi-Scale Dynamics and Control. *Proceedings of Amer. Control Conference*, 647-652.

Kiss, A. A., & Olujić, Ž. (2014). A review on process intensification in internally heat-integrated distillation columns. *Chemical Engineering and Processing: Process Intensification*, *86*, 125–144. https://doi.org/10.1016/j.cep.2014.10.017

Kotas, T. J. (1995). *The exergy method of thermal plant analysis*. Krieger Pub.

Liu, X. G., & Qian, J. X. (2000). Modeling, Control, and Optimization of Ideal Internal Thermally Coupled Distillation Columns. *Chemical Engineering and Technology*, *23*(3), 235–241. https://doi.org/10.1201/b11330-2

Mancera, J. A., Mendoza, D. F., & Riascos, C. A. M. (2018). HIDiC configuration selection based on exergetic analysis. *Chemical Engineering Transactions*, *69*. https://doi.org/10.3303/CET1869151

Matsuda, K., Iwakabe, K., Ohmori, T., & Nakaiwa, M. (2010). Dynamic behavior of an internally heat-integrated distillation column (HIDiC). *Chemical Engineering Transactions*, *21*, 127–132. https://doi.org/10.3303/CET1021022

Mendoza, D. F., & Riascos, C. A. M. (2011). Entropy minimization in design of extractive distillation system with internal heat exchangers. *Chemical Engineering Transactions*, *25*, 405–410. https://doi.org/10.3303/CET1125068

Nakaiwa, M., Huang, K., Endo, A., Ohmori, T., Akiya, T., & Takamatsu, T. (2003). Internally heat-integrated distillation columns: A review. *Chemical Engineering Research and Design*, *81*(1), 162–177. https://doi.org/10.1205/026387603321158320

Nakaiwa, M, Huang, K., Owa, M., Akiya, T., Nakane, T., Sato, M., & Takamatsu, T. (1997). Energy savings in heat-integrated columns. *Energy*, *22*(6), 621–625.

Nakaiwa, Masaru, Huang, K., Naito, K., Endo, A., Akiya, T., Nakane, T., & Takamatsu, T. (2001). Parameter analysis and optimization of ideal heat integrated distillation columns. *Computers and Chemical Engineering*, *25*(4–6), 737–744. https://doi.org/10.1016/S0098-1354(01)00649-4

Oliveira, S. (2013). Exergy: Production, Cost and Renewability. In *Green Energy and Technology*. Springer. https://doi.org/10.2174/97816080528511060101

Pulido, J. L. (2008). Study of a New Concept of Distillation Column: Heat-Integrated Distillation Column (HIDiC). In *Bachelor Thesis in Chemical Engineering*. Industrial University of Santander.

Suphanit, B. (2010). Design of internally heat-integrated distillation column (HIDiC): Uniform heat transfer area versus uniform heat distribution. *Energy*, *35*(3), 1505–1514. https://doi.org/10.1016/j.energy.2009.12.008

Chapter 6

Preliminary conceptual design of a distillation column with energy integration (HIDiC)

Highlights

- *Problem:* There is no methodology available for the selection of the type of HIDiC configuration for the separation of a particular mixture.
- *Contribution:* A methodology for the preliminary conceptual design of HIDiC columns based on exergetic criteria was established.
- The methodology involves five global steps: simulation in a conventional distillation column, HIDiC simulation for top or base configuration based on estimated number of stages, definition of pressures with a minimum temperature difference criterion, performing exergetic balance, and comparing results for configuration selection.
- The design procedure and simulations were applied to a propylene-propane binary mixture separation.
- Results of the preliminary conceptual design showed the reduction in exergy losses for the selected HIDiC compared to a conventional distillation column.

Abstract

Several procedures have been defined for the success in the design of conventional distillation columns. Into these procedures, definition of operation pressure, reflux ratio, minimum number of stages, feed stage are key steps. For non-conventional columns, such as Heat Integrated Distillation Columns (HIDiC), the complexity of the system adds difficulties to the definition of starting values for design and operational variables. The objective of this study is to propose a methodology for the preliminary conceptual design of a Heat Integrated Distillation Columns considering exergetic efficiency. The methodology considers five global steps to achieve a rational design for a concentric HIDiC. It starts with the simulation of the separation in a conventional distillation column; then, with the obtained results, the HIDiC simulation is carried out, either for top or base configuration which depends on the estimation of the number of stages for each section. Into the HIDiC simulation, pressures definition must consider a minimum temperature difference criterion; Once achieved, the respective HIDiC configurations are simulated and the exergetic balance is performed, the results are compared for the selection of the configuration. The design procedure and simulations are applied for the separation of a propylene-propane binary mixture. The results of the preliminary conceptual design are presented and the reduction in exergy lost for the selected HIDiC is verified in comparison against a conventional distillation column.

Keywords: Conceptual design, heat integrated distillation column, HIDiC, exergy analysis.

6.1. Introduction

Distillation is one of the most energy-intensive processes in the chemical industries (Gorak & Sorensen, 2014). The low thermodynamic efficiency of distillation operations can be explained by the high energy loads demanded by condensers and reboilers, as well as by the temperature differences between them. Many distillation configurations have been proposed to increase thermodynamic efficiency, such as dividing wall column (DWC), vapor recompression column (VRC), diabatic distillation, and internally heat integrated distillation column (HIDiC). All these configurations have been analyzed by Kiss *et al.* (2012) and, as a result, applicability ranges for each distillation technology were proposed.

The first steps towards the latter technology were made by Mah et *al.* (1977) researching new ways of improving the energy efficiency of distillation methods. Nowadays, HIDiCs are especially suitable for the distillation of mixtures whose components have boiling points that are very close to each other(Kiss & Olujić, 2014; Marin *et al.*, 2018; Nakaiwa *et al.*, 2003; Olujic *et al.*, 2003; Sun *et al.*, 2003). Despite both types of distillation columns having some common elements, HIDiCs differ from conventional columns by virtue of its geometric configuration and its use of a compressor (CP) and an expansion valve (V), see Fig. 6-1. Moreover, whereas the distillation sections of conventional columns are located one above the other, the rectification section is located inside the stripping one in a HIDiC. Hence, a heat integration between both sections may be achieved: the compressor-valve system allows the pressure and temperature of the column to be adjusted, which, in turn, contributes to the system's arriving at a vapor-liquid equilibrium.

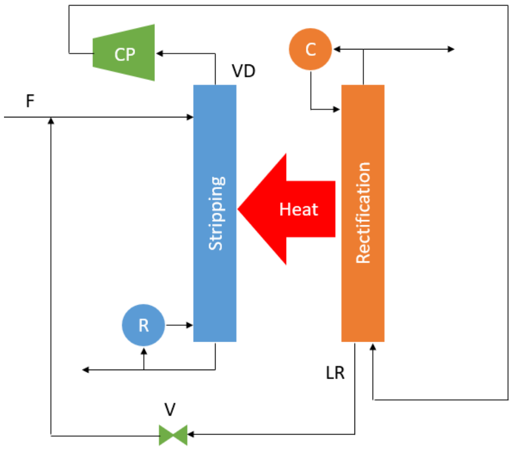

Figure 6-1: General representation of a HIDiC column

Concentric HIDiCs can be classified into basic and asymmetric HIDiCs. In basic HIDiCs, the rectification and stripping zones have an equal number of stages, while in asymmetric configurations the number of stages differs between sections. Basic HIDiCs can be subdivided into optimal feed columns and total HIDiCs. Asymmetric columns can be classified as top HIDiCs and bottom HIDiCs (Fig. 6-2).

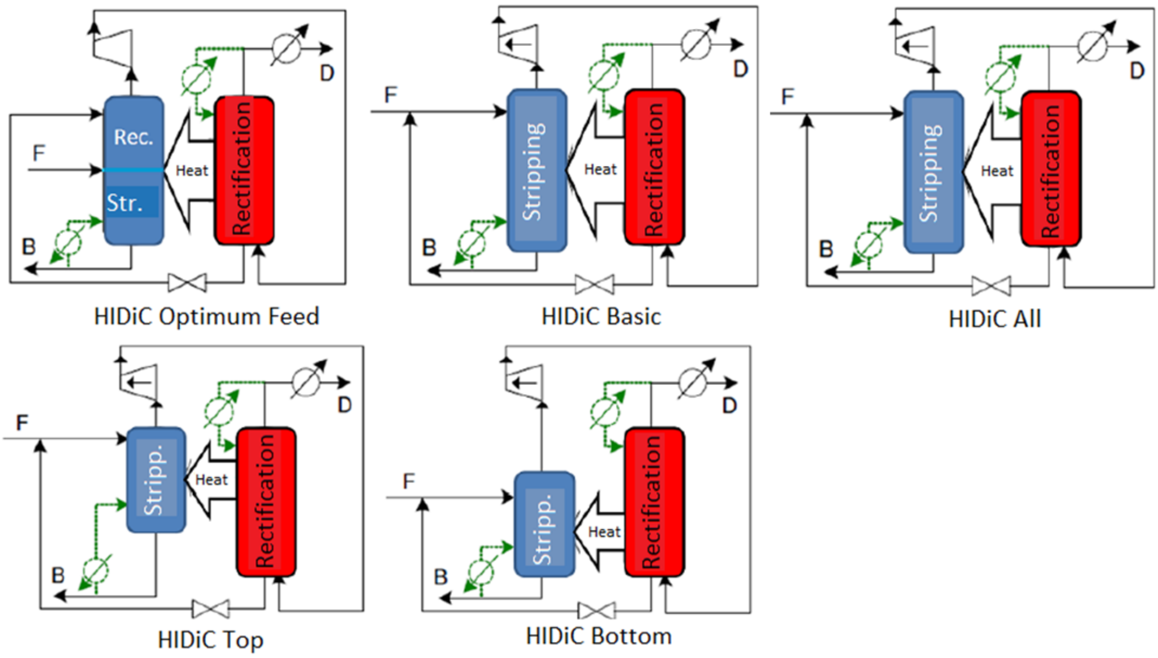

Figure 6-2: Configuration options for concentric HIDiC (Pulido, 2008)

Theoretical studies based on simulations and pilot-plant scale experiments (Naito *et al.*, 2000) show substantial energy savings (about 50%) when comparing HIDiCs against conventional columns in the separation of close boiling-point mixtures (Horiuchi *et al.*, 2008; Matsuda *et al.*, 2010). Furthermore, economic and controllability studies show the viability of implementing the HIDiC technology at an industrial scale (de Rijke, 2007; Harvindran & Foo, 2021; Olujić *et al.*, 2006; Ponce *et al.*, 2015). However, this implementation would also have significant issues, some of which were discussed in the previous chapters of this work and in other studies. For instance, the hydraulic behavior of HIDiCs (Chapter 2; Gadalla *et al.*, 2007), the heat and mass transfer phenomena associated with the internal heat integration and geometry of these type of columns (Chapter 4; de Rijke, 2007; Taylor & Krishna, 1993), and the need to find the most suitable HIDiC according to the characteristics of the system where it will be used (Chapter 1; Mancera *et al.*, 2018).

The first design stage is the conceptual design which focuses on the required main system characteristics according to the desired specification and application. In the case of conventional distillation columns, definition of operation pressure, reflux ratio, minimum number of stages, and feed stage are key factors to take into account in their conceptual design. In the case of non-conventional columns, such as HIDiCs, the system's special characteristics make it difficult to determine the starting values for the design and the operational variables.

Nowadays, methodologies for conceptual design of HIDiCs are based on pinch and hydraulic analysis (Gadalla *et al.*, 2005, 2007; Gadalla, 2009), economic criteria to find the optimal HIDiC configuration (Olujić *et al.*, 2006; Suphanit, 2010), and heat integration maximization (Marin *et al.*, 2018). The objective of this chapter is to propose a methodology for preliminary conceptual design of heat integrated distillation columns taking exergetic efficiency into account.

6.2. Methodology

In this section, a methodology for basic HIDiC design is presented. This methodology (see Figure 6-3) comprises five steps to ensure an optimal exergy-based design for HIDiC.

Step 1. System characterization and the separation task: In this step, the binary system to purify must be chosen, and the feed conditions (q, temperature, flow, composition, and pressure), and composition of the distillate and bottom products (X_D, X_B) must be determined. If the mixture has an azeotropic point, or if the normal boiling point difference (ΔT_b) is greater than 10°C, it is suggested to follow the procedure recommended by Kiss *et al.* (2012) instead of using HIDiC technology. However, if that is not the case, the procedure continues with a shortcut method (Fenske-Underwood-Gilliland-Kirkbride, FUGK) to estimate the number of theoretical stages, the flow ratio, the feeding stage, and the energy consumption in the condenser and reboiler. Then, a rigorous method (MESH: mass-equilibrium-sum of fractions-enthalpy balance equations) follows without taking into account pressure drop at stages and fixing the pressure to reduce condensation costs. This method is used to obtain the initial values for HIDiC design.

Step 2. Definition of HIDiC type and compression ratio: In this step, based on the results obtained from step 1, the first HIDiC analysis is developed. If the number of stages in the rectification section is 1.25 times greater than the number of stages in the stripping section (or vice versa), a top HIDiC is analyzed, otherwise, a basic HIDiC is preferred. If a basic HIDiC system is chosen, stages must be added to the smaller section in order to equalize the number of stages in both sections ($N_R = N_S$).

To define the compression ratio between the column sections, the point with the greatest temperature difference is identified while both sections operate adiabatically at the same pressure (Figure 6-4a), with the liquid compositions at the identified point. Then, the pressure in the rectification zone is increased by starting from a suggested delta P. This parameter can come from the literature for a similar system or for the same system but in similar columns that are not HIDiC and that work with a pressure difference between the sections; for example, the VRC. In case of not having some basic information, we start with an increase of 10%. A temperature vs. stage plot is then made to identify the minimum temperature difference (ΔT_{min}) between the columns, as shown in Figure 6-4b. The recommended minimum temperature difference is 3°C (Gadalla et al., 2007; Gadalla, 2009; Marin *et al.*, 2018; Suphanit, 2010). If ΔT_{min} is less than 3°C, the pressure difference between columns is increased by a further 10% in the rectification column. This step is repeated until ΔT_{min} is greater or equal to 3°C.

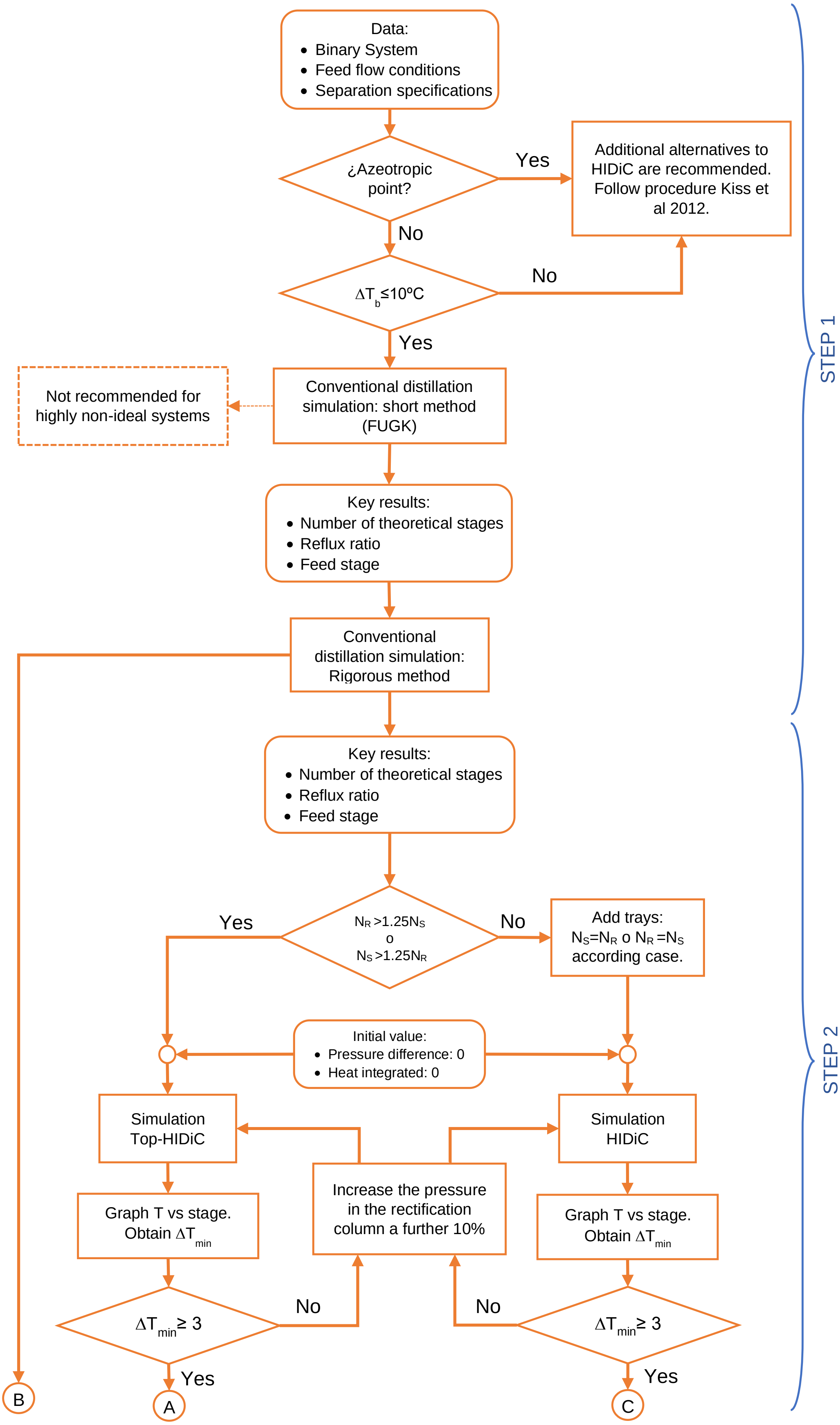

Data:
Binary System
Feed flow conditions
Separation specifications
¿Azeotropic point?
Yes
Additional alternatives to HIDiC are recommended. Follow procedure Kiss et al 2012.
No
ΔTb≤10ºC
No
Yes
Not recommended for highly non-ideal systems
Conventional distillation simulation: short method (FUGK)
Key results:
Number of theoretical stages
Reflux ratio
Feed stage
Conventional distillation simulation: Rigorous method
Key results:
Number of theoretical stages
Reflux ratio
Feed stage
NR >1.25NS o NS >1.25NR
Yes
No
Add trays: NS=NR o NR =NS according case.
Initial value:
Pressure difference: 0
Heat integrated: 0
Simulation Top-HIDiC
Simulation HIDiC
Increase the pressure in the rectification column a further 10%
Graph T vs stage. Obtain ΔTmin
Graph T vs stage. Obtain ΔTmin
ΔTmin≥ 3
No
No
ΔTmin≥ 3
Yes
Yes
B
A
C
STEP 1
STEP 2

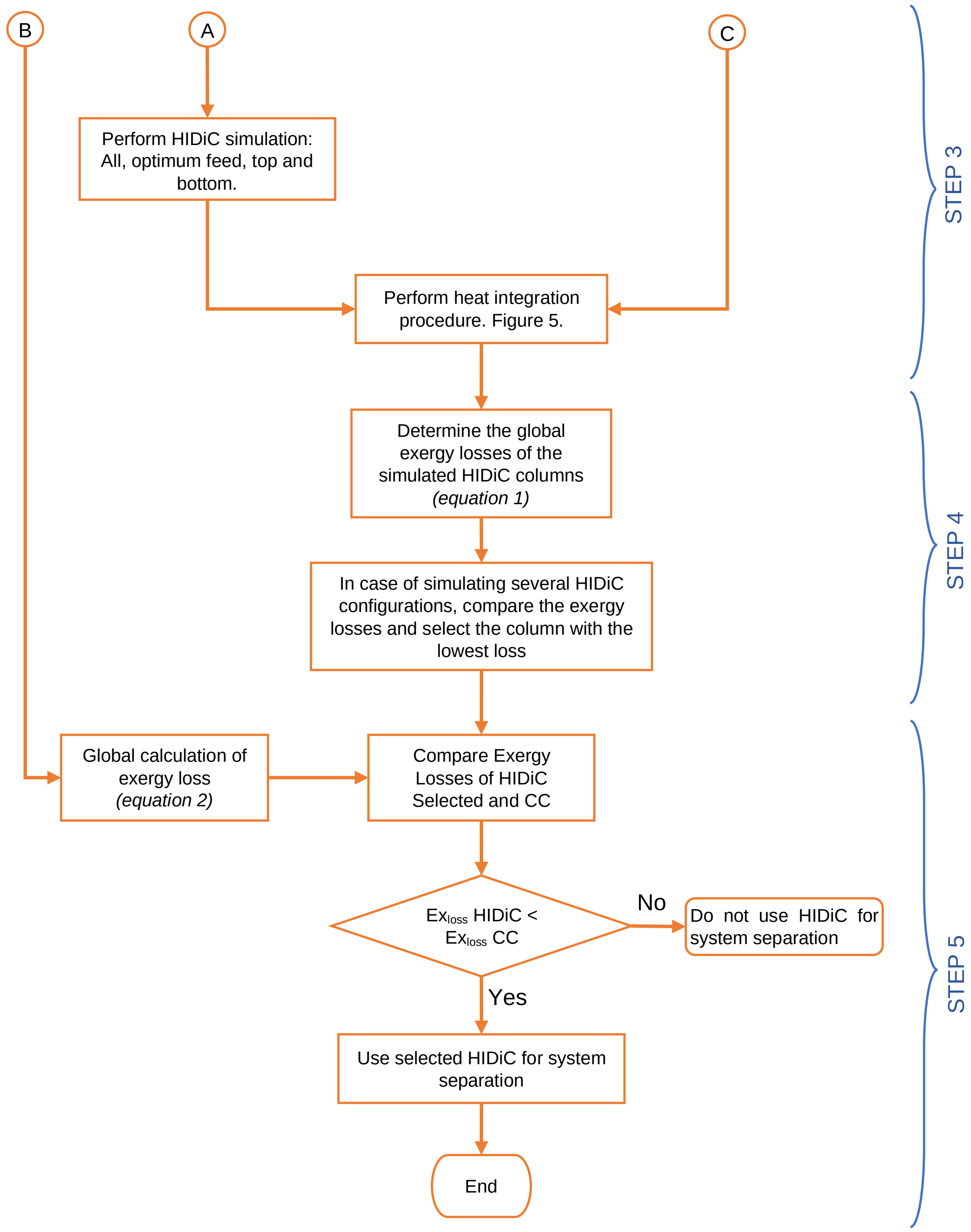

Figure 6-3: HIDiC Preliminary Design Procedure Flow Chart

Step 3. Definition of heat distribution: This step depends on the type of HIDiC simulated in the previous step. In the case of top HIDiC, three configurations (total, optimal feed, and bottom) are evaluated using the pressure difference obtained in step 2 and proceeding to find the heat distribution for each configuration according to Figure 6-5. If the selected HIDiC type is the basic HIDiC, the heat integration is obtained using the pressure difference found in step 2 (Figure 6-5).

Step 4. Determination of exergy loss: In this step, an exergy analysis of the selected configuration is performed. In the case of simulating different configurations, the selected column will be the one with the lowest exergy loss.

Step 5. Analysis of results: Finally, in this step, the exergy losses of the selected HIDiC are compared with those of the conventional column. The one with the lowest exergy losses is selected.

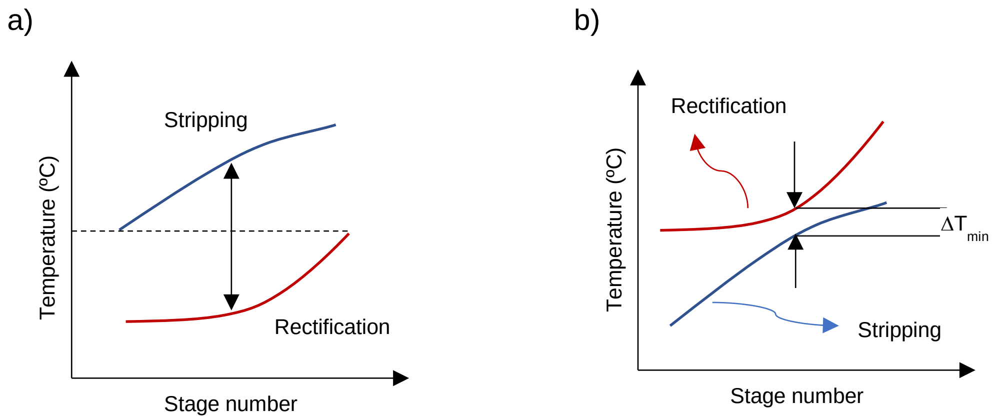

Figure 6-4: Temperature profile per stage before (a) and after (b) pressure setting

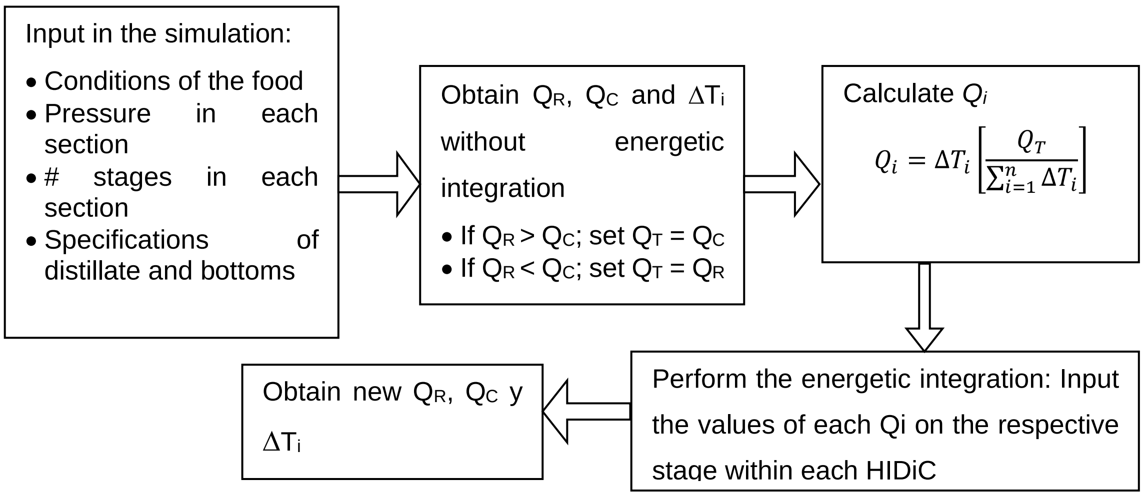

Figure 6-5: Estimation procedure of the heat flow distribution between the rectification section and the stripping section

6.3. Results and discussion

The results are presented by means of a case study. In this case, the separation of a propane-propylene mixture.

Step 1

The Peng-Robinson equation of state is used to describe the phase equilibrium. The feed composition is 50% (mol) of each component and a mass flow of 112000 kg/h. A summary of the specifications is shown in Table 6-1.

Table 6-1: Feed Flow Specifications and Separation Conditions

Features	Values
Feed flow (kg/h)	112000
Fraction mol feed (propylene)	0.57
Thermal condition feed (q)	0.37
Fraction mol distillate (propylene)	0.996
Fraction mol bottoms (propylene)	0.011
Operation pressure (bar)	11.2

The calculation of ΔTb for the system is 7.7 °C and the simulation is performed using the FUGK shortcut method. The results are shown in Table 6-2.

Table 6-2: Results of the short method for the case study

Features	Value
Reflux ratio	13.83
Stages rectification section	98
Stages stripping section	54
Feeding stage	99
Duty boiler (GJ/h)	299.96
Duty condenser (GJ/h)	313.69
Pressure (bar)	11.2

The parameters for the conventional simulation of the column using the rigorous method (MESH) are based on the results obtained using the shortcut results (Table 6-2). The rigorous simulation results, Table 6-3, are used as starting values to initialize the HIDiC simulation. The separation specifications are the propylene composition in the distillate and bottom streams. The design variables are the distillate flow and reflux ratio.

Table 6-3: Results of the rigorous method for the case study

Features	Value
Reflux ratio	17.15
Stages rectification section	98
Stages stripping section	54
Feeding stage	99
Duty boiler (GJ/h)	341.78
Duty condenser (GJ/h)	355.48
Pressure (bar)	11.2

Step 2.

According to the results obtained in Step 1, the number of stages of the rectification zone is greater than 1.25 times the number of stages of the stripping zone (98 > 1.25 × 54). Therefore, the Top HIDiC is the best choice to be simulated. The initialization parameters for the Top HIDiC are summarized in Table 6-4.

Table 6-4: HIDiC simulation initialization conditions

Features	Value
Reflux ratio	17.15
Stages rectification section	98
Stages stripping section	54
Feeding stage	99
Pressure (bar)	11.2

The objective of this step is to determine the pressure difference between the columns making sure that there is a minimum temperature difference of 3 °C to ensure proper column operation. The simulation is run using different pressures in the compressor according to the stablished methodology, and then the temperature difference in both sections is calculated. Table 6-5 shows the pressures evaluated together with the maximum, minimum and average temperature differences. The selected pressure difference is 3.4 bar, which yields a temperature difference of 3.76 °C, meeting the requirement. This pressure difference is selected since its cost is lower than that of a 4.48 bar column. The calculated reflux ratio for the chosen column is 20.48 to meet the separation specifications.

Table 6-5: Evolution of the temperature difference between the internal and external column according to the pressure difference

Stripping column pressure (bar)	Rectification column pressure (bar)	Pressure difference (bar)	ΔT_{min} (ºC)	ΔT_{max} (ºC)	ΔT_{aver} (ºC)
11.2	11.2	0	-7.13	-2.35	-4.69
11.2	12.32	1.11	-3.30	1.51	-0.84
11.2	13.44	2.24	0.28	5.13	2.77
11.2	14.6	3.4	3.76	8.66	6.28
11.2	15.68	4.48	6.82	11.76	9.37

Step 3:

Simulation of different HIDiC configurations (total, optimal feed, top, and bottom), using the pressure difference found in Step 2, is performed to find proper heat integration, as shown in Figure 5. A summary of the results is presented in Table 6-6.

Table 6-6: Operational conditions of the different HIDiC configurations

Features	Top-HIDiC	Bottom-HIDiC	Feed opt.-HIDiC	All-HIDiC
Rectification section Pressure (bar)	14.6	14.6	14.6 – 11.2	14.6
Stripping section pressure (bar)	11.2	11.2	11.2	11.2
Stages rectification section	98	98	98	98
Stages stripping section	54	54	54	54
Feeding stage	99	99	99	99
Trays in the Concentric Column	97	97	75	97
Trays in the Annular column	53	53	75	53
Feed flow (kg / h)	112000	112000	112000	112000
Fraction mol feed (propylene)	0.57	0.57	0.57	0.57
Thermal condition feed (q)	0.37	0.37	0.37	0.37
Fraction mol distillate (propylene)	0.996	0.996	0.996	0.996
Fraction mol bottoms (propylene)	0.011	0.011	0.011	0.011

Step 4:

The overall exergy loss of each configuration is calculated using Equation 1.

$$Ex^{loss} = S\left(Ex_{steam,in} - Ex_{steam,out}\right) + A\left(Ex_{watercool,in} - Ex_{watercool,out}\right) + W_{compressor} + FEx_F - DEx_D - BEx_B \quad (eq.1)$$

The results regarding exergy loss in the top, bottom, total, and optimal feed are shown in Table 6-7. It can be seen that the HIDiC with the lowest exergy loss is the top HIDiC, so this is the HIDiC of choice.

Table 6-7: Exergy losses of the different HIDiC configurations

Type of HIDiC	Loss exergy (GJ/h)
Top	49.58
All	49.77
Optimum Feed	68.69
Bottom	95.64

Step 5:

The exergy loss of the conventional column is obtained using Equation 2. This value is compared with the one obtained with the HIDiC selected in Step 4

$$Ex^{loss} = S\left(Ex_{steam,in} - Ex_{steam,out}\right) + A\left(Ex_{watercool,in} - Ex_{watercool,out}\right) + FEx_F - DEx_D - BEx_B \quad (eq.2)$$

A comparison of exergy loss between the Top HIDiC and the conventional columns, Table 6-8, shows that the Top HIDiC is more efficient than the conventional column (about 50% lower exergy loss).

Table 6-8: Loss exergy from the Top-HIDiC and the conventional column

Type of column	**Exergy loss (GJ/h)**
Top-HIDiC	49.58
Conventional	99.32

6.4. Conclusions and recommendations

Exergy is a good benchmark to evaluate the suitability of using a HIDiC for a separation task, as it ensures energy efficient designs. The proposed methodology aims to contribute to the development of a conceptual design methodology for thermodynamically efficient columns.

It is recommended to develop design methodologies that combine thermodynamic and economic assessment of different types of HIDiC columns. In this particular case study, an economic analysis is recommended since the exergy losses in Top and Total HIDiCs are similar.

Nomenclature

A	Water flow (kg/h)
B	Bottom flow (kg/h)
D	Distillation flow (kg/h)
Ex	Exergy (GJ/kg)
F	Feed flow (kg/h)
N	Stages
Q	Heat flow (GJ/h)
S	Vapor flow (kg/h)
T	Temperature (ºC)
W	Work (GJ/h)

Subscripts

B	Bottom stream
B	Boiling point
c	Condenser
$Compressor$	Compressor
D	Distillation stream
F	Feed stream
in	Inlet
$loss$	Exergy loss
max	Maxime
min	Minimum
n	Integrated tray pair
out	Outlet
prom	Average
R	Reboiler
Re	Rectification column
S	Stripping column
$steam$	Steam
T	Total
$watercool$	Cool water

Greek Symbols

Δ	Difference

References

de Rijke, A. (2007). *Development of a Concentric Internally Heat Integrated Distillation Column (HIDiC)*. Delft University of Technology, Netherlands.

Gadalla, M. A. (2009). Internal heat integrated distillation columns (iHIDiCs)-New systematic design methodology. *Chemical Engineering Research and Design*, *87*(12), 1658–1666. https://doi.org/10.1016/j.cherd.2009.06.005

Gadalla, M., Jiménez, L., Olujic, Z., & Jansens, P. J. (2007). A thermo-hydraulic approach to conceptual design of an internally heat-integrated distillation column (i-HIDiC). *Computers and Chemical Engineering*, *31*(10), 1346–1354. https://doi.org/10.1016/j.compchemeng.2006.11.006

Gadalla, M., Olujic, Z., Sun, L., de Rijke, A., & Jansens, P. J. (2005). Pinch analysis-based approach to conceptual design of internally heat-integrated distillation columns. *Chemical Engineering Research and Design*, *83*(8 A), 987–993. https://doi.org/10.1205/cherd.04301

Gorak, A., & Sorensen, E. (2014). *Distillation: Fundamentals and Principles*. Academic Press.

Harvindran, V., & Foo, D. C. Y. (2021). Design of Internally Heat-Integrated Distillation Column (HIDiC). *Process Intensification and Integration for Sustainable Design*, 117–129. https://doi.org/10.1002/9783527818730.ch6

Horiuchi, K., Nakaiwa, M., Iwakabe, K., Matsuda, K., & Toda, M. (2008). Intensification of the process flow in the pilot plant of an internally heat-integrated distillation column (HIDiC). *Kagaku Kogaku Ronbunshu*, *34*(1), 70–75. https://doi.org/10.1252/kakoronbunshu.34.70

Kiss, A. A., Flores Landaeta, S. J., & Infante Ferreira, C. A. (2012). Towards energy efficient distillation technologies - Making the right choice. *Energy*, *47*(1), 531–542. https://doi.org/10.1016/j.energy.2012.09.038

Kiss, A. A., & Olujić, Ž. (2014). A review on process intensification in internally heat-integrated distillation columns. *Chemical Engineering and Processing: Process Intensification*, *86*, 125–144. https://doi.org/10.1016/j.cep.2014.10.017

Mah, R. S. H., Nicholas, J. J., & Wodnik, R. B. (1977). Distillation with secondary reflux and vaporization: A comparative evaluation. *AIChE Journal*, *23*(5), 651–658. https://doi.org/10.1002/aic.690230505

Mancera, J. A., Mendoza, D. F., & Riascos, C. A. M. (2018). HIDiC configuration selection based on exergetic analysis. *Chemical Engineering Transactions*, *69*. https://doi.org/10.3303/CET1869151

Marin, M. D., Meyer, M., Mizzi, B., & Rouzineau, D. (2018). New conceptual design methodology for a concentric heat integrated distillation column (HIDiC). *Chemical Engineering Transactions*, *69*, 883–888. https://doi.org/10.3303/CET1869148

Matsuda, K., Iwakabe, K., Ohmori, T., & Nakaiwa, M. (2010). Dynamic behavior of an internally heat-integrated distillation column (HIDiC). *Chemical Engineering Transactions*, *21*, 127–132. https://doi.org/10.3303/CET1021022

Naito, K., Nakaiwa, M., Huang, K., Endo, A., Aso, K., Nakanishi, T., Nakamura, T., Noda, H., & Takamatsu, T. (2000). Operation of a bench-scale ideal heat integrated distillation column (HIDiC): An experimental study. *Computers and Chemical Engineering*, *24*(2–7), 495–499. https://doi.org/10.1016/S0098-1354(00)00513-5

Nakaiwa, M., Huang, K., Endo, A., Ohmori, T., Akiya, T., & Takamatsu, T. (2003). Internally heat-integrated distillation columns: A review. *Chemical Engineering Research and Design*, *81*(1), 162–177. https://doi.org/10.1205/026387603321158320

Olujic, Z., Fakhri, F., De Rijke, A., De Graauw, J., & Jansens, P. J. (2003). Internal heat integration - The key to an energy-conserving distillation column. *Journal of Chemical Technology and Biotechnology*, *78*(2–3), 241–248. https://doi.org/10.1002/jctb.761

Olujić, Ž., Sun, L., de Rijke, A., & Jansens, P. J. (2006). Conceptual design of an internally heat integrated propylene-propane splitter. *Energy*, *31*(15), 3083–3096. https://doi.org/10.1016/j.energy.2006.03.030

Ponce, G. H. S. F., Alves, M., Miranda, J. C. C., Maciel Filho, R., & Wolf Maciel, M. R. (2015). Using an internally heat-integrated distillation column for ethanol-water separation for fuel applications. *Chemical Engineering Research and Design*, *95*, 55–63. https://doi.org/10.1016/j.cherd.2015.01.002

Pulido, J. L. (2008). Study of a New Concept of Distillation Column: Heat-Integrated Distillation Column (HIDiC). In *Bachelor Thesis in Chemical Engineering*. Industrial University of Santander.

Sun, L., De Rijke, A., Olujic, Z., & Jansens, P. (2003). *Process innovation and intensification*.

Suphanit, B. (2010). Design of internally heat-integrated distillation column (HIDiC): Uniform heat transfer area versus uniform heat distribution. *Energy*, *35*(3), 1505–1514. https://doi.org/10.1016/j.energy.2009.12.008

Taylor, R., & Krishna, R. (1993). *Multicomponent Mass Transfer*. Wiley, New York.

Future works

As the field of Computational Fluid Dynamics (CFD) continues to advance, its potential for revolutionizing the analysis of distillation columns becomes increasingly evident. Some of the future works that could be carried out at a general level are:

1. Multi-Scale Modeling for Enhanced Accuracy: Future research could delve into multi-scale modeling, combining macroscopic CFD simulations with microscopic molecular simulations. This fusion could offer a more comprehensive understanding of phenomena occurring at different length scales within the column, leading to more accurate predictions.
2. Integration of Reaction Kinetics: Incorporating reaction kinetics into CFD models opens up possibilities for studying reactive distillation columns. Investigating chemical reactions, coupled with fluid dynamics and heat transfer, could lead to innovations in optimizing both separation efficiency and reaction yields.
3. Multi-Objective Optimization: Exploring multi-objective optimization techniques within the CFD framework offers the potential to simultaneously optimize conflicting objectives, such as separation efficiency and energy consumption. This could lead to Pareto-optimal solutions that strike a balance between competing goals.
4. Advanced Visualization for Insights: Incorporating advanced visualization techniques, such as virtual reality or augmented reality, could transform the way we interpret CFD results. Researchers could interact with simulations in real-time, facilitating deeper insights into fluid behavior and column dynamics.
5. Machine Learning Integration: The integration of machine learning algorithms with CFD simulations holds promise for accelerating convergence, automating parameter tuning, and enhancing predictive capabilities. This synergy could lead to faster and more efficient column analysis.

More specifically, based on this thesis, some of the works that could be continued would be the following: T-HIDiC Column Design Optimization, simulation by CFD with other types of plates (bubble caps, valves) and other types of material in the structure of the plate, implementation of different types of descent channels and of different types of weirs, integration with other separation technologies such as extractive distillation, integration of Artificial Intelligent-Aspen-Ansys Fluent, include in the exergetic analysis the chemical exergy, study of new systems like air distillation (HIDiC applications), and to include structural analysis of the HIDiC column along with fluid dynamics and exergy.

Bibliography

Bejan, A. (2013). Entropy generation minimization: the method of thermodynamic optimization of finite-size systems and finite-time processes. CRC press.

Hanley, N., McGregor, P., Swales, J., & Tuner, K. (2009). Do increases in resource productivity improve environmental quality and sustainability? Ecological Economics, 68(3), 692–709. https://dspace.stir.ac.uk/bitstream/1893/7707/1/Hanley et al Ecological Economics 2009_turner last.pdf

Hepbasli, A. (2008). A key review on exergetic analysis and assessment of renewable energy resources for a sustainable future. Renewable and Sustainable Energy Reviews, 12(3), 593–661. https://doi.org/10.1016/j.rser.2006.10.001

Kemp, I. C. (2007). Pinch Analysis and Process Integration: A User Guide on Process Integration for the Efficient Use of Energy (I. C. B. T.-P. A. and P. I. (Second E. Kemp (ed.); Second). Butterworth-Heinemann. https://doi.org/https://doi.org/10.1016/B978-075068260-2.50006-7

Kotas, T. J. (1995). The exergy method of thermal plant analysis. Krieger Pub.

Krishna, R., & Van Baten, J. M. (2003). Modelling sieve tray hydraulics using computational fluid dynamics. Chemical Engineering Research and Design, 81(1), 27–38. https://doi.org/10.1205/026387603321158168

Morar, M., & Agachi, P. S. (2010). Review: Important contributions in development and improvement of the heat integration techniques. Computers and Chemical Engineering, 34(8), 1171–1179. https://doi.org/10.1016/j.compchemeng.2010.02.038

Nakaiwa, M., Huang, K., Endo, A., Ohmori, T., Akiya, T., & Takamatsu, T. (2003). Internally heat-integrated distillation columns: A review. Chemical Engineering Research and Design, 81(1), 162–177. https://doi.org/10.1205/026387603321158320

Sun, A. (2010). Internal heat exchange in a concentric tray heat integrated distillation column (HIDiC). DELF UNIVERSITY OF TECHNOLOGY.

Tu, J., Yeoh, G. H., & Liu, C. (2018). Computational fluid dynamics: a practical approach (Third). Butterworth-Heinemann.

González Plaza, M., Ferreira, A., Santos, J., Ribeiro, A., Müller, U., Trukhan, N., Loureiro, J., & Rodrigues, A. (2011). Propane/propylene separation by adsorption using shaped copper trimesate MOF. Microporous and Mesoporous Materials - MICROPOROUS MESOPOROUS MAT, 157. https://doi.org/10.1016/j.micromeso.2011.06.024

Kiss, A. A., & Olujić, Ž. (2014). A review on process intensification in internally heat-integrated distillation columns. Chemical Engineering and Processing: Process Intensification, 86, 125–144. https://doi.org/10.1016/j.cep.2014.10.017

Liu, X. G., & Qian, J. X. (2000). Modeling, Control, and Optimization of Ideal Internal Thermally Coupled Distillation Columns. Chemical Engineering and Technology, 23(3), 235–241. https://doi.org/10.1201/b11330-2

Matsuda, K., Iwakabe, K., Ohmori, T., & Nakaiwa, M. (2010). Dynamic behavior of an internally heat-integrated distillation column (HIDiC). Chemical Engineering Transactions, 21, 127–132. https://doi.org/10.3303/CET1021022

Mendoza, D. F., Palacio, L. M., Graciano, J. E. A., Riascos, C. A. M., Vianna, A. S., & Roux, G. A. C. Le. (2013). Real-Time Optimization of an Industrial-Scale Vapor Recompression Distillation Process . Model Validation and Analysis. Industrial and Engineering Chemistry Research, 52, 5735–5746.

Mendoza, D. F., & Riascos, C. A. M. (2011). Entropy minimization in design of extractive distillation system with internal heat exchangers. Chemical Engineering Transactions, 25, 405–410. https://doi.org/10.3303/CET1125068

Nakaiwa, M., Huang, K., Naito, K., Endo, A., Akiya, T., Nakane, T., & Takamatsu, T. (2001). Parameter analysis and optimization of ideal heat integrated distillation columns. Computers and Chemical Engineering, 25(4–6), 737–744. https://doi.org/10.1016/S0098-1354(01)00649-4

Nakaiwa, M., Huang, K., Owa, M., Akiya, T., Nakane, T., Sato, M., & Takamatsu, T. (1997). Energy savings in heat-integrated columns. Energy, 22(6), 621–625.

Olujić, Ž., Sun, L., de Rijke, A., & Jansens, P. J. (2006). Conceptual design of an internally heat integrated propylene-propane splitter. Energy, 31(15), 3083–3096. https://doi.org/10.1016/j.energy.2006.03.030

Pulido, J. L. (2008). Study of a New Concept of Distillation Column: Heat-Integrated Distillation Column (HIDiC). In Bachelor Thesis in Chemical Engineering. Industrial University of Santander

Suphanit, B. (2010). Design of internally heat-integrated distillation column (HIDiC): Uniform heat transfer area versus uniform heat distribution. Energy, 35(3), 1505–1514. https://doi.org/10.1016/j.energy.2009.12.008

ANSYS Release 19. (2018). ANSYS Fluent Theory Guide.

Bennett, D. L., Agrawal, R., & Cook, P. J. (1983). New pressure drop correlation for sieve tray distillation columns. AIChE Journal, 29(3), 434–442. https://doi.org/10.1002/aic.690290313

Bhole, M. R., Joshi, J. B., & Ramkrishna, D. (2008). CFD simulation of bubble columns incorporating population balance modeling. Chemical Engineering Science, 63(8), 2267–2282. https://doi.org/10.1016/j.ces.2008.01.013

Chen, G., Xiong, Q., Morris, P. J., Paterson, E. G., Sergeev, A., & Wang, Y.-C. (2014). OpenFOAM for Computational Fluid Dynamics. Notices of the American Mathematical Society, 61(4), 354. https://doi.org/10.1090/noti1095

Gesit, G., Nandakumar, K., & Chuang, K. T. (2003). CFD modeling of flow patterns and hydraulics of commercial-scale sieve trays. AIChE Journal, 49(4), 910–924. https://doi.org/10.1002/aic.690490410

Grace, J. R., Wairegi, T., & Brophy, J. (1978). Break-up of drops and bubbles in stagnant media. The Canadian Journal of Chemical Engineering, 56(1). https://doi.org/10.1002/cjce.5450560101

Gupta, A., & Roy, S. (2013). Euler-Euler simulation of bubbly flow in a rectangular bubble column: Experimental validation with Radioactive Particle Tracking. Chemical Engineering Journal, 225. https://doi.org/10.1016/j.cej.2012.11.012

Hofer, H. (1983). Influence of gas-phase dispersion on plate column efficiency. German Chemical Engineering, 6(2).

Ishii, M., & Zuber, N. (1979). Drag coefficient and relative velocity in bubbly, droplet or particulate flows. AIChE Journal, 25(5), 843–855. https://doi.org/10.1002/aic.690250513

Kaltenbacher, E. (1984). On the Effect of the Bubble Size Distribution and the Gas-Phase Diffusion on the Selectivity of Sieve Trays. Chemical Engineering Fundamentals, 1(47).

Kataoka, I., & Serizawa, A. (1989). Basic equations of turbulence in gas-liquid two-phase flow. International Journal of Multiphase Flow, 15(5). https://doi.org/10.1016/0301-9322(89)90045-1

Krishna, R., Urseanu, M. I., Van Baten, J. M., & Ellenberger, J. (1999). Rise velocity of a swarm of large gas bubbles in liquids. Chemical Engineering Science, 54(2), 171–183. https://doi.org/10.1016/S0009-2509(98)00245-0

Krishna, R., Van Baten, J. M., Ellenberger, J., Higler, A. P., & Taylor, R. (1999). CFD simulations of sieve tray hydrodynamics. Chemical Engineering Research and Design, 77(7), 639–646. https://doi.org/10.1205/026387699526575

Laborde-Boutet, C., Larachi, F., Dromard, N., Delsart, O., & Schweich, D. (2009). CFD simulation of bubble column flows: Investigations on turbulence models in RANS approach. Chemical Engineering Science, 64(21). https://doi.org/10.1016/j.ces.2009.07.009

Li, X., Yang, N., Sun, Y., Zhang, L., Li, X., & Jiang, B. (2014). Computational fluid dynamics modeling of hydrodynamics of a new type of fixed valve tray. Industrial and Engineering Chemistry Research, 53(1), 379–389. https://doi.org/10.1021/ie400408u

Liang, X. F., Pan, H., Su, Y. H., & Luo, Z. H. (2016). CFD-PBM approach with modified drag model for the gas–liquid flow in a bubble column. Chemical Engineering Research and Design, 112, 88–102. https://doi.org/10.1016/j.cherd.2016.06.014

Lockett, M. J. (1986). Distillation tray fundamentals. Cambridge University Press.

Lockett, M. J., Kirkpatrick, R. D., & Uddin, M. S. (1979). Froth regime point efficiency for gas-film controlled mass transfer on a two-dimensional sieve tray. Trans Inst Chem Eng, 57(1).

Lopez de Bertodano M, Lahey RT, J. O. (1994). Development of a k-e model for bubbly two-phase flow. Journal of Fluids Engineering, 116. https://doi.org/https://doi.org/10.1115/1.2910220

Lote, D. A., Vinod, V., & Patwardhan, A. W. (2018). Comparison of models for drag and non-drag forces for gas-liquid two-phase bubbly flow. Multiphase Science and Technology, 30(1), 31–76. https://doi.org/10.1615/MultScienTechn.2018025983

Magolan, B., Lubchenko, N., & Baglietto, E. (2019). A quantitative and generalized assessment of bubble-induced turbulence models for gas-liquid systems. Chemical Engineering Science: X, 2, 100009. https://doi.org/10.1016/j.cesx.2019.100009

Rahimi, R., Mazarei Sotoodeh, M., & Bahramifar, E. (2012). The effect of tray geometry on the sieve tray efficiency. Chemical Engineering Science, 76, 90–98. https://doi.org/10.1016/j.ces.2012.01.006

Roshdi, S., Kasiri, N., Hashemabadi, S. H., & Ivakpour, J. (2013). Computational fluid dynamics simulation of multiphase flow in packed sieve tray of distillation column. Korean Journal of Chemical Engineering, 30(3), 563–573. https://doi.org/10.1007/s11814-012-0166-1

Rzehak, R., & Krepper, E. (2013a). Bubble-induced turbulence: Comparison of CFD models. Nuclear Engineering and Design, 258, 57–65. https://doi.org/10.1016/j.nucengdes.2013.02.008

Rzehak, R., & Krepper, E. (2013b). CFD modeling of bubble-induced turbulence. International Journal of Multiphase Flow, 55, 138–155. https://doi.org/10.1016/j.ijmultiphaseflow.2013.04.007

Sadripour, M., Rahimi, A., & Hatamipour, M. S. (2012). Experimental Study and CFD Modeling of Wall Deposition in a Spray Dryer. Drying Technology, 30(6), 574–582. https://doi.org/10.1080/07373937.2011.653613

Sato, Y., Sadatomi, M., & Sekoguchi, K. (1981). Momentum and heat transfer in two-phase bubble flow-I. Theory. International Journal of Multiphase Flow, 7(2). https://doi.org/10.1016/0301-9322(81)90003-3

Schiller, L., & Naumann, Z. (1935). A drag coefficient correlation. In Z.Ver.Deutsch.Ing (Vol. 77, Issues 13–14). https://doi.org/10.1016/j.ijheatmasstransfer.2009.02.006

Simonin, O., & Viollet, P. L. (1990). Prediction of an oxygen droplet pulverization in a compressible subsonic coflowing hydrogen flow. American Society of Mechanical Engineers, Fluids Engineering Division (Publication) FED, 91.

Sun, Z. M., Liu, B., Yuan, X. G., Liu, C. J., & Yu, K. T. (2005). New turbulent model for computational mass transfer and its application to a commercial-scale distillation column. Industrial and Engineering Chemistry Research, 44(12), 4427–4434. https://doi.org/10.1021/ie049382y

Tomiyama, A. (1998). Struggle with computational bubble dynamics. Multiphase Sci Technol. Multiphase Science Technology, 10.

Treybal, R. E. (1981). Mass Transfer Operations 3th edition. In McGraw-Hill.

Troshko, A. A., & Hassan, Y. A. (2001). A two-equation turbulence model of turbulent bubbly flows. International Journal of Multiphase Flow, 27(11). https://doi.org/10.1016/S0301-9322(01)00043-X

Van Baten, J. M., Ellenberger, J., & Krishna, R. (2001). Hydrodynamics of reactive distillation tray column with catalyst containing envelopes: Experiments vs. CFD simulations. Catalysis Today, 66(2–4), 233–240. https://doi.org/10.1016/S0920-5861(00)00625-8

Wang, T., & Wang, J. (2007). Numerical simulations of gas-liquid mass transfer in bubble columns with a CFD-PBM coupled model. Chemical Engineering Science, 62(24), 7107–7118. https://doi.org/10.1016/j.ces.2007.08.033

Wang, T., Wang, J., & Jin, Y. (2005). Population balance model for gas - Liquid flows: Influence of bubble coalescence and breakup models. Industrial and Engineering Chemistry Research, 44(19), 7540–7549. https://doi.org/10.1021/ie0489002

Wang, T., Wang, J., & Jin, Y. (2006). A CFD-PBM coupled model for gas-liquid flows. AIChE Journal, 52(1), 125–140. https://doi.org/10.1002/aic.10611

Xing, C., Wang, T., & Wang, J. (2013). Experimental study and numerical simulation with a coupled CFD-PBM model of the effect of liquid viscosity in a bubble column. Chemical Engineering Science, 95, 313–322. https://doi.org/10.1016/j.ces.2013.03.022

Yang, G., Guo, K., & Wang, T. (2017). Numerical simulation of the bubble column at elevated pressure with a CFD-PBM coupled model. Chemical Engineering Science, 170, 251–262. https://doi.org/10.1016/j.ces.2017.01.013

Zhao, H., Li, Q., Yu, G., Dai, C., & Lei, Z. (2019). Performance analysis and quantitative design of a flow-guiding sieve tray by computational fluid dynamics. AIChE Journal, 65(5), 1–13. https://doi.org/10.1002/aic.16563

Abbasnia, S., Nasri, Z., & Najafi, M. (2019). Comparison of the mass transfer and efficiency of Nye tray and sieve tray by computational fluid dynamics. Separation and Purification Technology, 215. https://doi.org/10.1016/j.seppur.2019.01.010

Biddulph, M. W., & Dribika, M. M. (1986). Distillation efficiencies on a large sieve plate with small-diameter holes. AIChE Journal, 32(8), 1383–1388. https://doi.org/10.1002/aic.690320817

Bird, R., Stewart, W., & Lightfoot, E. (1958). Transport Phenomena (2nd ed.).

Morel, C. (1995). An order of magnitude analysis of the two-phase k–e model. International Fluid Mechanics. https://doi.org/10.1615/InterJFluidMechRes.v22.i3-4.30

Dejanović, I., Matijašević, L., & Olujić, Ž. (2010). Dividing wall column-A breakthrough towards sustainable distilling. Chemical Engineering and Processing: Process Intensification, 49(6), 559–580. https://doi.org/10.1016/j.cep.2010.04.001

Dribika, M. M., & Biddulph, M. W. (1986). Scaling-up distillation efficiencies. AIChE Journal, 32(11), 1864–1875. https://doi.org/10.1002/aic.690321112

Guevara, M. A., Guevara, F. A., & Belalcazar, L. C. (2018). Experimental Data and New Binary Interaction Parameters for Ethanol- Water VLE at Low Pressures Using NRTL and UNIQUAC. TECCIENCIA, 8(24), 17–26. https://doi.org/http://dx.doi.org/10.18180/tecciencia.2018.24.3

Guevara, M., & Belalcazar, L. (2017). NGL supersonic separator: modeling, improvement, and validation and adjustment of k-epsilon RNG modified for swirl flow turbulence model. Revista Facultad de Ingeniería, 82, 82–93. https://doi.org/10.17533/udea.redin.n82a11

Higbie, R. (1935). The rate of absorption of a pure gas into a still liquid during short periods of exposure. Transactions of the American Institute of Chemical Engineers, 35, 365–389.

Kockmann, N. (2014). 200 Years in Innovation of Continuous Distillation. ChemBioEng Reviews, 1(1), 40–49. https://doi.org/10.1002/cben.201300003

Lamont, J. C., & Scott, D. S. (1970). An eddy cell model of mass transfer into the surface of a turbulent liquid. AIChE Journal, 16(4). https://doi.org/10.1002/aic.690160403

Yanagi, T., & Sakata, M. (1982). Performence of a comercial scale 14% hole area sieve tray. Industrial & Engineering Chemistry Process Design and Development, 21(4), 712–717. https://doi.org/https://doi.org/10.1021/i200019a029

Malvin, A., Chan, A., & Lau, P. L. (2014). CFD study of distillation sieve tray flow regimes using the droplet size distribution technique. Journal of the Taiwan Institute of Chemical Engineers, 45(4), 1354–1368. https://doi.org/10.1016/j.jtice.2014.01.002

Noriler, D., Barros, A. A. C., Wolf Maciel, M. R., & Meier, H. F. (2010). Simultaneous momentum, mass, and energy transfer analysis of a distillation sieve tray using CFD techniques: Prediction of efficiencies. Industrial and Engineering Chemistry Research, 49(14), 6599–6611. https://doi.org/10.1021/ie9013925

Noriler, D., Meier, H. F., Barros, A. A. C., & Wolf Macel, M. R. (2009). Prediction of efficiencies through simultaneous momentum, mass and energy transfer analyses in a distillation sieve tray by CFD techniques. In Computer Aided Chemical Engineering (Vol. 27, Issue C). Elsevier Inc. https://doi.org/10.1016/S1570-7946(09)70415-8

Olujić, Ž., Jödecke, M., Shilkin, A., Schuch, G., & Kaibel, B. (2009). Equipment improvement trends in distillation. Chemical Engineering and Processing: Process Intensification, 48(6), 1089–1104. https://doi.org/10.1016/j.cep.2009.03.004

Rahimi, M. R., Rahimi, R., Shahraki, F., & Zivdar, M. (2006). Prediction of temperature and concentration distributions of distillation sieve trays by CFD. Tamkang Journal of Science and Engineering, 9(3), 265–278.

Ranz, W. E., & Marshall, W. R. (1952). Evaporation from drops. Parts I & II. Chem. Eng. Progr, 48(22).

Sun, Z. M., Yu, K. T., Yuan, X. G., & Liu, C. J. (2007). A modified model of computational mass transfer for distillation column. Chemical Engineering Science, 62(7), 1839–1850. https://doi.org/10.1016/j.ces.2006.12.021

Van Baten, J. M., & Krishna, R. (2000). Modelling sieve tray hydraulics using computational fluid dynamics. Chemical Engineering Journal, 77(3), 143–151. https://doi.org/10.1016/S1385-8947(99)00164-3

Versteeg, H. K., & Malalasekera, W. (1995). An Introduction to Computational Fluid Dynamics The Finite Volume Method. In Fluid flow handbook. McGraw-Hill …. Longman Scitific & Technical. https://doi.org/10.2514/1.22547

Wang, T., Wang, J., & Jin, J. (2004). An efficient numerical algorithm for "A novel theoretical breakup kernel function of bubble/droplet in a turbulent flow." Chemical Engineering Science, 59(12), 2593–2595. https://doi.org/10.1016/j.ces.2004.03.011

Ashrafizadeh, S. A., Amidpour, M., & Abolmashadi, M. (2013). Exergy analysis of distillation column using concept of driving forces. Journal of Chemical Engineering of Japan, 46(7), 434–443. https://doi.org/10.1252/jcej.11we038

Bernal, D., Castellanos, O., Bejarano, P., & Rodriguez, G. (2011). Analisis y diseño de platos y columnas de platos. Universidad Nacional de Colombia.

Claumann, C. A., Peruzzo, T., Felice, V. De, Marangoni, C., & Machado, R. A. F. (2015). Modeling and process optimization: an approach using aspen plus and matlab in the energy integration study of distillation columns. VIII Congreso Argentino de Ingeniería Química y 3 JASP, 1.

Gadalla, M., Olujić, Ž., de Rijke, A., & Jansens, P. J. (2006). Reducing CO2 emissions of internally heat-integrated distillation columns for separation of close boiling mixtures. Energy, 31(13), 2409–2417. https://doi.org/10.1016/j.energy.2005.10.029

Gadalla, M. A. (2009). Internal heat integrated distillation columns (iHIDiCs)-New systematic design methodology. Chemical Engineering Research and Design, 87(12), 1658–1666. https://doi.org/10.1016/j.cherd.2009.06.005

Harvindran, V., & Foo, D. C. Y. (2021). Design of Internally Heat-Integrated Distillation Column (HIDiC). Process Intensification and Integration for Sustainable Design, 117–129. https://doi.org/10.1002/9783527818730.ch6

Heng Yeoh, G., & Tu, J. (2010). Computational Techniques for Multi-Phase Flows. ELSEVIER.

Khosravi Nikou, M. R., & Ehsani, M. R. (2008). Turbulence models application on CFD simulation of hydrodynamics, heat and mass transfer in a structured packing. International Communications in Heat and Mass Transfer, 35(9), 1211–1219. https://doi.org/10.1016/j.icheatmasstransfer.2008.05.017

Kister, H. Z. (1992). Tray Design and Operation. McGraw-Hill Professional, 1, 9–11.

Mancera, J. A., Mendoza, D. F., & Riascos, C. A. M. (2018). HIDiC configuration selection based on exergetic analysis. Chemical Engineering Transactions, 69. https://doi.org/10.3303/CET1869151

Olujic, Z., Fakhri, F., De Rijke, A., De Graauw, J., & Jansens, P. J. (2003). Internal heat integration - The key to an energy-conserving distillation column. Journal of Chemical Technology and Biotechnology, 78(2–3), 241–248. https://doi.org/10.1002/jctb.761

Pulido, Jeffrey León, Martínez, E. L., Wolf, M. R., & Filho, R. M. I. (2011). Heat transfer study of heat-integrated distillation column (HIDiC) using simulation techniques. AIP Conference Proceedings, 1373, 242–254. https://doi.org/10.1063/1.3627209

Rahimi, R., Rahimi, M. R., Shahraki, F., & Zivdar, M. (2006). Efficiencies of sieve tray distillation columns by CFD simulation. Chemical Engineering and Technology, 29(3), 326–335. https://doi.org/10.1002/ceat.200500285

Riaño, S., Guevara, M. A., & Belalcázar, L. C. (2017). CFD Modeling and Evaluation of a Bi-Stable Micro-Diverter Valve. Ciencia, Tecnologia y Futuro, 8(1), 77–84. https://doi.org/10.29047/01225383.94

Shenvi, A. A., Herron, D. M., & Agrawal, R. (2011). Energy efficiency limitations of the conventional heat integrated distillation column (HIDiC) configuration for binary distillation. Industrial and Engineering Chemistry Research, 50(1), 119–130. https://doi.org/10.1021/ie101698f

Winkle, M. V. (1967). Distillation. McGraw-Hill.

Boles, M. A., & Cengel, Yunus A. (2014). Thermodynamics: An Engineering Approach. McGraw-Hill Education. https://books.google.com.co/books?id=Ao95ngEACAAJ

de Koeijer, G., & Rivero, R. (2003). Entropy production and exergy loss in experimental distillation columns. Chemical Engineering Science, 58(8), 1587–1597. https://doi.org/10.1016/S0009-2509(02)00627-9

Delmar, T. (2019). An introduction to exergy and its evaluation using Aspen Plus. University of Utah.

Gorak, A., & Sorensen, E. (2014). Distillation: Fundamentals and Principles. Academic Press.

Grassmann, P. (1959). The exergy and the flow diagram of the technically available power. Allg Warmetech, 9, 79–86.

Jogwar, Sujit S. & Daoutidis, Prodromos (2009). Vapor Recompression Distillation: Multi-Scale Dynamics and Control. Proceedings of Amer. Control Conference, 647-652

Oliveira, S. (2013). Exergy: Production, Cost and Renewability. In Green Energy and Technology. Springer. https://doi.org/10.2174/97816080528511060101

Gadalla, M., Jiménez, L., Olujic, Z., & Jansens, P. J. (2007). A thermo-hydraulic approach to conceptual design of an internally heat-integrated distillation column (i-HIDiC). Computers and Chemical Engineering, 31(10), 1346–1354. https://doi.org/10.1016/j.compchemeng.2006.11.006

Gadalla, M., Olujic, Z., Sun, L., de Rijke, A., & Jansens, P. J. (2005). Pinch analysis-based approach to conceptual design of internally heat-integrated distillation columns. Chemical Engineering Research and Design, 83(8 A), 987–993. https://doi.org/10.1205/cherd.04301

Horiuchi, K., Nakaiwa, M., Iwakabe, K., Matsuda, K., & Toda, M. (2008). Intensification of the process flow in the pilot plant of an internally heat-integrated distillation column (HIDiC). Kagaku Kogaku Ronbunshu, 34(1), 70–75. https://doi.org/10.1252/kakoronbunshu.34.70

Mah, R. S. H., Nicholas, J. J., & Wodnik, R. B. (1977). Distillation with secondary reflux and vaporization: A comparative evaluation. AIChE Journal, 23(5), 651–658. https://doi.org/10.1002/aic.690230505

Marin, M. D., Meyer, M., Mizzi, B., & Rouzineau, D. (2018). New conceptual design methodology for a concentric heat integrated distillation column (HIDiC). Chemical Engineering Transactions, 69, 883–888. https://doi.org/10.3303/CET1869148

Naito, K., Nakaiwa, M., Huang, K., Endo, A., Aso, K., Nakanishi, T., Nakamura, T., Noda, H., & Takamatsu, T. (2000). Operation of a bench-scale ideal heat integrated distillation column (HIDiC): An experimental study. Computers and Chemical Engineering, 24(2–7), 495–499. https://doi.org/10.1016/S0098-1354(00)00513-5

Ponce, G. H. S. F., Alves, M., Miranda, J. C. C., Maciel Filho, R., & Wolf Maciel, M. R. (2015). Using an internally heat-integrated distillation column for ethanol-water separation for fuel applications. Chemical Engineering Research and Design, 95, 55–63. https://doi.org/10.1016/j.cherd.2015.01.002

Taylor, R., & Krishna, R. (1993). Multicomponent Mass Transfer. Wiley, New York.